Dye Regeneration Kinetics in Dye Sensitized Solar Cells Studied by Scanning Electrochemical Microscopy

(Kinetische Untersuchungen zur Farbstoffregeneration in farbstoffsensibilisierten Solarzellen mittels elektrochemischer Rastermikroskopie)

Von der Fakultät für Mathematik und Naturwissenschaften
der Carl von Ossietzky Universität Oldenburg
zur Erlangung des Grades und Titels eines

Doktors der Naturwissenschaften (Dr. rer. nat.)

angenommene **Dissertation**

von Herrn

M.Sc. Chemiker **Ushula Mengesha Tefashe**
geboren am 13. 10. 1978 in Wolayita, Äthiopien

Oldenburg, December 2011

This work was carried out from April 2008 to December 2011 at the Carl von Ossietzky University of Oldenburg, Faculty of Mathematics and Science, Center of Interface Science (CIS), Department of Pure and Applied Chemistry under the supervision of Prof. Dr. Gunther Wittstock.

Part of this work has been published and is cited as [A#]. The list of own work cited is given after the Bibliography.

Gutachter:	Prof. Dr. Gunther Wittstock
Zweitgutachter:	Prof. Dr. Rüdiger Beckhaus
Tag der Disputation:	19.03.2012

Abstract

The overall efficiency of light-induced charge separation in dye-sensitized solar cells (DSSCs) depends on the kinetic competition between back electron transfer and dye regeneration processes by the redox electrolyte. This thesis reports a comprehensive series of experiments involving local measurements of dye regeneration kinetics. The reduction of intermittently formed photo-oxidized dye molecules by iodide ions from the electrolyte was investigated using the feedback mode of scanning electrochemical microscope (SECM). This was illustrated by model DSSCs based on Eosin Y or indoline dye (D149)-sensitized zinc oxide and ruthenium dye (N719)-sensitized titanium oxide in iodide/tri-iodide (I^-/I_3^-) electrolyte. A quantitative model was developed and verified by studying the regeneration rate at different excitation wavelength, light intensities and mediator concentrations. Further refinement of the model was performed to consider detailed molecular mechanism of the regeneration process that involves intermediate species. Different film thickness and dye content in the films was investigated to understand the influence of internal mass transport by systematically varied internal film structure. These experiments were compared to steady-state photoelectrochemical and time-resolved photovoltage measurements. The effect of electrolyte cations and solvent identities on regeneration rate was also measured by SECM feedback mode. In addition to steady-state feedback mode, SECM in chronoamperometic regime was also investigated. Further experiments about shear force based distance regulation for high resolution SECM was developed and demonstrated with various model surfaces. This was intended to open the way for high resolution SECM imaging of DSSC.

Zusammenfassung

Die Gesamteffektivität der lichtinduzierten Ladungstrennung in farbstoffsensibilisierten Solarzellen (DSSCs) hängt von der kinetischen Konkurrenz zwischen Elektronenrücktransfer und Farbstoffregenerationsprozessen durch den Redoxelektrolyten ab. In dieser Dissertation wird eine Reihe von Experimenten vorgestellt, die sich mit lokalen Messungen der Farbstoffregenrationskinetik befassen. Die Reduktion der intermediär gebildeten photooxidierten Farbstoffmoleküle durch Iodidiionen aus der Lösung wurde mit Hilfe eines elektrochemischen Rastermikroskops (SECM) im Feedback-Modus untersucht. Dazu wurden Modell-DSSCs bestehend aus mit Eosin Y oder Indolinfarbstoff (D149) sensibilisiertem Zinkoxid, bzw. mit Rutheniumfarbstoff (N719) sensibilisiertem Titandioxid in Iodid/Triiodid-Elektrolyt (I^-/I_3^-) verwendet. Zur Interpretation wurde ein quantitatives Modell entwickelt und anhand der Regenerationsgeschwindigkeit bei unterschiedlichen Anregungswellenlängen, Lichtintensitäten und Mediatorkonzentrationen überprüft. Dieses Modell wurde für den detaillierten molekularen Mechanismus des Regenrationsprozesses weiter verfeinert. Unterschiedliche Filmdicken und Farbstoffgehalte in den Filmen wurden untersucht, um den Einfluss des internen Massentransports bei systematisch variierter innerer Filmstruktur zu verstehen. Diese Experimente wurden mit integralen stationären und zeitaufglösten photoelektrochemischen und zeitaufgelösten Messungen verglichen. Der Einfluss von Elektrolytkationen und Lösungsmittel auf die Regenerationsgeschwindigkeit wurde ebenfalls mit SECM im Feedback-Modus untersucht. Zusätzlich zu Messungen im stationären Feeback-Modus wurde auch chronoamperometrische Messungen herangezogen. Weiterhin wurden Experimente zur scherkraftbasierten Abstandsregulierung für hochauflösende SECM entwickelt und mit unterschiedlichen Modelloberflächen getestet. Damit soll der Weg für hochaufgelöste SECM-Bildgebung an DSSCs eröffnet werden.

Acknowledgement

I offer my deepest gratitude and special affection first and foremost to my supervisor Prof. Dr. Gunther Wittstock, for introducing me to the field of scanning electrochemical microscopy and for his unlimited, excellent guidance, encouragement followed by suggestions and comments. The convenient working environment he has created is greatly appreciated. It is great privilege to work with him. I would also like to express my sincere gratitude to Prof. Dr. Rüdiger Beckhaus for writing me reference letters to recommend my scholarship extension and for accepting as a second examiner for my PhD.

Special thanks are due to Prof. Dr. Derck Schlettwein and his graduate students, Dr. Thomas Loewenstein and Ms. Melanie Rudolph, at the Justus Liebig University of Giessen for valuable collaboration and joint work. The discussions with them always brought up interesting ideas for new studies and possible interpretations of the data. Part of this thesis was developed in collaboration with Prof. Dr. Anders Hagfeldt at the University of Uppsala. I would like to express my thanks to him and his team members, Dr. Kazuteru Nonomura and Dr. Dr. Nikolaos Vlachopoulos for our joint work. I am indebted to all my former and current colleagues in the group of Prof. Dr. Gunther Wittstock for their help in one way or another for my success.

It is my pleasure to express my due thanks to Dr. Pooi See Lee from Nanyang Technological University and Dr. Guy Denuault from University of Southampton for ongoing valuable discussion and for the exchange of knowledge.

I would like to express my sincere thanks to my family for their encouragement and unlimited help during the whole work both emotionally and physically. German Academic Exchange Service (DAAD) is gratefully acknowledged for sponsoring this doctoral work. I further thank the Max Buchner Research Foundation grant for the ongoing project on high resolution scanning electrochemical microscopy.

Table of Contents

1. Introduction

Energy flows from many sources, it exists in a variety of interchangeable forms and drives all systems. It is fundamental to the quality of our lives and human beings are entirely dependent on an abundant and uninterrupted supply of energy for living and working. It is the essence of the sustainability of the human civilization. Presently, the global energy supplies depend predominantly on fossil fuels (e.g. oil, natural gases and coal) and nuclear technologies [1, 2]. Depletion of fossil fuel reserves in the near future along with dangerous environmental pollution and a very tight safety regulation in modern nuclear energy necessitates imperatively the use of alternative energy sources.

Renewable energy sources such as the solar radiation, wind, hydromechanical and geothermal energy are clean, cheap, available in plentiful supply and do not introduce direct contamination of the environment. With the exception of hydromechanical power stations that are bound to selected geographic locations, they require relatively low cost instruments for the energy conversion and they deliver the energy in low energy density format. This may be an advantage, if an expensive energy distribution infrastructure is not needed. Alternatively, solar energy technologies can provide significant socio-economic benefit in areas such as Africa, where large parts of the population still live in remote areas without access to electrical grid structure and in extreme poverty. Therefore, renewable energy resources and their technology can provide direct and rapid benefit at local and national level besides contributing to a more sustainable global energy balance.

Solar energy is available at any location on the earth’s surface and considered to be one of the most promising renewable energy sources for our future energy needs. The total amount of solar radiation striking earth's atmosphere is approximately 174 PW which is over 10^4 times the entire global energy consumption [3]. Also, the area that needs to be covered with solar panels to power the whole world economy is no more than 10^5 km^2. These indicate the enormous potential that lies in the Sun, even if some practical issues limit its full scale utilization. As a result considerable research work has been aimed at harnessing solar energy. Solar cells (photovoltaic cells) are the smallest basic unit of solar electric devices that convert solar energy directly into electrical energy. The first experiment on photovoltaic solar energy conversion was performed in 1839 by the French physicist E. Becquerel [4], who demonstrated that photovoltage and photocurrent are produced when a silver coated platinum electrode in an electrolyte solution is illuminated. But the modern era of photovoltaics began only in 1954 at Bell Laboratories when Chapin, Fuller and Pearson reported a solar conversion efficiency of 6% for a single crystal silicon *p-n* semiconductor junction cell [5]. Since that time continued research effort has lead to various types of solar cells and some of them will be briefly addressed in the following paragraphs.

Crystalline silicon solar cells are the most efficient and widely used solar cells to date. The theoretical efficiency limit for this type of device is about 31% [6]. Stable devices and the possibility to use knowledge and technologies from the microelectronics industry have given crystalline solar cells a leading role among other types of solar cells. To meet the demand of reducing material and purification costs thin film solar cells have been developed. Thin film solar cells are based on thin layers of various semiconductor materials such as amorphous silicon, cadmium telluride (CdTe) [7] and copper indium gallium diselenide (CIGS) [8]. Even though the thin film solar cell requires less material, the complex production processes of the different combinations of rare materials are expensive and may limit a future large-scale production.

An alternative solar cell technology is the dye-sensitized solar cell (DSSC) also known as Grätzel cell [9], which has attracted much attention and is the subject of this thesis. They are based on nanocrystalline metal oxide electrodes. As such they can be inexpensive, light weight, portable, flexible and transparent relative to classical solid state heterojunction solar cells [9-11]. The fundamental difference between DSSCs and *p-n* junction solar cells is the functional components. In the latter, the semiconductor assumes both the task of light absorption and charge carrier transport, while these two functions are separated in the DSSC. Furthermore, the solar energy conversion mechanism in DSSC accentuates the interfacial processes rather than the bulk processes as in *p-n* junction cells [12]. Hence, most studies on DSSC are intended to understand the prevailing role of electron transfer dynamics and kinetics at nanocrystalline metal oxide/sensitizer dye/electrolyte interfaces [13]. Despite enormous and continued research on this subject, limited understanding of the kinetics of the interfacial processes remains an impediment to improve the efficiency and to scale up DSSC manufacturing. This is partly due to the experimental difficulties encountered with conventional electrochemical, photoelectrochemical and spectroscopic measurement techniques. Most commonly the dye regeneration kinetics has been studied by transient absorbance techniques and it has been proven that its regeneration reaction does not produce any measurable electrical signal [14].

The objective of the work presented in this thesis was to investigate the kinetics of dye regeneration by redox ions from the electrolyte using a novel electroanalytical technique based on scanning electrochemical microscopy (SECM). SECM has already been proven to be a powerful technique to investigate heterogeneous kinetics involved in processes of particular relevance for energy production [15-17] (see Section 4.4). Using SECM, the quantification of dye regeneration kinetics is based on the measurement of steady state feedback mode approach curves on the illuminated DSSC sample. As model DSSCs Eosin-Y/ZnO, D149/ZnO and N719/TiO_2 based photoelectrodes were investigated in contact with an electrolyte containing the iodide/tri-iodide (I^-/I_3^-) redox couple. Other works concerning non-optical shear force distance control was intended to open the way for high resolution

SECM imaging of DSSC. At the illuminated dye-sensitized electrode, the inhomogeneity in localized photoelectrochemical activity was investigated with nanoelectrode SECM probes.

2. Principle of photoelectrochemical solar energy conversion

One of the many research fields which show promise for solar energy conversion is photoelectrochemistry [18, 19]. Photoelectrochemical reactions for solar photon conversion are usually directed to produce either electric power (photovoltaics) or making chemical products through a chemical change in the electrode or in a compound contained in the electrolyte (solar fuels). Since the photoeffects at electrodes are typically bound to semiconductor electrodes, there has been continued interest in understanding of such electrodes. Gerischer [20, 21] conducted pioneering electrochemical and photoelectrochemical studies on semiconductor electrodes. Subsequently, application of this knowledge to energy conversion was revealed by Fujishima et al. in 1969 [22], who demonstrated the photodecomposition of water at a TiO_2 electrode. Several review articles and books have been published on this subject [23-30]. This thesis deals with charge transfer kinetics in dye-sensitized photoelectrochemical cells for conversion of solar energy to electrical energy.

In the following Section, an overview of the fundamental principles of photoelectrochemical solar energy conversion based on solid-state semiconductor will be discussed. Knowledge of these provides a starting point for understanding the behaviour of dye-sensitized photoelectrochemical cells presented in the next Chapter. Several detailed reviews covering the science and application of semiconductor-electrolyte junction photoelectrochemical cells (PECs) are available [20, 21, 31].

2.1. The semiconductor/electrolyte interfaces

Every solid has a characteristic energy band structure, and the difference in electrical properties depends on the Fermi level E_F. The Fermi level denotes the energy at which the probability that a state occupied amounts to 50%. The band gap E_g is the difference between the highest energy of the valence band E_{VB} and the lowest energy of the conduction band E_{CB}.

According to electronic band theory there are three classes of solids materials: metals, semiconductors and insulators distinguished by E_g. Figure 2.1 shows the energy diagram and the occupation of the bands in these materials. In metals two situations occur. Either the uppermost energy band containing electrons is only partially filled, or alternatively, a filled band overlaps with empty band. These electrons are free to move in a field, since at the energy E_F occupied and unoccupied orbitals are available in large number. This results in very high conductivities. In insulators the valence band VB is fully occupied, the conduction band CB is empty and no net motion of charge results from the application of an electric field. An insulator typically has E_g > 4 eV. In semiconductors the situation is similar to that in insulators, except that the band gap is smaller. Semiconductor E_g commonly fall in the range of 1–4 eV [31]. By thermal or optical excitation, an electron can be excited from the VB to the CB. This process generates charge carriers (a mobile electron in CB and a hole in the valence band). On account of their favourable optoelectronic properties and chemical versatility, semiconductors have been electrode materials of choice for solar photoconversion.

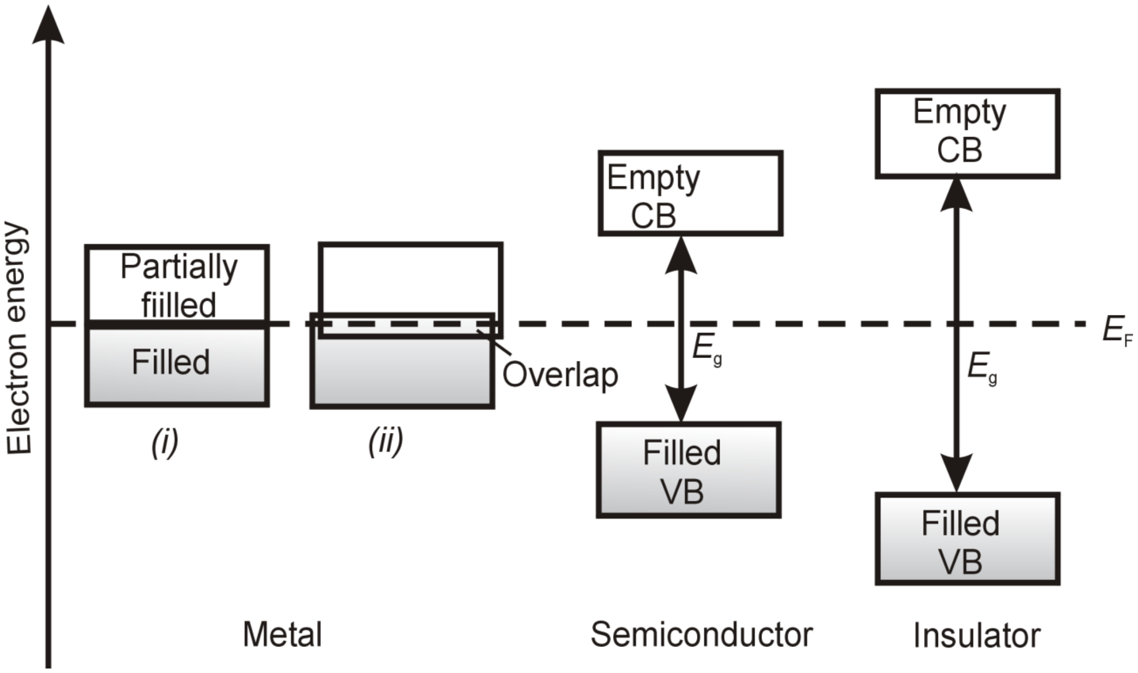

Figure 2.1 A schematic of energy band diagrams showing electron occupation for metals, semiconductors and insulators

For semiconductors the electrochemical potential of electron is given by the Fermi level. Changes in electrode potential of the semiconductor or doping it with another material change the position of its Fermi level with respect to the reference energy, which is the energy of an electron in vacuum. For intrinsic semiconductors the Fermi level lies at the midpoint of the band gap (Figure 2.1). The electrochemical potential of the solution phase is determined by the redox potential in the electrolyte. For a reversible redox system (O + $ne^- \rightleftharpoons$ R), this is given by the Nernst equation [31].

$$E_{\mathrm{redox}} = E^{\mathrm{o}}_{\mathrm{redox}} + \frac{RT}{nF}\ln\left(\frac{a_{\mathrm{O}}}{a_{\mathrm{R}}}\right) \tag{2.1}$$

in which $E^{\mathrm{o}}_{\mathrm{redox}}$ is the standard redox (O is oxidized form and R is reduced form) potential of the redox couple, a_{O} and a_{R} are the activities of the oxidized and reduced species of the redox system, and n is the number of electrons that are exchanged per molecule. Usually, concentration instead of activity is employed given by $a = \gamma c$, where γ is the activity coefficient. If supporting electrolyte is used γ remains constant and the term of the activity coefficients is summarized with $E^{\mathrm{o}}_{\mathrm{redox}}$ to the formal potential $E^{\mathrm{o}\prime}_{\mathrm{redox}}$.

$$E_{\mathrm{redox}} = E^{\mathrm{o}}_{\mathrm{redox}} + \frac{RT}{nF}\ln\left(\frac{\gamma_{\mathrm{O}}c_{\mathrm{O}}}{\gamma_{\mathrm{R}}c_{\mathrm{R}}}\right) = E^{\mathrm{o'}}_{\mathrm{redox}} + \frac{RT}{nF}\ln\left(\frac{c_{\mathrm{O}}}{c_{\mathrm{R}}}\right) \tag{2.2}$$

The electrochemical potential of a redox system is given with respect to a reference, usually the normal hydrogen electrode (NHE).

To treat the process occurring in photoelectrochemical cells (PECs) quantitatively, the Fermi level of the semiconductor and that of the electrolyte must be placed on a common energy scale. Using the absolute energy scale, the energy of a redox couple ($E_{\mathrm{F,redox}}$) is given by

$$E_{\mathrm{F,redox}} = E_{\mathrm{ref}} - eE_{\mathrm{redox}} \tag{2.3}$$

where E_{redox} is the redox potential versus NHE and E_{ref} is the energy of the reference electrode versus the vacuum level. The usual value of E_{ref} taken for NHE is -4.5 eV, although measurements range from -4.5 to -4.7 eV [32-34]. Then Eq. (2.3) could be re-written as $E_{\mathrm{F,redox}} = -4.5\ \mathrm{eV} - eE_{\mathrm{redox}}$ with respect to vacuum level. The relationship between energy in a semiconductor and the electrochemical potential in an electrolyte, using the solid state scale and that of the electrochemical scale of a redox couple, are shown in Figure 2.2.

Most of the PECs are quite analogous to Schottky barrier solar cells, with the metal layer being replaced by an electrolyte containing a redox couple. Both ZnO and TiO_2 used in this work are *n*-type semiconductor. When an *n*-type semiconductor is brought into contact with an electrolyte containing a redox couple R and O, rapid exchange of electrons between the redox species and the electrode occurs because of the difference in electrochemical potentials. If the initial Fermi level (or electrochemical potential) in a semiconductor is above the initial Fermi level in the electrolyte, then the equilibration of the two Fermi levels occurs by transfer of electrons from the semiconductor to the electrolyte, i.e., a reduction of O. This lowers the Fermi level in the semiconductor. The net charge transfer process stops when the electrochemical potentials of both phases are equal, that is, when equilibrium has been reached. This produces a positive space charge layer in the semiconductor (also called a depletion layer since the region is depleted of majority charge carriers) and a negative charge in the electrolyte. As a result the conduction and valence band edges are bent upward such that a potential barrier is established against further electron transfer into the electrolyte (Figure 2.3). Like the situation in Schottky barrier, the magnitude of the potential barrier is determined by the bulk properties of the semiconductor, the redox level in the electrolyte, and by the interface properties of the junction.

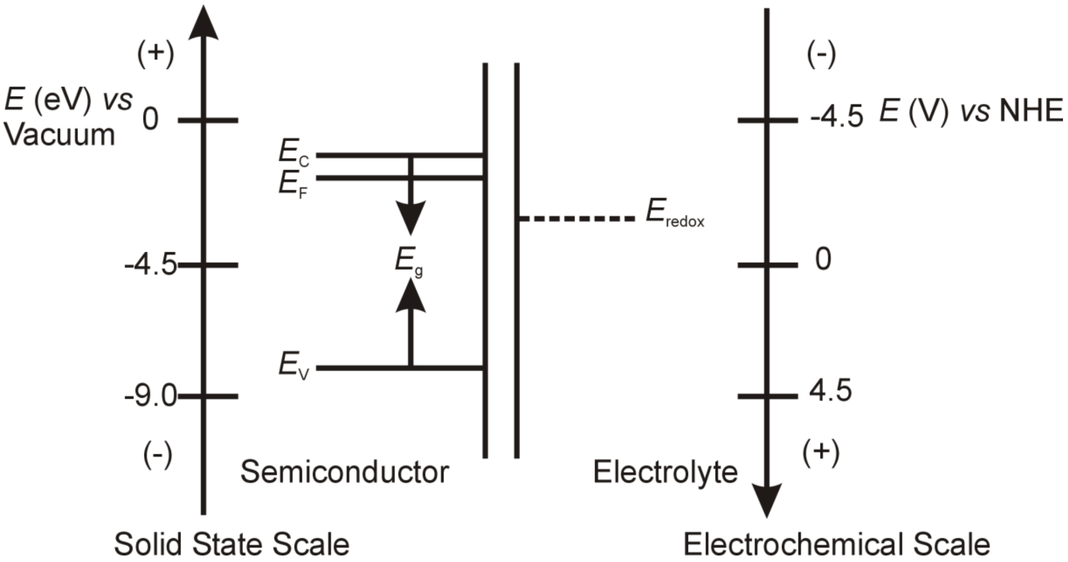

Figure 2.2 Schematic showing the relationship between the energy in semiconductor and the electrochemical potential in an electrolyte. E_F is the energy Fermi level, E_C the conduction band edge, E_V the valence band edge, and E_g the energy band gap.

The inverse but analogous situation occurs with *p*-type semiconductors having an initial Fermi level below that of the electrolyte. A negative charge depletion layer is formed in the semiconductor, with the valence and conduction bands bending downward to produce a potential barrier against further hole transfer into the electrolyte.

A charged layer, known as the Helmholtz layer, also exists in the electrolyte adjacent to the interface with the solid electrode. This layer consists of ions from the electrolyte adsorbed onto the solid electrode surface. These ions are of opposite sign to the charge induced on the solid electrode. The width of the Helmholtz layer is generally on the order of a few Angstroms. The potential drop across the Helmholtz layer depends upon the specific ionic equilibrium at the surface. A very important consequence of the presence of the Helmholtz layer is that it markedly affects the band bending that develops in the semiconductor when it equilibrates with the electrolyte. Without the Helmholtz layer, the band bending would simply be expected to be equal to the difference in initial Fermi levels between the two phases (i.e, the difference between their respective work functions).

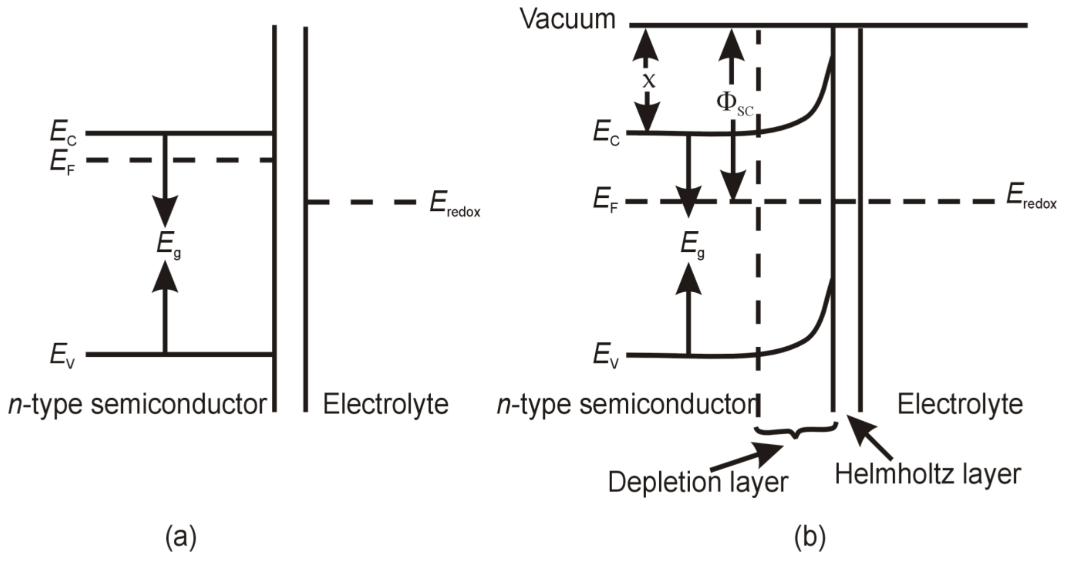

Figure 2.3 Energy level diagram for the junction between an *n*-type semiconductor and an electrolyte in the dark. (a) Before contact. (b) After contact and equilibrium condition. ϕ_{SC} is the work function and χ the electron affinity.

Because of the high charge density and small width of the Helmholtz layer, the potential drop across the Helmholtz layer does not vary with applied electrode potential or charge transfer across the semiconductor/electrolyte interface. Instead, all of the externally applied voltage drops across the depletion layer in the semiconductor. Consequently, at a given electrolyte composition the band edges of the semiconductor at the surface are fixed with respect to the redox potential of the liquid electrolyte, and are independent of the applied voltage across the semiconductor/electrolyte interface.

2.2. Photoinduced charge transfer at the semiconductor/electrolyte interface

To convert solar energy into electrical energy and/or chemical energy, a current must flow across the semiconductor/electrolyte junction [19]. In the dark, no current flows in the cell. When *n*-type semiconductor/electrolyte junction is illuminated with light, photons having energies greater than E_g are absorbed whereby, electrons are freed from the VB and move into the CB. The free charges can then be separated under influence of the electric field present in the space charge region. The electric field in the space charge does not require a constant energy input from an external source; rather, it occurs spontaneously whenever two phases with different electrochemical potentials (Fermi potentials) are brought into contact. Electron-hole pairs produced by absorption of photons beyond the depletion layer will separate if the minority carriers can diffuse to the depletion layer before recombining with majority carriers. If they do not disappear by recombination, either by direct coulombic interaction or by collision with other carriers in their path through the space charge layer, the minority carriers in the semiconductor are swept to the surface where they are subsequently “injected into the electrolyte” i.e., they derive an electrolysis. On the other hand, the majority carriers are swept towards the semiconductor bulk, where they subsequently leave the semiconductor via an ohmic contact. The current loop can be closed by a metallic counter electrode where the reverse reaction to that at semiconductor/solution interface occurs. Since the electrons and holes travel in opposite directions, a continuous current will flow as long as the cell is illuminated and connected to an external load. The type of the redox species used is governed by the type of the semiconductor and the position of the energy bands. For *n*-type semiconductors, minority holes are injected to produce an oxidation reaction, while for a *p*-type semiconductors, minority electrons are injected to produce a reduction reaction. Oxidations for *n*-type semiconductors will occur from holes in the valence band if the solution species Fermi level lies above the surface valence band level, that is the *n*-type semiconductor electrode acts as a photoanode. Reductions for *p*-type semiconductors will occur from electrons in the conduction band if the solution species Fermi level lies below the surface conduction band level. The representation of photoelectrochemical process in band energy terms for *n*-type semiconducting photoelectrode is shown in Figure 2.4.

The photogeneration causes the Fermi level in the semiconductor to return towards its original position, before the semiconductor/electrolyte junction was established (Figure 2.4). Under open circuit conditions between an illuminated semiconductor electrode and a metal counter electrode, a photovoltage is produced. The photovoltage produced between the electrodes is equal to the difference between the Fermi level in the semiconductor and the redox potential of the electrolyte. Under short circuit conditions, the Fermi level in the system is equalised and photovoltages exist between the two electrodes.

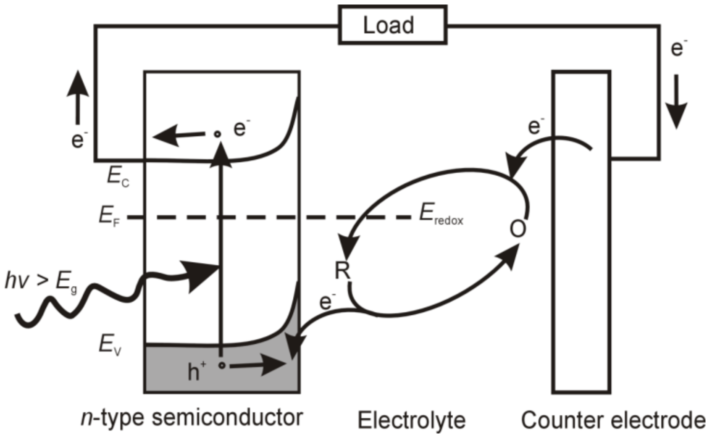

Figure 2.4 Energy level diagram of a junction between a semiconductor and an electrolyte under illumination.

3. Dye sensitized solar cells

As introduced in Chapter 1, DSSCs exhibit a range of interesting features as inexpensive renewable energy sources [11, 35]. As the basis of DSSCs, the dye-sensitization technique was started in 1873 by Vogel in Berlin, in which he associated dyes with silver halide grains [36]. Systematic mechanistic studies started only in the late 1960's by Gerischer and Memming with a dye-sensitisation process on ZnO [37] and SnO_2 [38, 39] electrodes. The breakthrough of DSSC was achieved using mesoporous TiO_2 electrodes with high surface area by B. O'Regan and M. Grätzel [9]. At the time of writing this thesis, the record efficiency of a DSSC reached 12.3% [40] based on dye-sensitised mesoporous TiO_2 electrodes in contact with an electrolyte containing a cobalt complex redox electrolyte for dye regeneration. However, the most often used system relay on the iodide/tri-iodide system [9, 41-45]. Record efficiencies for those cells are 11.3%. However, most cells reach efficiencies in the range of 4-9%.

In general, intensive research work is underway to understand the parameters that control the performance of these devices in order to improve the conversion efficiency and stability. Special attention has focused on the development of sensitizers to harvest a larger region of the solar spectrum [42, 46-53]. Efforts were made to develop highly porous nanostructured films consisting of semiconductors with a wide band gap [54-58]. Attempts are also in progress to optimize the redox electrolyte [58-64].

Most of the current researches on DSSC focus on understanding the mechanism of operation in order to find a way to improve the performance efficiency of these devices. Among these the sequence of events during light to electrical energy conversion, i.e., photon absorption, charge separation, dye regeneration, electron injection, diffusion and recombination, plays a pivotal role to influence the efficiency.

In the following Sections the materials, their properties and methods used to investigate the physics and chemistry occurring in DSSCs will be described. The description also highlights the different disciplines contributing to an understanding of DSSC operation.

3.1. Materials, device structure and operational principle

The photoelectrode in DSSC is a dye-sensitized mesoporous semiconductor attached to a conducting substrate. The conducting substrate is usually a plate of glass coated with a thin layer of transparent conducting oxide layer; usually fluorine doped tin oxide (FTO) or indium tin oxide (ITO). Most of the earlier studies on DSSC used nanocrystalline TiO_2 in the anatase form as wide band gap semiconductor. It is preferred because it is chemically inert, non-toxic, transparent to the visible region of light, easy to produce in large scale at low cost and it can be sensitized by a large variety of dyes, allowing efficient energy conversion.

In addition to TiO_2 other semiconductor materials such as ZnO, SnO_2, and Nb_2O_5 have been investigated as alternatives. ZnO has attracted particular interest because it offers good electrical properties (e.g. a high electron mobility) [65, 66] and can be synthesized with high crystallinity under mild conditions, which allows its deposition on temperature-sensitive substrates like plastics or textiles [58, 67, 68]. Electrochemical deposition in the presence of a structure-directing agent (SDA) represents a low-temperature (~70°C) and low-cost method for the preparation of porous yet highly crystalline ZnO electrodes that are well suited for application in dye-sensitized solar cells [58, 69-71]. The processing at low temperature also decreases the energy “investment” necessary to produce the cells. Except for ZnO which was usually synthesized electrochemically, others were usually synthesised chemically by sintering or pressing semiconducting nanoparticles onto the conducting substrate. The film thickness can range up to 30 µm and has porous structures with a large internal surface.

Details about the preparation procedure of TiO_2 and ZnO nanoporous films are given in Section 5.2.

Figure 3.1 shows the surface band gap energies of some semiconducting materials in comparison to the elemental silicon for photoelectrochemical application [18]. Due to the large bandgap energy of the semiconductors (~3.2 eV), they only absorb light in the UV region of the solar spectrum. To increase the efficiency by the absorption of more light, the films are sensitized with a dye. The sensitization ideally creates a monolayer of dye attached to the semiconductor surface.

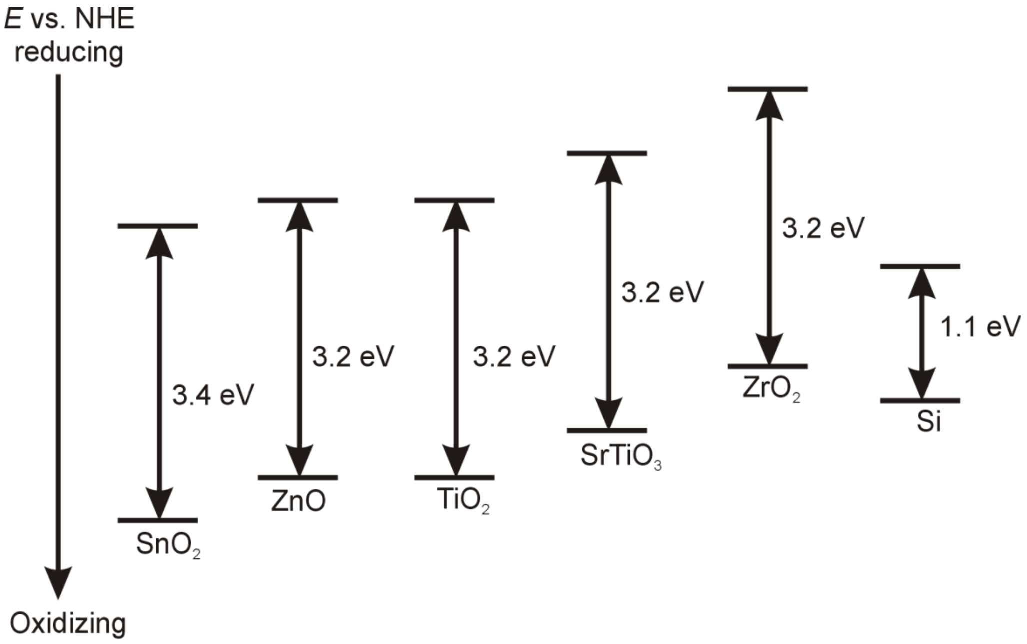

Figure 3.1 Relative position of band edges in various semiconductor metal oxides shown with respect to NHE. The numbers indicate E_g.

Dyes serve as the solar energy absorber in DSSC, whose properties will have much effect on the light harvesting efficiency and the overall photoelectric conversion efficiency. The ideal sensitizer for DSSCs should absorb all light below a threshold wavelength of about 920 nm. In addition, it should be firmly grafted to the semiconductor oxide surface and inject electrons to the conduction band with a quantum yield of unity. Its redox potential should be sufficiently high that it can be regenerated rapidly via electron donation from the electrolyte or a hole conductor. Finally, it should be stable enough to sustain at least 10^8 redox turnovers under illumination corresponding to about 20 years of exposure to natural light [72]. The commonly used dyes in DSSC research are inorganic ruthenium compounds [73]. Due to their practical importance they are named by short codes. For instance N719 stands for di-tetrabutylammonium cis-bis(isothiocyanato)bis(2,2′-bipyridyl-4,4′-dicarboxylato)ruthenium (II) and N3 stands for cis-bis(isothiocyanato) bis(2,2’-bipyridyl-4,4’-dicarboxylato ruthenium(II). Organic dyes such as Eosin Y (disodium 2-(2,4,5,7-tetrabromo-6-oxido-3-oxoxanthen-9-yl)benzoate) and inodline dye D149 (5-[[4-[4-(2,2-diphenylethenyl)phenyl]-1,2,3,3a,4,8b-hexahydrocyclopent[b]indol-7-yl]methylene]-2-(3-ethyl-4-oxo-2-thioxo-5-thiazolidinylidene)-4-oxo-3-thiazolidineacetic acid) showed efficient light harvesting and are promising due to their shorter and simpler synthesis route [69]. They do not contain rare elements like Ru. The structural formulas of all of these dyes are shown in Figure 3.2. The efficiency record is 11.3% for dye sensitized solar cells based on Ru dye with I^-/I_3^- electrolyte [74]. The Grätzel group [75] reported a 9.03% conversion efficiency for solar cells with D149 as sensitizer after optimizing nanocrystalline TiO_2 films.

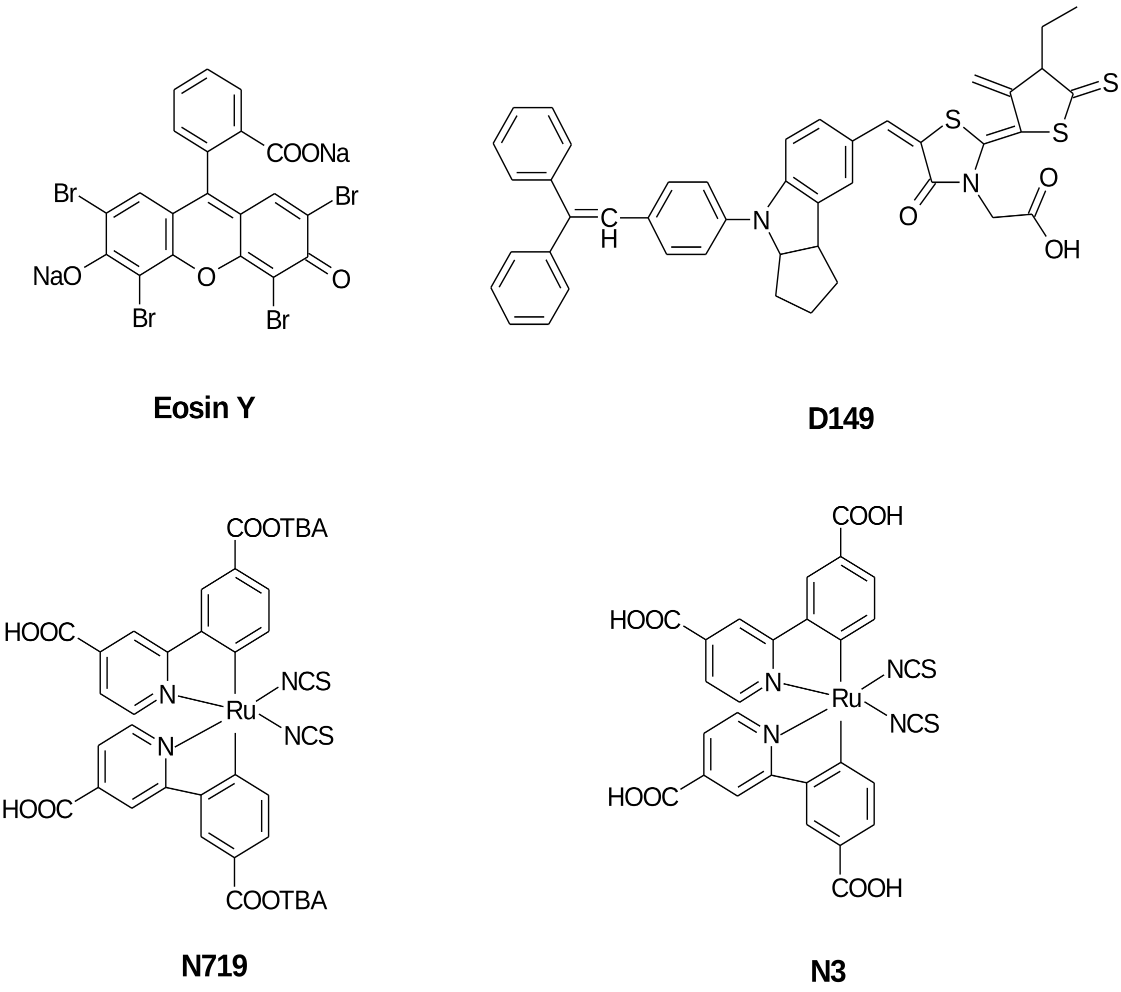

Eosin Y **D149**

N719 **N3**

Figure 3.2 Chemical structures of sensitizing dyes used in these studies

The electrolyte components can range from simple ionic species in a solvent to conducting polymers. It is a key component in DSSC and its properties have much effect on the conversion efficiency and stability of the solar cells. Most often used electrolyte contained a redox couple (I^-/I_3^-) with counter ions (e.g., Li^+, K^+, Na^+, Mg^{2+}, or tetrabutylammonium TBA^+) [9, 76-78] and additives (e.g. 4-tert-butylpyridine 4TBP, 1-methylbenzimidazole or guanidium thiocyanate) in organic solvent (e.g. acetonitrile, propylene carbonate, methoxyacetonitrile or ethylene carbonate). The redox couple I^-/I_3^- is typically employed to reduce the photo-oxidized dye. Full details of the characteristics of I^-/I_3^- redox mediator in SECM-DSSC measurements can be found in Section 6.1. Developing alternatives to the I^-/I_3^- couple, including $(SeCN)_2/SeCN^-$, $(SCN)_2/SCN^-$ [62, 79], Br_3^-/Br^- [80] and Co(II)/Co(III) [63] is an active area of research, although device efficiencies remain relatively low for these couples because they have slower kinetics at the counter electrode and lead to photovoltage losses.

The main problem of DSSC is sealing permanently an organic solvent. To avoid this problem, hole conducting polymers and room temperature ionic liquids (RTIL) have been introduced [59, 81-83]. The use of RTILs as one of the solvents is particularly interesting and relevant, as many researchers believe that RTILs may one day replace conventional solvents in DSSC. RTILs as non-volatile solvents for DSSC can simultaneously serve as iodide source. In addition to desirable low vapor pressure, ionic liquids also possess high electrical conductivity, non-flammability and good electrochemical stability [59, 84]. Their main disadvantage, however, is high viscosity resulting in low diffusion coefficients of redox active species [59]. Most widely used RTILs in DSSC are imidazolium compounds [78, 85, 86].

The counter electrode is commonly a glass plate with an ITO or FTO layer covered with a catalytic layer of platinum (Pt). The Pt is required onto ITO because it improves charge transfer kinetics between ITO and I^-/I_3^- redox couple. It is known that the I^-/I_3^- oxidation-reduction reaction is irreversible at bare ITO.

The basic structure of DSSC for completed DSSC is shown in Figure 3.3. It contains a dye-sensitized metal oxide working electrode, the I_3^-/I^- redox electrolyte, and a counter electrode.

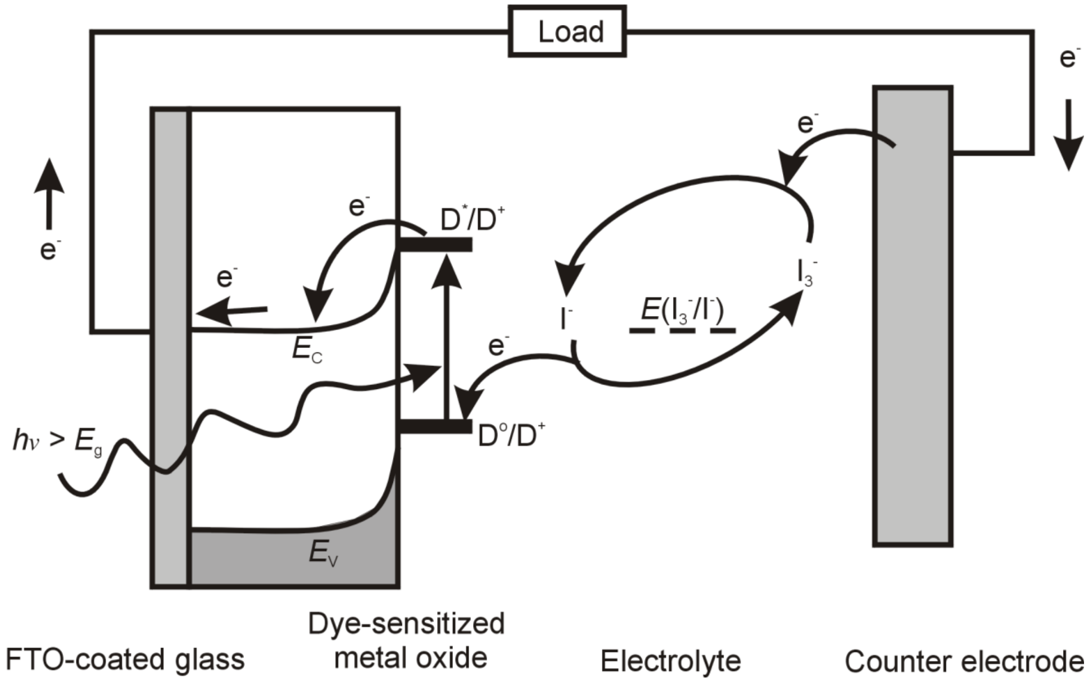

Figure 3.3 The basic structure of a completed working dye-sensitized solar cell.

The absorption of photons by the adsorbed dye molecules results in dye photo-excitation

$$\mathrm{D} + \mathrm{h}\nu \xrightarrow{\phi_{h\nu} J_{h\nu}} \mathrm{D}^* \tag{3.1}$$

which then rapidly injects electron into the conduction band of a wide band gap semiconductor

$$\mathrm{D}^* \xrightarrow{k_{\mathrm{inj}}} \mathrm{D}^+ + \mathrm{e}^- \tag{3.2}$$

After a successful injection, the charge separation takes place in such a way that the oxidized dye is positively charged and the semiconductor is negatively charged. The electrons in the semiconductor are transported through the mesoporous network and are collected at the back contact (FTO). The reduced species of the redox couple (I^-) in the electrolyte will then regenerate the oxidized dye

$$\mathrm{D}^+ + 1.5\mathrm{I}^- \xrightarrow{k_{\mathrm{ox}}} \mathrm{D} + 0.5\mathrm{I}_3^- \tag{3.3}$$

The sustained regeneration of oxidized dye requires a constant supply of new I^- species, which is produced at the counter electrode in completed cell or at the SECM probe

$$I_3^- + 2e^- \rightarrow 3I^- \qquad (3.4)$$

The regeneration of dye molecules by electron transfer (ET) from dissolved electron donors in the electrolyte is crucial to the operation of the cell, because it is the necessary elementary step to produce a photocurrent [87]. Fast kinetics of this regeneration step are required in order to suppress competing decomposition reactions of the photooxidized dye and the back transfer of electrons from the conduction band of the semiconductor, a major recombination route and hence loss mechanism in DSSC. The energy conversion scheme in Figure 3.3 relies on a series of sequential photoelectrochemical reactions that are kinetically coupled (serial arrangement) and in competition with others that lead to energy dissipation (parallel arrangement). The efficiency of photocurrent formation depends on the relative magnitudes of the reaction rates of the involved sequential and competing reactions. Detailed description on this subject is given in Section 3.2.

3.2. Charge transport mechanism and interfacial kinetic processes

DSSC is a heterogeneous solar cell where the charge carriers are electrons in porous oxide film and redox species in a liquid electrolyte. For efficient solar energy conversion, it is essential to maintain the separated charge carriers in their respective independent conduction channels until they are collected at the contacts. Several researchers reported that charge transport in nanostructured materials depends on the chemical structure and morphology of the film, and the properties of electrolyte in the pores. Electron transport in the film is inherently coupled to the ion transport in solution. Once the electron entered into the conduction band, its transient electric fields is screened by the ions in solution. As a result it does not feel the positive charge of the photo-oxidized dye [88]. This facilitates charge separation and reduces the probability of electron back transfer.

Different mechanisms for the charge transport in DSSC have been discussed in the literatures, e.g. tunneling through potential barriers between the particles [89] and a trapping/detrapping mechanism [90, 91]. These mechanisms are all random walk processes and cannot always be separated out by the measurements. Various studies have shown that the transport of electrons in TiO_2 or ZnO films occurs via diffusion rather than drift [92-94]. A general one dimensional diffusion equation is usually considered to describe a steady state electron transport in nanostructured material:

$$\frac{\partial n(x)}{\partial t} = D_{\text{eff}} \frac{\partial^2 n(x)}{\partial x} + G(x,t) - R(x,t) = 0 \tag{3.5}$$

where D_{eff} is the effective diffusion coefficient for the electrons coupled to its image charge, x is distance from the back contact, t is time, n is electron concentration, G is generation rate and R is recombination rate of electrons. This expression tells us that the difference of generation (G) and recombination of electrons (R) is balanced by the diffusion of electrons at the steady state. Detailed description of the steady state solutions for Eq. (3.5) is beyond the scope of this thesis and for full description, the reader is directed to reference [95].

Another most popular model of electron transport in nanocrystalline TiO_2 is Kopidakis's ambipolar diffusion D_{amb} mechanism Eq. (3.6) [96]:

$$D_{\text{amb}} = \frac{n' + p'}{\dfrac{n'}{D_{p'}} + \dfrac{p'}{D_{n'}}} \tag{3.6}$$

where n' and $D_{n'}$ are the negative charge density and diffusion coefficient, respectively, and p' and $D_{p'}$ are the positive ones. According to this model photoinjected electrons in TiO_2 were surrounded by an electrolyte consisting of various kinds of ionic species.

The general outcome of analysing Eq. (3.5) and (3.6) enables to determine quantities like D_{eff}, electron lifetime τ and diffusion length L [72, 95, 97]. These quantities are usually obtained by small perturbation kinetic measurements that do not modify the steady state over which they are measured (see Section 3.3). Experimental values of D_{eff} in nanostructured TiO_2 reported in various literatures range from 1×10^{-2} [98, 99] to 1×10^{-7} cm^2 s^{-1} [100].

Concerning the transport of redox mediator in DSSC, typical redox electrolytes consisting of I^-/I_3^- in acetonitrile have a high conductivity and high ionic strength so that the influence of electric field and transport by migration is negligible. In various papers, the experimental diffusion coefficient of I_3^- ion D_{ion} in the nanoporous network of TiO_2 has been determined to be 7.6×10^{-6} cm^2 s^{-1}[101]. For comparison, typical values for I^-/I_3^- diffusion coefficient D in solution bulk are 1.37×10^{-5} cm^2 s^{-1}. In viscous electrolytes like ionic liquids and amorphous hole conductors, diffusion coefficients can be too low to maintain a sufficiently large flux of redox components. The diffusion coefficient of I^-/I_3^- is usually determined by microelectrode voltammetric technique (see Section 6.1.1). Apart from diffusion, the alternative type of charge transport in highly concentrated I^-/I_3^- in viscous electrolytes involve Grotthuss-like transport mechanism which leads to a low series resistance in completed cells [102-104]:

$$I_3^- + I^- \rightarrow I^- \cdots I_2 \cdots I^- \rightarrow I^- + I_3^- \qquad (3.7)$$

A general model for the performance of DSSC [105, 106] focuses on transport and recombination processes within the porous electrode network and assumes ideal electron transfer behaviour and does not take into account possible limitations imposed by the reaction between the redox electrolyte and the photosensitized dye. A fast reaction between dye cations and the donors in the electrolyte solution was discussed as critical for the long term stability of the sensitizer and also to keep the back reaction of an electron from the semiconductor suppressed [72, 105, 107, 108]. An illustration of the different dynamic processes in a DSSC is shown in Figure 3.4. The figure summarizes the energetic level and the series of competing reactions that occur upon photo-excitation of adsorbed dye molecules. The thermodynamic and charge transfer kinetic parameters at semiconductor/dye/electrolyte interfaces have been widely investigated for DSSC.

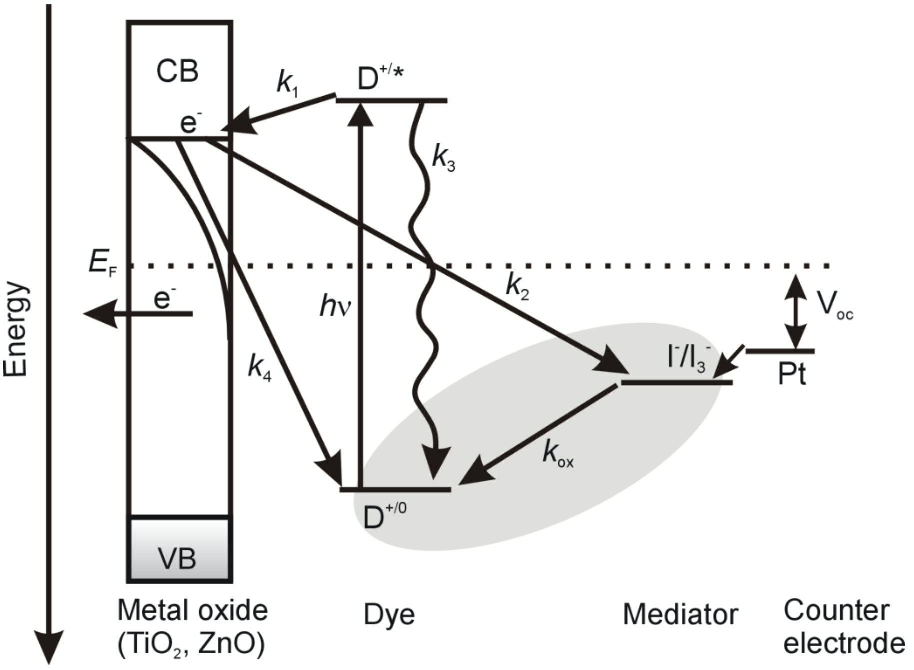

Figure 3.4 Schematic diagram of energy level and interfacial electron-transfer processes at dye-sensitized heterojunction: k_1, electron-injection rate constant; k_2, rate constant of reaction between conduction band electrons and oxidized redox species; k_3, dye excited-state relaxation rate constant; k_4, back-electron transfer rate constant; k_{ox}, dye regeneration rate constant.

Several methods were developed to measure the kinetics of electron transfer in dye-sensitized electrodes [35, 109-111]. Detailed mechanistic studies have been performed most often by spectroscopic and spectroelectrochemical techniques or by photoelectrochemical characterization of complete cells [14, 112-114]. For instance, pump-probe* experiments showed a rate constant of electron injection k_1 from the excited dye molecule to the conduction band of the semiconductor in the orders of magnitudes faster than the competing back reaction of the electron to the oxidized dye molecule k_3 [110, 111]. Transfer of the injected electron back to the

---

* A pump-probe experiment involves a pump pulse to excite the sample. A subsequent probe pulse is used for probing the sample after an adjustable delay time

electrolyte by reduction of tri-iodide k_2 was detected as a loss mechanism which could be suppressed by coadsorbates on the semiconductor which blocked the surface not covered by the sensitizer [35].

The dye regeneration kinetics is little studied relative to other processes. This is because the experimental study requires more difficult transient absorbance techniques, according to several literature reports [14, 112-114] and is complicated by mass transport. Initial studies have largely addressed the iodide oxidation kinetics following UV excitation of TiO_2 colloidal particles. Results obtained with $Ru(dcbpy)_2(NCS)_2$ [dcbpy = 4,4′-dicarboxy-2,2′-bipyridine]-sensitized colloids in aqueous iodide have been interpreted in terms of the formation of an iodide-ruthenium(III) complex intermediate, enhancing the efficiency of this reaction [115]. In contrast, Kamat et al. [114] have indicated that the kinetics of dye cation re-reduction by iodide are approximately first-order for a small range of iodide concentrations with no evidence for complex formation. Montanari et al. [112] employed transient absorption spectroscopy to investigate the kinetic competition between dye regeneration reaction by recombination with injected electrons or by electron transfer from iodide ions in the redox electrolyte in $Ru(dcbpy)_2(NCS)_2$-sensitized nanocrystalline film TiO_2 electrodes immersed in a propylene carbonate electrolyte.

In this thesis scanning electrochemical microscopy (SECM) in the feedback mode used to study locally the kinetics of dye regeneration at isolated dye sensitized photoanodes (Eosin-Y/ZnO, D149/ZnO and N719/TiO_2) in acetonitrile-based and RTIL-based I^-/I_3^- electrolytes [A1], [A2], [A4], [A5]. The measurement principles are based on examining the steady-state rate of mediator regeneration under the active area of a microelectrode probe. Compared to a completed operational DSSC, the photoanaode operated here under conditions of I^- starving in order to make the measurements sensitive for the regeneration rate. This measurement allows estimating the effective rate of the dye regeneration reaction k_{ox}.

3.3. Review of DSSC characterization techniques

This section provides an overview of some techniques previously developed to characterize complete DSSC. The relevance of this overview is to discuss the methods used in a collaboration work [A5], which presents correlation studies of macroscopic photovoltaic characteristics of whole cells and SECM kinetics of dye-sensitized samples with varied structural features. The most commonly used techniques are current-voltage characteristics [116], transient photocurrent measurements [92, 100, 117], incident photon to current conversion efficiency (IPCE), photovoltage decay, intensity modulated photovoltage spectroscopy (IMVS) [118], intensity modulated photocurrent spectroscopy (IMPS) [119, 120], and electrochemical impedance spectroscopy (EIS) [80, 121]. While photoelectrochemical techniques have proved to be most adequate for the study of electron transport, time-resolved optical spectroscopy remains the leading tool for the study of interfacial electron transfer [122, 123]. Dye regeneration and recombination reactions have been studied by femto-to-nanosecond laser spectroscopy [14, 113]. These methods are well established in solar cell research and detailed discussions are far beyond the scope of this thesis. For full description of the methods, the reader is directed to a book by Archer et al.[124]. In the following paragraphs, brief descriptions of some of the methods are outlined.

The optimisation of current–voltage (J-V) characteristic is the most fundamental aim in the research of the DSSC. To illustrate the solar cell output parameters derived from J-V curve of the device, let us consider an ideal Schottky diode. When the cell is illuminated, the total current density J is equal to the difference of the photocurrent density J_{ph} and the dark current density J_{dark} [101].

$$J = J_{\mathrm{ph}} - J_{\mathrm{dark}} \tag{3.8}$$

The dark J-V characteristic of the solar cell is expressed as:

$$J_{\text{dark}} = J_{\text{o}} \left[\exp\left(\frac{qV}{k_{\text{B}}T} \right) - 1 \right] \tag{3.9}$$

where J_{o} is the saturation current density which is the current density flowing under sufficiently high reverse bias, q the electron charge, k_{B} the Boltzmann constant, T the absolute temperature and V the applied voltage. Thus, the J-V characteristic of an illuminated solar cell that behaves as the ideal diode is given by:

$$J = J_{\text{ph}} - J_{\text{o}} \left[\exp\left(\frac{qV}{k_{\text{B}}T} \right) - 1 \right] \tag{3.10}$$

According to several reports in the literature there is no consensus as to what physical information can be extracted from J-V curves of DSSCs rather than just performance values. The ideal J-V characteristics of the solar cell in the dark and under illumination are shown in Figure 3.5. Key factors are the short-circuit current density J_{sc}, the open-circuit voltage V_{oc}, the maximum power point $J_{\text{MP}}V_{\text{MP}}$ and the fill-factor ($J_{\text{MP}}V_{\text{MP}}/J_{\text{sc}}V_{\text{oc}}$) giving the overall efficiency of a cell Eq. (3.11):

$$\eta = \frac{J_{\text{MP}}V_{\text{MP}}}{P_{\text{in}}} \tag{3.11}$$

where P_{in} is the incident photon power. In general, if an external field is applied to a solar energy conversion device, it acts to diminish the effects of the internal barrier field. The current flowing for a given positive external voltage is quite different from the current flowing at the same negative voltage. Thus, the junction acts as a rectifier which is typical of diodes.

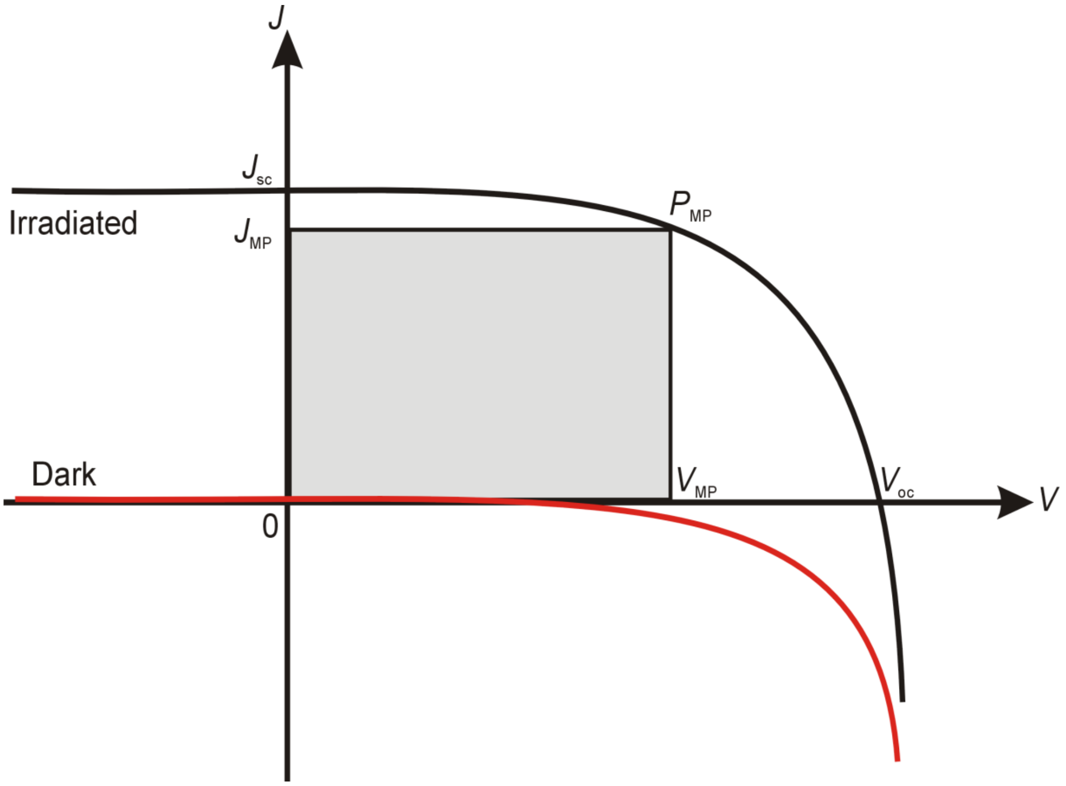

Figure 3.5 Typical current density-voltage characteristics of Schottky diodes in the dark and under illumination.

The IPCE is a measure of how efficient the cell is at absorbing photons of a specific wavelength λ at a given incident light intensity I_{in} to generate photocurrent density J_{sc} in the external circuit under short circuit condition. It can be calculated using Eq. (3.12):

$$\mathrm{IPCE} = \frac{1240 J_{\mathrm{sc}}}{\lambda I_{\mathrm{in}}} \tag{3.12}$$

Light of different wavelengths is absorbed at different depths in the solar cell film. Knowing the IPCE of a particular cell, J_{sc} can be estimated by integrating the response over the incident irradiation spectrum Eq. (3.13):

$$J_{\mathrm{sc}} = q\int_0^{\infty} \mathrm{IPCE}(\lambda) I_{\mathrm{in}}(\lambda) d\lambda \tag{3.13}$$

Under operating conditions at the maximum power point, an efficient DSSC delivers current density in excess of 10 mA cm^{-2} [105].

The open-circuit photovoltage decay techniques allows to measure the apparent electron life time τ_n using the expression [Eq. (3.14)]:

$$\tau_n = -\frac{k_B T}{q}\frac{\partial V_{oc}}{\partial t} \tag{3.14}$$

where e is the elementary charge and t is the time [125]. The measurement involves illuminating the cell maintained at open-circuit. When the illumination is interrupted the photovoltage transient is recorded.

Intensity modulated photovoltage spectroscopy (IMVS) and intensity modulated photocurrent spectroscopy (IMPS) measure frequency dependent magnitude and phase shift of the photovoltage and photocurrent generated by the modulated light intensity, respectively. The intensity of the light can be modulated using mechanical chopper or LED. IMVS and IMPS measurements provide information about the internal dynamics of the DSSC, such as electron lifetime and electron-hole recombination dynamics under open-circuit and short-circuit conditions, respectively. The information obtained from IMVS at open circuit is similar to that extracted from photovoltage decay technique i.e., the apparent electron life time τ_n related to the frequency response ω as from IMVS $\tau_n = \omega^{-1}$. Figure 3.6 shows a typical experimental arrangement for IMVS/IMPS using LED as intensity modulator.

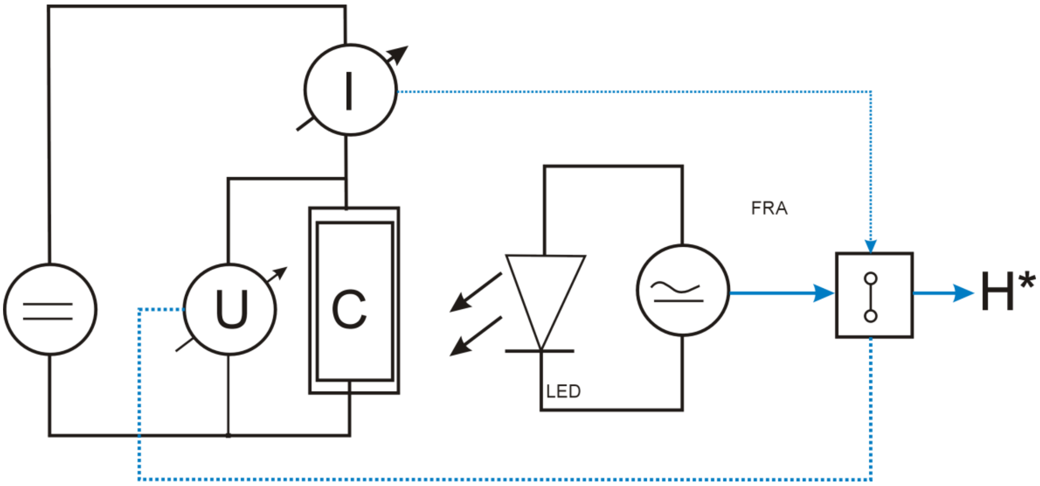

Figure 3.6 Experimental set-up for IMVS/IMPS from literature. = is steady state set value, U is cell voltage, I is cell current, C is cell, LED is light emitting diode, FRA is Frequency response analyzer

The function generator output of an FRA supplies an LED light source with modulated current or voltage. The current (or voltage) is correlated with the LED flux to calculate the photoelectrochemical transfer function H^*. IMVS data corresponds to the values of H^* between the modulated light intensity and the measured AC potential of the cell at open-circuit Eq. (3.15), whereas IMPS data corresponds to the values of H^* between the modulated light intensity and the measured AC current of the cell at short-circuit Eq. (3.16).

$$H^*_{\mathrm{IMVS}} = \frac{\Delta \mathrm{V}}{\Delta J_{hv}} \exp(i.\varphi) \tag{3.15}$$

$$H^*_{\mathrm{IMPS}} = \frac{\Delta I}{\Delta J_{hv}} \exp(i.\varphi) \tag{3.16}$$

where H^*_{IMVS} and H^*_{IMPS} are the transfer function, ΔV and ΔI are the variation of the cell voltage and cell current, ΔJ_{hv} is the variation of photon flux and φ is the phase angle.

In general, this technique allows determining the electron life time and diffusion coefficient of electrons in the solar cell electrode

4. Theory and principles of scanning electrochemical microscopy

4.1. Overview

Scanning electrochemical microscopy (SECM) is a scanning probe technique that allows probing electrochemical reactivity and topography of a wide range of sample surfaces and phases [126-128]. The term scanning electrochemical microscopy was first used by Bard et al. [129], when they used scanning tunnelling microscopy (STM) to measure Faradaic currents close to surfaces. Afterwards, a number of reviews [126, 130-132] have been published to illustrate the versatility of SECM. In recent years new attempts were made to apply SECM for applied problems and to overcome some typical limitations including difficult probe handling, limited range of media suitable for SECM experiments and limited range of sample area to be scanned [133-136]. The use of SECM technique continued to advance for many applications and dozens of SECM-related articles and reviews have been published. To avoid any repetition and because of volume limitations, only the basics of SECM theory and operation relevant for this work are described here. For full discussion of SECM the reader is directed to these references [126, 137].

The original idea behind SECM was to place a microelectrode (UME) near the surface of interest (sample or substrate) and to use the flux of electrochemically active molecules as a probe for visualizing the substrate and investigating its chemical properties. The UME can be scanned locally in x, y or z direction with respect to the substrate using a high precision positioning devices (e.g. different forms of piezoelectric actuators, stepper motor, etc). The lateral resolution of SECM is principally dictated by the size of the UME, the resolution of the positioning devices and/or the size of investigated diffusion layer. The smaller the UME size the higher the spatial resolution of the SECM experiments that can be obtained provided that no other factor is limiting.

Several SECM experiments are known but the standard ones include:

(*i*) *Approach curve measurement*. The change in the probe response is recorded as the probe moved vertically towards to the sample surface. They are commonly used to obtain kinetic information. The major part of this thesis deals with approach curve measurements to derive kinetic information of dye regeneration in DSSC.

(*ii*) *Horizontal line scans*. The probe is positioned close to the interface and its response is recorded as a function of distance along either *x* or *y* direction. Apart from several selected application, this experiment is important to make tilt correction in ordinary experiments.

(*iii*) *Images*. The probe is located close to the surface and its response is recorded as a function of *x* and *y* with fixed or varied *z* position. In the work presented in this thesis both line scan and imaging in conventional SECM mode were implemented to investigate DSSC (Section 6.4, [A2]). Furthermore, high resolution SECM imaging with shear force distance regulation was used with model electrode surfaces. A full description of the concept of shear force distance regulation can be found in Chapter 10 and [A7].

(*iv*) *Close proximity mode voltammetry and chronoamperometry*. In close proximity to the interface, UME-substrate voltammetry and chronoamperometry can be performed to derive kinetic information. The full discussion of UME-substrate voltammetry is not intended in this thesis but the specific example investigating electroactive ions at MnO_2 pseudocapacitive electrodes for supercapacitor devices can found in own publication [A6]. SECM chronoamperomety is implemented to investigate the kinetics of dye regeneration (Chapter 9).

In this Chapter the properties of microelectrodes (or ultramicroelectrodes) and the different SECM working modes relevant for this thesis are introduced. The rest of this Chapter is organized as follows: the reviews of SECM application for photoelectrochemical reactions are described in Section 4.4, and Section 4.5 outlines shear force distance control for high resolution. Note that shear force distance control is discussed in detail in Chapter 10.

4.2. Properties of ultramicroelectrodes

Microelectrodes, also known as ultramicroelectrodes, have dimensions typically micro or even nanometre range ($\leq$ 50 µm [138]). Different microelectrodes are known for various applications but here the discussion is restricted to the microdisk UME which are common for many SECM applications. In order to understand SECM, it is essential to address the difference in electrochemistry at macroelectrodes and microelectrodes.

In electrochemistry the use of microelectrodes was primarily inspired by their advantages to overcome the limitations by macroelectrodes with respect to charging current and uncompensated resistance as well as the possibility to perform electrochemical studies in small volumes (e.g. measurements of neurotransmitters in the brain of animals [139]). The microelectrodes behave differently to macroelectrodes mainly by the different nature of mass transport scheme around the electrode. At UME the mass transport occurs by hemispherical diffusion and the molecules are transported from three space directions to one point (Figure 4.1a). In contrast to macroscopic electrodes, where linear diffusion dominates (Figure 4.1c), a constant flux can be maintained during continuous electrolysis. Although a net reaction occurs (the situation is not in equilibrium), the concentration remains constant at each point in space. We call this situation a steady state. Of course, also the hemispherical diffusion layer must be established and this requires a certain time. A detailed text about quantitative estimates for the time to establish a steady state can be found in reference [31]. If the experiment is performed faster than this time, the transport to a microelectrode is dominated by linear diffusion. The smaller the electrode the faster the steady state is established. For a continued electrolysis a macroelectrode current tends to zero, while at the microelectrode a measurable steady-state current results due to an enhanced radial diffusion. The steady state limiting current $i_{\mathrm{T},\infty}$ passing at a microdisc UME is given by $i_{\mathrm{T},\infty} = 4nFDc^*r_\mathrm{T}$ [140, 141], where D is the diffusion coefficient of the mediator, c^* is the bulk concentration of the reactant, r_T is the radius of the active part of the UME. This equation is the solution of the corresponding partial differential equation [142]. Also shown in Figure 4.1a are the geometrical description of the UME body. For explanatory purposes the kinetically uncomplicated reduction of O to R at the electrodes were assumed. The species, either O or R is often called mediator.

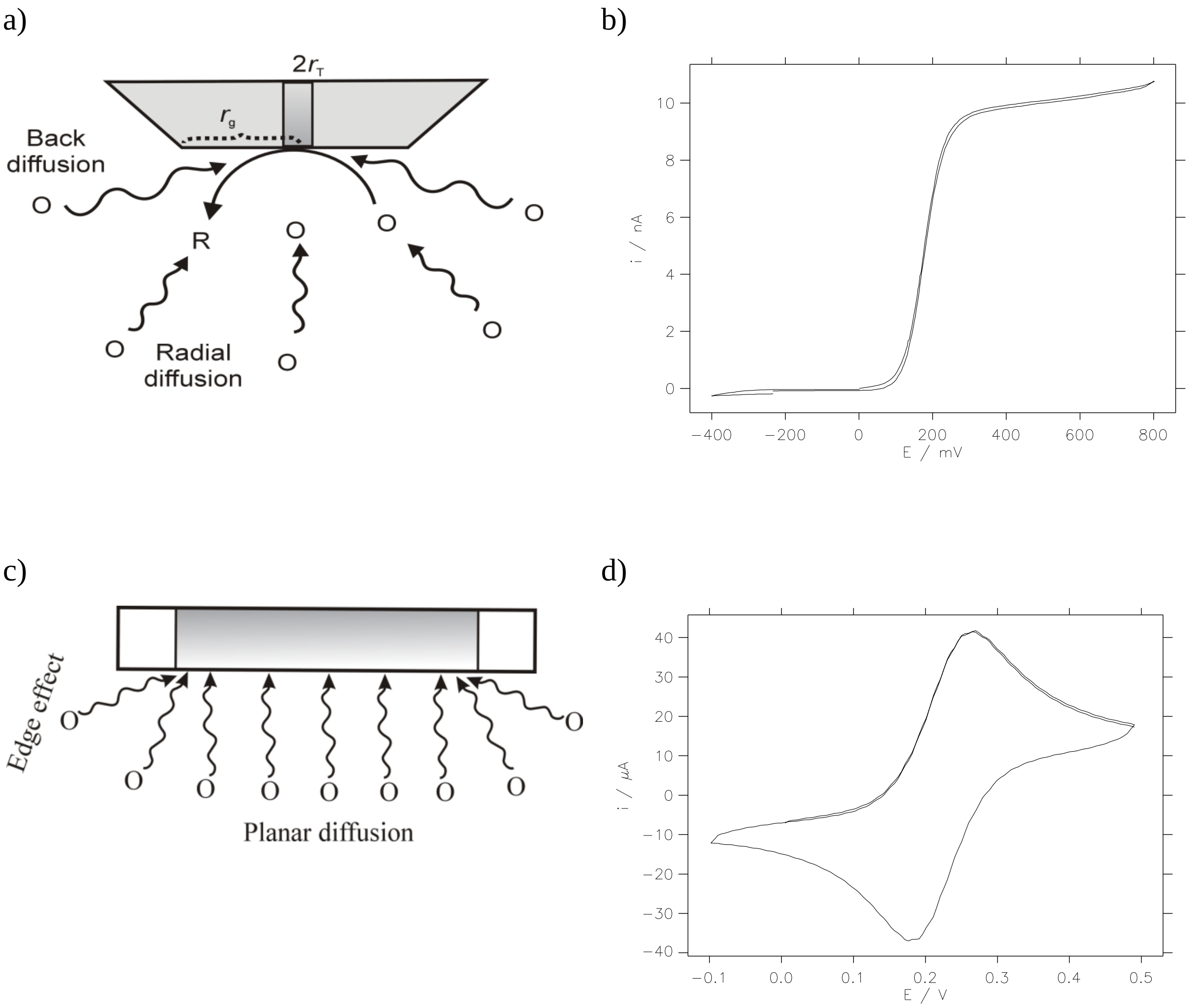

Figure 4.1 The nature of mass transport towards the (a) microelectrode and (c) macroelectrode. Hemispherical (radial) diffusion dominates towards the microelectrode and planar (linear) diffusion is predominant towards macroelectrode. Typical cyclic voltamograms of 2 mM FcMeOH in acetonitrile (b) at Pt UME (r_T = 12.5 µm), d) at macroscopic Pt electrode with diameter 1 mm.

4.3. SECM operation modes

SECM can be operated in different working modes [126] but in this Chapter the discussion is restricted to the feedback (FB), generation-collection (GC) and redox competition (RC) modes, since these are the most relevant SECM modes for energy research.

4.3.1. The feedback mode

The SECM feedback mode refers to a way by which electrochemical reactions at the probe and at the sample are coupled. The type of substrate and the experimental and technical conditions that are used will have an impact on UME current, whose response can be used to describe processes occurring at the substrate. In order to explain the SECM feedback mode, we assume that the solution contains the oxidized form O of a redox mediator and that the potential of the UME is at a value such that the oxidized mediator is reduced at a diffusion controlled rate. Corresponding experiments are also possible if R is used as redox species.

The feedback mode is widely used to investigate electron transfer kinetics at the interface [143-145]. A very popular experiment using this mode is approach curve measurements. When the UME is approached towards a sample, within a few r_T two limiting cases exist. Hindered diffusion ("negative feedback") is observed if the sample is electrically insulating (e.g. glass, Figure 4.2b, d). In this case the UME-generated species R cannot react at sample surface. The surface simply hinders the diffusion of O towards the UME and i_T decreases with decreasing working distance d ($i_T < i_{T,\infty}$). Diffusion controlled mediator recycling ("positive feedback") occurs if the sample is conductive and the electron transfer reaction $R \rightarrow O + e^-$ is very fast, i.e. "diffusion controlled" (e.g. at gold, Figure 4.2c, e). Here, the R species formed at the UME diffuses to the sample where it is instantly oxidized back to O. This reaction increases the flux of O to the UME and hence increases the UME-current (i_T

$> i_{T,\infty}$). In both cases, the SECM tip is approached perpendicularly to the substrate such that the flat end of the tip with the embedded micro-disc is placed parallel to the substrate. Mass transfer to the UME, and therefore its electrochemical response will be a function of the inter-electrode distance. This is a powerful feature of SECM since the tip-substrate distance can be selected and varied and if made small, it can offer high fluxes to the sample (amount of molecules per area and time) not easily accessible with other electrochemical techniques.

There is an intermediate situation where regeneration of O occurs at a limited rate. This is called finite kinetics. In this regime the balance between chemical flux and diffusional flux depends on the rate of electron transfer and the normalized UME-substrate distance L. For discussion let us consider the approach curve recorded on gold sample with an inhibiting contamination layer (Figure 4.2f). When the UME is approached a few r_T to the substrate, regeneration of O is fast enough to compete with the speed of diffusion of species O and R. Thus, the i_T increases with decreasing UME-substrate distance. As the UME gets closer, the diffusion of species O and R within the thin electrolyte layer between the UME and the substrate becomes faster. Now, the regeneration of O at the sample limits the feedback because the sample is not able to reduce so much O per time and area as the UME provides and the current i_T decreases. This allows studying the kinetics of reactions at various substrates.

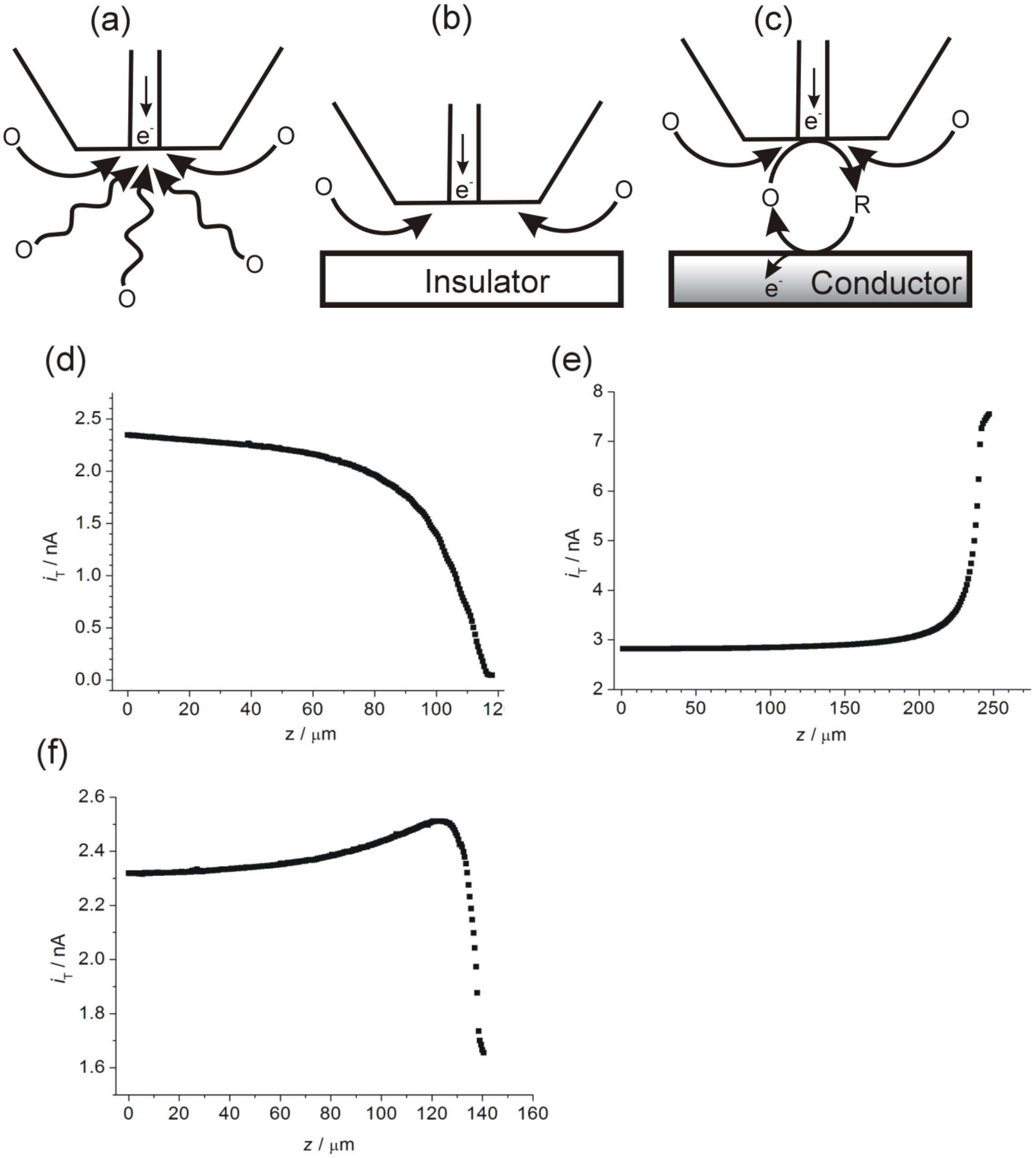

Figure 4.2 A schematic of SECM feedback mode showing (a) hindered diffusion, (b) diffusion controlled feedback, SECM approach curves to (d) glass and (e) gold samples and (f) excessively used gold samples

4.3.1.1. Theoretical feedback mode approach curves

To enable quantitative studies by SECM, one needs to simulate UME current-distance curves with the help of a computer by solving the underlying partial differential equations. From the results of many such simulations for different UME geometries and kinetics, analytical approximations were derived by several authors [146-148]. Comparison of the different analytical approximations is not trivial because the degree of sophistication of the underlying simulation varies in the accurate description of the SECM geometry, the accuracy of the numerical solutions and the accuracy of the analytical approximations of the discrete simulation results.

A brief overview of the analytical expressions present in the literature which model SECM feedback response is presented here. All the expressions describe dimensionless current-distance curves and they are valid only for an inlaid disk UME, equal diffusion coefficients of O and R and an infinitely large substrate, i. e., Eq. (4.1) [149, 150].

$$r_S \geq r_\mathrm{T} + 1.5d \tag{4.1}$$

where r_S is the radius of the substrate. The first description of approach curves over a conductor and an insulator by Kwak and Bard [151] did not consider the diffusion from behind the plane of the electrode. A better solution was formulated by Amphlett and Denuault [146] because the simulation space was expanded beyond the edge of the insulator sheath and diffusion from behind was taken into account. Their expression for the diffusion-controlled positive feedback with the UME geometry of RG = 10.2 is [146]:

$$I_\mathrm{T,cond}(L) = \frac{i_T}{i_{\mathrm{T},\infty}} = 0.72627 + \frac{0.76651}{L} + 0.26015\exp\left(\frac{-1.41332}{L}\right) \tag{4.2}$$

While their expression for the current distance curve controlled by hindered diffusion negative feedback with the UME geometry of RG = 10.2 is:

$$I_\mathrm{T,ins}(L) = \frac{i_T}{i_{\mathrm{T},\infty}} = \frac{1}{0.40472 + \dfrac{1.60185}{L} + 0.58819\exp\left(\dfrac{-2.37294}{L}\right)} \tag{4.3}$$

where $I_\mathrm{T,cond}$ is the current for diffusion-controlled mediator recycling at the sample ("positive feedback") and $I_\mathrm{T,ins}$ is the normalized UME current when the substrate is an insulator. $I_\mathrm{T} = i_\mathrm{T}/i_{\mathrm{T},\infty}$ where i_T being the current on the UME, $i_{\mathrm{T},\infty}$ being the steady-state limiting current. The normalized distance $L = (z_{\max} - z + d_0)/r_T$ obtained from the vertical position z (increasing with approach towards the sample), the position $z_{\max}$ at which mechanical contact of the glass sheath occurred with the sample and the distance d_0 of the active electrode area to the sample, r_T being the radius of the UME.

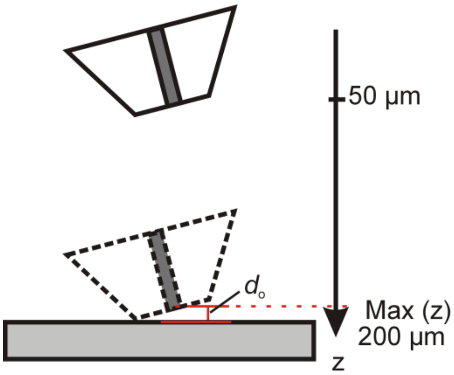

Figure 4.3 Determination of z_{offset} and L for increasing z for decreasing d. The misalignment of the UME is exaggerated.

In order to fit the experimental negative feedback approach curves for "hindered diffusion" on non-illuminated dye-sensitized electrode, Eq. (4.3) is used in this thesis. To use the expressions by Amphlett and Denuault with other *RG* values, the reader is directed to the reference [146]. Lefrou [152] introduced an analytical expression describing the positive feedback with *RG* parameter which can be varied continuously. The author used conformal mapping transformations to derive an expression made of a combination of mathematical functions containing arctan(L) and arcos($1/RG$) (see below). Cornut and Lefrou [153] using a similar method studied also the case of the negative feedback for a microdisk electrode. There are still several good analytical approximations available in literatures for $I_{T,\text{cond}}$ and $I_{T,\text{ins}}$ [146-148, 154, 155] which are not described here because of volume limitation in this thesis. However, the analytical approximations for finite kinetics regime are very essential in this thesis is explained below. Generally the normalized approach curves in the SECM feedback mode can be described by Eq. (4.4) [156]

$$I_{\mathrm{T}}\left(L\right)=I_{\mathrm{T,ins}}+\left(1-\frac{I_{\mathrm{T,ins}}\left(L\right)}{I_{\mathrm{T,cond}}\left(L\right)}\right)I_{S}\left(L\right) \tag{4.4}$$

$I_{\mathrm{S}}(L) = i_{\mathrm{S}}/i_{\mathrm{T},\infty}$ describes the current at the substrate electrode normalized by the current of the microelectrode probe in the bulk phase of the solution. This has been simulated for finite kinetics of the reaction at the sample [156]. Cornut and Lefrou provided a more accurate simulation for the same case [157]. The analytical model of Cornut and Lefrou [157] for SECM approach curves in the feedback mode with irreversible heterogeneous first-order reactions of finite kinetics at the sample is given by:

$$I_{\mathrm{T}}(L,\kappa,RG)=I_{\mathrm{T,cond}}(L+\kappa^{-1},RG)+\frac{I_{\mathrm{T,ins}}(L,RG)-1}{(1+2.47RG^{0.31}L\kappa)(1+L^{0.006RG+0.113}\kappa^{-0.0236RG+0.91})} \tag{4.5}$$

where κ is the normalized heterogeneous rate constant for the mediator regeneration, RG is the ratio of the radius of the insulating sheath r_{glass} and r_{T}. The $I_{\mathrm{T,ins}}$ and $I_{\mathrm{T,cond}}$ are calculated according to following equations:

$$I_{\mathrm{T,ins}}(L,RG)=\frac{(2.08/RG^{0.358})(L-(0.145/RG))+1.585}{(2.08/RG^{0.358})(L+0.0023RG)+1.57+\dfrac{\ln RG}{L}+(2/\pi RG)(1+(\pi RG/2L)} \tag{4.6}$$

$$I_{\mathrm{T,cond}}(L+\kappa^{-1},RG)=\alpha(RG)+\frac{1}{2\beta(RG)\xi(L+\kappa^{-1})}+\left(1-\alpha(RG)-\frac{1}{2\beta(RG)}\right)\xi(L+\kappa^{-1}) \tag{4.7}$$

$$\alpha(RG)=\ln 2+\ln 2\left(1-\frac{2}{\pi}\arccos(RG^{-1})\right)-\ln 2\left(1-\left(\frac{2}{\pi}\arccos(RG^{-1})\right)^{2}\right) \tag{4.8}$$

$$\xi(RG)=1+0.639\left(1-\frac{2}{\pi}\arccos(RG^{-1})\right)-0.186\left(1-\left(\frac{2}{\pi}\arccos(RG^{-1})\right)^{2}\right) \tag{4.9}$$

This expression is valid for $RG \leq 20$ and $L \geq 0.1$ and any κ. It converges for large κ and small κ towards the limiting cases. From the fit of experimental data to Eqs. (4.5)-(4.9), κ can be determined. If the diffusion coefficient D and r_{T} are known from independent experiments the apparent heterogeneous first order rate constant k_{eff} can be calculated using Eq. (4.10).

$$k_{\mathrm{eff}} = \kappa D / r_{\mathrm{T}} \tag{4.10}$$

The fitting accuracy of Eq. (4.5) is not better than others present in the literature but the reduction of the number of adjustable parameters and an acceptable error (always largely lower than experimental errors) make this expression very useful. Figure 4.4 summarizes the simulated approach curves for different reaction rate at the substrate according to Cornut and Lefrou model [157]. This plot is of great importance for a number of SECM applications. A local reaction rate constant at any substrate can be extracted by comparing the experimental data to these curves.

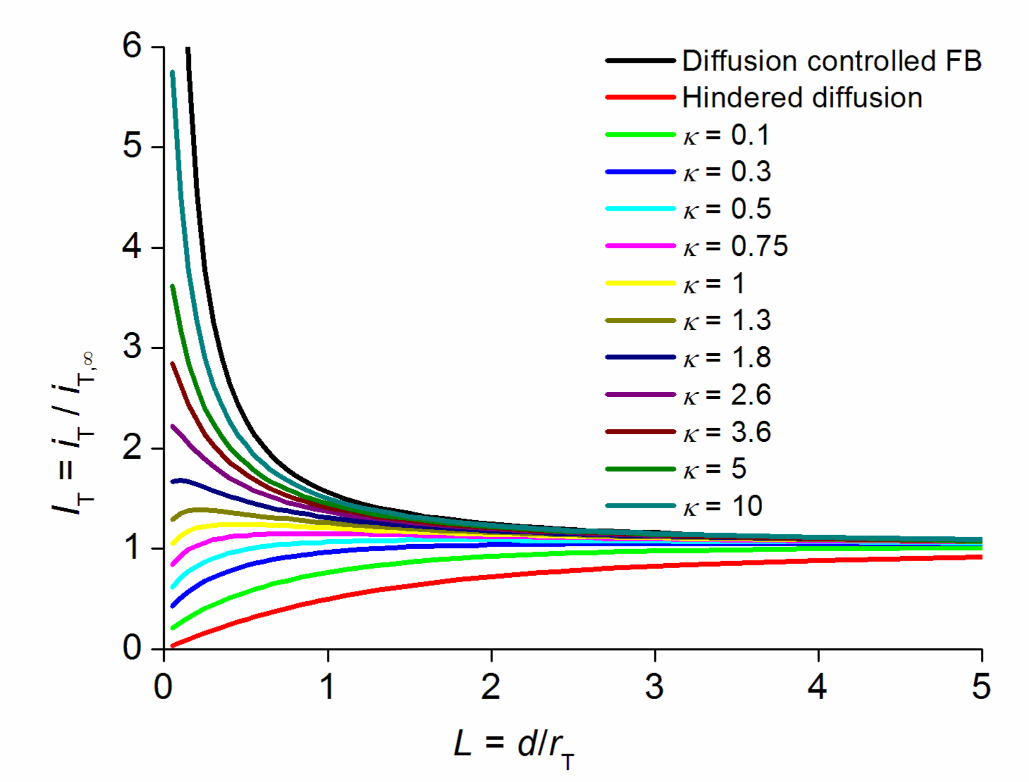

Figure 4.4 Simulated SECM feedback mode approach curves for hindered diffusion, diffusion controlled FB and kinetically controlled FB reaction on the substrate for kinetically uncomplicated reaction with apparent first order rate.

In this thesis Eqs. (4.5)-(4.9) are used to fit feedback approach curves on illuminated dye-sensitized electrodes. This model is preferred over others in the literature because of its simplicity for use. For this fitting the experimental i_{T} *vs.* d are listed in an Excel spread sheet with the Eqs. (4.5)-(4.9). Afterwards, normalized approach curves $I_T(L)$ have been calculated. Then, the corresponding theoretical $I_T(L)$ is calculated with Eqs. (4.5)-(4.9). The parameters r_T, d_o and RG are estimated from independent experiment. In the fitting procedure, the parameters κ and $i_{T,\infty}$ can be allowed to vary until the best possible agreement between measurement and theoretical approach curve is reached. The apparent heterogeneous first order rate constant k_{eff} for mediator regeneration is obtained using Eqs. (4.10).

4.3.2. Generation-collection and redox competition modes

In the generation-collection (GC) mode, the species produced at an active site of the sample are collected at the UME (SG-TC; Figure 4.5a) or tip generated species collected at the substrate (TG-SC; Figure 4.5b). In GC modes, the first step is always to place the UME at a certain known distance. UME positioning is often carried out in the other SECM mode (feedback mode) with a mediator different from the one that is generated and/or collected in the GC experiment. In such experiments, the sample should be as small as possible to minimize the background current. Particularly, SG-TC mode is more advantageous over other modes in that it has high collection efficiency and sensitivity. Typical GC experiments are the investigation of the activity of immobilized enzymes and the study of diffusion of metabolites released from living cells [158-162]. With respect to alternative energy research, the GC mode has been extensively used to study oxygen reduction reaction in fuel cells, biofuel cells and metal-air batteries [163, 164]. For complete details of GC mode in energy related research, the reader is directed to the recent review by Mirkin et al. [165] and the references therein. In Section 6.4 the use of SG-TC is described to differentiate illuminated regions of dye-sensitized electrodes from non-illuminated regions. Furthermore, in Chapter 9 SG-TC mode is demonstrated for localized dye regeneration by SECM chronoamperometeric measurement.

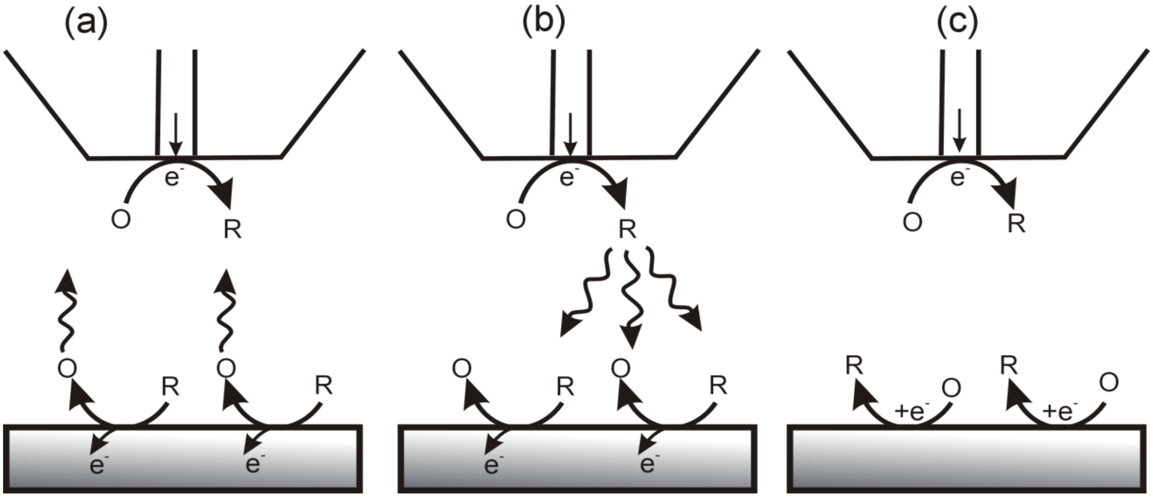

Figure 4.5 Schematics representation of SECM generation collection and redox competition modes; (a) SG-TC, (b) TG-SC and (c) redox competition RC modes

The SECM redox competition mode is based on the competition between probe and sample for the same redox species in the electrolyte (Figure 4.5c). The advantage of the RC mode is that there is no limitation on the sample size. It has been used to study electrocatalysis at various substrates. The most popular original idea on the use RC mode is the double potential step experiment by Schumann et al. [166] to study oxygen reduction reaction on different catalytic materials. Since then several papers were published in this field [167]. Moreover, the combination of this mode with shear force dependent constant distance mode allowed obtaining detailed information of catalytic process at shorter tip-substrate distances [168]. In this thesis we demonstrated a transient RC mode to investigate local photoelectrochemical processes in DSSCs (see Chapter 9).

4.4. SECM application for photoelectrochemical reactions

SECM has been demonstrated to be an effective technique of determining electron transfer kinetics at various interfaces including polymer/liquid [169], liquid/liquid interfaces [126, 156, 170, 171], redox enzymes on solid supports [158, 172]. Among the variety of studied processes, electron transfer reactions at semiconductor/electrolyte interfaces form an important group

[173-181]. Precursor sites on passivated valve metals (TiO_2, Ta_2O_5, Al_2O_3) were identified as locations at which electron transfer reactions occur to form dissolved species in the dark before the onset of pitting corrosion [173]. The kinetics of hole injection into GaAs by a probe-generated oxidizer in the dark was studied and applied to local semiconductor etching [178]. SECM feedback investigations at WSe_2 and Si immersed in an electrolyte showed a correlation between the heterogeneous redox kinetics at the sample and the concentration of the majority carriers in it [179].

Photoelectrochemical reactions at semiconductor surfaces have been studied at TiO_2 photocatalysts [180]. The behaviour of a TiO_2 (microcrystalline anatase) was compared to the characteristics of bare indium tin oxide (ITO). When probed with the $[Fe(CN)_6]^{4-/3-}$ redox couple, the surface behaved like an insulator in the dark and a conductor under UV illumination. The Unwin group studied the kinetics of photoelectrochemical decomposition of 4-chlorophenol at a TiO_2 particle film under UV illumination using a transient SECM working mode [181-183]. Haram and Bard [184] determined apparent pseudo-first-order rate constants from steady-state SECM feedback approach curves for the reduction of methyl viologen (MV^{2+}) to the methyl viologen radical cation (MV^{+}) at CdS thin films obtained from wet chemical deposition, as well as their dependence on light intensity and on the concentration of redox species in the electrolyte. In their study the holes in CdS particles were scavenged by dissolved triethanolamine. Bozic and Figgemeier [16] determined the diffusion coefficient of ferrocenium Fc^{+} ion in dye-sensitized nanostructured TiO_2 by time-of-flight experiments under working solar cell conditions with SECM SG-TC mode and fixed position of the microelectrode. The SECM with an optical fiber tip was used to study the photooxidation of iodide in acetonitrile at the photosensitizer arrays deposited on mesoporous TiO_2 electrodes [17]. The applicability of this technique to rapidly evaluate photosensitizers for DSSC was demonstrated. Lee et al. [185] employed an SECM-based method for rapid screening of photocatalysts. An optical fiber was used instead of the conventional SECM tip to quickly scan a micrometre-sized spot of light produced by a Xe lamp over an array of photocatalysts deposited onto FTO conducting glass substrate. The substrate photocurrent recorded as a function of the tip position was used to evaluate the photocatalytic effect.

4.5. Shear force distance regulation for high resolution SECM

Most often SECM imaging was performed by scanning an UME over the surface of a sample in the constant height mode by lateral translation in the x and y directions. Figure 4.6 shows the sketch of different substrate alignments with respect to UME for SECM imaging. Black dashed line refers to constant height mode and red dashed line refers to constant distance mode. The constant height imaging mode is usually adequate for a flat and non-tilted surface (Figure 4.6a) or for SG-TC mode with a probe positioned relatively far from the surface. The working distance is usually in the UME–substrate separation of $2r_T$. In this imaging mode UME crash will happen if the SECM probe is scanned in small UME-substrate separation over tilted surfaces or rough surface, when structures exceed $2r_T$ (Figure 4.6c). On the contrary, when the UME is scanned away from the tilted surface or during scanning across deep grooves or cavities, feedback or collection efficiency will be lost (Figure 4.6b). Another difficulty with constant-height mode arises if it is employed for surfaces with variations in both, the conductivity and topography. It is difficult to distinguish between these two effects. The typical example of such surfaces used for discussion in this Chapter is a platinum microstructure on ceramic substrate. Independent experiment showed Pt structures of 180 nm height and 45 µm width (full discussion is given in Chapter 10). Figure 4.6e shows an SECM feedback mode image in constant height mode with UME of $r_T = 12.5$ µm and $r_g = 125$ µm in aqueous solution of 1 mM FcMeOH + 0.1 M KNO_3. It is clear that the UME crash is less likely if the sample is not tilted because the surface roughness is much less than the probe size. However, topography had imposed measureable impact on i_T because in feedback mode i_T depends on UME-substrate distance. In this circumstance it is difficult differentiate both effects.

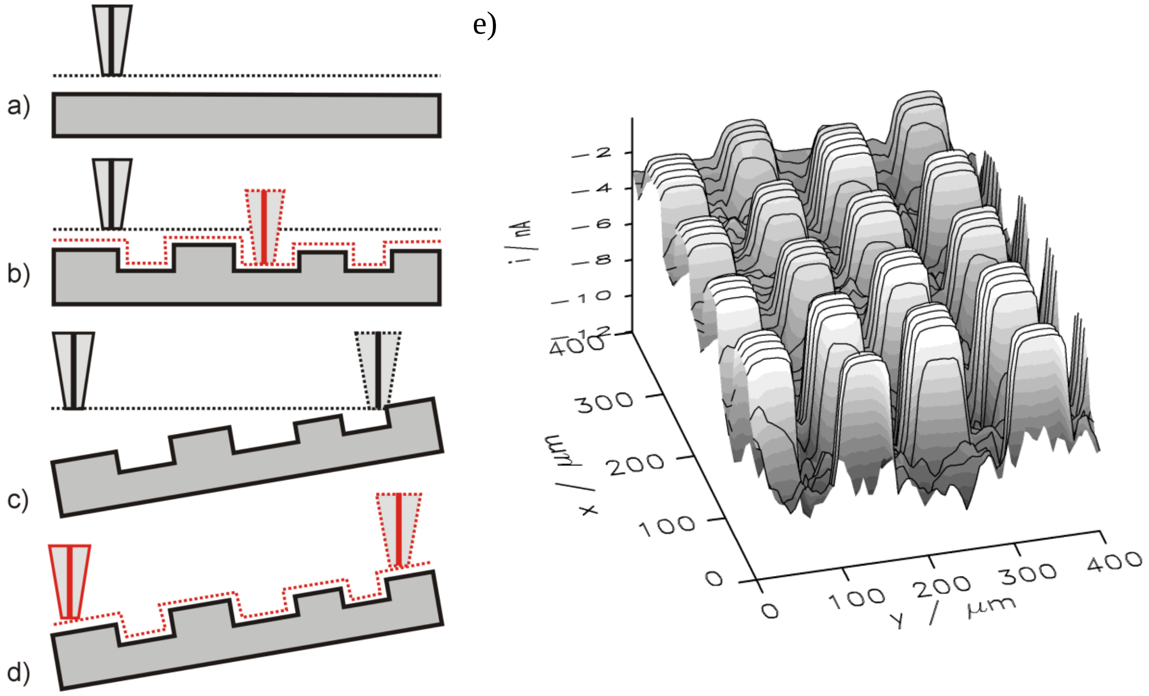

Figure 4.6a-d A schematic representation of the interaction of the microelectrode during constant height (black dashed line) and constant distance (red dashed line) scan. (e) SECM feedback mode image in constant height mode using platinum microstructure on a ceramic support.

Overcoming limitations of constant-height imaging is an important methodological progress in SECM research. SECM probe operated in constant distance mode follows the contours of the sample surface (Figure 4.6b, d; red dashed line) that could avoid probe crash and help to achieving simultaneous electrochemical reactivity and topography responses. Several strategies have been developed, particularly to use nanoelectrodes as an SECM probe to study structures and processes in nanoscale [186, 187]. This has been realized by the improvement of nanoelectrode fabrication [188-191], development of new modes of the SECM operation [192, 193] and selection of nanoscale systems suitable for SECM experiments [194]. SECM imaging with nanoelectrodes is challenging due to the difficulty to retain a constant L. This follows because a decrease of r_T requires a proportional decrease of d to maintain the same *L* and therefore the same relative contrast. Several methods have been demonstrated in order to maintain a constant *d*. These include the use of a shear force distance control [195-200], integrating SECM probes in AFM cantilevers where the geometry of the cantilever or the imaging in a lift-off mode provides the constant working distance [201-203], intermittent contact (IC) SECM [204], and the combination of SECM with scanning ion conductance microscopy (SICM)[186, 205]. Mirkin et al. [165] reported a more extensive review on developments in high resolution SECM imaging.

SECM-AFM method was reported as the most suitable to resolve surface topography effects from reactivity in the nanoscale imaging. However, the imperfect shape of steady-state voltammograms obtained by such probes (which is not good for quantitative electrochemical experiments) [206, 207] and imperfect electrochemical responses (AFM images usually appeared better than current maps) were realized [208-210]. Shear force distance control employs feedback signal based on hydrodynamic forces to maintain constant probe-substrate separation. Several types of shear-force detection system have been reported in the literature such as optical [195, 211], non-optical [198, 212, 213] based system. Schuhmann and co-workers [214, 215] introduced the non-optical shear force detection system for SECM following the procedure developed by Brunner et al [216]. The method involves nanoelectrode fastened by two piezoelectric plates. They are used as stimulator at one of the mechanical resonance frequencies of the probe (rather than at the resonance of a tuning fork) and detector of lateral probe vibrations. In this thesis a similar setup [198] was developed in combining it with a commercial PID feedback system. In our system shear-force is controlled independent from the SECM software. See Figure 5.6 for schematic illustration of a non-optical shear based SECM setup. A full description of shear force distance regulation for high resolution SECM imaging can be found in Chapter 10.

4.5.1. Experimental evaluation of SECM kinetic window

SECM imaging can provide reaction rate imaging if the current response follows the regime of finite kinetics at the sample [156, 157], i.e., if the response at the working distance (e. g. $d = r_T$) can be clearly distinguished from the prediction of an insulating, inert sample [146, 153] and from diffusion-controlled mediator recycling. The finite kinetics is described by a normalized dimensionless heterogeneous rate constant κ. If we assume that a response with $\kappa = 0.03$ can just be distinguished from the case of $\kappa = 0$ and $\kappa = 3.6$ can be separated from $\kappa = \infty$ (Figure 4.7a). We call the range $0.03 \leq \kappa \leq 3.6$ as the "kinetic window" in which reaction rate imaging is possible. A zone diagram is obtained by plotting k_{eff} *vs*. r_T with lines for $\kappa = 0.03$ and $\kappa = 3.6$ (Figure 4.7b). It illustrates clearly that smaller probe electrodes (desirable for high resolution) require increasing reaction rates [126, 149]. The normalized rate constant can be increased by decreasing D but this requires slower imaging to maintain a steady state situation [194]. These relations have also been verified experimentally [206]. Figure 4.7c illustrates the situation of a quasi-infinitely large uniform sample. Taking into account the dependence of the signal on the sample size, further limitations are imposed as shown in Figure 4.7c. If the radius of active sample regions $r_S < 0.05\ r_T$, the chemical flux generated by them becomes too small for detection [149]. This corresponds to the uncolored transparent regions in Figure 4.7c. On the other hand, if $r_S > r_T + 1.5\ d$, the sample behaves like an infinitely large sample (red, green, blue volumes in Figure 4.7c) where a kinetic investigation based on popular analytical approximations of simulation results are possible [157]. In between those regions there is transition region (olive in Figure 4.7c), in which imaging might be possible under favorable conditions but a quantitative analysis would require specific simulations for the sample under study. This review is reported in own publication [A7].

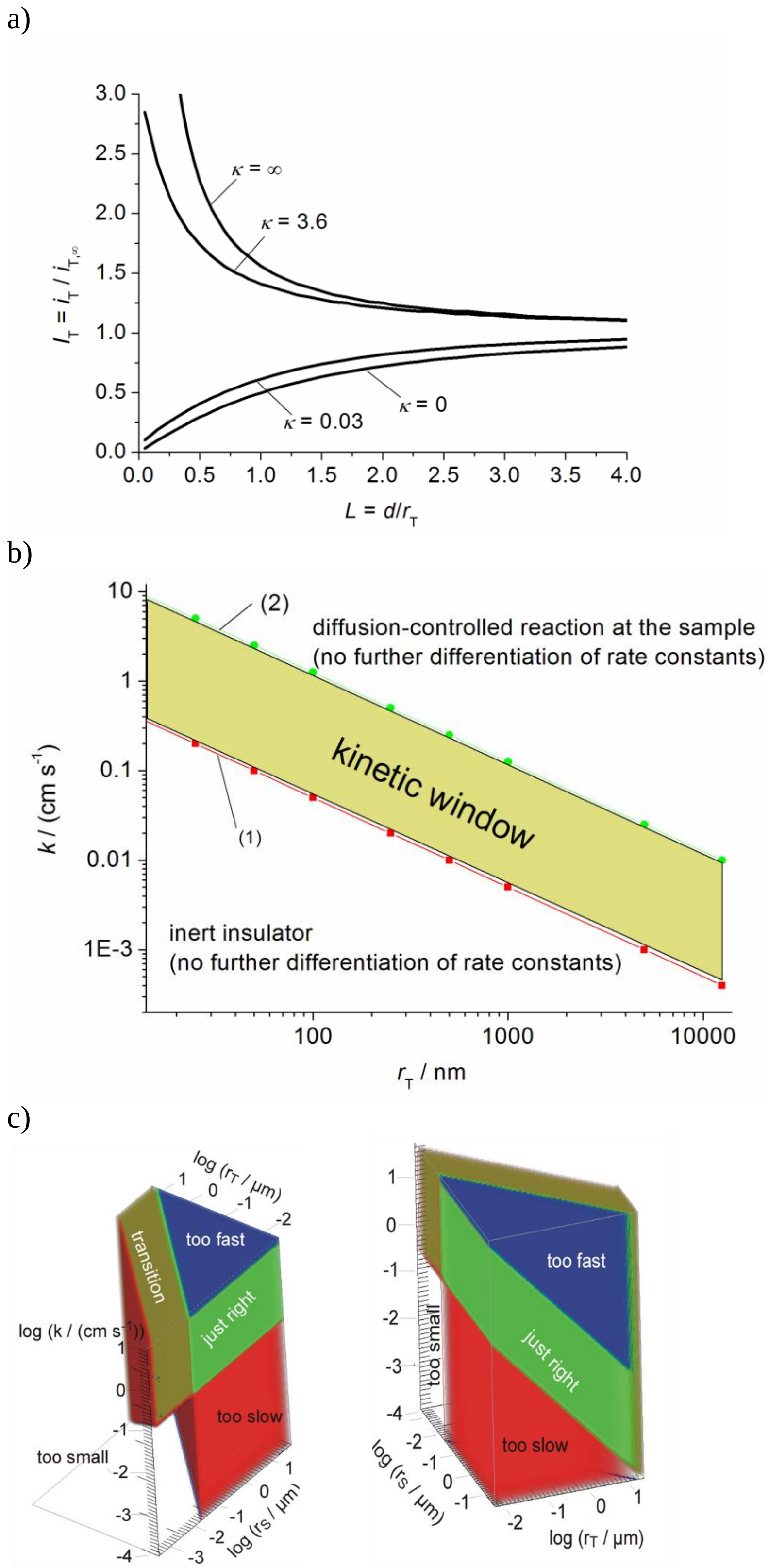

Figure 4.7 a) Calculated approach curves [157] for feedback mode for a disk of r_T = 12.5 µm, *RG* = 10; b) Plot of kinetic window defining the regions of finite kinetics of substrate reaction on quasi-infinitely large substrates, diffusion controlled response and hindered diffusion regime; c) SECM working regimes for finite kinetics and finite substrate sizes for $d = r_T$ and *RG* = 10. Figure reference [A7]

5. Experimental section

In this Chapter chemicals and materials used for SECM part of this thesis are listed in Section 5.1. Section 5.2 describes all the DSSC samples prepared for this study by our cooperating partners at Uppsala University and Giessen University. Section 5.3 considers the basic features of LED light sources used in this study. Section 5.4 describes the instrumental considerations of SECM for DSSC and for shear force distance control developed in this study. Finally, in Section 5.5 the fabrication and characterization of conventional UMEs and nanoelectrodes for high resolution SECM are illustrated.

5.1. Chemicals for SECM experiments

Acetonitrile (Spectrochem, HPLC grade), solvent for the mediator solution was purified by drying over molecular sieve 16 hours before use. For study of solvent effect on dye regeneration rate 1-ethyl-3-methylimidazolium bis(trifluoromethylsulfonyl)imide (EMimTFS; Figure 5.1a; io-li-tec, Heilbronn, Germany) was used as RTIL solvent. For studying cation effects in dye regeneration rate 1,2-dimethyl-3-propylimidazolium bis(trifluoromethylsulfonyl)imide (DMPimTFS) (Figure 5.1b; io-li-tec, Heilbronn, Germany), lithium bis(trifluoromethylsulfonyl)imide (LiTFS; Figure 5.1d) and anhydrous tetrabutylammonium trifluoromethanesulfonate (TBAS; Fluka, Basel, Germany) were used as supporting electrolyte without further treatment. I_2 was obtained from Merck or Fluka and was purified by sublimation before use. KI was pre-treated by heating at 140-150 ^{o}C for 3 hours and then dried in vacuum before use, lithium iodide LiI (Alfa Aesar, Karlsruhe, Germany), tetrabutylammonium iodide (TBAI) and 1,2-dimethyl-3-propylimidazolium iodide (DMPimI; io-li-tec, Heilbronn, Germany) served as sources of iodide. The electrolytes were dissolved either in acetonitrile or EMimTFS to give mixed electrolyte with the following compositions: $KI/I_2/TBAS$, $LiI/I_2/LiTFS$, $DMPimI/I_2/DMPimTFS$, and $TBAI/I_2/TBATFS$. Ferrocene methanol (FcMeOH, ≥97 %, Alfa Aesar, Karlsruhe, Germany), ethanol (VWR International S.A.S, Fontenay-sous-Bois, France) and KNO_3 (≥99 %, Carl Roth, Karlsruhe, Germany) were used as received. Deionized water was produced by Purelab® Classic (Elga LabWater, United Kingdom). $[Ru(NH_3)_6]Cl_3$ (ABCR, Karlsruhe, Germany) was used as mediator.

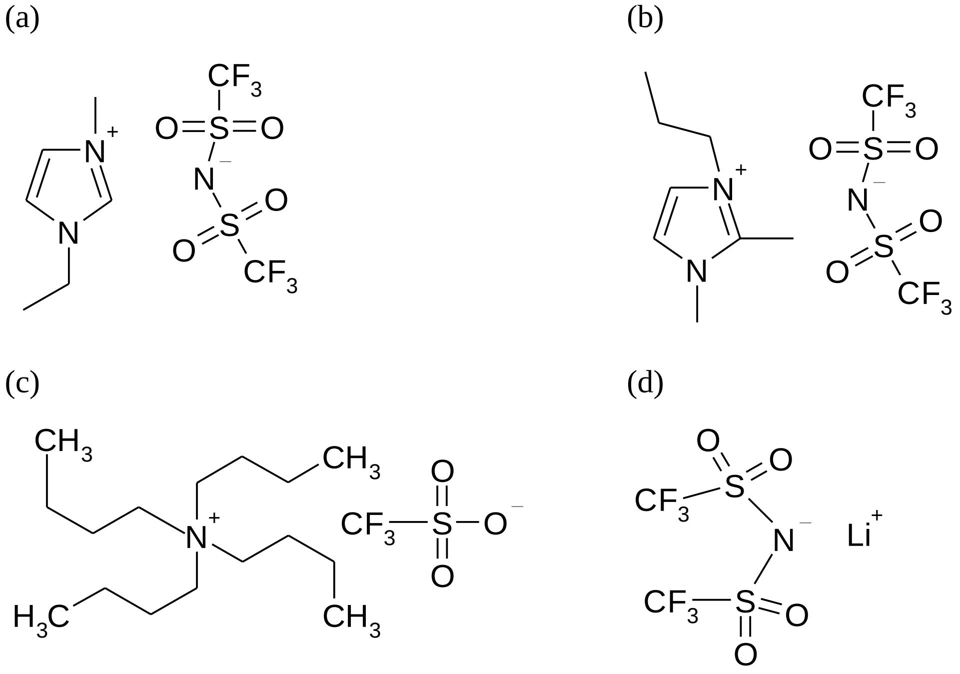

Figure 5.1 Chemical structures of (a) EMimTFS, (b) DMPimTFS, (c) TBAS and (d) LiTFS,

Model samples: Three model surfaces for shear force imaging were tested. Parallel gold bands on a glass slide prepared by standard photolithographic process (EPFL), platinum microstructure on ceramic substrates (Heraeus Sensor Technology GmbH, Germany) and gold microelectrode arrays fabricated on 125 µm thick polyimide Kapton HN® films (Goodfellow, Huntingdon, England) Reference [A3]

Instruments: To obtain topographic information, atomic force microscopy (AFM) in tapping mode (Nanoscope IIIA controller, Veeco Instruments Inc., NY, USA) and confocal laser scanning microscope (CLSM; TCS SP2 AOBS, Leica Microsystems GmbH, Wetzlar, Germany) in reflection mode were used. The scanning electron microscopy (SEM) measurements of nanoelectrode probes were performed with a Hitachi S-3200N (Scientific Instruments, Nissei Sangyo GmbH, Ratingen, Germany).

5.2. Descriptions of DSSC sample preparation

5.2.1. Preparation of N719/TiO_2 films

N719/TiO2 samples were prepared (group of Prof. Dr. Anders Hagfeldt, Uppsala University) by screen printing of TiO_2 nanoparticulate on fluoride-doped tin oxide glass plates (FTO, Pilkington TEC15). The nominal geometrical area of the TiO_2 films was 4 mm × 8 mm. The films were subsequently sintered at 500 °C for 30 minutes. The SEM micrograph for the film is shown in Figure 5.2. The thickness of the films was ca. 7 µm as measured by profilometer (Veeco Instrument, Dektak 150). These films were then kept immersed in the dye bath for 17-18 hours. The amount of dye acquired by the film was estimated by dissolving the dye in 7 M aqueous NH_3 solution and measuring the absorption spectrum in solution, from which the dye loading (amount of dye per geometric area) was estimated as ca. 6.3×10^{-8} mol cm^2 geometric area.

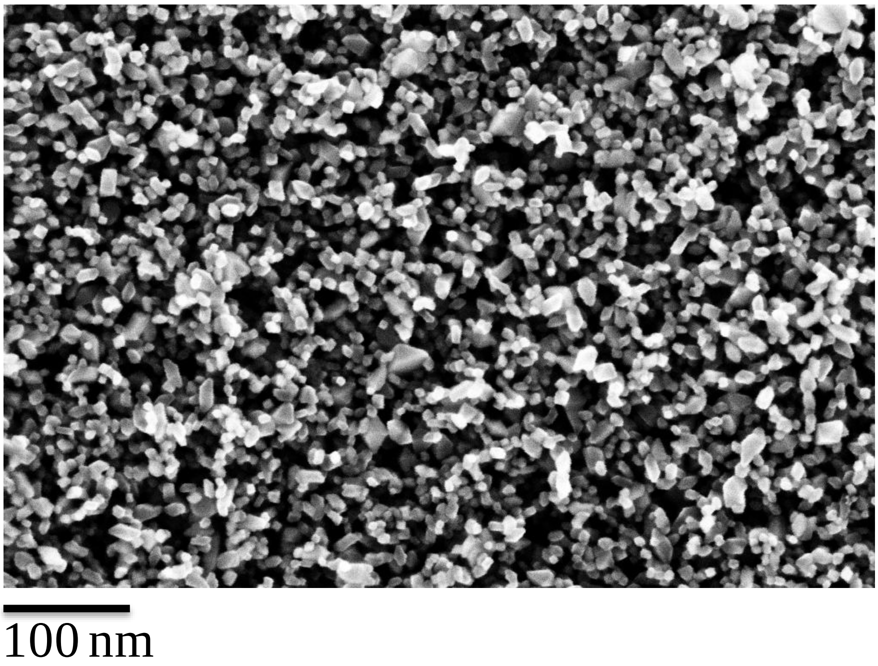

Figure 5.2 SEM image of nanocrystalline TiO_2 prepared by screen printing technique. SEM image was provided from collaboration partners in Uppsala University, group of Prof. Dr. Anders Hagfeldt.

5.2.2. Preparation of ZnO/Eosin-Y and ZnO/D149 films

Electrochemical deposition in the presence of a structure-directing agent (SDA) was carried out in a three electrode single compartment cell with a saturated calomel electrode (SCE) as reference electrode, a Zn wire as counter electrode and F-doped SnO_2 on glass (Asahi glass, sheet resistance <12 Ω per square, effective transmittance > 85%) as working electrode [217]. The FTO-coated glass substrate was pre-treated by immersing it into 45% HNO_3 (Roth) for 2 minutes. The FTO-glass substrate was mounted as a rotating electrode in a stainless steel holder providing mechanical and electrical attachment to a rotating disk electrode (RDE) system and was operated at 500 rpm. The deposition bath consists of an oxygen-saturated aqueous electrolyte containing 5 mM $ZnCl_2$ (Fluka), 0.1 M KCl (Roth, Karlsruhe, Germany) and 50 µM xanthene dye Eosin Y (Aldrich, Schnelldorf, Germany) as SDA [71]. Interaction of the SDA with the growing zinc oxide layer results in the formation of sponge-like, nanoporous ZnO crystals with eosin Y occupying the pores [58]. Following electrodeposition, the SDA can be removed from the hybrid film by soft alkaline treatment in pH 10.5 aqueous KOH [70, 217] for 24 hours. The adsorption was carried out in the dark at room temperature. The films were dried in air for 1 hour at 150 °C and subsequent adsorption of suitable sensitizers onto the large inner surface of the ZnO films yields active photoelectrodes for dye-sensitized solar cells [217].

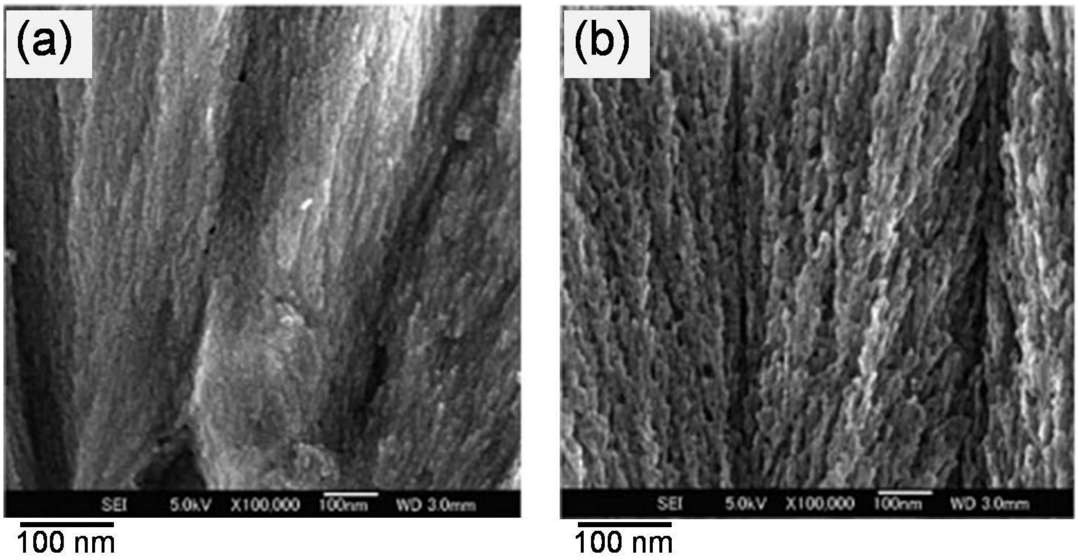

Figure 5.3 SEM images of (a) electrochemically deposited ZnO/Eosin Y hybrid film on FTO-glass substrate, (b) ZnO film after extraction of Eosin Y. The images were taken from Ref. [58]

For re-adsorption different dyes, among them Eosin Y can be used. Eosin Y was re-adsorbed from 250 µM Eosin Y aqueous solutions at 80 °C. The indoline dye D149 was adsorbed from a solution containing 0.5 mM D149 and 1 mM chenodeoxycholic acid (Fluka BioChemika, 98.0%) in a mixture (1:1 by volume) of acetonitrile (Sigma-Aldrich, 98%, anhydrous) and tert-butanol (Roth, ≥ 99.5%).

The total ZnO/D149 film thickness was determined from confocal laser microscopy images of small pieces cut out of the ZnO/D149 films recorded. At the cutting edges, the ZnO/D149 films were partly scratched off the FTO-coated glass substrate, to measure the step height between FTO and the ZnO/D149 films with a Keyence VK-9700K. The thickness was determined at three different sites of each piece of film and the obtained values were averaged. This method was confirmed by profilometry (tencor instruments α-step 10-00020) performed at the border of the films (defined during deposition by the insulating tape).

5.3. LEDs as light source

For part of the work ([A1], Section 7.1) ordinary light emitting diode (LED, 2000 MCD Blue, Green and Yellow. Reichelt Elektronik, Sande, Germany) were focused onto the back side of the ZnO/Eosin Y film. In all other experiments LEDs from Zahner electric, Kronach, Germany were used. This LED as light source was integrated into the basic SECM setup to investigate DSSC electrodes. The emitted light intensity from these LEDs was kept constant by a feedback control established via a photodiode and an XPOT potentiostat (Zahner electric, Kronach, Germany). The integrated light intensity at the position of the sample was measured using a laser power meter (FieldMaster, Coherent Inc., Santa Clara, USA). The LED intensities at the position of the sample are calibrated by plotting the intensity measured by power meter *versus* the intensity controlled by the light sensor integrated in the system (Figure 5.4a). The measured power density is expressed in terms of photon flux. The following example calculation is provided to clarify the expression of measured power in terms of photon flux density.

Consider an LED power P = 56 µJ s^{-1} is measured with a power meter at the illuminated area of A of 5.65×10^{-2} cm^2, using 474 nm LED as a light source. The corresponding energy of one photon is $E_{h\nu} = hc/\lambda = 4.19 \times 10^{-19}$ J, from which the number of photons per second, $N_{h\nu} = P/E_{\mathrm{h}\nu}$, is obtained as 1.34×10^{14} s^{-1}. The resulting photon flux expressed by $J_{h\nu} = N_{h\nu}/(A \times N_{\mathrm{A}})$ is determined to be 3.93×10^{-9} mol s^{-1} cm^{-2}.

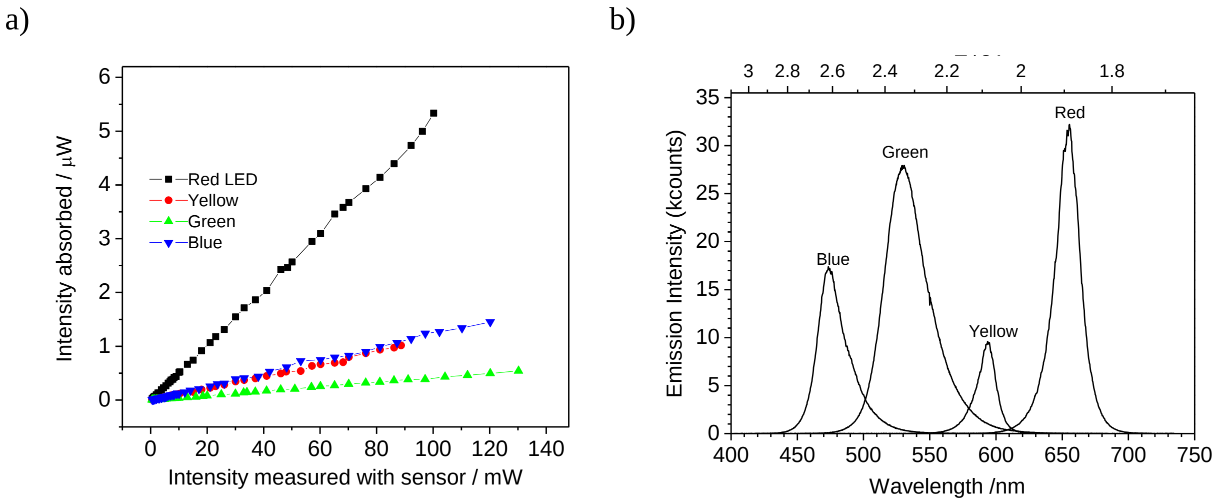

Figure 5.4a) LED intensity calibration measured with power meter against LED sensor at the position of the DSSC sample in SECM set-up. b) The emission spectra of blue, green, yellow and red LEDs from the inensity regulated illuminator used as light source.

The emission spectra of the LEDs were measured using an emission spectrometer (TRIAX 320, Horiba Jobin Yvon GmbH, München, Germany, Figure 5.4a). The spectra show that the excitation light does not contain contributions below 420 nm which otherwise could lead to direct photoexciation of ZnO or TiO_2 (band gap 3.2 eV corresponding to 386 nm). Using the maximum emission intensity 474 nm (blue LED), 529 nm (green LED) and 593 nm (yellow LED) and 647 nm (red LED), the corresponding excitation energies are 2.617 eV, 2.345 eV, 2.09 eV and 1.894 eV, respectively.

5.4. Instrumental considerations in SECM

5.4.1. SECM setup for solar cell electrodes

The basic SECM device developed in-house consisted of four main parts: a small volume electrochemical cell, a mono- or bi-potentiostat, a high resolution positioning system, and a computer as shown in block diagram in Figure 5.5. The electrochemical cell includes the UME as working electrode (WE1), the reference and auxiliary electrodes. The sample is fixed to the cell bottom between two O-rings. The potentiostat is capable of measuring currents down to the pA range. In case of a bipotentiostatic experiment, one channel is used to control the potential of the sample (WE2) and the other to control the UME potential and to measure the UME current (WE1). An important aspect of SECM is the positioning system, which includes the positioning elements (piezo actuators or stepping motors), translator stages that guide the motion, and a motor controller that transfers the digital command from the computer to electrical signals for the actuators. The positioning actuators move in three space dimensions with a high spatial resolution. The computer coordinates the positioning and data-acquisition system and displays the SECM data. We use a digital-to-analog converter (AD/DA) to convert the digital signal coming from the computer in order to feed potentiostat with an analog signal.

In specific case of DSSC study this home-built SECM instrument consisted of a positioning system (SPI Robot, Oppenheim, Germany) and a data acquisition board (CIO-DAS 1602/16, Plug-in Electronic GmbH, Eichenau, Germany), a stabilized LED light source (Zahner electric, Kronach, Germany) and was operated under the SECMx software, as schematized in Figure 5.5.

A three-electrode cell made of Teflon with small opening from the back side was placed on a home-made 2-axis tilt platform, which allowed parallel adjustment of the substrate with respect to the lateral movement of the SECM probe. The Teflon cell contained a Pt wire counter electrode, a Pt wire quasi reference electrode, and the dye-sensitized sample film was attached to the cell bottom and sealed by an O-ring. An extra Pt wire was used to connect the back contact of the sample with the electrolyte in order to operate the photoelectrochemical cell in a short-circuit setup. The irradiation from LEDs was focused by an objective lens (10x, Carl Zeiss, Jena, Germany) onto the back side of dye-sensitized film as described in Section 5.3. A potentiostat provided control of the potential of the ultramicroelectrode (UME), while the current response was acquired by an AD/DA data acquisition card using the in-house developed SECMx software [218]. All measurements were performed in a Faraday cage dark box [219]. The in-house software MIRA was used to process and analyze data.

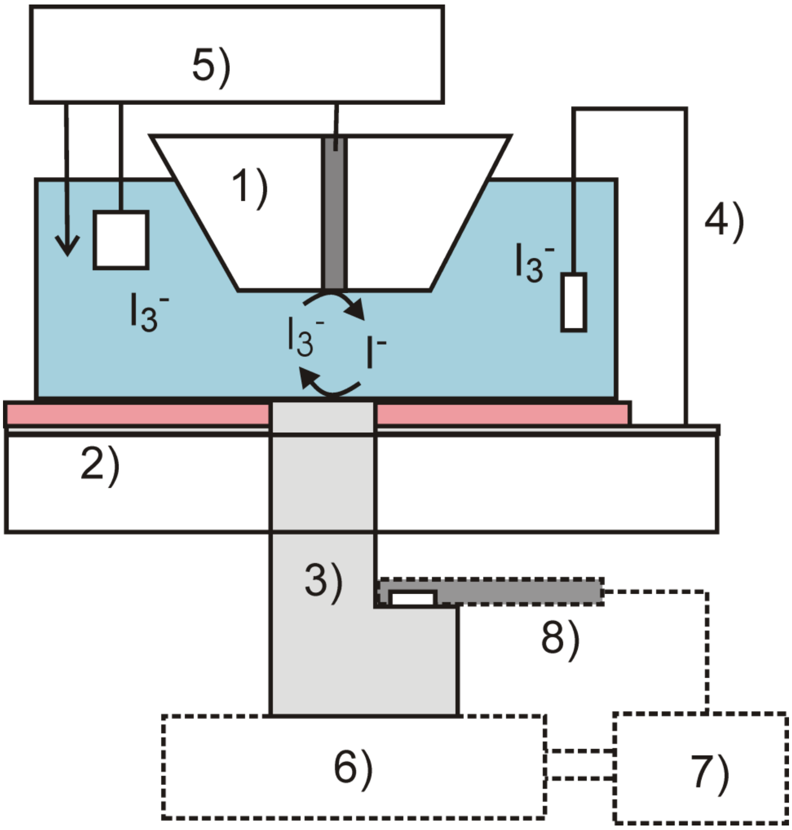

Figure 5.5 Schematic of SECM setup to investigate redox processes at a DSSC. 1) UME, 2) F-doped glass with coating of dye-sensitized film, 3) illumination path, 4) short contact of the DSSC, 5) potentiostat with UME as working electrode and reference and counter electrode. In case of intensity dependent measurement (dashed lines) regulated LED light source (6) was powered with a potentiostat (7) and checked by a light sensor (8).

5.4.2. SECM instrumentation with shear force distance regulation

Figure 5.6 shows a schematic of the home-made SECM with non-optical shear force distance control system. The shear-force unit consists of two piezoelectric plates, which are used to stimulate and detect the lateral oscillation of the SECM probe. The two piezoelectric plates were fixed to the nanoelectrode body at approximately 45° relative to each other [198]. The shear force regulation consisted of a DS4L controller with SXM software version 0.19f

(Anfatec Instruments AG, Oelsnitz, Germany), and excitation, detection and lock-in amplification of the vibration. The control SXM software runs on an independent personnel computer (PC). The vertical position control signal was fed into the piezo controller/amplifier E-662 (Physik Instrumente, Karlsruhe, Germany). The E-662 was operated in open loop. This controller drove a linear piezo stage P-780.20 with a translation range of 80 µm and an internal position sensor (Physik Instrumente, Karlsruhe, Germany).

The basic SECM system consisted of a positioning system (Märzhäuser GmbH & Co KG, Wetzlar, Germany) and a custom-made analog bipotentiopstat (M. Schramm, University of Düsseldorf, Germany) interfaced to the PC via an AD/DA board (PCI-DAS 1602/16, Plug-In Electronic GmbH, Eichenau, Germany). The measurements were made in a three electrode configuration with a Pt auxiliary electrode and a Ag wire as quasi-reference electrode (Ag QRE). The signal from the position sensor of the linear piezo stage was also read by the analog-digital board and used to construct a topographical image. This instrument is operated with the in-house developed control software SECMx [218]. Data are processed with the in-house developed software MIRA [219].

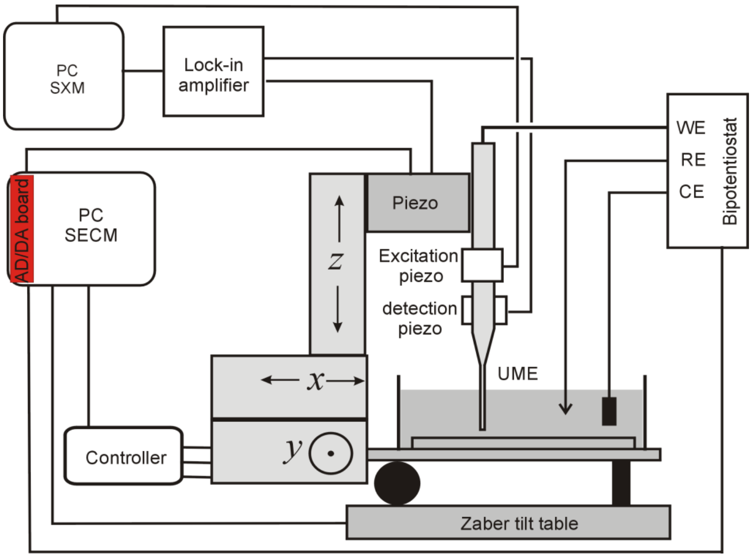

Figure 5.6 A simplified schematic of the SECM setup with a non-optical shear force constant distance control system.

5.5. Ultramicroelectrode fabrication

The 25 µm diameter Pt UMEs used for SECM-DSSC experiments were fabricated according to previously established procedure [220]. Briefly, a borosilicate glass capillary 10 cm long (Hilgenberg GmbH, Malsfeld, Germany) was rinsed with water and acetone prior to use. Then, it was cut into half by heat puller (Model PP-830, Narshige, Japan). A small piece of the tapered end was cut with a scalpel and sealed by burning with a portable torch. A 1 cm piece of a 25 µm diameter Pt wire (Goodfellow, Bad Nauheim, Germany) was cut on a white paper using a scalpel and cleaned with water, acetone consecutively to remove any dust and then dried. This piece was pushed inside the capillary by gently knocking vertically with the tapered end on a desk until the Pt wire was inserted at the end. The glass capillary was put back in the heat puller setup with its tapered terminal positioned in the centre of a tungsten coil. The open end of the capillary was connected to a vacuum pump by a thin silicon tube. Evacuating the tip during the melting process prevents formation of air bubbles between the Pt wire and the glass. The tungsten coil was heated electrically at about 45, 65 and 75 heating level for 5 minutes to melt the glass around the Pt wire and to fix the Pt wire at the tapered terminal. After finishing with melting, the electrode was left to cool down and inspected under the microscope to check whether the wire is completely sealed at the tip and to make sure that there is no air bubble. The Pt microdisk surface was exposed by polishing the sealed end vertically on a wheel with disks (Mechanical workshop, University of Oldenburg) and micropolishing cloth wetted with alumina suspension (0.3 µm and 0.05 µm) to a ratio $RG = r_{\text{glass}}/r_{\text{T}} \approx 10$, where r_{glass} is the radius of the insulating sheath and r_{T} is the radius of the active UME. The back connection between the Pt wire and copper was made by filling the capillary with a two component Ag epoxy. The Cu wire was fixed at the upper part of the capillary with a two component UHU* and dried in an oven. The resulting electrode is characterized by cyclic voltammetery and CLSM. Before each experiment, the UME was polished with 0.3 and 0.05 µm alumina powder and rinsed with water and the specific solvent under use.

5.6. Fabrication of Pt nanoelectrodes

The Pt nanoelectrodes were fabricated using a laser pipette puller as described earlier [221, 222]. Briefly, a pre-cleaned 1 cm long 25 µm diameter Pt wire was inserted in the middle of a pre-cleaned 10 cm long quartz glass capillary (inner diameter 0.3 mm, outer diameter 0.9 mm) (Goodfellow GmbH, Bad Nauheim; Germany). It was placed exactly at the middle of the laser heating chamber of a laser pipette puller (P-2000, Sutter Instrument Co., Novato, CA). The capillary was evacuated before and during heating by connecting its two ends via a Y-shape silicon tube. A two step sealing-pulling procedures were utilized that follow the recommendation of Ballestros Katemann et al [215]. The program parameters had to be adapted to our particular instrument and require periodic readjustment. The following set is a typical example: heat = 640, filament = 4, velocity = 100, delay = 100 and pull = 1 is used to seal the Pt wire and glass capillary together by a cycle of 15 seconds heating and 20 seconds cooling. The procedures is repeated five times while a specially designed clamp prevent a pulling process by holding the fixing screws of capillary holder of the laser puller. After a well sealed capillary is obtained, the clamp is removed and the final hard pulling was made with parameters heat = 640, filament = 2, velocity =100, delay = 100 and pull = 220. The produced nanoelectrodes have smooth surface and long tapers. All electrodes were polished at a 90° angle with a home-made rotary stage on a micropolishing cloth with suspension of 0.05 µm alumina particles. The characterization of nanoelectrodes is described in Section 10.1

6. SECM measurement of the dye regeneration rate

6.1. Model electrolyte

The redox couple I_3^-/I^- is typically employed to reduce the photo-oxidized dye cation and to shuttle electrons between the counter electrode and photoanode. The success of this redox couple has generally been attributed to its favourable kinetics and energetic towards to different semiconductor oxides and dye sensitizers. The I_3^- displays unusually slow kinetics for the reduction by electrons from the conduction band of the semiconductor interface, but fast kinetics for the reduction at the platinum catalyst-coated counter electrode of a DSSC. Iodide (I^-) exhibits favourable energetic and kinetics for the regeneration of the sensitizer molecules. These processes lead to coherent diffusion of I_3^- towards the counter electrode and I^- diffusion in the opposite direction towards to the photoelectrode [112, 120].

The main difficulty in the SECM feedback investigation is the selection and optimization of the mediator solution. It should contain only one redox form of the mediator couple and should not undergo homogeneous photochemical reactions. In theory, many possible ways of matching dyes and semiconductors with an electrolyte system exist. To generate a flux of I^- at the ultramicroelectrode (UME), we used a solution formed by mixing equimolar amounts of I_2 and KI solutions in acetonitrile with an inert supporting electrolyte. Since the equilibrium constant for the reaction $I^- + I_2 \rightleftharpoons I_3^-$ is 10^7 M^{-1} [223] in acetonitrile, the concentration of I^- and I_2 is only 1% of the concentration of I_3^- for a solution that contains a total of 1 mol cm^{-3} KI_3. The spectroscopy and dynamics of I_3^- have been extensively studied in solution. Its absorption spectrum consists of two broad bands centered at 360 nm and 290 nm [224]. Figure 6.1 shows the cyclic voltammogram of such a solution at a Pt microdisk electrode in the bulk phase of the solution with TBAS as an inert supporting electrolyte. It shows a well-defined reduction wave for reaction $I_3^- + 2e^- \rightarrow 3I^-$ and an oxidation wave for the reaction $I_3^- \rightarrow 1.5I_2 + 2e^-$. If an equimolar mixture of KI and I_2 is indeed obtained, there is a region around 0 V (versus the Pt pseudo-reference electrode) where no current flows. SECM experiments were carried out at a UME potential E_T = -0.7 V where a diffusion-controlled reduction of I_3^- took place and I^- was produced by the UME.

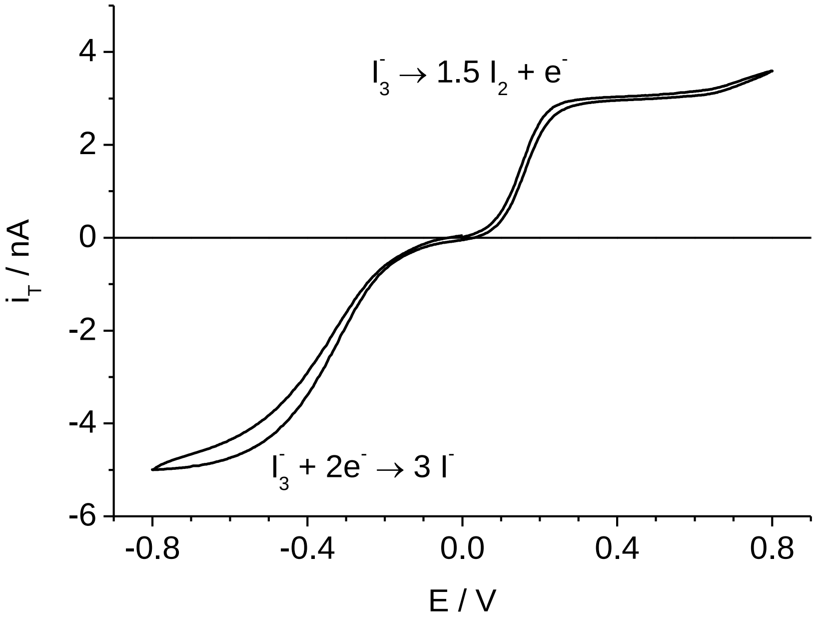

Figure 6.1 Cyclic voltammogram of 0.495 mM I_3^- + 0.1 M TBAS in acetonitrile solution at a Pt UME, scan rate 0.05 Vs^{-1}.

Preparation of the solution containing exclusively I_3^- from equimolar mixture of iodide salt and I_2 requires titration of the mixture until the plateau and zero current is established. This procedure is discussed by considering a specific example. For instance, initially 0.197 mM KI in 2.5 ml and 0.197 mM I_2 in 2.5 ml from corresponding 4 mM stock solution are made. The mixture of the two solutions produces a 5 ml solution containing I_3^- with residual I^- or I_2. The steady state CV at Pt UME for this solution showed a plateau at the region around 0 V shifted to cathodic currents. This implies that the mixture contained excess I_2. Systematic titration is conducted by adding defined amount of the salts and consequently checking the CV. In this particular example the following composition of salts was required.

KI 2.5 ml + 0.05 ml + 0.05 ml + 0.1 ml + 0.2 ml = 2.9 ml

I_2 2.5 ml + 0.05 ml + 0.05 ml = 2.6 ml

The actual $[I_3^-]$ was calculated by dilution formula as follows:

$[I_3^-] = (2.9 \text{ ml} \times 0.197 \text{ mM})/(2.9 \text{ ml} + 2.6 \text{ ml}) = 0.104 \text{ mM}$

6.1.1. Determining diffusion coefficient of I_3^- in RTILs

Figure 6.2 shows cyclic voltammograms for the redox reaction of I_3^- at Pt UME (r_T = 12.5 µm) in the electrolyte composed of 0.95 mM LiI, 0.95 mM I_2 and 0.01–2.55 M LiTFS in EMimTFS, measured at a scan rate of 50 mV s^{-1}. The voltammograms show a two sigmodal waves, corresponding to the reduction and oxidation of I_3^- to I^- and I_2, respectively. Like in acetonitrile solution, the ratio of cathodic and anodic wave heights is approximately 2/3 and the plateau at E = 0.05 V lies on zero current regime, confirming that equimolar amounts of I^- and I_2 were mixed, which yields I_3^- as the only relevant redox active species in the electrolyte [223]. The steady-state reduction currents for I_3^- gradually decreased as the concentration of inert supporting electrolyte increases, while the steady-state oxidation currents did not change. It should be noted that higher inert supporting electrolyte concentration is expected to increase the viscosity of the electrolyte. Accordingly, it is considered that this property reduces the mobility of ions and hence the steady-state currents at the UME. When the steady state condition is obtained, the diffusion coefficients D of I_3^- in different electrolytes concentration could be determined from diffusion-limited UME-currents using the following equation:

$$D = \frac{i_{T,\infty}}{8F[I_3^-]^* r_T} \tag{6.1}$$

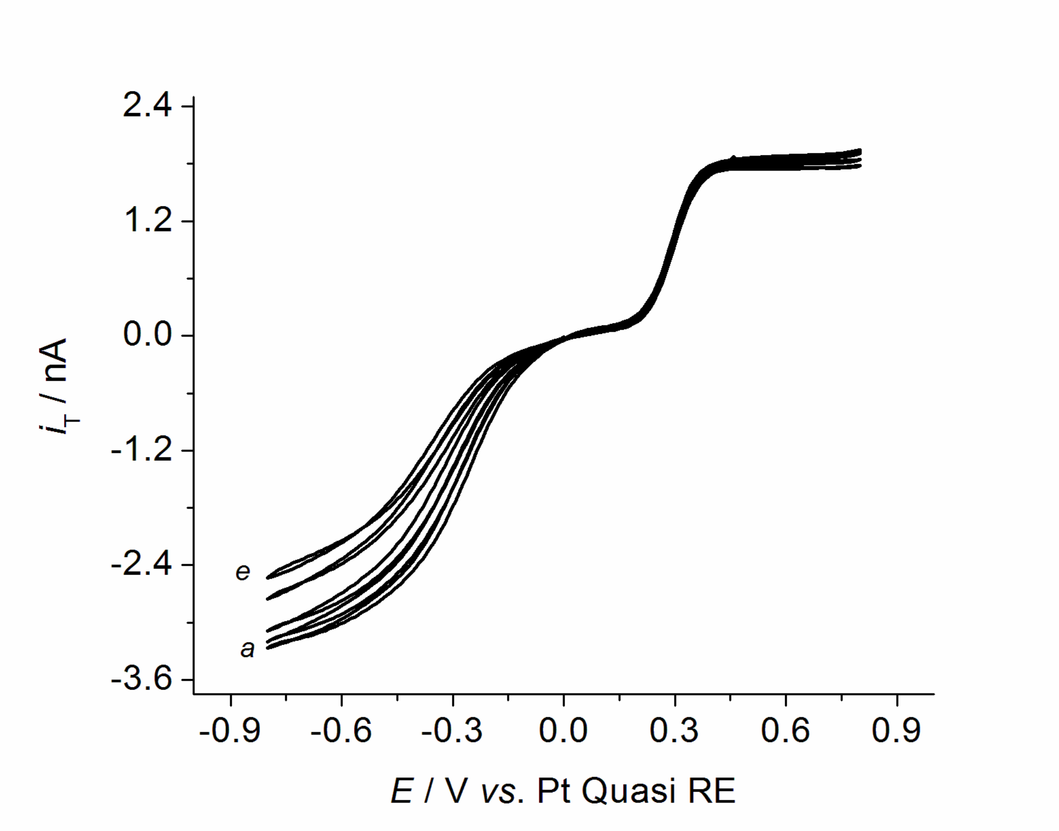

Figure 6.2 Typical cyclic voltammograms obtained at a Pt disk UME (r_T = 12.5 µm) in 0.95 mM I_3^-. The concentration of LiTFS from a to e are 0.02 M, 0.5 M, 1.05 M, 2.02 M and 2.5 M, respectively.

Table 6.1 Tri-iodide diffusion coefficients for the systems LiI/I_2/LiTFS, DMPimI/I_2/DMPimTFS and TBAI/I_2/TBATFS in EMimTFS with 0.95 mM $[I_3^-]$* and varying supporting electrolyte concentration ranging from 0.01 to 2.5 M.

Concentration of supporting electrolyte/M	D / 10^{-7} cm^2 s^{-1}		
	LiI/I_2/LiTFS	DMPimI/I_2/DMPimTFS	TBAI/I_2/TBATFS
0.01	8.10	7.36	2.26
0.5	6.27	5.45	1.09
1.05	5.18	4.64	1.03
1.51	4.36	4.17	1.01
2.02	3.82	3.08	0.99
2.5	2.90	2.45	0.90

6.2. Photoresponse of Pt UME and tri-iodide mediator

In order to exclude photochemical reaction of the mediator solution and the absence of photoelectrochemical effects at the Pt UME probe, feedback mode approach curves were recorded above glass substrates without a dye-sensitized film in the dark and under illumination (Figure 6.3). The curves are presented in normalized coordinates I_T(L) versus *L*. The curves agree within experimental error with the theoretical approach curve to an insulating and inert sample expected for a UME of this geometry. This curve, denoted by $I_{T,ins}(L)$, represents the effect of hindered diffusion only, because no reaction occurs at the glass surface. The perfect agreement of the experimental curves with the theory of hindered diffusion supports the general applicability of this mediator system.

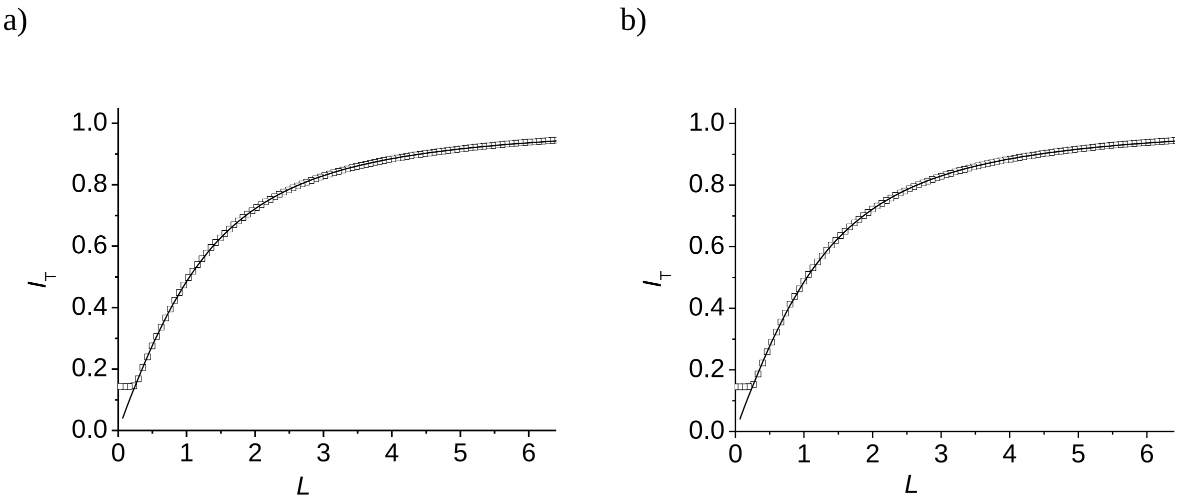

Figure 6.3 Normalized SECM feedback approach curves in 0.56 mM I_3^- for the approach of Pt disk electrode, r_T = 12.5 µm, toward glass (a) in the dark (b) under illumination by blueLED. Open symbols are experimental points and solid line is based on theoretical results calculated according to the discussion in Section 4.3.1.1. Other parameters are *RG* = 10, scan rate 1 µm s^{-1}, E_T = -0.7 V, d_0 = 0.1 µm

The corresponding experiments were carried out at ZnO/Eosin Y films in the dark. The response of $I_{T,ins}(L)$ is equal to that of glass. As an example see curve 1 in Figure 7.7. This indicates that in the absence of illumination, the flux of I^- generated at the UME is not oxidized at ZnO/Eosin Y film substrate and as a result the Eosin Y-sensitized ZnO film behaves as an inert and insulating substrate in the dark. This is expected from the semiconducting characteristics of ZnO but is remarkable since it shows efficient blocking of the conductive FTO back electrode by the porous ZnO. This fact is important in DSSC to hinder the back transfer of electrons (shunt in the cell).

6.3. Reaction at pristine FTO glass substrate

The FTO substrate plays an important role in determining cell performance, since electron transfer from the FTO to I_3^- ions provides a loss route. At the non-illuminated dye sensitized electrode the possible site for this reaction is the FTO surface which is not covered by the dye-sensitized film but is exposed to the electrolyte. The FTO substrate is highly doped and exhibits essentially metallic properties as far as outer sphere redox reactions are concerned. Gregg et al. [116] have shown that simple one-electron redox systems such as ferrocinium/ferrocene cannot be used as electrolytes in a dye-sensitized cell unless steps are taken to block the back reaction of electrons with the oxidized redox species. Figure 6.4 show SECM feedback mode line scan and image at the edge of FTO/D149-sensitized ZnO film electrode in the dark in a solution containing 2 mM FcMeOH + 0.1 mM TBAS in acetonitrile, with UME (r_T = 12.5 µm) at a scan rate of 2 µm s^{-1}. A classical behaviour of higher UME current over FTO and lower current over ZnO/D149-coated FTO surface is observed. Over D149-sensitized ZnO coated FTO, mediator regeneration at the back coat can occur either by direct tunnelling or diffusion through defects on the dye-sensitized layer. Some spike like features were realized in Figure 6.4 which can be attributed to artifacts or real features on the surface. The region with larger current corresponds to FTO surface.

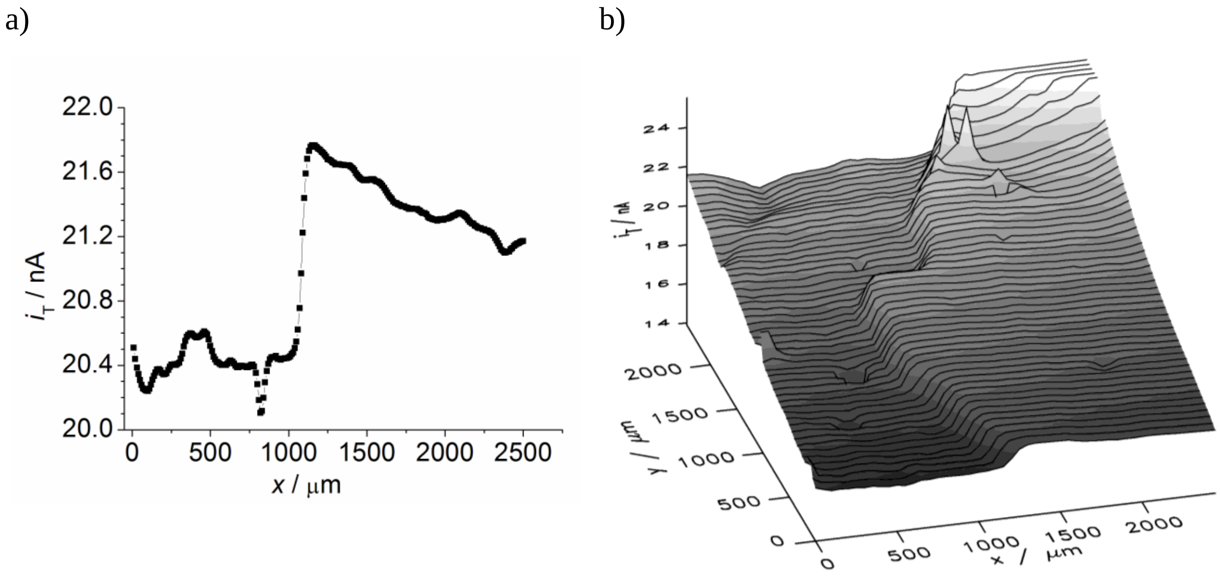

Figure 6.4 (a) Line scan and (b) two dimensional imaging at the edge of D149/ZnO film-FTO substrate. Experimental parameters: 2 mM FcMeOH + 0.1 mM TBAS, r_T = 12.5 µm, scan rate = 2 µm s^{-1}.

By using SECM feedback mode approach curves, clear differences are shown in the kinetics of electron transfer at the ZnO/D149-coated FTO and bare FTO with I_3^- or ferrocene methanol as mediators under no illumination (Figure 6.5a). Measurements are carried out in the dark with the electrode at open circuit potential. Figure 6.5a shows a schematic diagram that illustrates the mechanism proposed for the ET reaction between UME and the substrate with I_3^- as mediator. The oxidation of I^- at the surface is driven by the concentration gradient imposed by the I^- generation at the UME [196]. The mediators are chosen such that each has different properties. I^-/ I_3^- in acetonitrile is the common redox couple for obtaining high efficiencies in DSSC [114, 225]. The ferrocene methanol (FcMeOH) redox couple in the SECM is a common outer sphere redox couple often used as SECM mediator [16, 226, 227]. For each mediator an approach curve is recorded at the bare and D149/ZnO coated FTO electrode. The feedback effect of these two redox couples is considerably different towards one and the same bare and ZnO/D149-coated FTO surface (Figure 6.5b). The current response at the UME with FcMeOH corresponds to finite reaction kinetics for an approach to the ZnO/D149 film (Figure 6.5b, curve 3) and positive feedback for an approach to an FTO surface (Figure 6.5b, curve 4).

The approach with I_3^- as mediator to the bare FTO surface corresponds to the regime of finite kinetics (Figure 6.5b, curve 2) that is significantly slower than that of ferrocene methanol at the ZnO/D149 coated FTO. The approach with I_3^- as mediator to the ZnO/D149-coated surface is almost identical to a completely inert and insulating surface (Figure 6.5b, curve 1).

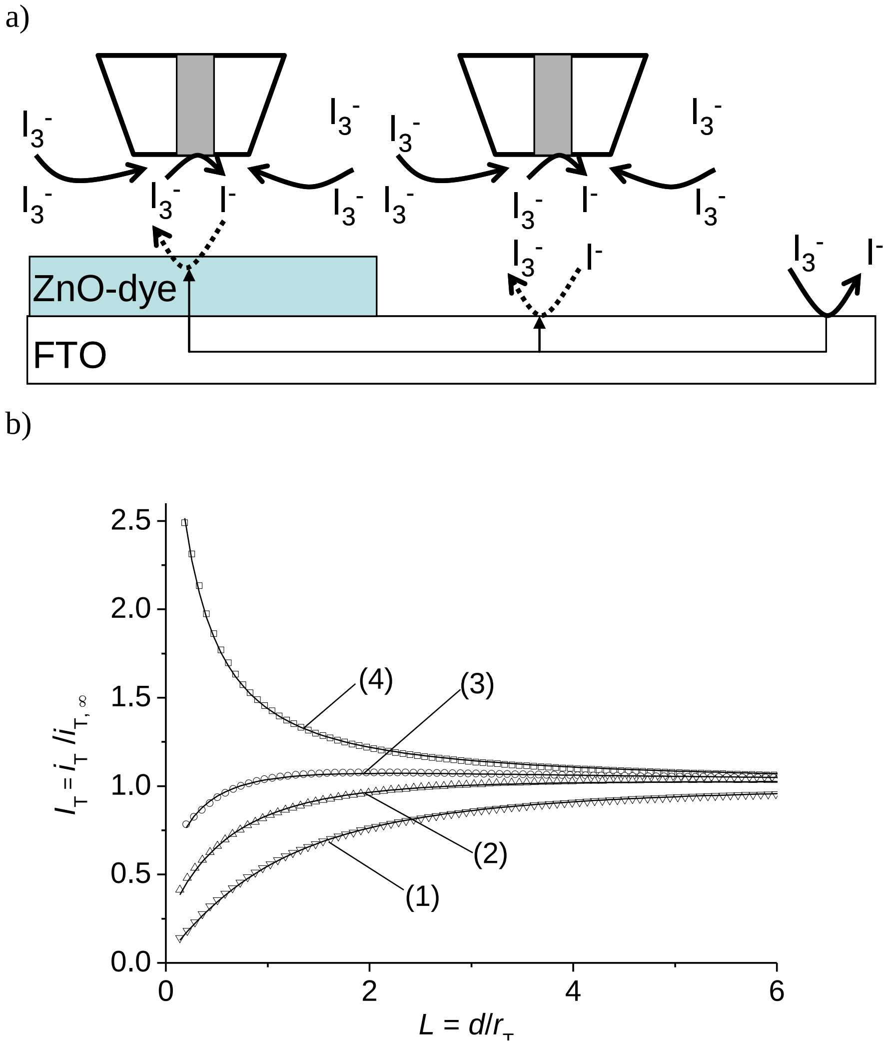

Figure 6.5 a) Schematic diagram that illustrates the mechanism proposed for the ET reaction between UME and the FTO substrate with I_3^- mediator. b) Normalized SECM FB approach curves at the non-illuminated DSSC electrode. Symbols are experimental data and lines are fits to the theory. From the best fit the normalized heterogeneneous first-order rate constant κ is 0.01 for (I_3^-, D149/ZnO, curve 1); 0.15 for (I_3^-, bare FTO, curve 2); 0.42 for (FcMeOH, D149/ZnO, curve 3) and 4.3 for (FcMeOH, bare FTO, curve 4). Scan rate 1 µm/s, 0.2 mM I_3^- or FcMeOH, E_T = 0.4 V (FcMeOH), -0.7 V (I_3^-).

Effective pseudo-first order rate constants k_{eff} derived from κ values were 1.01×10^{-4} cm s^{-1} (I_3^-, ZnO/D149, curve 1), 1.52×10^{-3} cm s^{-1} (I_3^-, bare FTO, curve 2), 0.0319 cm s^{-1}

(FcMeOH, ZnO/D149, curve 3) and 0.296 cm s^{-1} (FcMeOH, bare FTO, curve 4). The rate constant with FcMeOH was over 100 times higher than that with I_3^- on the FTO substrate. This observation is consistent with the well known fact that this mediator does not deliver high efficiencies in DSSC, which is mainly due to a fast electron transfer reaction at FTO back contact [116]. On the other hand, highly efficient DSSCs were achieved by using I^-/I_3^- as mediator system [114, 225]. This experiment indicates that SECM FB technique could enable rapid screening of redox species in the development of alternative redox couples for DSSC without necessarily assembling the entire solar cell system. It can also be used to check the homogeneity of the coating or additional blocking layers.

6.4. Light intensity distribution on illuminated area of dye-sensitized film

A SECM SG-TC experiment was used to examine the homogeneous distribution of illumination at a small scale on ZnO/D149 film electrodes. In the SG/TC mode, the UME detects the diffusion limited current of redox species generated at the substrate. When the UME was scanned horizontally over the D149 sensitized ZnO film in SG-TC mode i_T above the illuminated region was significantly higher than that above the non-illuminated surface. By moving the focusing objective lens up and down, the illumination intensity as well as the size of the illuminated spot could be varied. Figure 6.6a shows a schematic representation of the SG/TC mode at a D149-sensitized ZnO electrode. For instance, Figure 6.6b and c show the line scans over illuminated area with different spot size and illumination intensities. The solution contains only I^- and the UME potential is set to E_T = -0.7 V in order to detect I_3^- ions. I_3^- is generated in the course of the dye regeneration if the sample is illuminated.

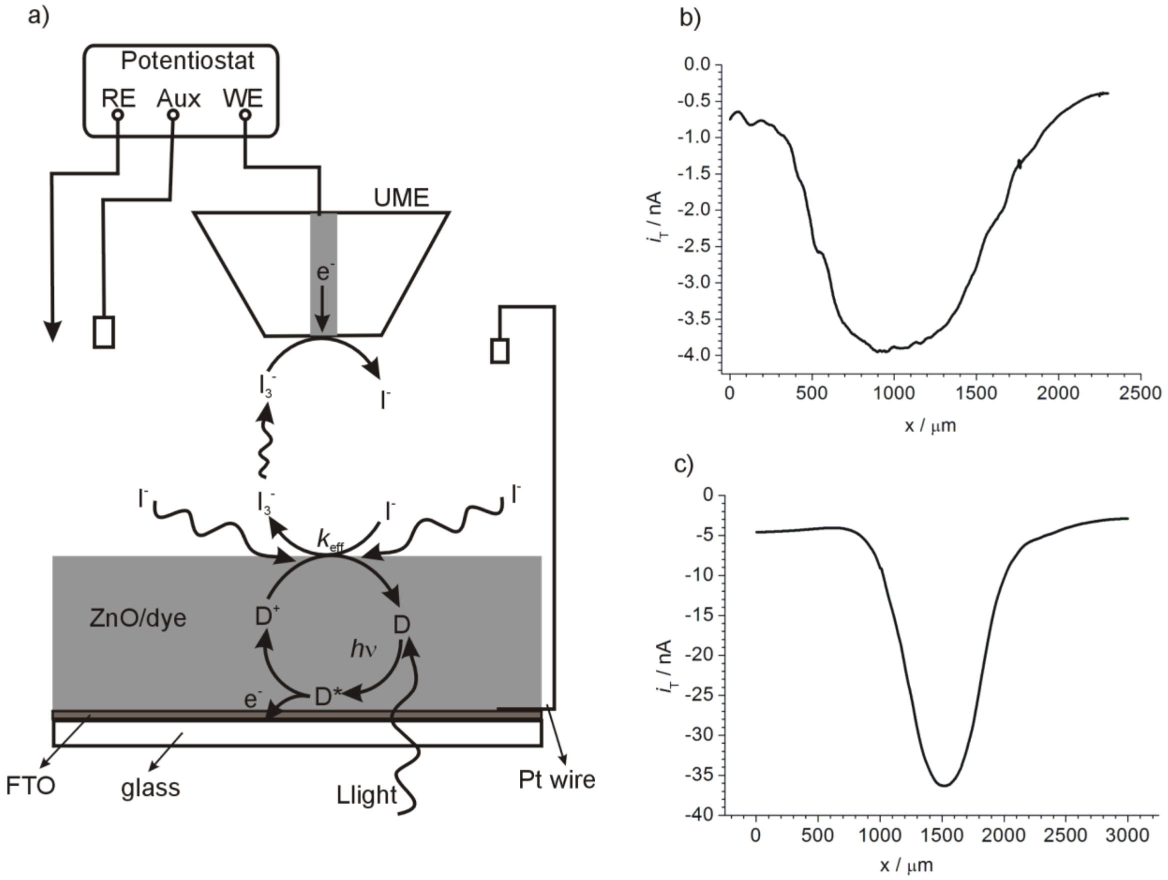

Figure 6.6 The light illuminated on a small scale area on the sensitized electrode. a) Basic arrangement of SECM substrate-generation tip-collection mode experiment of DSSC. UME line scan over illuminated D149/ZnO film (b) non-focused illumination (c) focused illumination in a solution containing 4 mM I^- mediator.

This gives us a clue to estimate the size of illuminated area, to differentiate illuminated region from non-illuminated region and to align UME for the subsequent feedback experiments. Figure 6.7 shows a SG-TC image obtained by scanning the UME from the part without illumination horizontally across an illuminated spot on the film. The SECM image shows that the photoelectrochemical generation of I_3^- is confined to the illuminated regions. The currents obtained at the UME above non-illuminated and illuminated regions were 0.2 nA and 1.0 nA, respectively. The GC mode was not able to resolve any difference in dye regeneration rate within the illuminated region. This is not expected because the electrochemically prepared film is smooth and homogeneous on a length scale corresponding to the 25 µm diameter of the UME. The shape of the spot roughly reflects the distribution of the light intensity within the illuminated area.

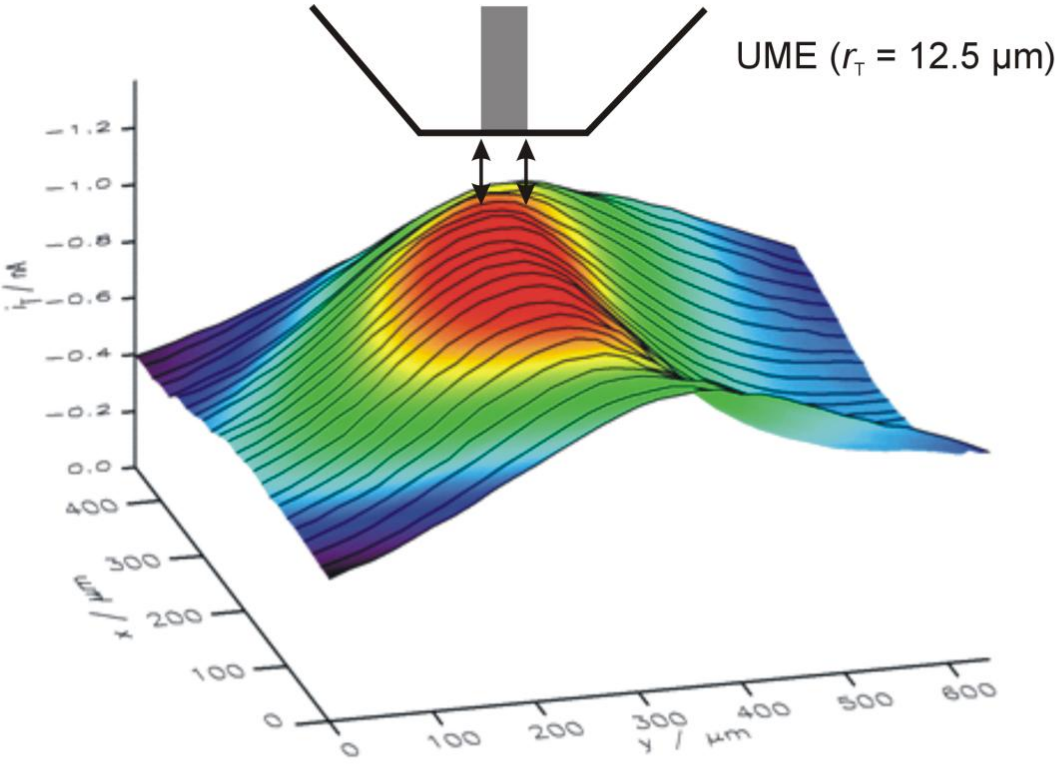

Figure 6.7 SECM SG/TC image of ZnO/D149 film with I^- mediator obtained by scanning UME across a focused light illuminated area. The circular region at the middle of the image corresponds to the illuminated spot on the electrode. r_T = 12.5 µm, ν_T = 20 µm/s, d = 30 µm, E_T = -0.7 V.

7. SECM model for dye regeneration rate of order 1.5 with respect to iodide

This Chapter describes the derivation of SECM kinetic model to analyse feedback mode measurements in DSSC. The model assumes a reaction rate law of order 1.5 with respect to I^-. This model was already used by Shen and Wittstock [228] before the work started for this thesis. This Chapter expands significantly on that work; describing the use of more efficient dye (D149) and exploring further the effects of changing mediator bulk concentration, illumination wavelength and intensity on the kinetics.

The general principle of light induced photoelectrochemical reaction at DSSCs was already described in Chapter 3 for operating solar cell. With SECM technique the electron flux at a microscopic probe above the DSSC is measured to investigate the kinetics of dye regeneration by redox species from the electrolyte.

Figure 7.1 illustrates the principle of SECM feedback mode in a DSSC system with Pt wire to close the loop for the photoanaode and placed several millimeters away from the investigated regions. The photoanode can drain electrons to a Pt wire. In feedback mode I^- is generated by an electrochemical reaction at the UME Eq.(3.4) and diffuses to the dye-sensitized electrode. When the substrate (ZnO/dye film) is illuminated from the back, I^- can transfer an electron to photo-oxidize dye (D^+) molecules Eq. (3.3). In this process the mediator is oxidized back to its original oxidation state I_3^-. After diffusion to the UME, I_3^- can be reduced again. Since the electrolyte contains initially only I_3^- a continuous current flow can only be maintained at those regions where the Pt UME provides I^- for dye regeneration. The experiment provides current variations at the UME as a function of UME–sample distance *d* and rate of I_3^- regeneration at the sample. From the mathematical description of the mass transport and interfacial kinetics at the sample, a pseudo-first-order rate constant k_{eff} for the reaction at the sample can be extracted, as discussed in Section 4.3.1.1.

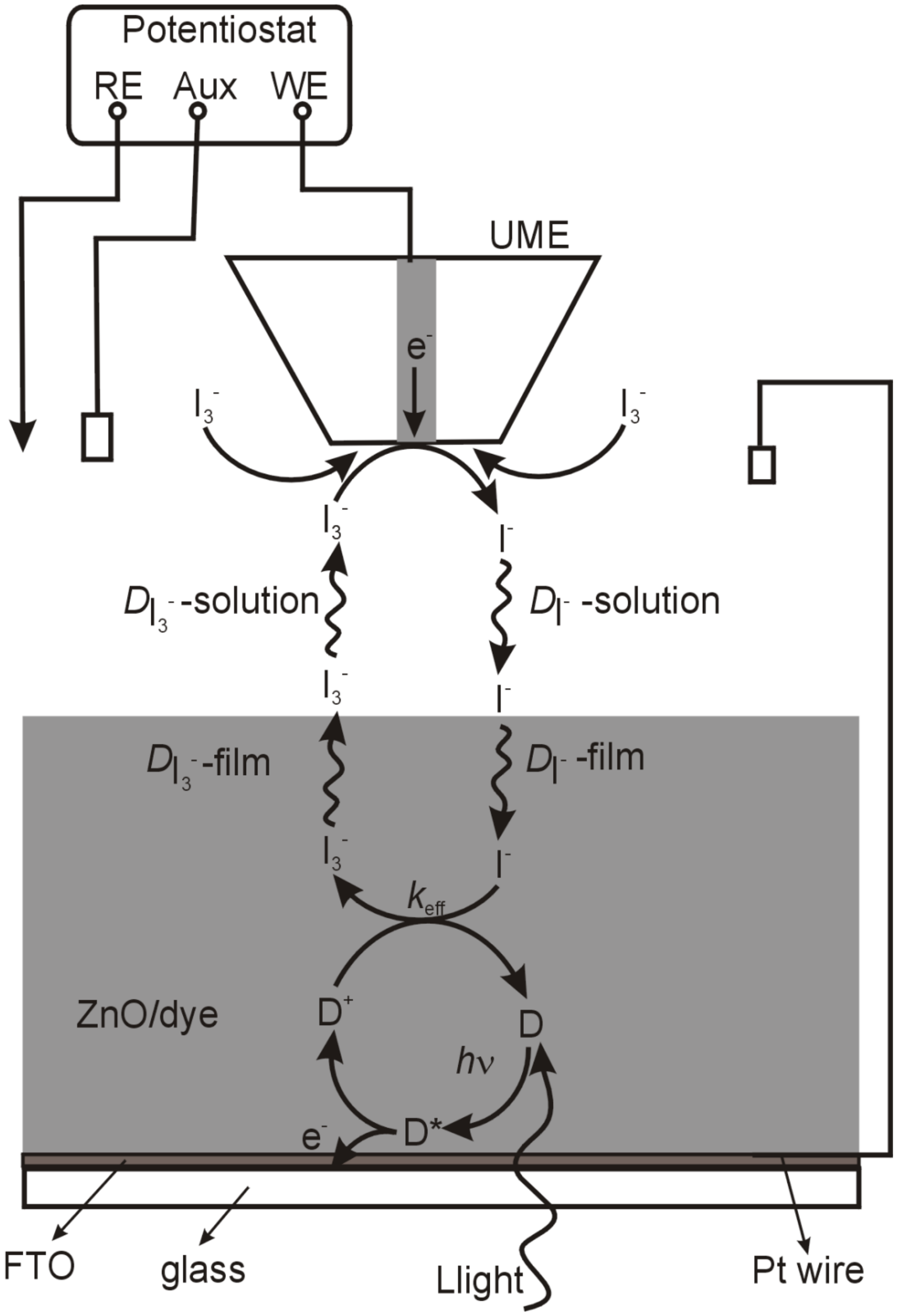

Figure 7.1 Schematic view of the processes involved in the SECM feedback experiment with dye sensitized ZnO film substrate and I_3^- redox mediator under illumination in short circuit photoelectrochemical cell configuration.

In order to relate the experimental k_{eff} to the case of dye regeneration, we followed a strategy used by Liu et al. [144] for relating the kinetics at ferrocene-terminated self-assembled monolayers to SECM feedback curves. Three major processes in which charges are transported between the UME and the back contact of the ZnO/dye electrode were considered in Figure 7.1. The idea is to derive expressions for I_S in case of more complicated mechanisms and make a comparison that relates k_{eff} to an effective rate constant for the more complicated reaction to be studied.

The first step is the reaction at the UME Eq. (3.4). The limiting current Eq. (7.1) will be measured if the reactions at the UME and at the sample are both diffusion-controlled.

$$i_{T,lim} = 8FD[I_3^-]^* r_T I_T(L) \tag{7.1}$$

$[I_3^-]^*$ denotes the I_3^- concentration in the (undisturbed) solution bulk. The second step is the heterogeneous reaction of I^- with the oxidized dye molecule. The analysis of kinetic expression for this situation has been carried out by assuming that the dye is uniformly accessible to light and mediator, that an effective rate constant for light absorption and electron injection $k_{h\nu,eff}$ can be obtained from the absorption cross section $\phi_{h\nu}$, the photon flux $J_{h\nu}$ and the rate constant of electron injection k_{inj}. The measurement of SECM approach curves in the feedback mode is a steady-state measurement and therefore steady-state concentrations have been assumed for the dye D in the ground state, the photo-excited dye D* and the photo-oxidized dye D^+. The dye content is expressed as dye loading Γ_D (amount of dye per geometric area).

The kinetically controlled substrate current i_K for the net reaction of dye regeneration process in Eq. (3.3) is described using Eq. (7.2)

$$i_K = nFA\left(k_{ox}\Gamma_{D^+}[I^-]_S^{3/2}\right) - i_{rec} \tag{7.2}$$

where $n = 1$ is the number of transferred electrons; F is Faraday constant; A is geometric area of the sample where I^- is converted, k_{ox} [$cm^{9/2}mol^{3/2}s^{-1}$] is heterogeneous rate constant of order 1.5; Γ_{D+} is steady-state surface concentration of photo-oxidized dye molecules; $[I^-]_S$ is concentration of dissolved I^- at the surface of the ZnO film. The recombination current i_{rec}

summarizes the current originating from the reaction of electrons from the conducting glass, the conduction band of semiconducting oxide and surface states with I_3^- (Figure 7.1). For the following analysis this contribution was not considered any further, as we work under the conditions of low light intensity and low $[I_3^-]^*$ we expect the recombination to play a minor role.

An expression for $\Gamma_{\mathrm{D+}}$ can be derived from the mass conservation of experimentally accessible total dye content D° comprising dye molecules of all possible states of the dye and the steady-state approximations for surface concentrations of the photoexcited dye $\Gamma_{\mathrm{D*}}$ Eq. (7.3) and the photo-oxidized dye $\Gamma_{\mathrm{D+}}$ Eq. (7.4).

Steady state expression for D*

$$\begin{aligned} \frac{\partial \Gamma_{\mathrm{D*}}}{\partial t} &= 0 = \phi_{h\nu} J_{h\nu} \Gamma_{\mathrm{D}} - k_{\mathrm{inj}} \Gamma_{\mathrm{D*}} \\ \frac{\Gamma_{\mathrm{D}}}{\Gamma_{\mathrm{D*}}} &= \frac{k_{\mathrm{inj}}}{\phi_{h\nu} J_{h\nu}} \end{aligned} \tag{7.3}$$

Steady state expression for D^+

$$\begin{aligned} \frac{\partial \Gamma_{\mathrm{D}^+}}{\partial t} &= 0 = k_{\mathrm{inj}} \Gamma_{\mathrm{D*}} - k_{\mathrm{ox}} \Gamma_{\mathrm{D}^+} [\mathrm{I}^-]_S^{3/2} \\ \frac{\Gamma_{\mathrm{D}^+}}{\Gamma_{\mathrm{D}}} &= \frac{k_{\mathrm{inj}}}{k_{\mathrm{ox}} [\mathrm{I}^-]_S^{3/2}} \end{aligned} \tag{7.4}$$

Mass balance for the dye loading

$$\Gamma_{\mathrm{D^o}} = \Gamma_{\mathrm{D}} + \Gamma_{\mathrm{D}^+} + \Gamma_{\mathrm{D*}} = \Gamma_{\mathrm{D*}} \left[\frac{\Gamma_{\mathrm{D}}}{\Gamma_{\mathrm{D*}}} + \frac{\Gamma_{\mathrm{D}^+}}{\Gamma_{\mathrm{D*}}} + 1 \right] \tag{7.5}$$

Appropriate substitutions of Eqs. (7.3) and (7.4) into the mass conservation law Eq. (7.5) yield an expression for $\Gamma_{\mathrm{D*}}$ Eq. (7.6) from which Eq. (7.7) for $\Gamma_{\mathrm{D+}}$ is obtained by applying Eq. (7.3)

$$\Gamma_{\mathrm{D^o}} = \Gamma_{\mathrm{D^*}}\left[\frac{k_{\mathrm{inj}}}{\phi_{h\nu}J_{\mathrm{h\nu}}} + \frac{k_{\mathrm{inj}}}{k_{\mathrm{ox}}[\mathrm{I^-}]_{\mathrm{S}}^{3/2}} + 1\right]$$

$$\Gamma_{\mathrm{D^*}} = \frac{\Gamma_{\mathrm{D^0}}}{\dfrac{k_{\mathrm{inj}}}{\phi_{h\nu}J_{h\nu}} + \dfrac{k_{\mathrm{inj}}}{k_{\mathrm{ox}}[\mathrm{I^-}]_{\mathrm{S}}^{3/2}} + 1} \tag{7.6}$$

$$\Gamma_{\mathrm{D^+}} = \frac{k_{\mathrm{inj}}}{k_{\mathrm{ox}}[\mathrm{I^-}]_{\mathrm{S}}^{3/2}}\Gamma_{\mathrm{D^*}} = \Gamma_{\mathrm{D^o}}\frac{1}{1 + \dfrac{k_{\mathrm{ox}}[\mathrm{I^-}]_{\mathrm{S}}^{3/2}}{\phi_{h\nu}J_{h\nu}} + \dfrac{k_{\mathrm{ox}}[\mathrm{I^-}]_{\mathrm{S}}^{3/2}}{k_{\mathrm{inj}}}} \tag{7.7}$$

The limiting substrate current would be reached if the iodide concentration is 3 time the tri-iodide concentration, i.e. all iodide formed at the tip is available to the sample without any dilution, $[\mathrm{I^-}]_{\mathrm{S}} = 3[\mathrm{I_3^-}]^*$. Substituting Eq. (7.7) into Eq. (7.2) under steady state yields Eq. (7.8) and (7.9)

$$i_{\mathrm{K,lim}} = FA\Gamma_{\mathrm{D^o}}\frac{\phi_{h\nu}J_{h\nu}k_{\mathrm{ox}}(3[\mathrm{I_3^-}]^*)^{3/2}k_{\mathrm{inj}}}{k_{\mathrm{ox}}(3[\mathrm{I_3^-}]^*)^{3/2}k_{\mathrm{inj}} + k_{\mathrm{inj}}\phi_{h\nu}J_{h\nu} + k_{\mathrm{ox}}\phi_{h\nu}J_{h\nu}(3[\mathrm{I_3^-}]^*)^{3/2}} \tag{7.8}$$

$$\frac{1}{i_{\mathrm{K,lim}}} = \frac{1}{FA\Gamma_{\mathrm{D^0}}k_{\mathrm{ox}}(3[\mathrm{I_3^-}]^*)^{3/2}} + \frac{1}{FA\Gamma_{\mathrm{D^0}}}\left(\frac{1}{\phi_{h\nu}J_{h\nu}} + \frac{1}{k_{\mathrm{inj}}}\right) \tag{7.9}$$

As this work was carried out with comparatively low light intensities and the electron injection process was found to occur in a femto- to pico second time regime [229], i.e. much faster than the other involved processes. Furthermore, the fluorescence of Eosin Y is completely quenched when the dye is adsorbed onto ZnO. It is reasonable to assume that k_{inj} is in the same order as for a fluorescence process. Therefore, the effective rate constant for the excitation and electron injection process for a given light intensity, wavelength and dye molecule (contained in $\phi_{h\nu} = \phi_{h\nu}(\lambda)$) can be defined as Eq. (7.10) and substituting Eq. (7.10) in Eq. (7.9) gives Eq.(7.11).

$$(k_{h\nu,\mathrm{eff}})^{-1} = (k_{\mathrm{inj}})^{-1} + (\phi_{h\nu}J_{h\nu})^{-1} \approx (\phi_{h\nu}J_{h\nu})^{-1} \tag{7.10}$$

$$\frac{1}{i_{\mathrm{K,lim}}} = \frac{1}{FA\Gamma_{\mathrm{D^0}}J_{h\nu}\phi_{h\nu}} + \frac{1}{3\sqrt{3}FA\Gamma_{\mathrm{D^0}}k_{\mathrm{ox}}[\mathrm{I_3^-}]^{*3/2}} \tag{7.11}$$

The total current across the dye-sensitized film/electrolyte interface can be influenced by the rates of several processes that occur in a serial fashion. Provided that the current distribution is uniform in the sample region directly below the microdisk electrode of the SECM probe, the reciprocal of the normalized substrate current is obtained as the sum of the reciprocal limiting currents of all the consecutive processes [156, 230] Eq. (7.12).

$$\frac{1}{I_\mathrm{S}} = \frac{1}{I_\mathrm{T,cond}} + \frac{i_\mathrm{T,\infty}}{i_\mathrm{K,lim}} + \frac{1}{I_\mathrm{el,lim}} \qquad (7.12)$$

where $I_\mathrm{T,cond}$ is the limiting normalized UME current due to diffusion of the I_3^- redox mediator, $I_\mathrm{K,lim} = i_\mathrm{K,lim}/i_\mathrm{T,\infty}$ represent the limiting kinetically controlled normalized substrate current of light absorption, electron injection and ET at the illuminated dye-sensitized electrode/electrolyte interface, $I_\mathrm{el,lim}$ limiting normalized current due to electron conduction across the nanoporous ZnO film. Because electron conduction in ZnO nanoporous films and ET at the underlying FTO/ZnO interface are fast compared to the other processes under conditions of low light intensities, $I_\mathrm{el,lim}$ are not rate-determining in the overall process ($1/I_\mathrm{el,lim} \approx 0$). The following detailed estimation shows that this assumption holds within the thickness investigated here.

The electron transport through the porous ZnO material is controlled by diffusion according to Fick's law [95]. We assume that the diffusion coefficient of electrons in ZnO is approximately equal to that of the charge-balancing ions D_ion in the electrolyte. Furthermore D_ion is similar to the diffusion coefficient D in the bulk solution. This agrees with determinations of electron diffusion coefficients by Oekermann and Nomomura for similar ZnO materials [231, 232]. The maximum electron concentration $N_\mathrm{el,max}$ occurs at the film electrolyte interface, i.e. at distance l. Under conditions of steady-state, the concentration gradient of $N_\mathrm{el,max}$ must be approximately linear if no loss processes are important. Thus, $i_\mathrm{el,lim}$ could be approximated as Eq. (7.13):

$$\begin{aligned} i_{\mathrm{el,lim}} &= D_{\mathrm{ion}} AF \frac{\partial N_{\mathrm{el}}}{\partial l} \approx D_{\mathrm{ion}} AF \frac{N_{\mathrm{el}}}{l} \\ I_{\mathrm{el,lim}} &= \frac{i_{\mathrm{el,lim}}}{i_{\mathrm{T},\infty}} = \frac{D_{\mathrm{ion}}\, \pi r_{\mathrm{T}} N_{\mathrm{el,max}}}{8Dl[\mathrm{I}_3^-]^*} \end{aligned} \tag{7.13}$$

The ratio of the maximum electron concentration $N_{\mathrm{el,max}}$ in ZnO and $[\mathrm{I}_3^-]^*$ is determined by the sequences of reactions at the film surface [Eqs. (8.1)-(8.5)] and back reaction of electrons from the ZnO conduction band $2\mathrm{e}^- + \mathrm{I}_3^- \rightarrow 3\mathrm{I}^-$. A typical value is $N_{\mathrm{el,max}} = 1.7 \times 10^{-4}$ mol cm^{-3} [233]. Using Eq. (7.13) quantitative data for $I_{\mathrm{el,lim}}$ can be obtained from known values of the following parameters: $D_{\mathrm{ion}} = D = 1.37 \times 10^{-5}$ cm s^{-1}, $r_{\mathrm{T}} = 12.5 \times 10^{-4}$ cm, $l = 1.4 \times 10^{-4}$ cm and $[\mathrm{I}_3^-]^* = 1.24 \times 10^{-7}$ mol cm^{-3}. The value of $I_{\mathrm{el,lim}} = 4804.5$ (normalized quantity) was obtained. This is greater than any of the normalized currents we might encounter in any of the SECM experiments which are carried out under condition of very low $[\mathrm{I}^-]$ compared to the operational DSSC. Even if l and $[\mathrm{I}_3^-]^*$ would be increased, $I_{\mathrm{el,lim}}$ would still be much larger than the kinetic current and thus not limiting for the overall current. Thus, one can assume that $i_{\mathrm{el,lim}} >> i_{\mathrm{T,cond}}$ or $i_{\mathrm{K,lim}}$ on the level of this very simplified kinetic analysis. By appropriate substitution of $i_{\mathrm{K,lim}}$ from Eq. (7.11) and $i_{\mathrm{T},\infty}$ from Eq. (7.1) into Eq. (7.12) and using $n = 2$ for the reaction at the SECM probe Eq. (3.4) and the area affected by the flux of probe-generated I^- to be πr_{T}^2, we obtain Eq. (7.14).

$$\frac{1}{I_{\mathrm{S}}} = \frac{1}{I_{\mathrm{T,cond}}} + \frac{4D}{\pi r_{\mathrm{T}}} \left[\frac{2[\mathrm{I}_3^-]^*}{\Gamma_{\mathrm{D^o}} \phi_{h\nu} J_{h\nu}} + \frac{2}{3\sqrt{3}\,\Gamma_{\mathrm{D^o}} k_{\mathrm{ox}} [\mathrm{I}_3^-]^{*3/2}} \right] \tag{7.14}$$

The expression for $1/I_{\mathrm{S}}$ in Eq. (7.14) must now be compared to the expression of uncomplicated electron transfer at the sample for which the analytical expressions of SECM approach curves are available Eq. (7.15).

$$\frac{1}{I_{\mathrm{S}}} = \frac{1}{I_{\mathrm{T,cond}}} + \frac{4D}{\pi r_{\mathrm{T}} k_{\mathrm{eff}}} \tag{7.15}$$

This provides $1/k_{\mathrm{eff}}$ for the SECM experiment as a function of $[\mathrm{I}_3^-]^*$ or $J_{\mathrm{h\nu}}$ Eq. (7.16)

$$\frac{1}{k_{\mathrm{eff}}} = \frac{2[\mathrm{I}_3^-]^*}{\Gamma_{\mathrm{D^o}}\phi_{h\nu}J_{h\nu}} + \frac{2}{3\sqrt{3}\Gamma_{\mathrm{D^o}}k_{\mathrm{ox}}[\mathrm{I}_3^-]^{*3/2}} \tag{7.16}$$

Experimentally we can vary in a controlled way the photon flux $J_{h\nu}$ and the bulk concentration of tri-iodide $[\mathrm{I}_3^-]^*$ from which I^- is formed by reduction at the SECM probe. Additionally the working distance, internal structure of the photoelectrode, the identity and structure of electrolyte could determine the amount of I_3^- that can diffuse from the bulk through the thin layer between sample and probe glass sheath to the active UME area and on which area the I^- formed at the UME are distributed. The latter fact complicated the interplay of mass transport in a thin layer configuration and a heterogeneous process at the sample (see Chapter 8). The discussions in Section 7.1 and 7.2 are intended to implement the kinetic model Eq. (7.16) to determine the k_{ox} of Eosin Y and D149 dyes sensitized in ZnO.

7.1. Dye regeneration kinetics in ZnO/Eosin Y film

The dye regeneration kinetics by electron transfer from I^- redox ions in the electrolyte was investigated for electrochemically deposited films of Eosin Y sensitized nanoporous ZnO by SECM approach curves under illumination with blue, green and yellow LEDs as light sources with systematically varied light intensity. Table 7.1 lists the measured wavelength of the three LEDs at maximum emission intensity in Figure 5.4b and summarizes the incident light power and photon flux.

Table 7.1 Summary of measured wavelength, incident light power on the illuminated area of 0.0565 cm^2 and photon flux density $J_{h\nu}$ of LEDs used as light source in the experiment.

LED	Wavelength/ nm	Power/ µW	Photo flux/ 10^{-9} mol s^{-1} cm^{-2}
Blue	474	58.0	4.06
Green	529	33.4	2.61
Yellow	593	21.1	1.85

7.1.1. Variation of [I_3^-]*

SECM feedback mode approach curve experiments were carried out at the ZnO/Eosin Y films at different [I_3^-]* with the three different LED illuminations. When the ZnO/Eosin Y film was illuminated from the back, the UME current became significantly larger than that in the dark (Figure 6.5b, curve 1). The increase in the UME current is attributed to a higher flux of I_3^- emerging from the sample. Figure 7.2 presents a set of normalized experimental approach curves to an Eosin Y-sensitized ZnO film for various [I_3^-]* under illumination of the film with blue, green and yellow LEDs. In each figure, the effect of [I_3^-]* on the approach curves was studied. Approach curves with yellow LED at various other [I_3^-]* were also carried out but only part of the data are presented in Figure 7.2c because the remaining curves overlap with those actually plotted. The UME current under illumination at various [I_3^-]* is typical for

SECM feedback experiments with finite electron transfer kinetics at the sample. Under this particular experimental condition, it is reasonable to assume that UME current response in this region was governed by a photo-induced charge transfer reaction at the illuminated film-electrolyte interface. Experimental approach curves $i_T(z)$ were normalized to $I_T(L)$ and the normalized heterogeneous rate constants κ have been extracted by fitting them to an analytical approximation of Cornut and Lefrou [157] [Eqs. (4.5)-(4.9)] for a first order reaction at the sample and infinitely fast reaction at UME (see Section 4.3.1.1). κ is obtained by fitting the experimental approach curve to the analytical approximations as discussed in Section 4.3.1.1. The apparent heterogeneous rate constant k_{eff} for the regeneration of the photo-oxidized dye by I^- is obtained using Eq. (4.9) with the diffusion coefficient of I_3^- in acetonitrile of 1.37×10^{-5} cm^2 s^{-1} [223] and r_T of the particular UME used. The results are summarized in Table 7.2 for blue, green and yellow LED illumination, respectively, and variation of $[I_3^-]^*$. At each LED illumination κ decreases with increased $[I_3^-]^*$ because the diffusion of I_3^- from the solution bulk dominates over the flux resulting from dye regeneration at the sample. A similar behaviour is known from SECM feedback measurements at enzyme-modified insulating surfaces [158, 159]. This similarity points at the decisive role of light absorption in the sensitizer as trigger of the photoelectrochemical redox cycle.

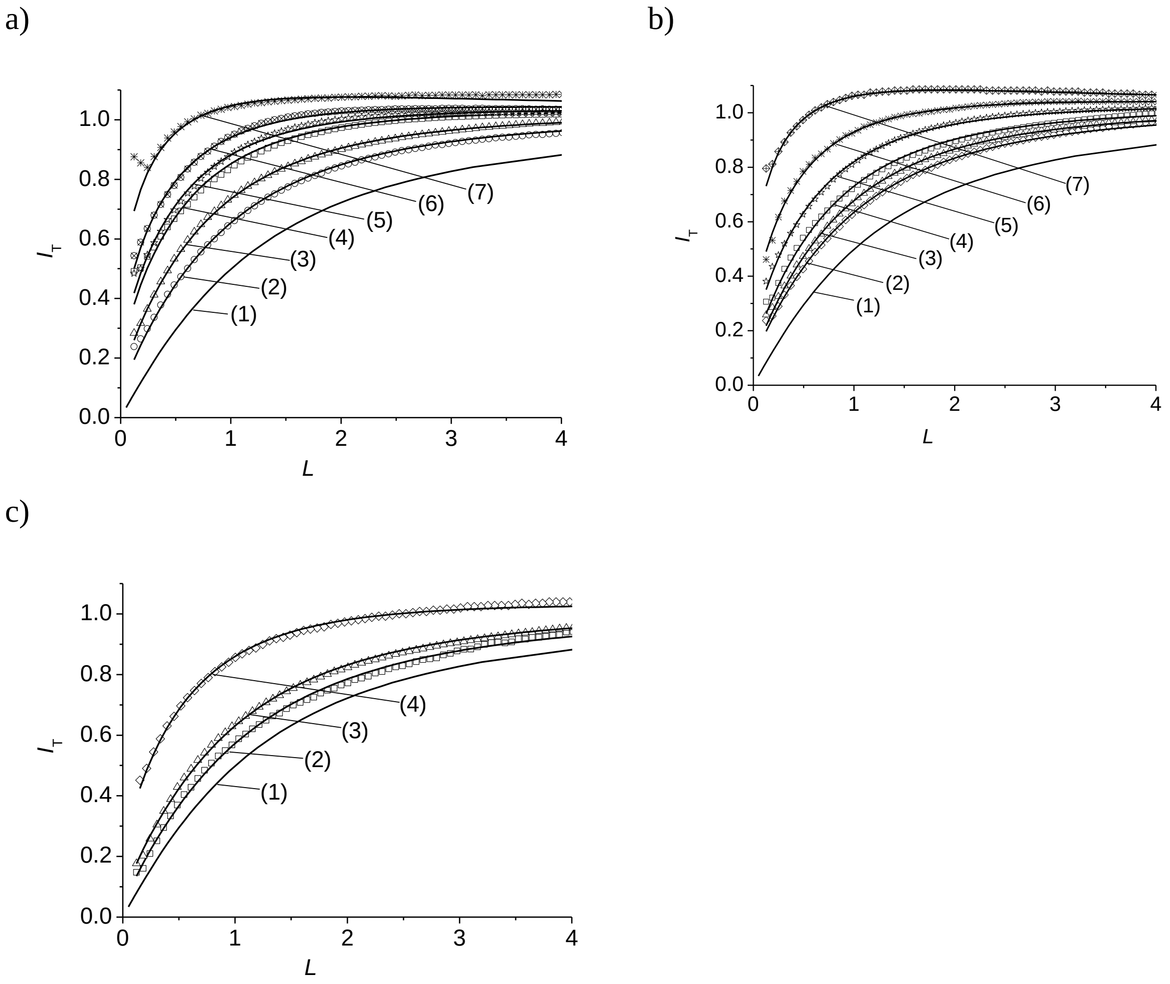

Figure 7.2 Normalized SECM feedback approach curves for the approach of a Pt disk electrode towards a ZnO/Eosin Y film under illumination by (a) blue LED, (b) green LED and (c) yellow LED at different [I_3^-]*; scan rate = 1 µm s^{-1}, E_T = -0.7 V, r_T = 16.5 µm. Solid lines are calculated curves for an approach of an UME with *RG* = 10 towards an inert insulating surface (curve 1), and to samples with first order kinetics of mediator recycling using normalized rate constants κ, Eq. (4.5)-(4.9)

Table 7.2 Normalized apparent heterogeneous first-order rate constants κ and apparent heterogeneous first-order rate constants $k_{\mathrm{eff}} = \kappa D/r_{\mathrm{T}}$ obtained for the reduction of photoexcited Eosin Y^+ by I^-; r_{T} = 16.5 µm, *RG* = 10, $D = 1.37 \times 10^{-5}$ cm^2 s^{-1}.

LED	$[I_3^-]$* $[10^{-6}$ mol cm$^{-3}]$[a]	κ[b]	k_{eff} $(10^{-3}$ cm s$^{-1})$
(a) Blue	0.063	0.45	3.7477
	0.13	0.265	2.2070
	0.248	0.196	1.6323
	0.512	0.167	1.3742
	1.238	0.085	0.6913
	2.00	0.03	0.250
(b) Green	0.063	0.43	3.9976
	0.13	0.25	2.0821
	0.248	0.14	1.166
	0.626	0.081	0.6746
	1.238	0.055	0.4581
	2.00	0.04	0.3331
(c) Yellow	0.063	0.174	1.4491
	0.248	0.036	0.2998
	1.05	0.017	0.1416

[a] Total concentration of I_3^-. [b] Dimensionless normalized pseudo-first order rate constant obtained by fitting experimental approach curves to Eq. (4.5)-(4.9).

Because of the strong spectral dependence of the absorption of Eosin Y, the normalized approach curves in Figure 7.2 therefore result in different values of k_{eff} for Eosin Y regeneration by I^- for illumination by the three different wavelengths of the blue, green or yellow LED. A larger value of k_{eff} for the green LED compared to the blue LED fits to the maximum absorption coefficient of Eosin Y of around 520 nm as it is evident from the absorption spectrum of the sensitized film (Figure 7.4). At longer wavelengths (such as yellow LED), the photon absorption by Eosin Y is very weak (Figure 7.4). Hence, as expected the k_{eff} values for the yellow LED are significantly lower than those for the blue or green LED at a given $[I_3^-]$*.

With each of the three LEDs k_{eff} was plotted against various $[\mathrm{I_3^-}]^*$ (Figure 7.3). From an independent experiment a film thickness $l = 3$ µm and a dye loading $\Gamma_{\mathrm{Do}} = 6 \times 10^{-8}$ mol cm^{-2} with homogeneous distribution of the dye within ZnO/Eosin Y film was obtained [217]. Therefore, the experimental data were fitted to Eq. (7.16) using one k_{ox} and three $k_{h\nu,\mathrm{eff}}$ (for blue, green and yellow LED). It is expected that the k_{ox} value is similar for all the three LED illumination for a given dye sensitized electrode and electrolyte mediator. However, $k_{h\nu,\mathrm{eff}}$ should vary with the wavelength of LEDs. From the best fit of the experimental data (Figure 7.3, solid lines) the following values were obtained $k_{\mathrm{ox}} = 1.82 \times 10^8$ cm$^{9/2}$ mol$^{-3/2}$ s^{-1} and the $k_{h\nu,\mathrm{eff}}$ values were 1.47×10^{-2} s^{-1}, 1.39×10^{-2} s^{-1} and 3.67×10^{-3} s^{-1} for blue, green and yellow LEDs, respectively. The result shows that $k_{h\nu,\mathrm{eff}}$ values are approximately ten-fold higher with blue and green LED than with yellow LED illumination. A lower $k_{h\nu,\mathrm{eff}}$ value at yellow LED illumination ($\lambda > 580$ nm) is consistent with low IPCE of Eosin Y-sensitized nanoporous ZnO based DSSC [217].

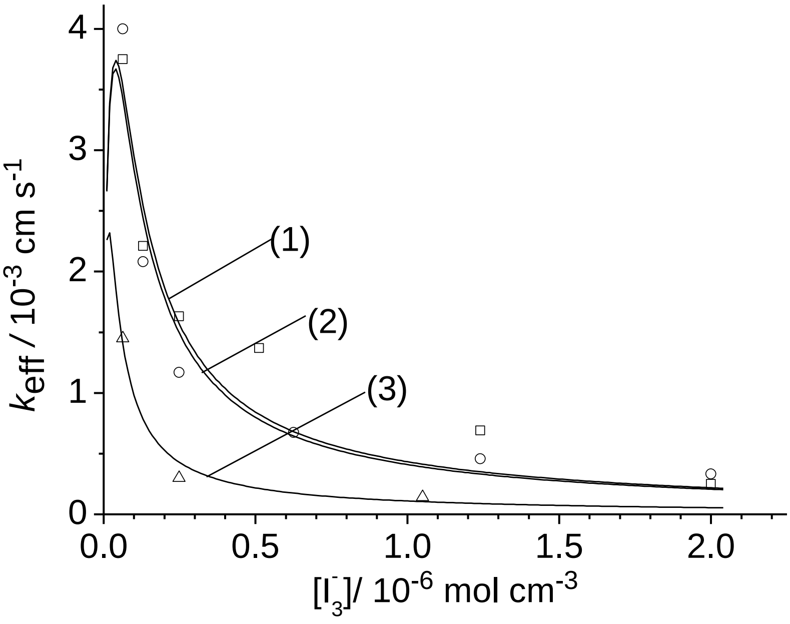

Figure 7.3 Plot of experimental values of k_{eff} vs. $[\mathrm{I_3^-}]^*$. The lines represent fits of k_{ox} and $k_{h\nu,\mathrm{eff}}$ in [Eq. (7.16)] to the data: (1, □) blue LED, (2, ○) green LED and (3, △) yellow LED.

One of the interesting findings in our model is that a uniform k_{ox} value provides a reasonable approximation for the kinetics of dye regeneration by I^- in Eosin Y-sensitized ZnO cells. The constant k_{ox} is itself an effective rate constant summarising the kinetics of the electron transfer from I^- to the oxidized dye and all follow-up processes that lead to the formation of I_3^-. Currently, it is impossible to further detail those individual steps by SECM investigations.

From the measured $J_{\mathrm{h\nu}}$ values in Table 7.1 and the values of $k_{h\nu,\mathrm{eff}}$ from the fits in Figure 7.3, the photoexcitation cross-section of Eosin Y $\phi_{h\nu}$ at each LED wavelength can be estimated using Eq. (7.10) as 6.0×10^{-2}, 8.8×10^{-2}, 3.3×10^{-2} Å^2 per individual dye molecule for blue, green and yellow LED, respectively. The dependence of $\phi_{h\nu}$ of Eosin Y molecules on the wavelength of the incident LED follows closely the absorption spectrum of Eosin Y-sensitized ZnO film with a maximum at the wavelength of the green LED (Figure 7.4). As expected the spectral dependence of $\phi_{h\nu}$ basically reflects the absorption properties of the dye molecule adsorbed in nanoporous ZnO, a confirmation of the kinetic model proposed in Ref. [228]. It also yields a constant value of k_{ox} that is independent of the tri-iodide concentration.

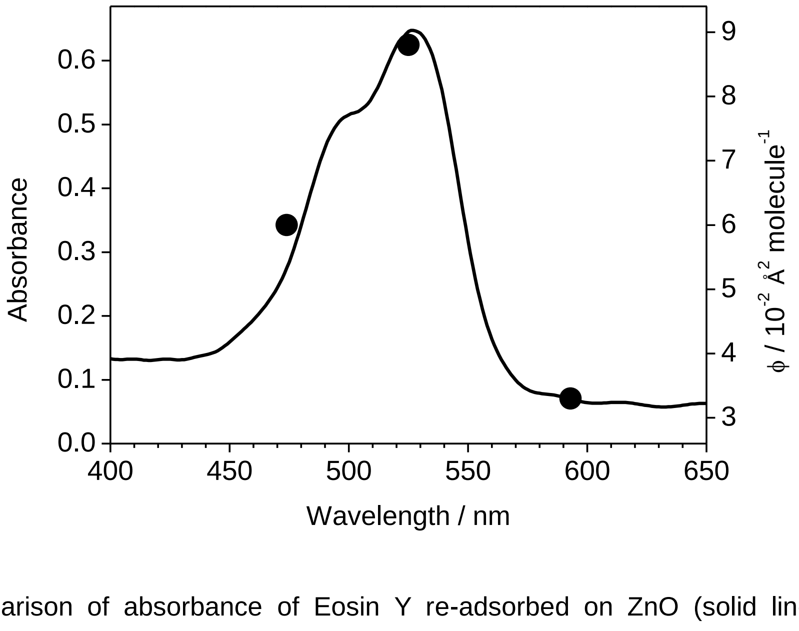

Figure 7.4 Comparison of absorbance of Eosin Y re-adsorbed on ZnO (solid line, left axis) and excitation cross-sections (●, right axis) for ZnO/Eosin Y film plotted as a function of excitation wavelength.

7.1.2. Variation of the illumination intensity

In order to verify the intensity dependence of the SECM feedback signal predicted by Eq. (7.16), feedback measurements were performed for a fixed mediator concentration ($[I_3^-]^* = 0.104$ mM) with the three LEDs. For this purpose a LED illuminator with adjustable intensity was employed instead of a simple LED (Figure 5.5, components in dashed line). The spectral properties of the LEDs in this light source are very similar to that of the blue, green and yellow LED applied before as described in Section 5.3. The incident photon flux at the location of the sample was measured for each setting of the illuminator with the same power meter as with the LED light source employed before. Figure 7.5 shows the approach curve results for the blue, green and yellow LED. With increasing illumination intensity higher UME currents are recorded. For instance, at an intensity of 22.4×10^{-9} mol cm^{-2} s^{-1} the response saturates and further increase in illumination intensity does not lead to increased currents (Figure 7.5a-c, curve 6). This corresponds to the prediction of Eq. (7.16). From the extracted κ of each curve, k_{eff} can be calculated.

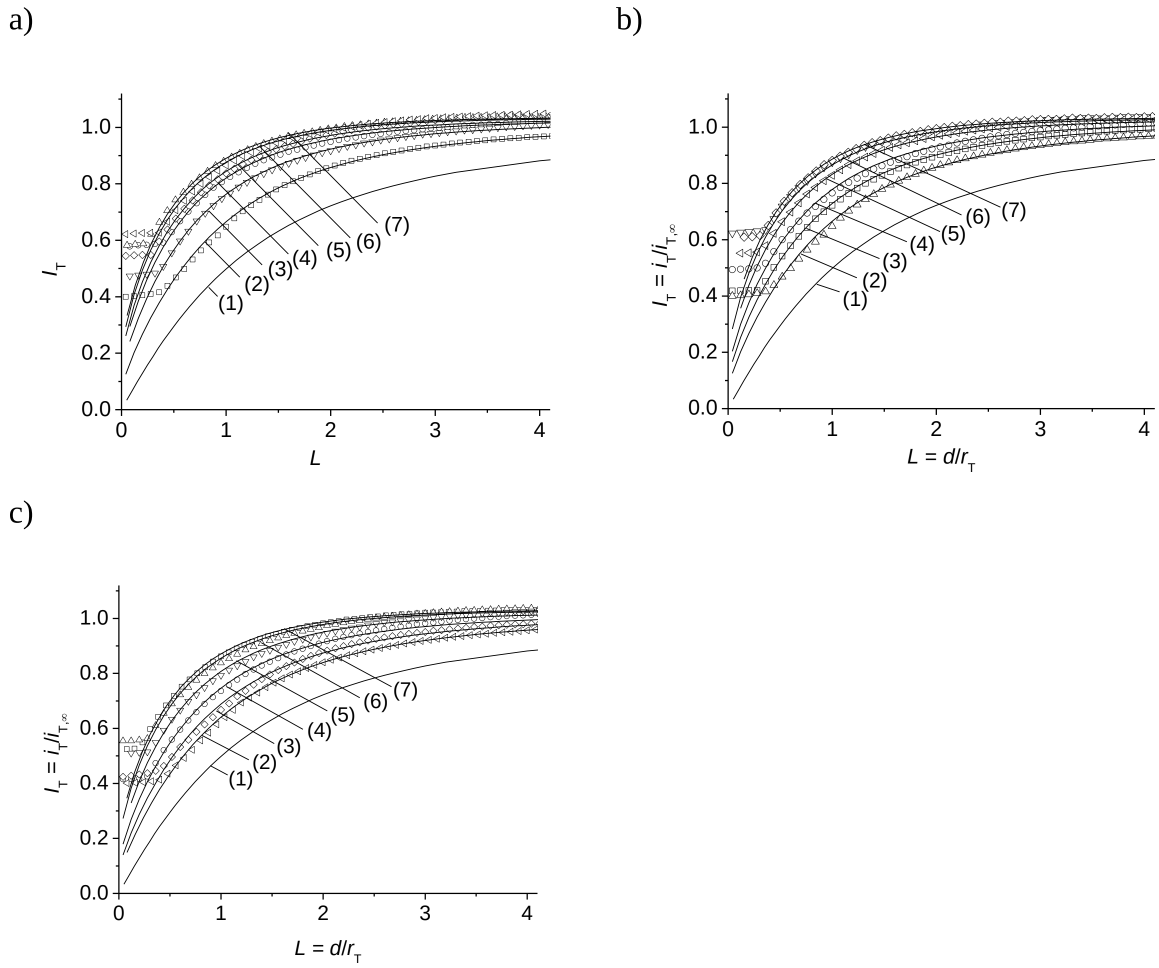

Figure 7.5 Normalized SECM feedback approach curves for the approach of a Pt disk UME towards a ZnO/Eosin Y film under illumination by a blue LED with intensities expressed in terms of photon flux density in mol cm^{-2} s^{-1} 2) 0.978 × 10^{-9}, 3) 2.95 × 10^{-9}, 4) 6.95 × 10^{-9}, 5) 11.4 × 10^{-9}, 6) 22.4 × 10^{-9}, 7) 28.4 × 10^{-9}; ν_T = 1 µm s^{-1}, [I$_3^-$]* = 0.104 mM, r_T = 12.5 µm, E_T = -0.7 V; Solid lines are calculated curves for an approach of an UME towards inert insulating surface (curve 1), and to samples with first order kinetics of mediator recycling using normalized rate constants κ: (2) 0.05, (3) 0.1, (4) 0.14, (5) 0.16, (6) 0.19, (7) 0.205.

Table 7.3 Normalized apparent heterogeneous first order rate constants κ and apparent heterogeneous first-order rate constants k_{eff} obtained for the reduction of photoexcited Eosin-Y by I^- for different illumination intensities of blue, green and yellow LEDs light sources and $[I_3^-]^* = 0.104$ mM, $D = 1.37 \times 10^{-5}$ cm^2 s^{-1}, $r_T = 12.5$ µm, $RG = 10$, $k_{\mathrm{eff}} = \kappa D/r_T$

LED	$J_{h\nu}$ (10^{-9} mol cm^{-2} s^{-1})	κ	k_{eff} (10^{-3} cm s^{-1})
(a) Blue	28.4	0.205	2.25
	22.4	0.19	2.08
	11.4	0.16	1.75
	6.95	0.14	1.53
	2.95	0.1	1.10
	0.987	0.05	0.548
(b) Green	25.5	0.20	2.19
	15.1	0.18	1.97
	9.10	0.15	1.64
	4.50	0.11	1.21
	1.70	0.08	0.877
	0.982	0.05	0.548
(c) Yellow	30.01	0.185	2.03
	23.1	0.17	1.86
	8.10	0.13	1.42
	4.50	0.09	0.986
	2.50	0.06	0.658
	0.990	0.04	0.438

Using the analytical approximation Eq. (7.16), k_{eff} can be expressed as function of $J_{h\nu}$. The corresponding data are shown in Figure 7.6. Using k_{ox} and $\phi_{h\nu}(\lambda)$ as adjustable parameters the data can be fitted to Eq. (7.16) yielding $k_{\mathrm{ox}} = 0.472 \times 10^8$ cm$^{9/2}$ mol$^{-3/2}$ s^{-1} and 3.69×10^{-2}, 4.67×10^{-2}, 2.24×10^{-2} Å^2 molecule^{-1} as $\phi_{h\nu}(\lambda)$ for the blue, green and yellow LEDs, respectively. The k_{ox} is slightly smaller than the k_{ox} determined from the variation of the concentration. The determination method introduces an uncertainty which has been estimated to about 60%. Uncertainties in the preparation of the DSSC add to this value. Since the parameter Γ_{D° and k_{ox} are highly coupled in Eq. (7.16), a variation of the Γ_{D° would be reflected in a changed k_{ox}. The experimentally determined dye loading is an average value, where integration occurs across a macroscopic sample and is averaged between a limited numbers of samples. Uncertainties in the preparation will also cause slight changes in the $\phi_{h\nu}(\lambda)$ values. However, for one and the same sample, Eq. (7.16) provides a consistent quantitative description of the observed behaviour. This is not necessarily expected as the assumption of uniform accessibility of all dye molecules by light and by the I^- ions is not obvious when looking at electron microscopic images of the dye-modified ZnO.

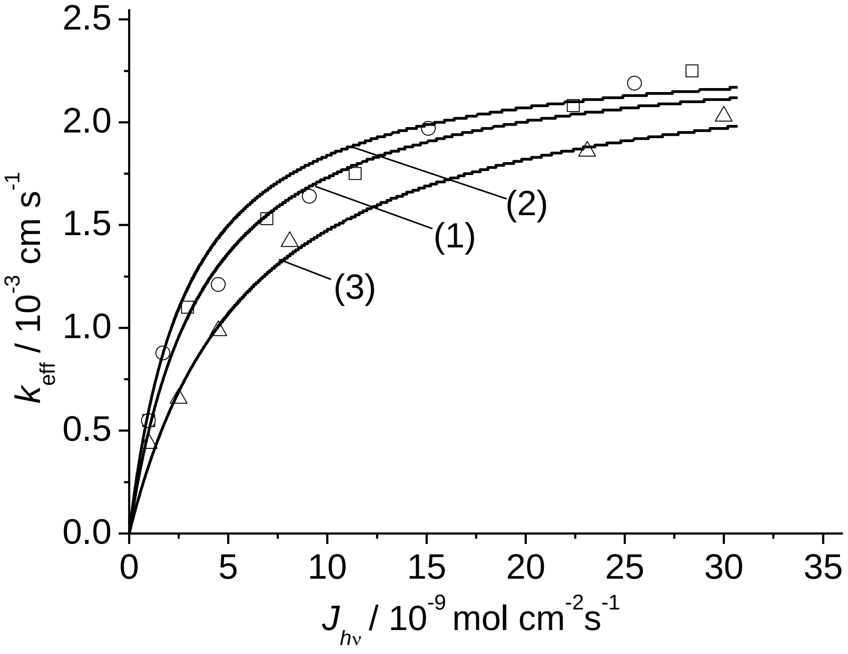

Figure 7.6 Plot of experimental values of k_{eff} *vs*. $J_{h\nu}(\lambda)$. The lines represent fits of k_{eff} according to Eq. (7.16) with k_{ox} and $\phi_{h\nu}(\lambda)$ as adjustable parameters. Green LED (curve 2), blue LED (curve 1) and yellow LED (curve 3)

7.2. Dye regeneration kinetics in D149-sensitized ZnO films

To extend the work on ZnO/Eosin Y, SECM feedback mode approach curves on ZnO/D149 films were measured at different wavelengths and light intensities with a fixed $[I_3^-] = 0.1$ mM to determine the regeneration rate of D149. The sensitization of ZnO by the indoline dye D149 was found to be considerably more efficient (up to $\eta = 5.6\%$) than other organic dye sensitizers [58]. Figure 7.7 shows the normalized experimental approach curves recorded with an UME ($r_T = 12.5$ µm) to ZnO/D149 film under illumination with a blue, green, yellow and red LEDs at different illumination intensities in a solution of 0.1 mM $[I_3^-]^*$. An increase in the illumination intensity (while keeping the LED wavelength constant) leads to a higher feedback current with each of the four LEDs (Figure 7.7, curves 2-7).

The approach curves were recorded at six $J_{h\nu}$ in the average range from 1×10^{-10} to 3×10^{-8} mol cm^{-2} s^{-1} for each of the LEDs. The values of normalized rate constant κ obtained from fitting the experimental approach curves to the theory show that an approximately 30-fold increase in photon flux results in more than 3-fold increase in κ. The corresponding k_{eff} increased from 2×10^{-3} to 6.4×10^{-3} cm s^{-1} in the applied intensity range (Table 7.4). The k_{eff} for the heterogeneous dye regeneration process in ZnO/D149 based DSSC exhibits a remarkable dependence on the wavelength and intensity in the order of k_{eff} (blue LED) ≈ k_{eff} (green LED) > k_{eff} (yellow LED) > k_{eff} (red LED) at $[I_3^-]^* = 0.1$ mM.

Experimental $k_{\mathrm{eff}}(J_{h\nu})$ were fitted to the kinetic model Eq. (7.16) for a single k_{ox} value and four different values of $\phi_{\mathrm{h\nu}}(\lambda)$ as adjustable parameters (Figure 7.8), following similar procedure as in Figure 7.6. Using the experimental dye content $\Gamma_{\mathrm{D^\circ}} = 7 \times 10^{-8}$ mol cm^{-2} from an independent measurement, the obtained rate constant for the regeneration reaction according to Eq. (7.16) for all experiments is $k_{\mathrm{ox}} = 9.55 \times 10^{7}$ cm$^{9/2}$ mol$^{-3/2}$ s^{-1} and $\phi_{h\nu}(\lambda)$ takes values of 9.12×10^6, 9.97×10^6, 5.31×10^6 and 3.53×10^6 cm^2 mol^{-1} for the blue, green, yellow and red LED, respectively. The rate constant k_{ox} is of similar magnitude as values reported for ZnO/Eosin-Y (see Section 7.1). The result of both samples could be fitted with a reaction order 1.5 with respect to [I$^-$] despite very different overall efficiencies of light-induced charge transfer found for the two dyes that are obvious from the $\phi_{h\nu}$ values for Eosin Y and D149.

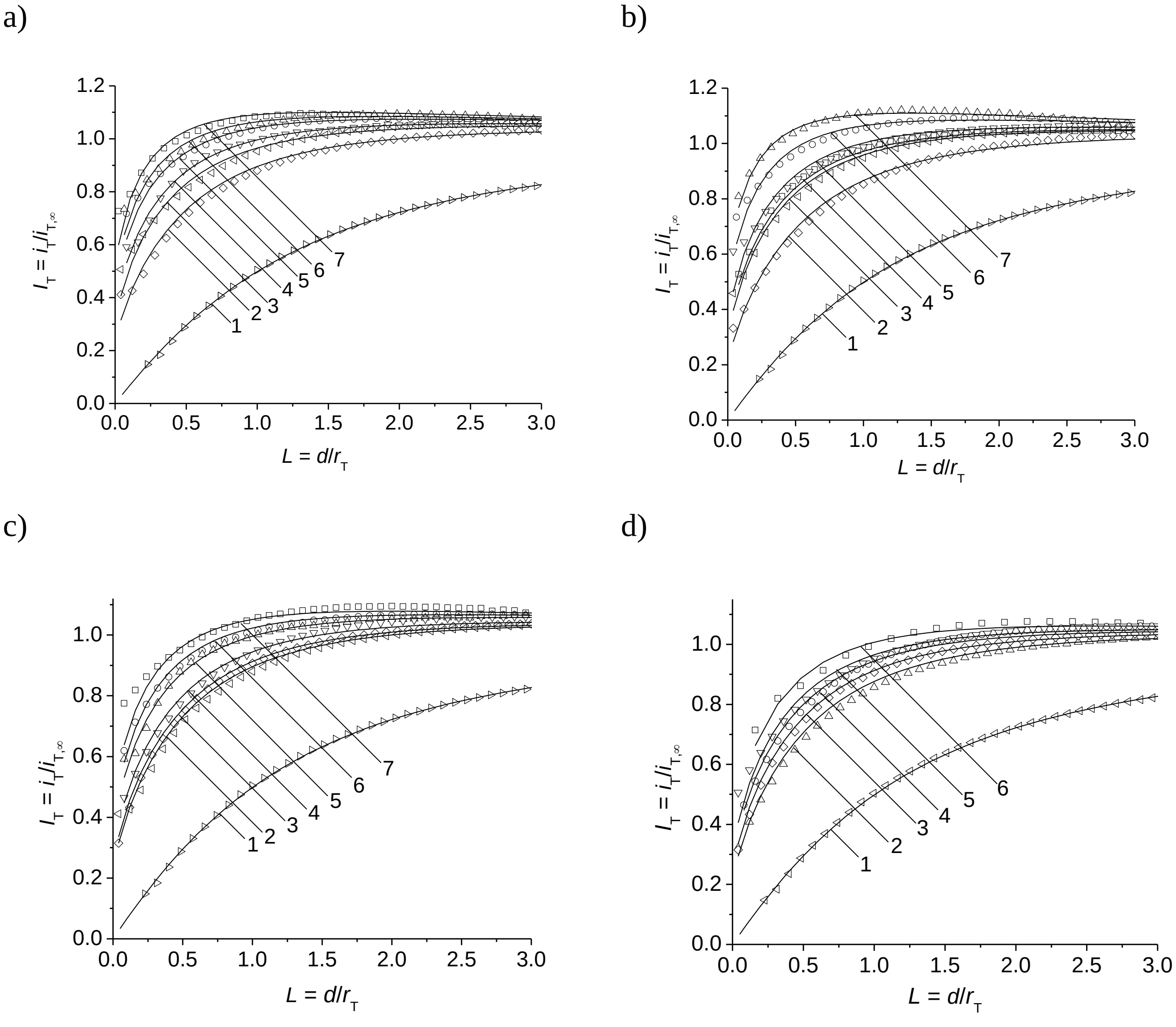

Figure 7.7 Normalized SECM feedback approach curves for the approach of a Pt disk UME towards a ZnO/D149 film in the dark (curve 1) and under illumination by (a) blue, (b) green, (c) yellow and (d) red LED. Photon flux density of LED, normalized rate constants κ and k_{eff}. $\nu_T = 1$ µm s^{-1}, $E_T = -0.7$ V, $[I_3^-]^* = 0.1$ mM. Solid lines are calculated curves and symbols are experimental curves. Lines are given in Table 7.4

Table 7.4 Normalized apparent heterogeneous first order rate constants κ and apparent heterogeneous first-order rate constants k_{eff} obtained for the reduction of photoexcited D149 by I^- for different illumination intensity of blue, green, yellow and red LEDs and $[I_3^-]^* = 0.1$ mM, $D = 1.37 \times 10^{-5}$ cm^2 s^{-1}, $r_T = 12.5$ µm, $RG = 10$, $k_{\mathrm{eff}} = \kappa D/r_T$

LED	approach Curve	$J_{h\nu}$ (10^{-9} mol cm^{-2} s^{-1})	κ	k_{eff} (10^{-3} cm s^{-1})
a) Blue	2	0.99	0.21	2.3
	3	2.95	0.30	3.29
	4	6.95	0.35	3.84
	5	11.40	0.44	4.82
	6	22.40	0.49	5.37
	7	28.40	0.56	6.14
b) Green	2	0.98	0.180	1.97
	3	1.7	0.290	3.18
	4	4.5	0.328	3.59
	5	9.1	0.397	4.35
	6	15.1	0.477	5.23
	7	25.5	0.582	6.38
c) Yellow	2	0.99	0.21	2.30
	3	2.5	0.23	2.52
	4	4.5	0.27	2.96
	5	8.1	0.35	3.84
	6	23.1	0.4	4.38
	7	30	0.46	5.04
d) Red	2	0.90	0.190	2.08
	3	1.60	0.228	2.50
	4	2.50	0.270	2.96
	5	7.95	0.290	3.18
	6	15	0.337	3.69
	7	26	0.398	4.36

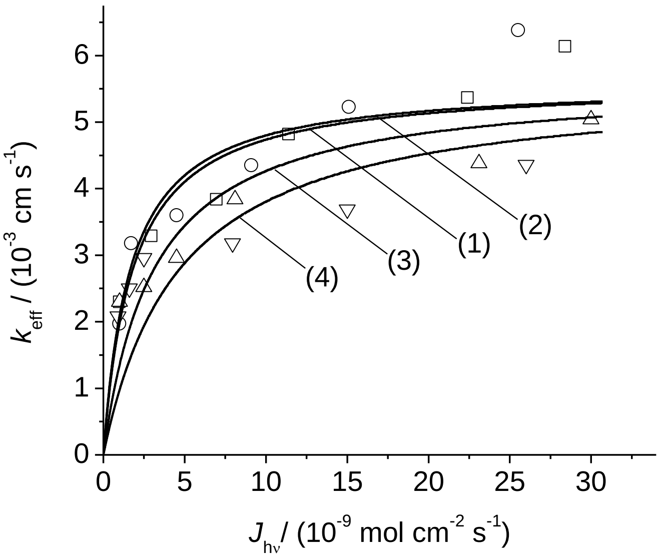

Figure 7.8 Intensity dependence of effective heterogeneous first-order rate constant plotted as k_{eff} *vs.* photon flux of four different LEDs. Symbols correspond to the values calculated from the experimental data. Lines are theoretical fittings to the model described in Eq. (7.16). The fitting results are k_{ox} = 9.55 × 10^7 $cm^{9/2}mol^{-3/2}s^{-1}$ and $\phi_{h\nu}$ = 1.52 × 10^{-1}, 1.66 × 10^{-1}, 8.82 × 10^{-2} and 5.86 × 10^{-2} Å^2 per molecule of dye for blue (curve 1), green (curve 2), yellow (curve 3) and red LED (curve 4), respectively.

Another interesting finding in our study is the direct correlation of the optical absorbance of D149-sensitized ZnO films and the light absorption cross section $\phi_{h\nu}(\lambda)$ of D149 molecules as obtained from the fit. Figure 7.9 shows the absorption spectrum of D149 in solution as well as that of D149 adsorbed to ZnO compared with $\phi_{h\nu}(\lambda)$ for the excitation wavelengths used in SECM study. The obtained values of $\phi_{h\nu}(\lambda)$ nicely fit to the spectrum of the film and follows the broadened absorption spectrum of the adsorbed sensitizer molecule. Small deviations are consequence of the various uncertainties in the experimental procedures. It is also interesting to correlate $\phi_{h\nu}(\lambda)$ from our model with the light harvesting efficiency *LHE* using Lambert-Beer's law Eq. (7.17) [42].

$$LHE = 1 - 10^{-A} = 1 - 10^{-\Gamma_{D^\circ}\phi_{h\nu}(\lambda)} \qquad (7.17)$$

where A is the absorbance of the film, Γ_{D° is dye loading (mol cm^{-2}) and $\phi_{h\nu}$ photon absorption cross section (cm^2 mol^{-1}). Accordingly, the calculated light harvesting efficiencies at the absorption wavelengths 467 nm, 529 nm, 593 nm and 647 nm were 77%, 80%, 58% and 43%, respectively, as calculated from $\phi_{h\nu}$.

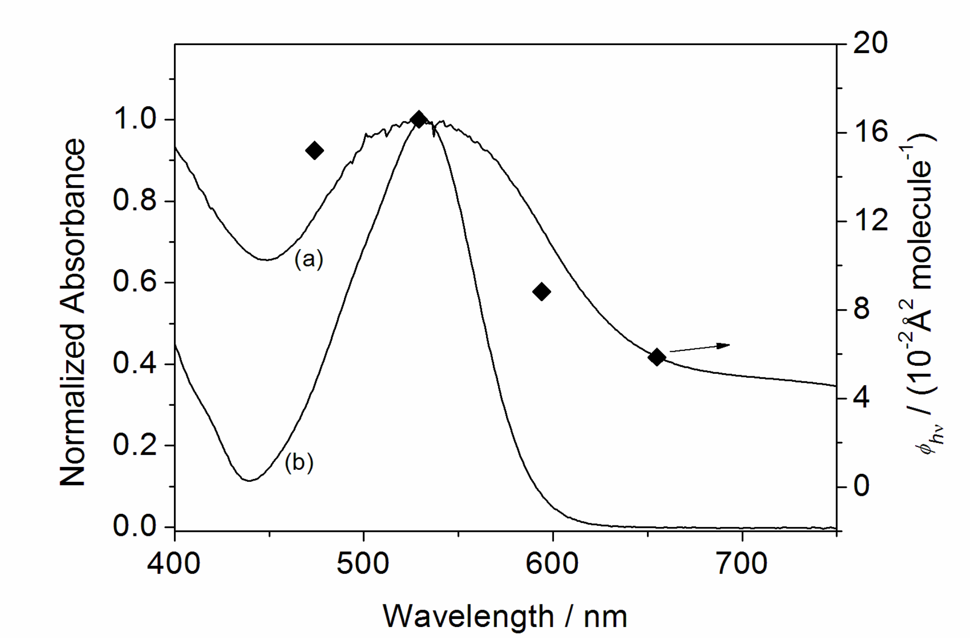

Figure 7.9 Comparison of absorption spectrum of electrochemically deposited D149 sensitized ZnO film and the monomolecular dye dissolved in N,N-dimethylformamide (left ordinate) and photon excitation cross-section (right ordinate) for the dye D149 molecules as a function of excitation wavelength.

From Section 7.1 and 7.2 it can be concluded that SECM feedback mode approach curves has been shown to be a successful approach for the investigation of the kinetics of dye regeneration by iodide ions in a DSSC, which is an important factor to improve energy conversion efficiencies for the DSSC. Using one model for different LED illumination, consistent values of experimentally k_{ox} were determined. A direct correlation between optical absorbance of D149-sensitized ZnO films and the photoexcitation cross-section of D149 molecules was observed from SECM kinetic data analysis. Furthermore, the SECM study shows that the difference in the apparent heterogeneous first order rate constant for LEDs irradiation with different wavelength could be due to the excitation cross section of the adsorbed dye, which is related to the dye molecular properties.

8. SECM model for dye regeneration rate of first order with respect to iodide

This Chapter describes the derivation of SECM kinetic model for first order rate law with respect to [I^-] for the dye regeneration. The motivation to revise the kinetic model used in previous Chapter for a reaction order of one with respect to [I^-] is described below.

The kinetic model Eq. (7.16) derivation based on a brutto reaction Eq. (3.3) remained unsatisfactory from the perspective of spectroscopic and spectroelectrochemical experiments available in literatures on this subject. Detailed molecular mechanism for TiO_2/Ru-dyes solar cells is available in various literatures. However, there has been some controversy about the exact mechanism of dye regeneration and very recently a number of new studies and reviews have appeared on the subject [112, 114, 234]. Anderson et al.[14] proposed three mechanisms and found strong experimental evidence that a first order rate law with respect to I^- provides the best description. They also state that different mechanisms could be effective in parallel [14]. The most likely mechanism according to several studies is

$$D/TiO_2 + h\nu \xrightarrow{\phi_{h\nu}} D^*/TiO_2 \tag{8.1}$$

$$D^*/TiO_2 \xrightarrow{k_{inj}} D^+/TiO_2 + e^-_{CB}(TiO_2) \tag{8.2}$$

$$D^+/TiO_2 + I^- \xrightarrow{k_1} [D^{\cdots}I]/TiO_2 \tag{8.3}$$

$$[D^{\cdots}I]/TiO_2 + I^- \xrightarrow{k_2} D/TiO_2 + I_2^{-\bullet} \tag{8.4}$$

$$2\, I_2^{-\bullet} \xrightarrow{k_2} I_3^- + I^- \tag{8.5}$$

The existence of $I_2^{-\bullet}$ has been confirmed in DSSC by nanosecond transient spectroscopy [14, 112, 234, 235] and pseudo steady-state photoinduced absorption spectroscopy [236]. Experimental evidence for the formation of a surface complex between the dye and iodide (designated by [$D^{\cdots}I$] in the mechanisms) was found by Clifford et al. using transient absorption spectroscopy

[115] for a particular dye [Ru(dcbpy)$_2$(CN)$_2$]. Also the formation of a iodine atom as a result of reaction Eq. (8.3) followed by a reaction with I$^-$ would lead to two consecutive steps being first order with respect to I$^-$ as observed for the overall mechanisms by Anderson et al.[14] In view of this results, we repeated the kinetic treatment outlined in Chapter 7 for a reaction order of one with respect to [I$^-$]. The full details of SECM kinetics model derivation is given below. Due to ongoing attempt to model DSSC and to follow common practice of expressing dye content in the film, the dye loading Γ_D (amount of dye per geometric area) in previous treatment is replaced by the volume concentration [D°] (amount of dye per volume of the porous metal oxide electrode). The amount of dye interacting with the SECM probe is thus $A\,\Gamma_\mathrm{D} = A\,l\,[\mathrm{D}°]$, where A is the projected area of the SECM probe and l the film thickness of the porous dye-sensitized electrode. The steady state expressions for [D*], [D$\cdots$I] and [D$^+$] given by Eq. (8.6), Eq. (8.7) and Eq. (8.8), respectively

$$\begin{aligned}&\frac{\partial[\mathrm{D^*}]}{\partial t} = 0 = \phi_{h\nu} J_{h\nu}[\mathrm{D}] - k_\mathrm{inj}[\mathrm{D^*}]\\ &\frac{[\mathrm{D}]}{[\mathrm{D^*}]} = \frac{k_\mathrm{inj}}{\phi_{h\nu} J_{h\nu}}\end{aligned} \tag{8.6}$$

$$\begin{aligned}\frac{\partial[\mathrm{D\cdots I}]}{\partial t} &= 0 = k_1[\mathrm{D^+}][\mathrm{I^-}]_\mathrm{S} - k_2[\mathrm{D\cdots I}][\mathrm{I^-}]_\mathrm{S}\\ &= k_1[\mathrm{D^+}] - k_2[\mathrm{D\cdots I}]\\ \frac{[\mathrm{D\cdots I}]}{[\mathrm{D^+}]} &= \frac{k_1}{k_2}\end{aligned} \tag{8.7}$$

$$\begin{aligned}&\frac{\partial[\mathrm{D^+}]}{\partial t} = 0 = k_\mathrm{inj}[\mathrm{D^*}] - k_1[\mathrm{D^+}][\mathrm{I^-}]_\mathrm{S}\\ &\frac{[\mathrm{D^+}]}{[\mathrm{D^*}]} = \frac{k_\mathrm{inj}}{k_1[\mathrm{I^-}]_\mathrm{S}}\end{aligned} \tag{8.8}$$

Combining Eq. (8.7) and Eq. (8.8) provides Eq. (8.9)

$$\frac{[\mathrm{D\cdots I}]}{[\mathrm{D^*}]} = \frac{k_\mathrm{inj}}{k_2[\mathrm{I^-}]_\mathrm{S}} \tag{8.9}$$

The mass conservation of the total dye content [D°] comprising dye molecules of all possible states can be expressed Eq. (8.10)

$$\begin{aligned}[\mathrm{D^o}] &= [\mathrm{D}]+[\mathrm{D^+}]+[\mathrm{D^*}]+[\mathrm{D\cdots I}] \\ &=[\mathrm{D^*}]\left(\frac{[\mathrm{D}]}{[\mathrm{D^*}]}+\frac{[\mathrm{D^+}]}{[\mathrm{D^*}]}+\frac{[\mathrm{D\cdots I}]}{[\mathrm{D^*}]}+1\right)\end{aligned} \tag{8.10}$$

Appropriate substitution of Eq. (8.6), Eq. (8.7) and Eq. (8.9) in Eq. (8.10) yields steady state expression for ratio of [D$^{\mathrm{o}}$] Eq. (8.11)

$$\begin{aligned}[\mathrm{D^o}] &= [\mathrm{D^*}]\left(\frac{k_{\mathrm{inj}}}{\phi_{h\nu}J_{h\nu}}+\frac{k_{\mathrm{inj}}}{k_1[\mathrm{I^-}]_{\mathrm{S}}}+\frac{k_{\mathrm{inj}}}{k_2[\mathrm{I^-}]_{\mathrm{S}}}+1\right) \\ [\mathrm{D^*}] &= \frac{[\mathrm{D^o}]}{\dfrac{k_{\mathrm{inj}}}{\phi_{h\nu}J_{h\nu}}+\dfrac{k_{\mathrm{inj}}}{k_1[\mathrm{I^-}]_{\mathrm{S}}}+\dfrac{k_{\mathrm{inj}}}{k_2[\mathrm{I^-}]_{\mathrm{S}}}+1}\end{aligned} \tag{8.11}$$

The expression for kinetically controlled substrate current i_{K} is given by Eq. (8.12)

$$i_{\mathrm{K}} = nFA\left(k_1 l[\mathrm{D^+}][\mathrm{I^-}]_{\mathrm{S}}\right) \tag{8.12}$$

Substitution of the bracketed term using the Bodenstein principle for the steady state experiment $k_{\mathrm{inj}}[\mathrm{D^*}] = k_1 l[\mathrm{D^+}][\mathrm{I^-}]_{\mathrm{S}}$ ($n = 1$) yields Eq. (8.13).

$$i_{\mathrm{K}} = FAk_{\mathrm{inj}}l[\mathrm{D^*}] \tag{8.13}$$

Appropriate substitution of the expression for [D*] from Eq. (8.11) into Eq. (8.13) results in Eq. (8.14) which is further simplified to Eq. (8.15)

$$i_{\mathrm{K}} = FAk_{\mathrm{inj}}l\,\frac{[\mathrm{D^\circ}]}{\dfrac{k_{\mathrm{inj}}}{\phi_{h\nu}J_{h\nu}}+\dfrac{k_{\mathrm{inj}}}{k_1[\mathrm{I^-}]_{\mathrm{S}}}+\dfrac{k_{\mathrm{inj}}}{k_2[\mathrm{I^-}]_{\mathrm{S}}}+1} \tag{8.14}$$

$$\frac{1}{i_{\mathrm{K}}} = \frac{1}{FAl[\mathrm{D^\circ}]\phi_{h\nu}J_{h\nu}}+\frac{1}{FAl[\mathrm{D^\circ}]k_1[\mathrm{I^-}]_{\mathrm{S}}}+\frac{1}{FAl[\mathrm{D^\circ}]k_2[\mathrm{I^-}]_{\mathrm{S}}}+\frac{1}{FAl[\mathrm{D^\circ}]k_{inj}} \tag{8.15}$$

Further simplifications are obtained by introduction of effective constants for light absorption and dye regeneration Eq. (7.10), $(k'_{\mathrm{ox}})^{-1} = (k_1)^{-1} + (k_2)^{-1}$ and considering the case of limiting substrate current ($[\mathrm{I^-}]_{\mathrm{S}} = 3[\mathrm{I_3^-}]^*$) gives Eq. (8.16)

$$\frac{1}{i_{\mathrm{K,lim}}}=\frac{1}{FAl[\mathrm{D}°]k_{h\nu,\mathrm{eff}}}+\frac{1}{3FAl[\mathrm{D}°]k'_{\mathrm{ox}}[\mathrm{I}_3^-]^*} \tag{8.16}$$

Note that the rationalization for Eq. (7.12) is generally valid. The reciprocal of normalized total substrate current Eq. (8.17) is obtained by appropriate substitution of Eq. (8.16) in Eq. (7.12).

$$\begin{aligned}\frac{1}{I_{\mathrm{S}}}&=\frac{1}{I_{\mathrm{T,cond}}}+\frac{8FD[\mathrm{I}_3^-]^*r_{\mathrm{T}}}{F\pi r_{\mathrm{T}}^2 l[\mathrm{D}°]\phi_{h\nu}J_{h\nu}}+\frac{8FD[\mathrm{I}_3^-]^*r_{\mathrm{T}}}{3F\pi r_{\mathrm{T}}^2 l[\mathrm{D}°]k'_{\mathrm{ox}}[\mathrm{I}_3^-]^*}\\&=\frac{1}{I_{\mathrm{T,cond}}}+\frac{4D}{\pi r_{\mathrm{T}}}\left[\frac{2[\mathrm{I}_3^-]^*}{l[\mathrm{D}°]\phi_{h\nu}J_{h\nu}}+\frac{2}{3l[\mathrm{D}°]k'_{\mathrm{ox}}}\right]\end{aligned} \tag{8.17}$$

The expression for $1/I_{\mathrm{S}}$ must now be compared to the expression Eq. (7.15) for the uncomplicated electron transfer at the sample for which the analytical expressions of SECM approach curves are available. This provides k_{eff} for the SECM experiment Eq. (8.18)

$$\frac{1}{k_{\mathrm{eff}}}=\frac{2[\mathrm{I}_3^-]^*}{l[\mathrm{D}°]\phi_{h\nu}J_{h\nu}}+\frac{2}{3l[\mathrm{D}°]k'_{\mathrm{ox}}} \tag{8.18}$$

The relationship between kinetic models Eq. (8.18) and Eq. (7.16) is the replacement of the term $3^{1/2}k_{\mathrm{ox}}[\mathrm{I}_3^-]^{3/2}$ by k'_{ox} $[\mathrm{I}_3^-]$. Please note that both k_{ox} and k'_{ox} can also sum up other processes that are not explicitly considered in Eqs. (8.1)-(8.5). Here recombination and mass transport limitations inside the porous electrode are also summed up by the effective rate constant.

The analysis of the data in Chapter 7 using model Eq. (8.18) showed that the results can be reasonably well described by models assuming a brutto reaction rate law of order 1.5 or one with respect to I^-. The real situation is further complicated by different mechanisms of recombination and quenching of the excited state [114]. They are not explicitly considered in our model. Their effects will manifest themselves in k'_{ox} which represents an effective constant. It should be remarked that under the condition of low light intensity and low $\mathrm{I}_3^-/\mathrm{I}^-$ concentration, recombination effects are less important than at higher concentrations [112]. The new model still assumes uniform accessibility of dye molecules for I^- and light within different depth of the porous film as it is commonly implied in the analysis of such thin films. These assumptions are needed for reducing the complexity of the problem. Internal mass transport limitations can however occur, particularly at low concentration of the redox electrolyte. We also do not consider explicitly any hindrance by the electron diffusion in TiO_2.

8.1. Dye regeneration kinetics in N719-sensitized TiO_2 films

In this Section we extended SECM investigation of DSSC to nanoparticulate TiO_2 films sensitized by a more efficient dye, N719. Here, we exploit the possibility to easily change the electrolyte for one and the same sample to investigate the influence of different cations, and solvent identity on the dye regeneration kinetics. This may guide the selection of cations for highly efficient DSSCs. Specifically, the common RTIL 1-ethyl-3-methylimidazolium bis(trifluoromethylsulfonyl)imide (EMimTFS) was compared to acetonitrile based electrolytes each of them containing various concentrations of purposefully added Li^+, 1,2-dimethyl-3-propylimidazolium ($DMPim^+$), and TBA^+ cations. The data are analyzed with the help of a revised kinetic model Eq. (8.18) for relating steady state approach curves in the SECM feedback mode to an effective rate constant for the dye regeneration process.

8.1.1. Effect of solvent identity: acetonitrile *versus* RTIL

SECM has already been applied for eliciting details regarding local reactions on metal/RTIL interfaces [237-241]. SECM investigations in RTIL have also demonstrated the inequality in diffusion coefficients of oxidized and reduced forms of redox mediators [242, 243]. The efficiency of dye regeneration by iodide in N719/TiO_2 photoelectrochemical cell was found to be strongly affected by the nature of solvent [244-246]. SECM approach curves on illuminated N719/TiO_2 substrate were measured in two electrolytes: LiI and I_2 dissolved either in the conventional solvent like acetonitrile with 0.01 M LiTFS as supporting electrolyte or in the EMimTFS with 0.01 M LiTFS as an example of a RTIL. For SECM feedback measurements, the electrolyte contains the oxidized form I_3^- only. This was achieved by "titrating" the initially contained I^- ions with a solution of I_2 in the respective solvent until a microelectrode cyclic voltammogram (CV) showed a plateau around 0 V (*vs*. pseudo reference electrode) with a current of 0 nA (Figure 6.1). From that stock solution different electrolytes were prepared by diluting with 0.01 M LiTFS in the respective solvent. The influence of both triiodide bulk concentration $[I_3^-]^*$ and light intensity $J_{h\nu}$ on approach curves were examined for comparing the associated kinetics for dye regeneration at illuminated substrates.

Figure 8.1 shows the normalized SECM approach curves at fixed $J_{h\nu}$ in (a) acetonitrile and (b) EMimTFS for a range of $[I_3^-]^*$ between 0.064 mM and 2.21 mM. Following the same procedure as in the previous Chapter, fitting experimental approach curve the theory [Eqs. (4.5)-(4.9)], yields κ as adjustable parameter, that in turn leads to the corresponding k_{eff} for iodide oxidation. The diffusion coefficients D for I_3^- in the electrolyte solutions were evaluated for each electrolyte composition from steady state diffusion-limited currents at a microelectrode for the reaction of $I_3^- + 2e^- \rightarrow 3I^-$. Details and values are given in Section 6.1.1. Typical values are 1.4×10^{-5} cm^2 s^{-1} in acetonitrile [223] and 7.3×10^{-7} cm^2 s^{-1} in EMimTFS in agreement with literature values [103, 104, 247]. For increasing $[I_3^-]^*$ from 0.064 mM to 2.21 mM and green LED photon flux of 25.5×10^{-9} mol cm^{-2} s^{-1}, k_{eff} decreased from 19.7×10^{-3} cm s^{-1} to 0.658×10^{-3} cm s^{-1} in acetonitrile and from 0.336×10^{-3} cm s^{-1} to 0.025×10^{-3} cm s^{-1} in EMimTFS (Table 8.1a). The decrease of k_{eff} with increasing $[I_3^-]^*$ is expected as the I_3^- flux from the bulk solution towards the microelectrode probe increases linearly with $[I_3^-]^*$ while the dye regeneration process can only provide a flux that is limited by the dye-loading and the light absorption. However, for a given mediator concentration and light intensity, significantly larger values of k_{eff} were obtained with acetonitrile compared to EMimTFS.

Compared to ZnO/Eosin Y and ZnO/D149-based DSSC (see Chapter 7) the cells based on TiO_2/N719 showed much larger k_{eff} values under comparable conditions.

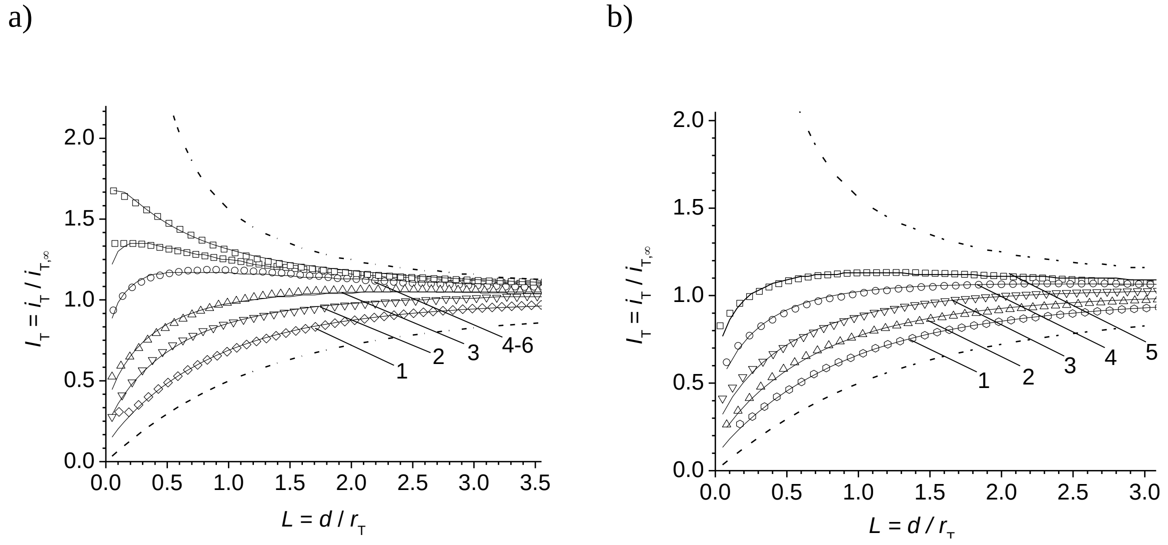

Figure 8.1 Comparison of normalized SECM approach curves between (a) acetonitrile and (b) EMimTFS solution and 0.1 M LiTFS inert supporting electrolyte with Pt UME (r_T = 12.5 µm) on TiO_2/N719 film under illumination with blue LED at intensity $J_{h\nu}$ of 25.5 x 10^{-9} mol cm^{-2} s^{-1} for the following $[I_3^-]^*$ in mM (1) 2.21, (2) 1.24, (3) 0.953, (4) 0.622, (5) 0.134, and (6) 0.064. Top and bottom dashed lines indicate hindered diffusion and diffusion-controlled positive feedback. The values of κ obtained from the best fit of experimental approach curve (open symbols) to theoretical model (thin solid curves) were (a) (1) 0.06, (2) 0.17, (3) 0.67, (4) 0.32, (5) 1.22 and (b) (1) 0.048, (2) 0.14, (3) 0.20, (4) 0.40, (5) 0.75.

The influence of light intensities (green LED) with $[I_3^-]^*$ = 0.064 mM was also compared for the two solvents acetonitrile (Figure 8.2a) and EMimTFS (Figure 8.2b). Without illumination, both solvents yielded normalized approach curves corresponding to the hindered-diffusion of I_3^- towards the microelectrode probe. At weaker LED intensities, k_{eff} values for I_3^- regeneration were very small and close to the value consistent with hindered-diffusion. With increasing LED intensity, the regeneration kinetics became faster as reflected by higher k_{eff} (Table 8.1b).

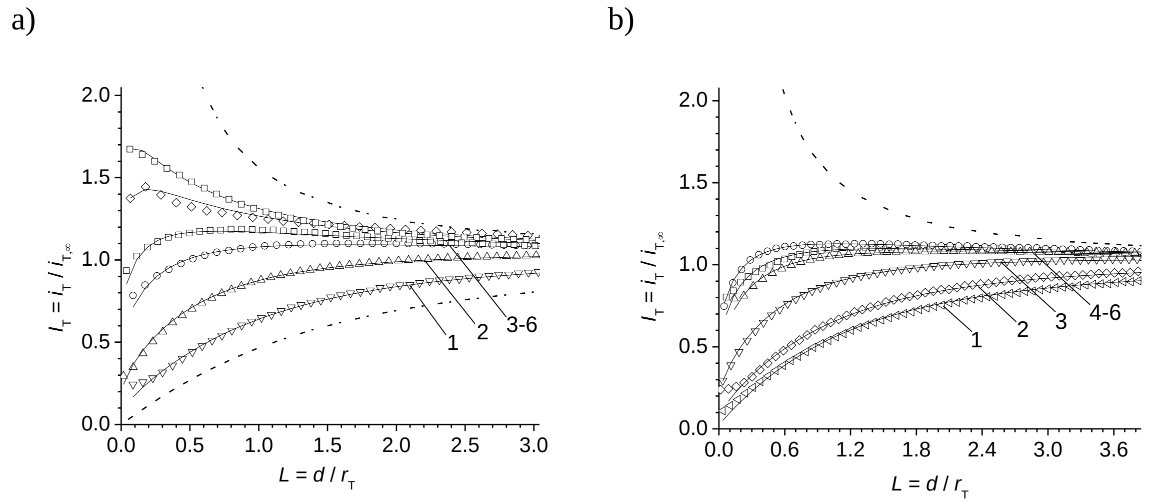

Figure 8.2 Comparison of normalized SECM approach curves between (a) acetonitrile and (b) EMimTFS solution with 0.064 mM $[I_3^-]^*$ and 0.01 M LiTFS inert supporting electrolyte with Pt UME (r_T = 12.5 µm) on TiO_2/N719 film for LED intensities $J_{h\nu}$ in 10^{-9} mol cm^{-2} s^{-1} of (1) 0.982;, (2) 1.7; (3) 4.5; (4) 9.1; (5) 15.1; and (6) 25.5. Dashed lines indicate hindered diffusion and diffusion-controlled positive feedback. The κ obtained from the best fit of experimental approach curve (open symbols) to the theoretical model (thin solid curves) were (a) (1) 0.042, (2) 0.19, (3) 0.53, (4) 0.8, (5) 1.38, (6) 1.8 and (b) (1) 0.009, (2) 0.042, (3) 0.2, (4) 0.46, (5) 0.54, (6) 0.67.

Table 8.1 Apparent heterogeneous first-order rate constants k_{eff} derived from normalized apparent heterogeneous first order rate constants κ for the reduction of photoexcited N719 by I^- in acetonitrile and in EMimTFS. $D(I_3^-)$ is 1.37 × 10^{-5} cm^2 s^{-1} in acetonitrile, and 7.31 × 10^{-7} cm^2 s^{-1} (Table 6.1) in EMimTFS, r_T = 12.5 µm, RG = 10, $k_{\mathrm{eff}} = \kappa D/r_T$

(a) For varying $[I_3^-]^*$ at a fixed LED illumination intensity, $J_{h\nu} = 25.5 \times 10^{-9}$ mol cm^{-2} s^{-1}

$[I_3^-]^*$ / 10^{-6} mol cm^{-3}	k_{eff} / 10^{-3} cm s-1	
	acetonitrile	EMimTFSI
0.064	19.73	0.336
0.136	13.37	0.201
0.622	8.22	0.104
0.953	3.51	0.1
1.24	1.86	0.052
2.21	0.658	0.025

(b) For varying LED illumination intensity at fixed $[I_3^-]^*$ = 0.064 mM

$J_{h\nu}$ / 10^{-9} mol cm^{-2} s^{-1}	k_{eff} / 10^{-3} cm s^{-1}	
	acetonitrile	EMimTFS
0.982	0.464	0.0053
1.7	2.87	0.0246
4.5	5.82	0.114
9.1	8.83	0.269
15.1	15.2	0.316
25.5	19.9	0.392

Fitting experimental k_{eff} to the theoretical approximation model Eq.(8.18) allows determining k'_{ox} and $\phi_{h\nu}$ as the fitting parameters. Figure 8.3a shows the fit of k_{eff} vs. $[I_3^-]^*$ and Figure 8.3b is the fit of k_{eff} vs. $J_{h\nu}$ for the acetonitrile-based electrolyte (left ordinates) and for EMimTFS (right ordinates). The individual k_{eff} values are documented in Table 8.1. For both electrolytes *one* set of fitting parameters k'_{ox}, $\phi_{h\nu}$ provided simultaneously a reasonable fit for the data in Figure 8.3a and Figure 8.3b. However, between the two electrolyte systems considerable differences are observed in both values (Table 8.2).

Considerably different double layer structures are expected in different RTIL-based electrolyte that may slow down the dye regeneration and could explain the differing k'_{ox} values. Recently Yu et al.[248] reported that the electron life time in TiO_2 is higher when TiO_2 is contact with RTIL compared to acetonitrile cell due to faster recombination between electrons in TiO_2 and I_3^- that could further be manipulated by electrolyte additive. The effect was attributed to a shift of the conduction band edge that influences electron injection efficiencies and the electron life time in open circuit conditions [248].

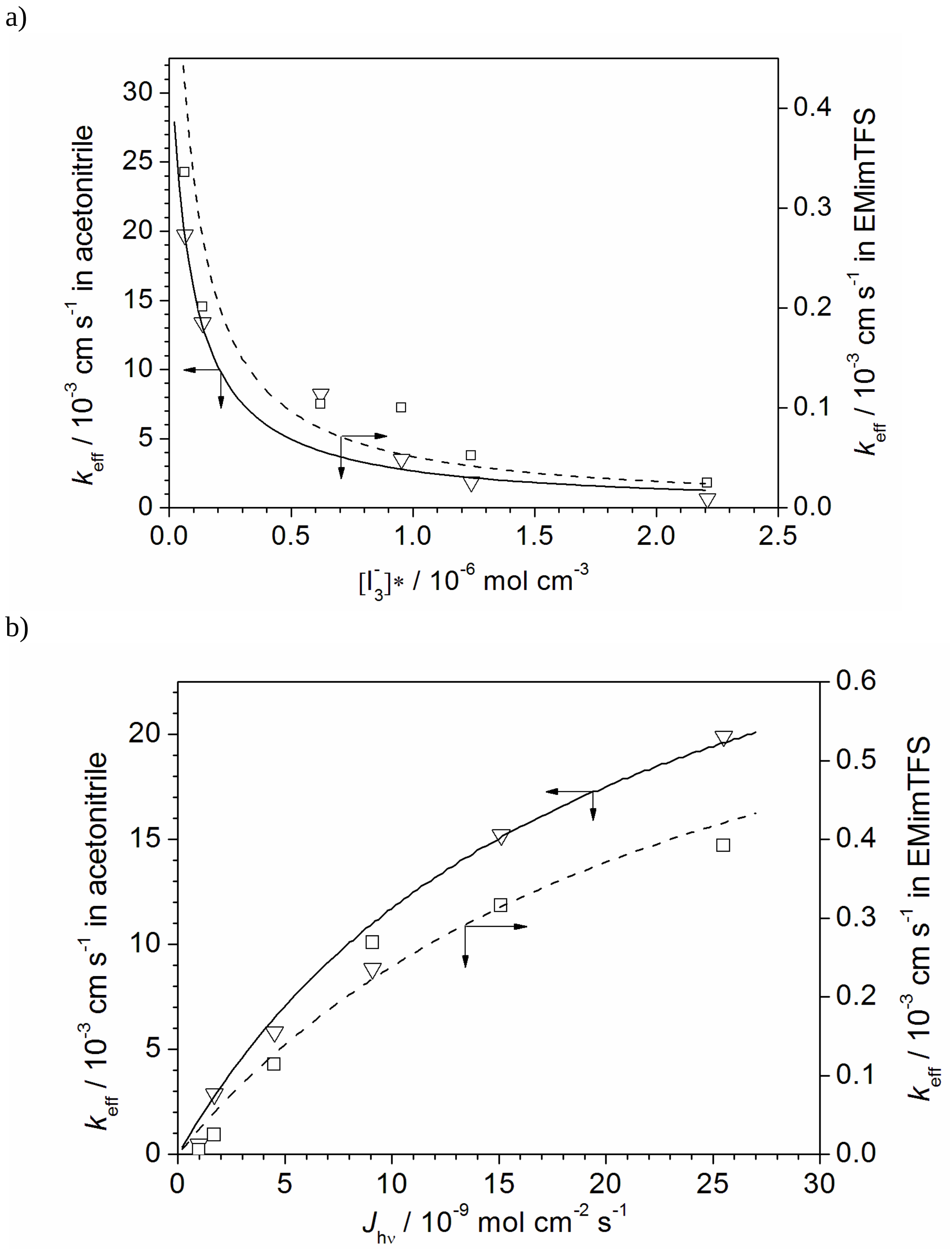

Figure 8.3 Plot of (a) k_{eff} *vs.* $[I_3^-]$* and (b) k_{eff} *vs.* $J_{h\nu}$ for N719-sensitized TiO_2 photoelectrochemical electrodes in acetonitrile or EMimTFS solution. (∇) experimental data for EMimTFS, (∇) experimental data for acetonitrile, (----) fit for EMimTFS, (—) fit for acetonitrile to the model described in Eq. (8.18). Fitting results are given in Table 8.2

Table 8.2 The results from fitting Eq. (8.18) to experimental k_{eff} *vs.* $[I_3^-]^*$ or k_{eff} vs. $J_{h\nu}$ values. For each electrolyte a common set of fitting constants was used.

Parameters	In acetonitrile	In EMimTFS
$\phi_{h\nu}$ /cm^2 mol^{-1}	3.60×10^6	6.80×10^4
k'_{ox} /mol^{-1} cm^3 s^{-1}	3.66×10^5	8.80×10^3

Influences of dye regeneration kinetics and slower diffusion in pores filled by a viscous electrolyte have not been discussed but could add to the observed effects. External mass transport limitation (e.g. diffusion between microelectrode and film/solution interface) are taken into account when calculating k_{eff} from κ. Therefore external mass transport effects cannot serve as an explanation for the effect in SECM experiments. A further work for films of different thicknesses with and without scattering layer to gain more detailed understanding and to vary systematically the internal mass transport condition is given in Chapter 8.2. Somewhat surprising is the large difference on the fitted $\phi_{h\nu}$ between the two electrolyte systems. This may be caused by a different dissolution behavior of the dyes in the different electrolyte systems. Another effect may be introduced by different scattering behavior in the two electrolyte solutions that may lead to a different local light intensity directly under the SECM probe when light is scattered out of the region probed by the SECM microelectrode. Such influences would be reflected in the fitted $\phi_{h\nu}$ values.

8.1.2. Effect of cation in RTIL and in acetonitrile on dye regeneration

The diffusion of I^-/I_3^- redox species as well as the electron diffusion through the film and its lifetime in DSSCs are strongly cation-dependent [76, 249, 250]. Adsorbed inert ions may modify the injection rates from the adsorbed dye to the photo anode. By improving the ionic transport in the electrolyte, the electron diffusion in TiO_2 can be enhanced. There are only a limited number of studies regarding the effect of inert electrolyte composition on dye regeneration rate [251-253]. By using SECM approach curves in the feedback mode, clear evidence is found for the influence of particular cation and its concentration on dye regeneration rate.

SECM approach curves on N719-sensitized TiO_2 photoelectrochemical electrodes were investigated for three different electrolytes in 0.01 M LiTFS and additionally added Li^+, $DMPim^+$ and TBA^+ cations. The cations were selected in such a way that they have a large difference in their size and adsorption properties [76, 93, 250]. Lithium inclusion in electrolyte has been commonly used in DSSCs, where Li^+ adsorbs onto the metal oxide surface and increases the charge injection efficiency of dyes by shifting the conduction band edge to more positive potentials [254, 255]. It was also reported that imidazolium cations adsorb on the metal oxide surface and align the anion species due to electrostatic interaction, and thereby facilitate electron transport [256].

For the study of the electrolyte effect, approach curves for different concentration of each of the cations (Li^+, $DMPim^+$, TBA^+) in the electrolyte (Figure 8.4a-c, curves 1-6) on the *same* sample thus excluding possible electrode-to-electrode variations from the analysis were analysed. $[Li^+]$, $[DMPim^+]$ and $[TBA^+]$ were varied independently of $[I_3^-]^*$ by the addition of LiTFS, DMPimTFS and TBATFS, respectively. The cation concentration was changed from the lowest to the highest cation concentration. The sample was changed when moving to another cation to be investigated. Even if the cations are not involved as reaction partner in Eqs. (8.1)-(8.5) experimental k_{eff} values show significant and systematic variations in dye regeneration rate with the structure and concentration of the inert cation in the electrolyte. For instance, with illumination at $J_{h\nu} = 25.5 \times 10^{-9}$ mol cm^{-2} s^{-1} and $[I_3^-]^* = 0.064$ mM, we found a monotonic decrease in k_{eff} with increasing cation concentration for each of the investigated cations (Figure 8.4a). For example, while $[Li^+]$ increases from 0.11 to 35.19 mM, k_{eff} decreases from 2.24×10^{-4} cm s^{-1} to almost zero and the resulting normalized approach curve overlaps with the theoretical curve for hindered diffusion, the bottom curve (curve 1) in Figure 8.4d. The data are given in Table 8.3. A similar behaviour is noticed for $DMPim^+$. A more gradual decrease in k_{eff} was observed for TBA^+. TBA^+ is bulkier and probably less adsorptive [93, 250] than $DMPim^+$. The larger size of TBA^+ could increase the double layer thickness for TBA^+-containing electrolytes (Ref. [93], scheme 2). As a result, the concentration of I^- near the N719/TiO_2 surface could decrease and hence lower flux of I_3^- emerges from the sample to the UME, reflected by a decreased regeneration rate at the sample surface. At higher concentration of the added cations, the behaviour converges for all of the studied cations (Figure 8.4d).

The approach curves in acetonitrile with the same cations (Li^+, $DMPim^+$, TBA^+) showed the same trend of decreasing k_{eff} with increasing cation concentration of the supporting electrolyte. Also the relative order for the same cation concentration followed the trend found in the RTIL. The data are given in Figure 8.5. However, the overall rate of regeneration was higher in acetonitrile than in EMimTFS under otherwise comparable conditions.

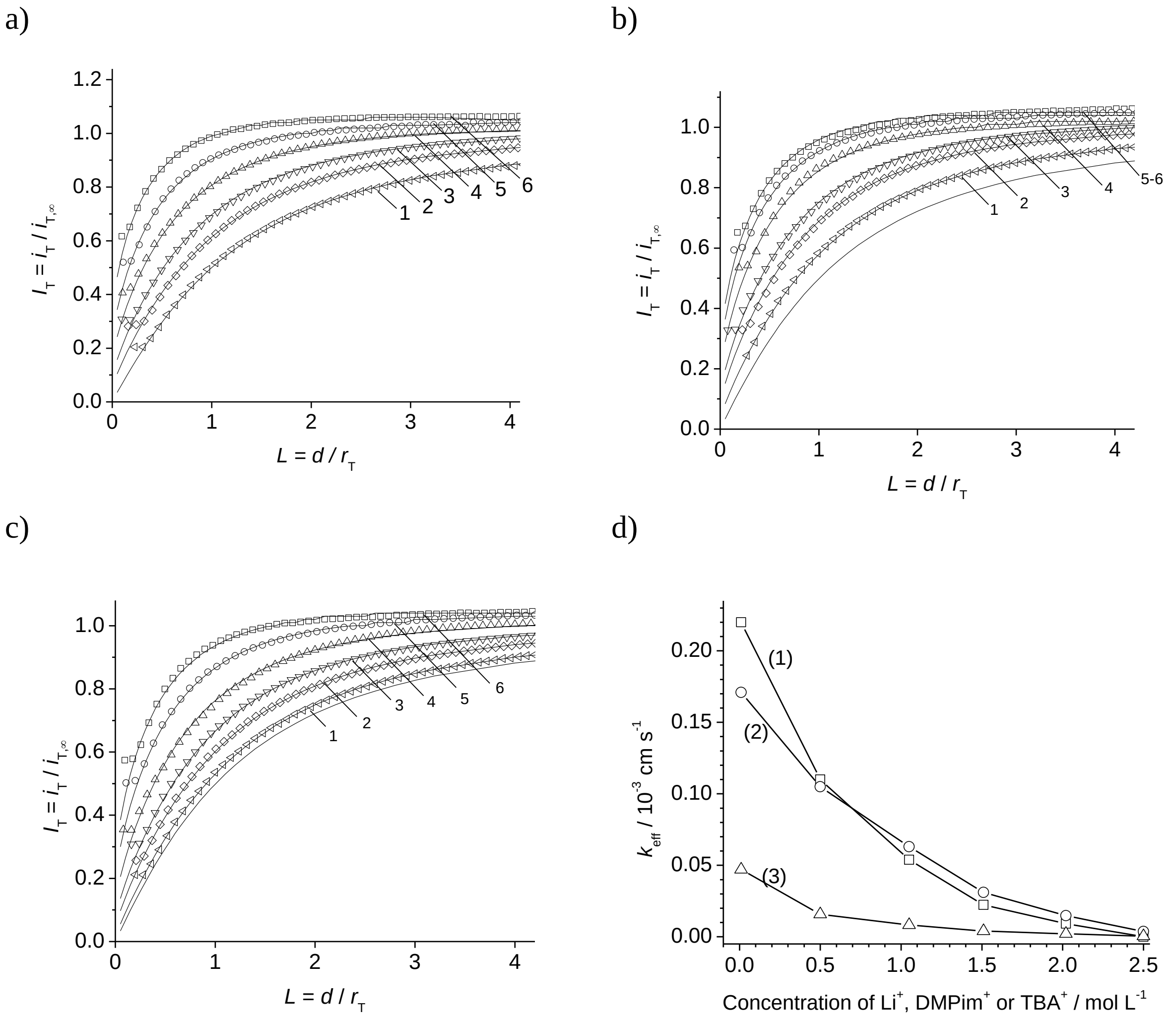

Figure 8.4 (a) Normalized SECM approach curves with Pt UME (r_T = 12.5 µm) on TiO_2/N719 film illuminated with green LED intensity of 25.5 × 10^{-9} mol cm^{-2} s^{-1} and in solution containing 0.064 mM $[I_3^-]$* using various concentration of (a) [LiTFS], (b) DMPimTFS and (c) TBATFS in EMimTFS, as inert supporting electrolytes in EMimTFS. (1) 2.5 M, (2) 2.02 M, (3) 1.51 M, (4) 1.05 M, (5) 0.5 M, and (6) 0.01. The summary of κ values obtained from the best fit of experimental approach curve (open symbols) to the theoretical model (thin solid curves) were respectively (a) (1) 1 x 10^{-4}, (2) 0.03, (3) 0.064, (4) 0.13, (5) 0.22, and (6) 0.34 for LiI/I_2/LiTFS; (b) (1) 0.019, (2) 0.06, (3) 0.093, (4) 0.17, (5) 0.24, (6) 0.29 for DMPimI/I_2/DMPimTFS; (c) (1) 0.006, (2) 0.026, (3) 0.05, (4) 0.10, (5) 0.18, (6) 0.26 for TBAI/I_2/TBATFS in EMimTFS . (d) Plot of k_{eff} as a function of cation concentration for three different electrolytes compositions varying only in terms of cation counter ions (1) LiI/I_2/LiTFS, (2) DMPimI/I_2/DMPimTFS, (3) TBAI/I_2/TBATFS in EMimTFS. Lines are guides to the eye.

Table 8.3 Apparent heterogeneous first-order rate constants k_{eff} derived from normalized apparent first order rate constants κ for the reduction of photo-oxidized N719 by I^- in EMimTFS for the electrolyte compositions LiI/I$_2$/LiTFS, DMPimI/I$_2$/DMPimTFS and TBAI/I$_2$/TBAS with a fixed $[I_3^-]$* and varying cations concentration. $D(I_3^-)$ was calculated for each concentration of the inert supporting electrolyte r_T = 12.5 µm, RG = 10, $k_{\mathrm{eff}} = \kappa D/r_T$

Concentration of added supporting electrolyte [M]	k_{eff} / 10^{-4} cm s^{-1}		
	LiI/I$_2$/LiTFS	DMPimI/I$_2$/DMPimTFS	TBAI/I$_2$/TBAS
0.01	2.24	1.71	0.47
0.5	1.1	1.05	0.157
1.05	0.539	0.63	0.0824
1.51	0.223	0.31	0.0404
2.02	0.0092	0.148	0.0206
2.5	2.32×10^{-4}	0.0037	$\times 10^{-3}$

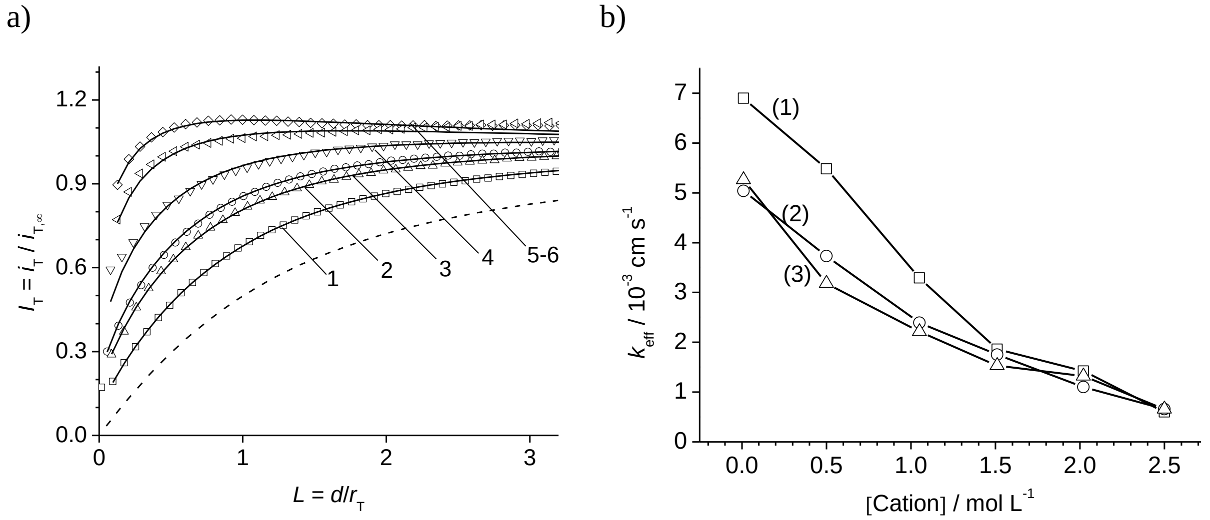

Figure 8.5 Normalized SECM approach curves on TiO$_2$/N719 film at the same conditions as in Figure 8.4 for various concentrations of LiTFS in acetonitrile: (1) 2.5 M, (2) 2.02 M, (3) 1.51 M, (4) 1.05 M, (5) 0.5 M, and (6) 0.01. The summary of κ values from the best fit were, κ = (1) 0.055, (2) 0.13, (3) 0.17, (4) 0.3, (5) 0.5, and (6) 0.63, respectively.

Table 8.4 Apparent heterogeneous first-order rate constants k_{eff} derived from normalized apparent first order rate constants κ for the reduction of photo-oxidized N719 by I^- in acetonitrile for the electrolyte compositions $LiI/I_2/LiTFS$, $DMPimI/I_2/DMPimTFS$ and $TBAI/I_2/TBAS$ with a fixed $[I_3^-]^*$ and varying cations concentration. $D(I_3^-)$ was calculated for each concentration of the inert supporting electrolyte $r_T = 12.5$ µm, $RG = 10$, $k_{\mathrm{eff}} = \kappa D/r_T$

Concentration of added supporting electrolyte [M]	k_{eff} / 10^{-3} cm s^{-1}		
	$LiI/I_2/LiTFS$	$DMPimI/I_2/DMPimTFS$	$TBAI/I_2/TBAS$
0.01	6.9	5.04	5.26
0.5	5.48	3.73	3.18
1.05	3.29	2.39	2.21
1.51	1.86	1.75	1.53
2.02	1.42	1.1	1.32
2.5	0.60	0.66	0.66

In summary, acetonitrile electrolytes resulted in faster N719 regeneration rates than EMimTFS, chosen as an example of RTIL. The rate is still faster after correction for the faster external diffusion of the redox electrolyte. Approach curves showed that kinetics of dye regeneration depends on the nature and concentration of inert cations present in the electrolyte. The effect of the studied cations is qualitatively the same in acetonitrile and RTIL-based electrolyte solutions. The effect of cations such as Li^+ is a down shift of the conduction band edge that is expected to accelerate the injection rate of the photoexcited dye but also the recombination rate between electrons and dye molecules. Several further reasons could additionally contribute to the observation made here such as differences in surface concentration of I^- induced by cation adsorption, the changes in local viscosity of the electrolytes and variation in the internal structure of the dye sensitized electrode due to intermolecular interaction of dye and specific cations. Even though the SECM feedback method obtains measure (k'_{ox}) of the combined effect of dye regeneration kinetics and recombination processes, it offers some new complementing aspects to established methods of DSSC characterization because it works on a single dye-sensitized electrode rather than on a complete cell. This allows rather straight forward testing of different electrolyte compositions on one and the same substrate without the need to construct series of complete cells. Further work is under way to use SECM for a more detailed characterization of the internal mass transport within the porous electrode.

8.2. Photovoltaic performance, electron recombination and dye regeneration kinetics in D149-sensitized ZnO with varied dye loading and film thickness

Both the dye content as well as the film thickness can significantly influence the photovoltaic performance of dye-sensitized solar cells [75, 257]. For instance, increasing the film thickness and thus the internal surface area while keeping the total dye content constant was found to decrease the open circuit photovoltage because of the presence of additional electron recombination pathways [75]. In terms of quantum efficiency, this corresponds to decreased charge collection efficiency, i.e. a smaller fraction of photo-injected electrons will be able to reach the back contact. However, thicker films can be loaded with more dye and hence absorb a larger fraction of incident light [258]. In thinner films, an increased dye loading will increase the aggregation probability, which promotes radiationless decay and thereby decreases the probability of electron injection [259, 260].

In this Chapter, ZnO/D149 films of different film thickness and dye loading were prepared by varying the ZnO deposition time as well as the residence time in the D149 adsorption solution by Schlettwein et. al. [Gießen]. The samples were then divided as shown schematically in Figure 8.6 and different tests were carried out on parts of identical samples. The dye loading Γ_D [mol cm^{-2}], i.e. the amount of dye per geometric sample area of the

ZnO/D149 films was measured using UV/Vis absorption spectroscopy. This allowed determining the amount of D149 via the Lambert-Beer law using an extinction coefficient of 68000 L mol^{-1} cm^{-1} of D149 in DMF solution at 531 nm [261]. The D149 loading was then calculated by dividing this amount by the area of the piece of film determined by pixel count analysis of photographic images of the pieces using image analysis software. The ratio $\Gamma_{\mathrm{D}}/(p \cdot l_{\mathrm{porous}})$, the dye concentration referred to the total pore volume in the film, is used as a rough measure for the amount of dye per internal surface area of the films. This is valid if the pore geometry and size are assumed to be constant for all films.

Atomic absorption spectrometry was used to determine the zinc content of small pieces of the ZnO/D149 samples of known area. The AAS measurements yielded the zinc concentration of the sample solutions, from which the amount of zinc oxide in the film was calculated. Porosities p of the samples were calculated as the ratio of the amount of ZnO in the porous part of the film and the volume of the porous part of the film determined by the thickness l_{porous} of the porous layer. The blocking layer thickness and the amount of ZnO in the blocking layer were estimated from the amount of charge transferred during the blocking layer electrodeposition using Faraday's law and assuming a current efficiency of 90% for the electrodeposition of compact ZnO [262].

Basic photovoltaic parameters of the films (open-circuit photovoltage and short-circuit photocurrent) were determined from current-voltage characterization. Time-resolved photovoltage measurements were used to derive the effective electron lifetime τ_n, which is a key parameter determining the charge-collection efficiency [263, 264]. The kinetics of D149 regeneration by iodide ions in the electrolyte was studied using SECM feedback mode approach on the films at two different experimental conditions (varying I_3^- mediator bulk concentration and illumination intensity). The result was interpreted using a revised SECM kinetic model for dye regeneration. The perspective of correlating SECM kinetic parameter to the macroscopic solar cell characteristics is discussed.

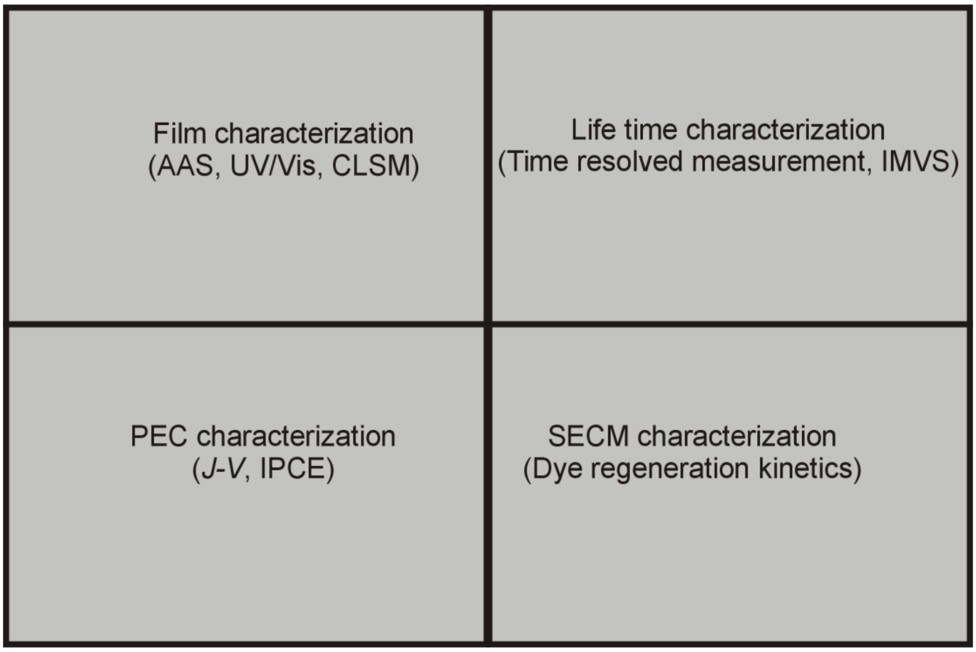

Figure 8.6 The scheme of D149/ZnO sample divided into four pieces to characterize with different techniques

8.2.1. Film characterization

Figure 8.7 shows absorption spectra of D149 adsorbed on the porous ZnO films of varied thickness and dye loading. The spectra clearly reveal a broad absorption band peaking at approximately 532 nm, superimposed with a background signal due to scattering of light by the zinc oxide film. This proves the successful impregnation of the films with the dye and thus accessibility of the pores for all films. The absorption maximum for 120 min adsorption time (film thickness 2.8 µm) is out of scale, i.e. the transmitted light intensity was below the detection limit of the instrument. This is probably due to high dye loading in the film and/or pronounced light scattering. Table 8.7a summarizes the thickness l_{porous} of the porous part of the ZnO films, their porosities p, the dye loading Γ_{D} and the ratio $\Gamma_{\mathrm{D}}/(p \cdot l_{\mathrm{porous}})$, as determined by solution UV/Vis absorption spectroscopy after dissolving the dye out of the films. For effective description, the following sample codes were assigned: S1 for film thickness of 1.4 µm, S2 for thickness of 2.8 µm, S3 for thickness of 3.1 µm, S4 for thickness of 5.3 µm, S5 for thickness of 2.3 µm and S6 for thickness of 3.1 µm (Table 8.7a). The trend of the Γ_D as a function of residence time in the dye bath and film thickness is in line with the trend of peak heights in the solid-state absorption spectra (Figure 8.7). However, the sample S2 shows a smaller Γ_D than S3, although its absorbance measured by solid-state UV/Vis spectroscopy appeared to be higher (out of scale). This means that the off-scale absorbance was probably caused by strong light scattering rather than by a large Γ_D.

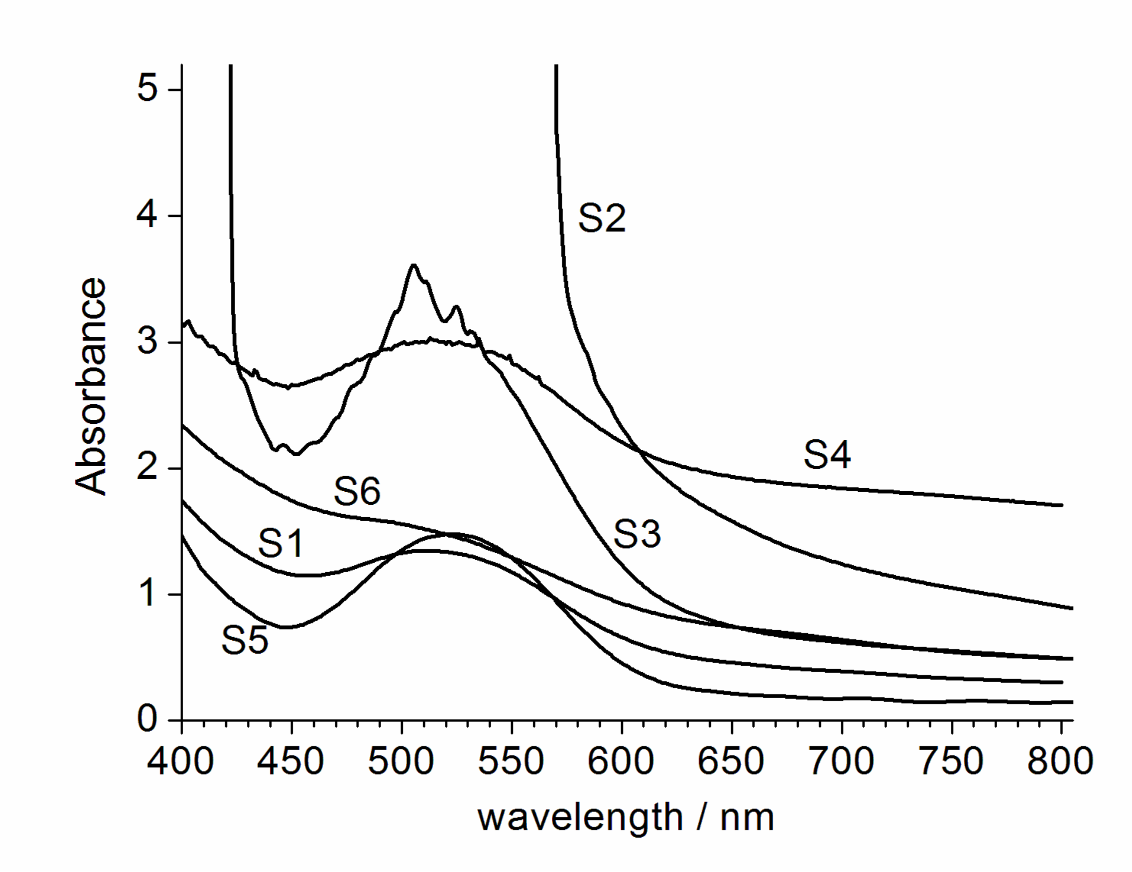

Figure 8.7 Optical absorption spectra of ZnO/D149 films of different thickness (S1) 1.4 µm, (2) 2.8 µm (S3) 3.2 µm, (S4) 4.8 µm, (S5) 2.3 µm and (S6) 3.1 µm after immersion in the D149 bath for 15 min (S5), 30 min (S3), 60 min (S6), 90 min (S1, S4) or 120 min (S2). These data were measured by cooperating partner [group of Schlettwein, University of Giessen].

8.2.2. Photoelectrochemical properties of D149-sensitized ZnO photoelectrodes

8.2.2.1. Current-voltage characteristics

Figure 8.8 and Table 8.7a show current-voltage (*J*-*V*) characteristics of the nanoporous D149/ZnO films S1 to S6 in contact with an I^-/I_3^- redox electrolyte at an illumination intensity of 100 mW cm^{-2}. Changes are observed both in open-circuit voltage V_{oc} and short-circuit current density J_{sc} for the films of different l_{porous} and Γ_D. A correlation was computed among all the quantities investigated here (Table 8.7b). The J_{sc} increases with increasing Γ_D, characteristic for an increased absorption of light. J_{sc} also increases with $\Gamma_D/(p \cdot l_{porous})$, even more significantly. It is thereby indicated that the efficiency of electron injection is not limited by deactivation of excited states by dye aggregates which becomes more likely at increased proximity of dye molecules on the inner ZnO surface. Close proximity of indoline dye molecules on oxide semiconductor surfaces can on the other hand lead to direct hole hopping among the molecules [265]. Such additional charge transport could lead to an increased photocurrent by facilitated dye regeneration as explicitly investigated below.

As can be seen from Table 8.7a, the open-circuit photovoltages observed for the samples analyzed in this study range from -404 mV to -515 mV. No clear correlation between V_{oc} and any of the structural characteristics is found (Table 8.7b). In the present experiments V_{oc} seems to be mainly determined by recombination processes between the semiconductor and the electrolyte and is widely independent of either blocking of recombination by adsorbed dye molecules or dye-mediated recombination. It is reasonable to assume that the observed variation of V_{oc} stems from changes in the density and energetic distribution of trap states in ZnO which are not explicitly analyzed in the present study.

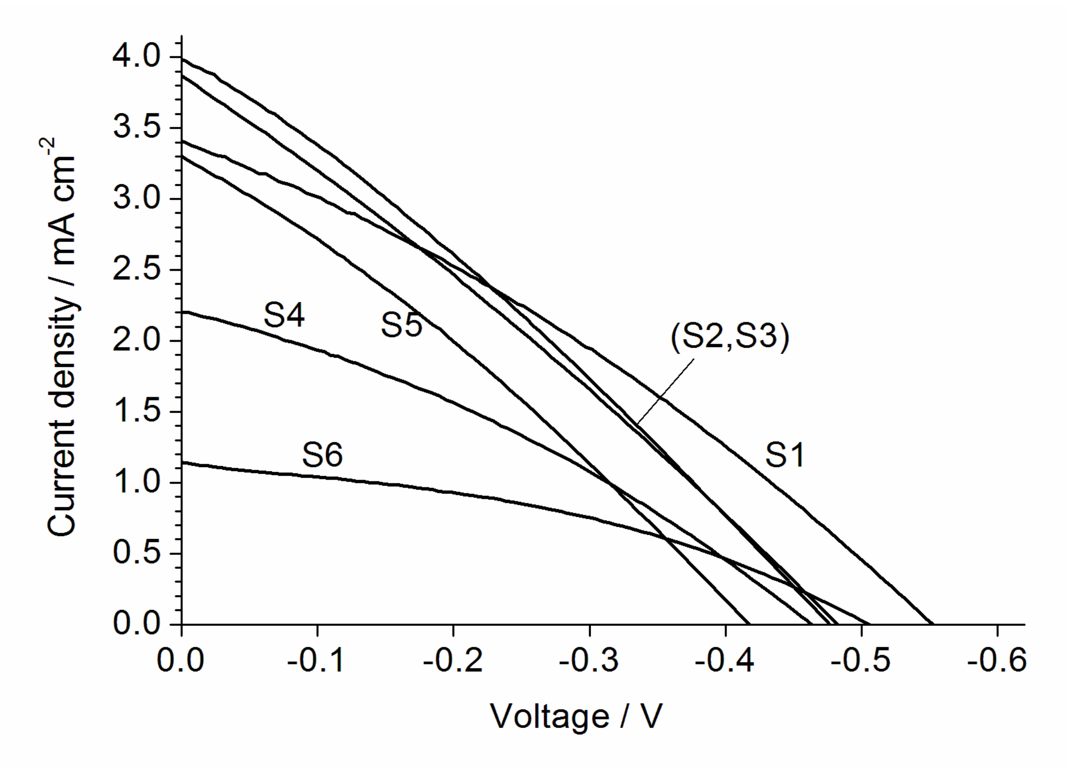

Figure 8.8 Current-voltage characteristics of ZnO/D149 films of different thickness and different D149 loading with white light illumination intensity of 100 mW cm^{-2} (close to AM 1.5 conditions). The film thickness and dye loading were provided in Table 8.7a. A three-electrode arrangement with the ZnO/D149 film as working electrode, a Pt wire counter electrode, an organic Ag/AgNO$_3$ reference electrode and a redox electrolyte composed of 0.05 M I$_2$ and 0.5 M TBAI dissolved in acetonitrile:ethylenecarbonate (1:4) was used. The rest potential of the working electrode in the dark is assumed as the potential of short circuit (0 V in the plot). These data were measured by cooperating partner [group of Schlettwein, University of Giessen]

8.2.2.2. Time-resolved photovoltage measurement

Time-resolved measurements of the decay of the open-circuit voltage following an illumination pulse are used to characterize the recombination dynamics in D149/ZnO solar cells. The decay curve provides access to the electron lifetime τ_n in the dye-sensitized porous semiconductor as a function of the open-circuit voltage (i.e. the position of the electron quasi-Fermi level) via the relationship [Eq. (3.14)]. Because a compact ZnO blocking layer has been deposited below the porous ZnO/D149 films in the present set of samples, recombination events between the FTO substrate and the electrolyte can most likely be excluded. In consequence, the lifetime is expected to be determined only by recombination of electrons from electronic states in zinc oxide.

The observed decay of the open-circuit photovoltage after closure of the shutter (at t = 0 s) following illumination at 100 mW cm^{-2} is shown in Figure 8.9 for the D149/ZnO films with varied l_{porous} and Γ_{D}. It can be seen that within one to two seconds after interruption of the illumination, V_{oc} rapidly decreased to about 50% of its initial value. After this large initial drop, the slope of the decay curves decreased. At the end of the measurement, V_{oc} had decayed to values between -0.05 and 0 V. To compare electron lifetimes for the different samples at a constant thermodynamic driving force for recombination, the lifetimes were obtained from the slope of the voltage decay at a constant voltage of -0.4 V. It can be seen that the values are strongly correlated with the open-circuit voltage (Table 8.7b). This indicates that the differences in the V_{oc} of the samples of different l_{porous} and Γ_{D} are caused by different rates of electron recombination.

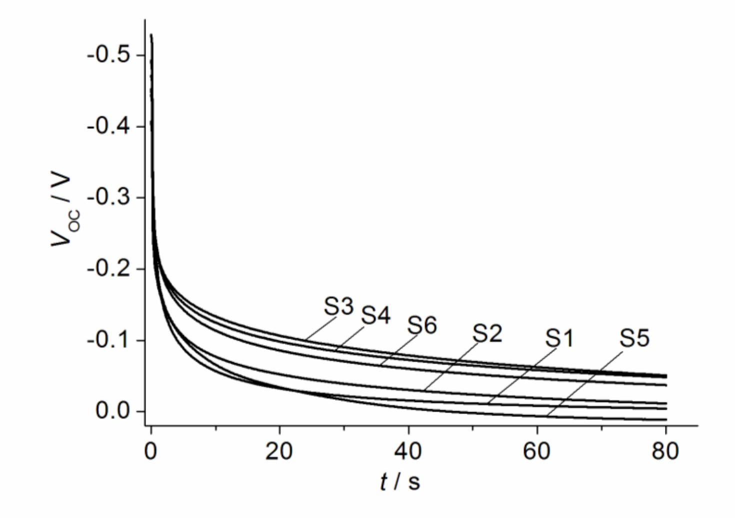

Figure 8.9 Time-resolved photovoltage of ZnO/D149 films of different thickness and different D149 loading. The film thickness and dye loading were provided in Table 8.7a. These data were measured by cooperating partner [group of Schlettwein, University of Giessen]

8.2.3. Dye regeneration kinetics in D149-sensitized ZnO with varied dye loading and film thickness

There is a serious lack of systematic studies on the effect of dye loading and film thickness on rate of dye regeneration. A lot of studies about film thickness and dye loading refer to macroscopic characteristics of solar cells (e.g. V_{oc} and J_{sc}) and not to reaction rate e.g. rate of dye regeneration. These quantities depend on the rate of regeneration but also on rates of other phenomena. SECM feedback measurement allowed analysis of dye regeneration kinetics at a microscopic sample [228]. The extent of feedback at the dye-sensitized substrate could effectively be controlled by regulating $[I_3^-]^*$, J_{hv}, dye loading and film thickness.

SECM approach curves on D149/ZnO film electrodes of varied thickness and dye loading were performed in the electrolyte solution containing I_3^- redox species with UME biased at a tip potential of -0.7 V against Pt quasi-reference electrode with an approach speed of 2 µm s^{-1}. The approach curves on each film were measured under different I_3^- mediator bulk concentrations $[I_3^-]^*$ and illumination intensities expressed in photon flux J_{hv}. The experimental k_{eff} values were extracted from κ by the same procedure as described above.

8.2.3.1. Approach curves with varying $[I_3^-]^*$

Figure 8.10 show the normalized SECM approach curves recorded with Pt UME (r_T = 12.5 µm) approaching to D149/ZnO films of varied film thickness and dye loading. The working solution contained different $[I_3^-]^*$ in 0.1 M TBAS-acetonitrile solution. The top and bottom dashed lines represent theoretical curves for diffusion-controlled reaction at the substrate (positive feedback) and hindered diffusion (no reaction at the sample, “negative feedback”), respectively. Open symbols are experimental data and solid lines are theoretical fits to the analytical approximation by Cornut and Lefrou for first order finite heterogeneous kinetics at the substrate [157] (see above). Table 8.5a summarizes the effective heterogeneous first order rate constant k_{eff} derived from the corresponding normalized pseudo-first order rate constant κ, $k_{\mathrm{eff}} = \kappa D/r_{\mathrm{T}}$ as a function of $[\mathrm{I}_3^-]^*$. A common feature for all curves in Figure 8.10 is that they all lie in the finite kinetics regime, indicating that heterogeneous finite reaction at the substrate are slower than the mediator diffusion. It must be emphasized that the low $[\mathrm{I}_3^-]^*$ and the comparatively large radius of the UME (r_{T} = 12.5 µm) were intentionally selected to drive the reaction into a kinetically controlled regime that allows analysis of the substrate kinetics. The normalized approach curves depend very strongly on the thickness of the film and concentration of adsorbed dye. It is found that for the given $J_{h\nu}$ and $[\mathrm{I}_3^-]^*$, k_{eff} decreased with increasing film thickness and dye loading. For example, D149 regeneration at $J_{h\nu} = 9.1 \times 10^{-9}$ mol cm^{-2} s^{-1} and $[\mathrm{I}_3^-]^* = 0.124$ mM yields k_{eff} of 1.03×10^{-2} cm s^{-1} with sample S1, while sample S2 under the same condition produces only 8.22×10^{-3} cm s^{-1} (Table 8.5a). For a given sample (characterized by Γ_{D} and l) one expects a decrease of k_{eff} with increasing $[\mathrm{I}_3^-]^*$. An increase of $[\mathrm{I}_3^-]^*$ increases $[\mathrm{I}^-]$ after diffusion controlled reduction at the UME. At sample surfaces with a limited number of reaction sites, increasing the available $[\mathrm{I}^-]$ does not lead to proportionally increased reaction currents at the sample. On the other hand $i_{\mathrm{T},\infty}$ increases proportionally to $[\mathrm{I}_3^-]^*$. The normalized current $I_{\mathrm{T}} = i_{\mathrm{T}}/i_{\mathrm{T},\infty}$, thus decreases with increasing mediator concentration at such samples. Similar effects are common for the investigation of immobilized redox enzymes.[158, 266]

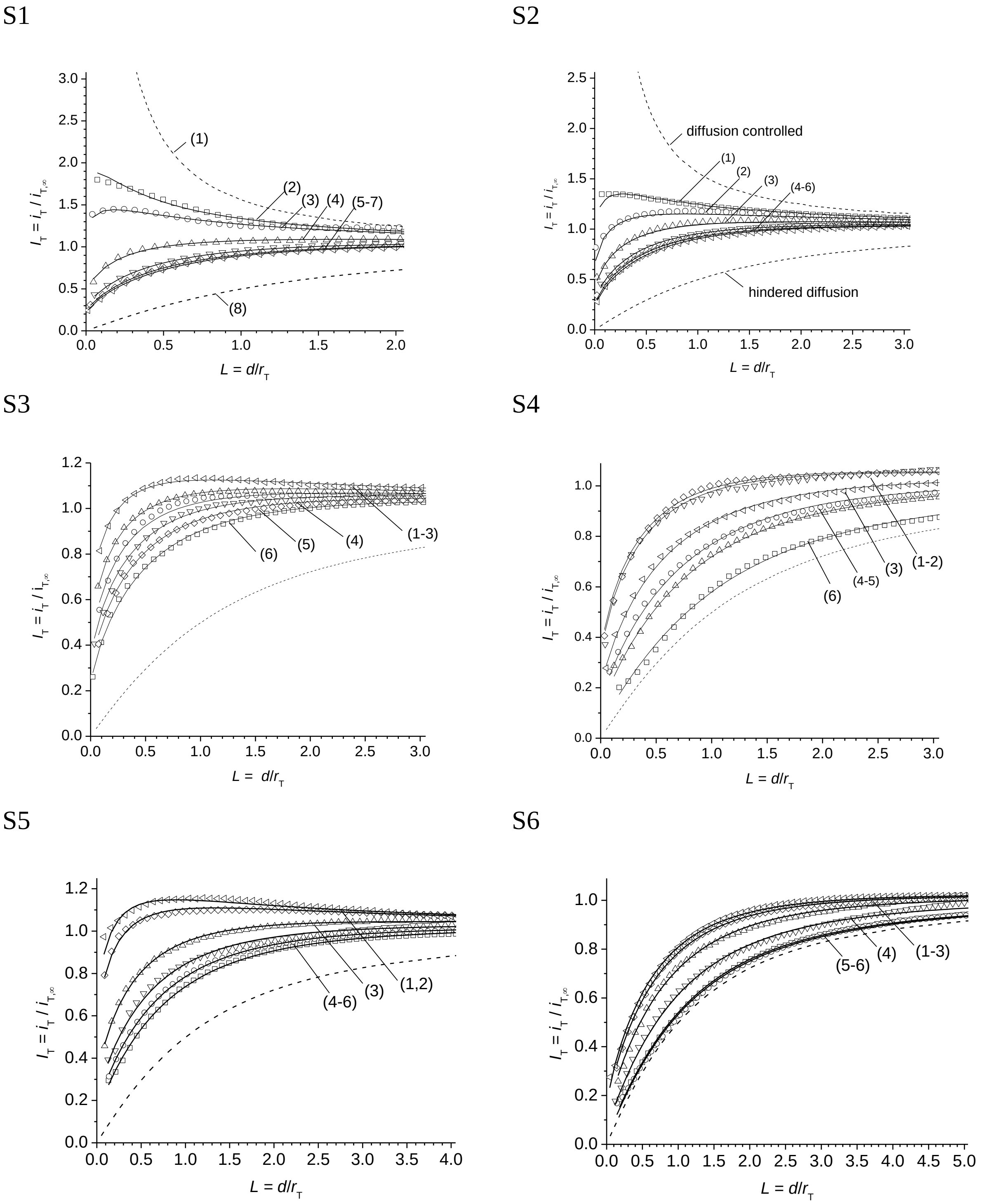

Figure 8.10 Normalized SECM approach curves obtained with Pt UME (r_T = 12.5 μm) on D149/ZnO films in solution containing different $[I_3^-]^*$: (2) 0.057 mM, (3) 0.124 mM, (4) 0.248 mM, (5) 0.687 mM, (6) 1.24 mM and (7) 2.01 mM with E_T = -0.7 V and $J_{h\nu} = 9.1 \times 10^{-9}$ mol cm^{-2} s^{-1}. The summary of κ obtained from the best fits of experimental data (open symbols) to theoretical model (solid lines) were, S1: (2) 2.1, (3) 1.4, (4) 0.5, (5) 0.28, (6) 0.22, (7) 0.206; , S2: (1) 1.18, (2) 0.75, (3) 0.44, (4) 0.285, (5) 0.24, (6) 0.22; S3: (1) 0.66, (2) 0.50, (3) 0.407, (4) 0.34, (5) 0.28, (6) 0.212, S4: (1) 0.40, (2) 0.284, (3) 0.18, (4) 0.093, (5) 0.057, (6) 0.019; S5: (1) 0.74, (2) 0.6, (3) 0.42, (4) 0.276, (5) 0.114, (6) 0.085; S6 (1) 0.131, (2) 0.114, (3) 0.075, (4) 0.03, (5) 0.0083, (6) 0.0064. The top and bottom dashed curves represent responses limited by diffusion-controlled feedback and hindered diffusion, respectively.

8.2.3.2. Approach curves under varied light intensity

The influence of illumination intensity on the kinetics of dye regeneration was studied in the presence of a fixed $[I_3^-]^*$. Figure 8.11 show normalized approach curves acquired above sample S1, S2, S3, S4, S5 and S6 in a solution with $[I_3^-]^* = 0.124$ mM and illuminated at different $J_{h\nu}$. For low intensities κ values for I_3^- regeneration at the surface are very close to the value obtained at the non-illuminated D149/ZnO film, whereas its value increases strongly as the $J_{h\nu}$ is increased. Increasing $J_{h\nu}$ increased κ and hence k_{eff}, which levels off at higher $J_{h\nu}$. A similar behavior was observed for other D149/ZnO electrode. However, in these cases lower overall lower κ were found (except for S2). The summary of $J_{h\nu}$ and k_{eff} values was given in Table 8.5b.

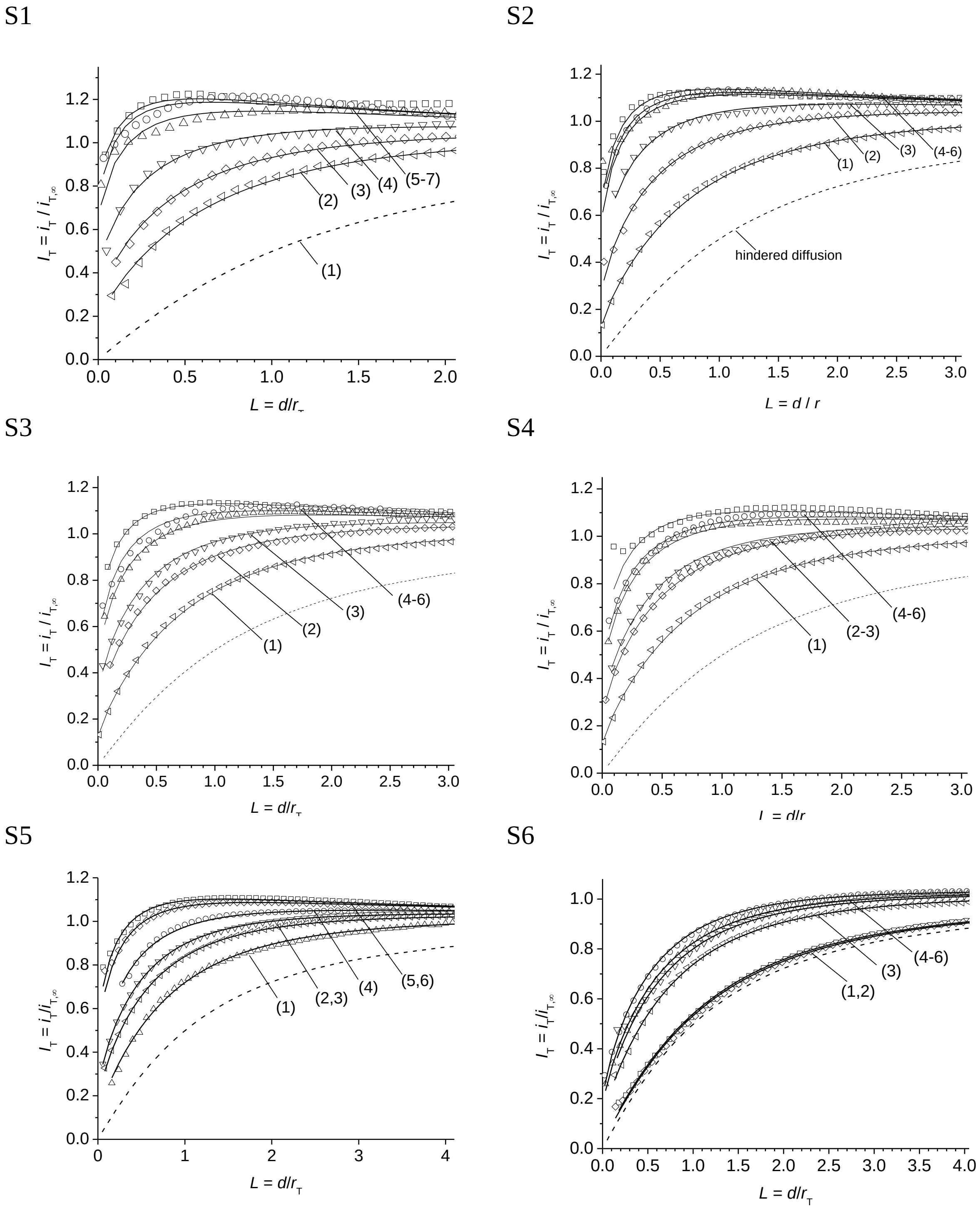

Figure 8.11 Normalized SECM approach curves obtained with Pt UME (r_T = 12.5 µm) on D149/ZnO films of sample S1 with electrolyte containing 0.124 mM I_3^- in acetonitrile-0.1 M TBAS solution with irradiation of different green LED intensities $J_{h\nu}$ (10^{-9} mol cm^2 s^{-1}): (2) 0.982, (3) 1.70, (4) 4.50, (5) 9.10, (6) 15.1 and (7) 25.5, with E_T = -0.7 V. The summary of κ obtained from the best fits of experimental data (open symbols) to the theoretical model (solid lines) were: (2) 0.144, (3) 0.254, (4) 0.435, (5) 0.730, (6) 0.830, (7) 0.900; S2: (1) 0.182, (2) 0.250, (3) 0.430, (4) 0.615, (5) 0.650, (6) 0.700; S3: (1) 0.094, (2) 0.22, (3) 0.301, (4) 0.476, (5) 0.560, (6) 0.680, S4: (1) 0.089, (2) 0.15, (3) 0.218, (4) 0.302, (5) 0.380, (6) 0.450; S5: (1) 0.075, (2) 0.155, (3) 0.211, (4) 0.314, (5) 0.5. (6) 0.57; S6: (1) 0.0064, (2) 0.0083, (3) 0.085, (4) 0.125, (5) 0.143, (6) 0.181. Dashed lines represent response controlled by hindered diffusion.

Table 8.5 Apparent heterogeneous first-order rate constants keff derived from normalized pseudo first order rate constants κ for the reduction of photoexcited D149 by I^- for D149-sensitized ZnO photoelectrochemical electrodes of d and Γ_D. (a) For varying $[I_3^-]^*$ at a fixed $J_{h\nu} = 9.1 \times 10^{-9}$ mol cm^{-2} s^{-1} and (b) for varying $J_{h\nu}$ at fixed $[I_3^-]^* = 0.124$ mM, $D = 1.37 \times 10^{-5}$ cm^2 s^{-1}, $r_T = 12.5$ µm, $RG = 10$, $k_{eff} = \kappa D/r_T$.

(a) For varying $[I_3^-]^*$

$[I_3^-]^*$ / mM	k_{eff} / 10^{-3} cm s^{-1}					
	S1	S2	S3	S4	S5	S6
0.057	23.02	12.93	7.23	4.33	8.11	1.44
0.124	15.34	8.22	5.48	3.11	6.58	1.25
0.248	5.480	4.82	4.46	1.97	4.60	0.822
0.687	3.07	3.12	3.73	1.02	3.02	0.329
1.24	2.41	2.63	3.07	0.621	1.25	0.091
2.01	2.26	2.41	2.32	0.212	0.93	0.070

(b) For varying LED intensity

$J_{h\nu}$ / 10^{-9} mol cm^2 s^{-1}	k_{eff} / 10^{-3} cm s^{-1}					
	S1	S2	S3	S4	S5	S6
25.5	9.86	7.67	7.45	4.93	6.25	1.98
15.1	9.104	7.12	6.14	4.16	5.48	1.57
9.10	8.10	6.74	5.22	3.31	3.44	1.38
4.50	4.77	4.71	3.30	2.39	2.31	0.93
1.70	2.78	2.74	2.41	1.64	1.70	0.091
0.982	1.57	1.99	1.03	0.97	0.822	0.071

8.2.3.3. Analysis of k_{eff} for dye regeneration rate

The parameters k'_{ox} and $\phi_{h\nu}$ can be extracted from fitting experimental k_{eff} to the kinetic model Eq. (8.18). The values of Γ_D were as defined above. Figure 8.12a show the fit of k_{eff} *vs*. $[I_3^-]^*$ and Figure 8.12b show the fit of k_{eff} *vs*. $J_{h\nu}$ for six samples with systematically varied *l* and

Γ_D. For each sample in both plots, the best fit of experimental and theoretical response of $k_{eff}([I_3^-]^*, J_{h\nu})$ yielded the same k'_{ox}. Furthermore, all samples have been fitted with identical $\phi_{h\nu} = 2.91 \times 10^7$ cm^2 mol^{-1}.

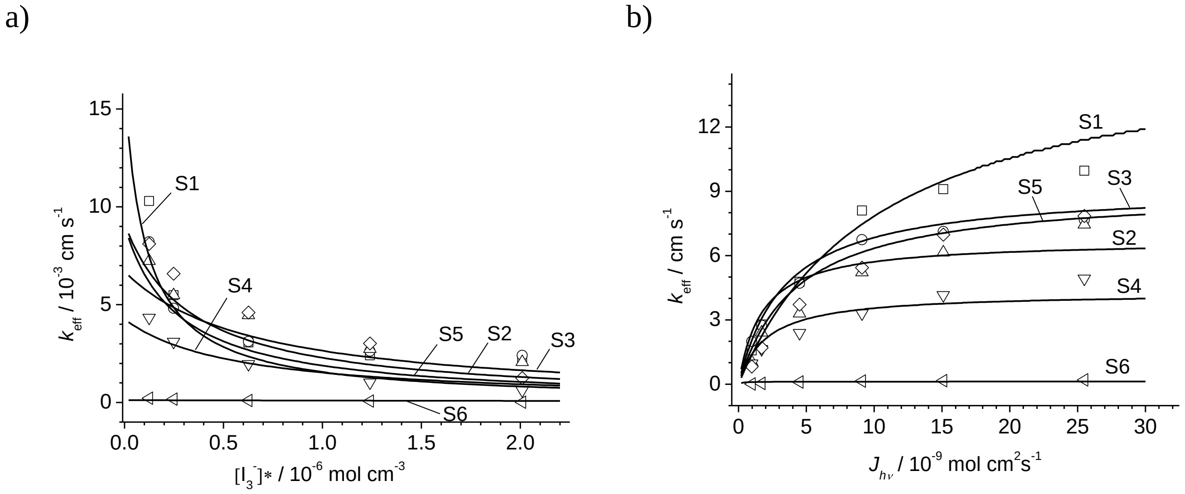

Figure 8.12 Plot of (a) k_{eff} *vs.* $[I_3^-]^*$ and (b) k_{eff} *vs.* $J_{h\nu}$ for six different D149-sensitized ZnO photoelectrodes with systematically varied thickness and dye loading. The corresponding data for $[I_3^-]^*$, $J_{h\nu}$ and k_{eff} were given in Table 8.5. Symbols correspond to experimental k_{eff} data and lines are theoretical fittings of the model described in Eq. (7.16). The best fit of experimental and theoretical $k_{eff}([I_3^-]^*, J_{h\nu})$ yields $\phi_{h\nu}$ value of 2.91×10^7 cm^2 mol^{-1} and k'_{ox} values given in Table 8.7a

The k_{eff} values decrease with increasing $[I_3^-]^*$ and increase with increasing $J_{h\nu}$ as expected by the model. Steady-state plateaus are reached at high values of $[I_3^-]^*$ or $J_{h\nu}$ for all samples investigated. We have also analyzed these data using the kinetic equation of the dye regeneration reaction order 1.5 with respect to $[I^-]$. For this kinetic model consistent values of k'_{ox} and $\phi_{h\nu}$ were found as well, suggesting that either model could empirically describe the feedback approach curve data for dye regeneration. However, in contrast to Eq. (7.16), the kinetic model for the reaction order of 1.5 predicts a decrease of k_{eff} for very low mediator concentrations Figure 8.13. This decrease has never been observed experimentally for mediator concentration as low as 0.06 mM. But this alone may not be a sufficient reason to reject another reaction order because experimental uncertainties in this concentration range might be substantial. A reaction order of 1.5 could occur in porous solids in contact with a fluid phase. Typical example occurs in heterogeneous catalysis if transport in the internal solid is important [267]. In such cases the apparent reaction order is $n_{\mathrm{app}} = 0.5(n_{\mathrm{real}} + 1)$. If the real reaction order n_{real} is one, also the apparent order would be one. If $n_{\mathrm{real}} = 2$, n_{app} would be 1.5.

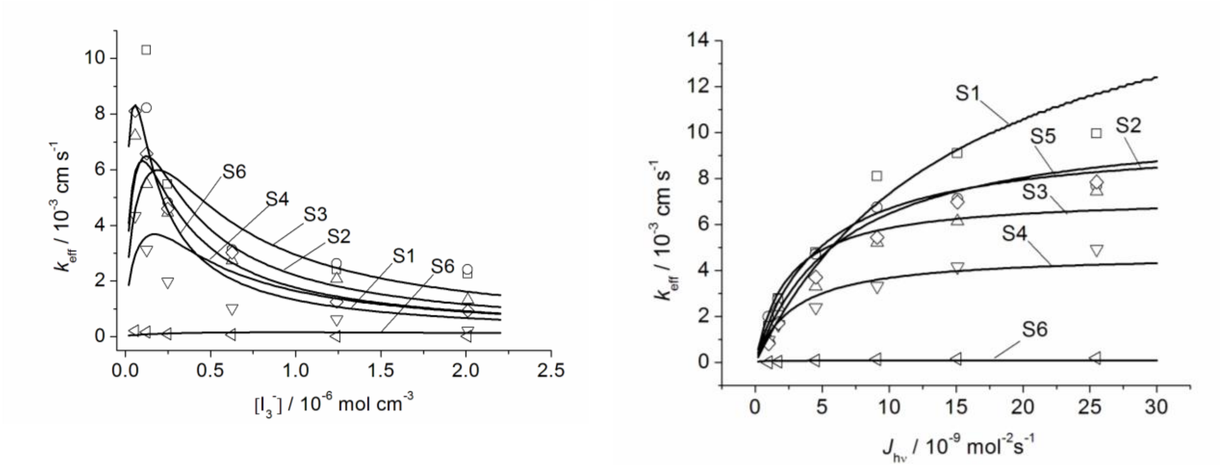

Figure 8.13 Plot of (a) k_{eff} *vs.* $[I_3^-]^*$ and (b) k_{eff} *vs.* $J_{h\nu}$ for six different D149-sensitized ZnO photoelectrodes with systematically varied thickness and dye loading. The corresponding data for $[I_3^-]^*$, $J_{h\nu}$ and k_{eff} were given in Table 8.5. Symbols correspond to experimental k_{eff} data and lines are theoretical fittings of the model described in Eq. (7.16). The best fit of experimental and theoretical $k_{\mathrm{eff}}([I_3^-]^*, J_{h\nu})$ yields $\phi_{h\nu}$ value of 2.29×10^7 $cm^2 mol^{-1}$ and k_{ox} values given in Table 8.6

Table 8.6 The k_{ox} obtained using the D149 regeneration reaction rate law of order 1.5.

Sample	S1	S2	S3	S4	S5	S6
k_{ox}	1.59×10^9	4.65×10^8	2.40×10^8	2.87×10^8	6.45×10^8	2.23×10^7

Furthermore, from Eq. (8.18) it can be seen that $1/k_{\mathrm{eff}}$ should be proportional to the ratio $[I_3^-]^*/J_{h\nu}$ and the intercept of the plot of $1/k_{\mathrm{eff}}$ *vs*. $[I_3^-]^*/J_{h\nu}$ provides a constant from which k'_{ox} can be obtained. It is found that for small ratios of $[I_3^-]^*/J_{h\nu}$ the data are indeed on a line with reasonable scatter. The k'_{ox} of 6.28×10^5 mol^{-1} cm^3 s^{-1} can be obtained for sample S1 from the linear fit of the points positioned on the line (Figure 8.14) and it is in reasonable agreement with the values that found from fitting all data values. For larger ratios of $[I_3^-]^*/J_{hv}$ the results for the variation of $[I_3^-]^*$ and J_{hv} clearly depart from each other. Variation of light intensity seems to follow the linear trend found for small ratios $[I_3^-]^*/J_{h\nu}$, but variation of concentration seems to fall below the expectation of the linear model. It means that we observe a higher rate constant than what one would expect from the initial trend at low $[I_3^-]^*$. Similar trends are observed for other samples.

As confirmed by various fitting procedures, a considerable difference is observed in k'_{ox} values among the six D149/ZnO electrodes of varied Γ_D and l. It is found that k'_{ox} values are negatively correlated to the thickness of the ZnO layers but positively correlated to the total dye content (Table 8.7b). The very simplified model assumes uniform accessibility of the dye molecules with respect to illumination and I^- diffusion. The obtained k'_{ox} values are therefore effective parameters. This would be the real value if all dye molecules would have uniform accessibility for light and mediator. The effective quantities provide consistent descriptions if one electrode is analyzed under different mediator conditions (within the validity range of the model, i.e. at low mediator concentrations (≤ 1 mM) and low $J_{h\nu}$).

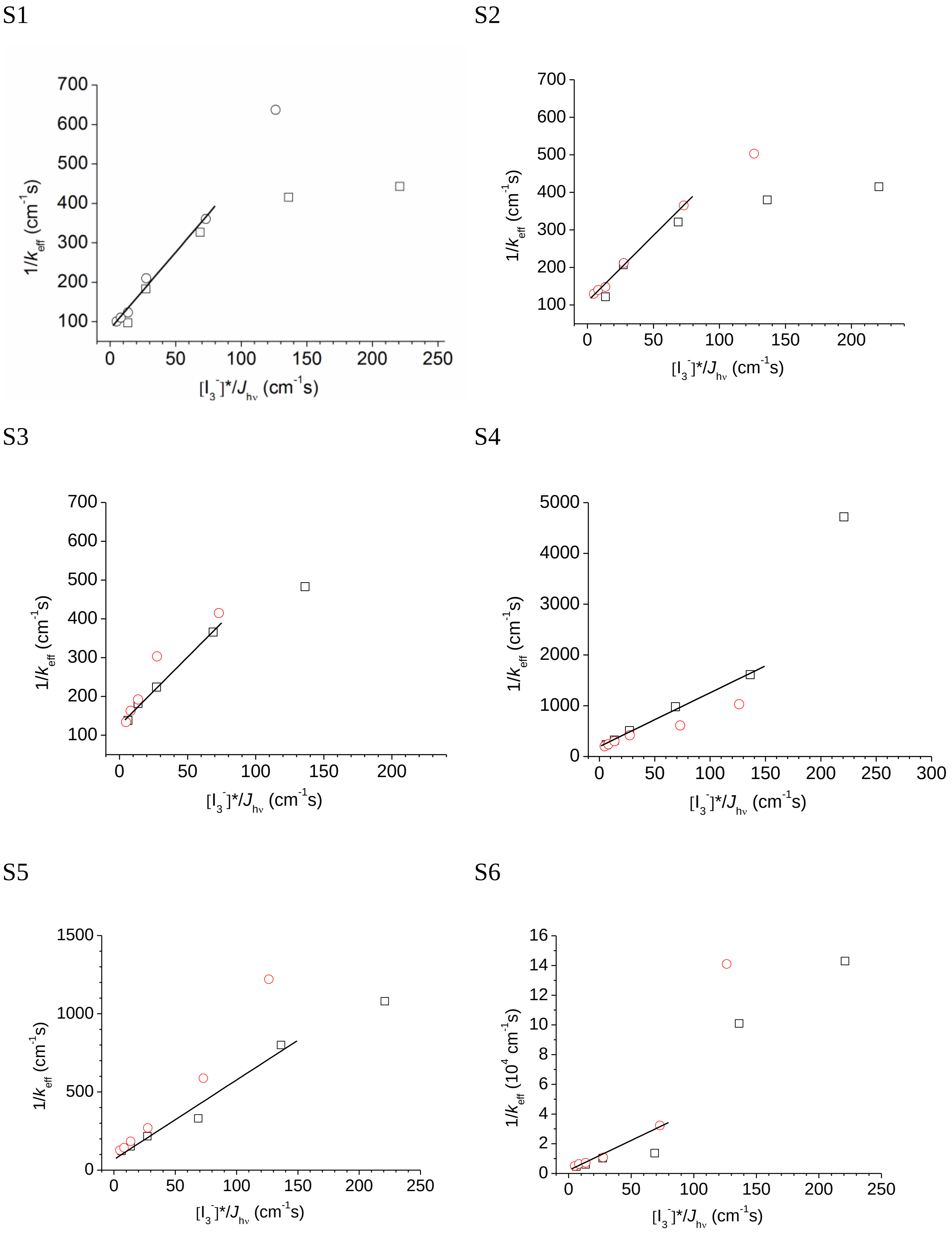

Figure 8.14. Plot of 1/k_{eff} *vs.* [I_3^-]*/$J_{hν}$ for sample S1, S2, S3, S4, S5 and S6 showing a linear fit of the data at lower [I_3^-]*/$J_{hν}$ ratio.

However, when comparing *different* samples, the internal mass transport processes of I^- inside the films become more important with increasing l and the effective k'_{ox} values tend to decrease with increasing electrode thickness as a consequence of the limitations by internal mass transport processes. An analogous behavior for the SECM investigations of immobilized enzymes in multilayer arrangements of intentionally reduced complexity have been seen [268, 269]. The situation in the DSSC is considerably more complex and it is remarkable that a similar conclusion could be drawn here. The other important parameter $\phi_{h\nu}$ came out as constant for all electrodes in our set. This is reasonable because it depends on the extinction coefficient of the dye which can be considered constant even at high packing densities of D149 since only very little spectral broadening was observed for D149 adsorbed on ZnO.

It was found that k'_{ox} shows direct correlation with $\Gamma_D/(p.l_{porous})$ which also correlated directly with J_{sc}. This shows that the distance between the dye molecules is of importance for the dye regeneration. With increasing concentration of D149 molecules, k'_{ox} increases, i.e. the regeneration of oxidized dye molecules is facilitated by hole conduction within adsorbed layers of D149, as also concluded from independent cyclic voltammetry at D149 adsorbed to TiO_2 [265]. The short-circuit photocurrent shows the same increase with Γ_D indicating the dependence on dye regeneration rate. It is concluded that regeneration of the oxidized sensitizer molecules rather than charge transport through the semiconductor matrix is limiting the photocurrent in the present system. Since no influence of the dye concentration on the open circuit photovoltage or the electron lifetime is seen, neither a blocking nor a facilitation of recombination by the dye molecules is detected in the present experiments.

Table 8.7a) Summary of structural parameters, photovoltaic characteristics (J_{sc}, V_{oc}, τ_n) and the effective dye regeneration rate constant (k'_{ox}). (b) Correlation matrix.

a) Cell characteristics

	Structural characteristics								*Functional characteristics*				
Sample	l / [µm]	$l_{blocking}$ / [µm]	l_{porous} / [µm]	p [%]	t_{ads} [min]	Γ_D [10^{-8} mol cm^{-2}]	Γ_D/l_{porous} [10^{-5} mol cm^{-3}]	Γ_D/(p l_{porous}) [10^{-5}mol cm^{-3}]	J_{sc} [mA cm^{-2}]	V_{oc} [V]	τ_n(V= -0.4V) [ms]	k'_{ox} [10^5 mol^{-1} cm^3 s^{-1}]^a	k'_{ox} [10^5 mol^{-1} cm^3 s^{-1}]^b
S1	1.4	0.17	1.2	52	90	1.30	11	20.0	3.3	0.515	22	8.25	6.28
S2	2.8	0.20	2.6	63	120	2.30	8.9	14.0	3.6	0.44	13	2.65	2.64
S3	3.2	0.18	3.0	72	30	3.30	11	15	3.8	0.447	11	1.35	1.61
S4	4.8	0.24	4.6	71	90	1.80	3.9	5.6	2.2	0.463	15	1.58	1.89
S5	2.3	0.19	2.1	61	15	1.80	8.5	14.0	3.2	0.404	9	3.35	5.42
S6	3.1	0.24	2.9	68	60	0.42	1.5	2.2	1.1	0.472	17	0.193	0.756

b) Correlation matrix

l_{porous}			1.00	0.86	0.09	0.18	-0.56	-0.70	-0.38	-0.21	-0.29	-0.73	-0.74
p				1.00	-0.23	0.33	-0.44	-0.66	-0.29	-0.36	-0.50	-0.92	-0.89
t_{ads}					1.00	-0.16	-0.10	0.00	-0.03	0.49	0.54	0.23	-0.06
Γ_D						1.00	0.68	0.47	0.81	-0.41	-0.59	-0.10	-0.08
Γ_D / l_{porous}							1.00	0.96	0.96	-0.06	-0.15	0.60	0.58
Γ_D/(p l_{porous})								1.00	0.88	0.10	0.06	0.79	0.75
J_{sc}									1.00	-0.24	-0.32	0.45	0.47
V_{oc}										1.00	0.97	0.49	0.10
τ_n(V= -0.4V)											1.00	0.55	0.20
k'_{ox} ^{a}												1.00	0.90
k'_{ox} ^{b}													1.00

[a] k'_{ox} values determined by fitting all data values in one set in Figure 8.12 using model Eq. (8.18), [b] k'_{ox} values determined from linear fit in Figure 8.14 using model Eq. (8.18)

In summary, the photovoltaic performance, electron recombination and dye regeneration kinetics by the I^-/I_3^- redox couple, all relevant in dye-sensitized solar cells, were studied depending on film thickness and dye loading of D149-sensitized ZnO photoelectrodes. It was found that the photocurrent increased with the total dye content Γ_D and, even more clearly, with the dye concentration on the inner surface $\Gamma_D/(p \cdot l_{porous})$. Close proximity of the sensitizer molecules seems to assist the photoelectrochemical efficiency rather than decreasing it by radiationless decay in dye aggregates. The photovoltage and the electron lifetime, however, showed no clear correlation to neither Γ_D nor $\Gamma_D/(p \cdot l_{porous})$ suggesting that they are mainly determined by the electronic structure of the semiconductor. k'_{ox} does not depend at all on Γ_D but correlates strongly with $\Gamma_D/(p \cdot l_{porous})$. The result shows that dye regeneration is heavily supported by close proximity of the sensitizer molecules. From SECM feedback approach curve analysis, considerably different effective heterogeneous first order rate constants k'_{ox} for the D149 regeneration are observed among the photoelectrodes of systematically varied thickness and dye loading. Compared to the various reports in the literature, we used very fast and less expensive method to determine the dye regeneration rate.

By systematic variation of film thickness and dye loading, non-uniform accessibility of dye molecules for I^- as well as unequal light intensity reaching dye molecules in different vertical distances from the back contact become more pronounced. The aggregation effects of the dye could be important and the dye loading may influence the tendency for recombination. The strong scattering in the films make a description of the local light intensity difficult. In addition it turned out to be challenging to prepare films in which only one parameter is changed while all other structural parameters are kept constant. Furthermore, gradients in dye concentration across the film thickness cannot be excluded because even after long adsorption times, the dye loading still seems to increase for a given material thickness. Furthermore, surface effects (ion absorption, Donnan exclusion) not considered in the model may influence the response. Adsorption or association of negatively charged ions within the pores in ZnO or at the dye molecules may hinder the access of negatively charged I^- into the pores (see Section 8.1). The extent of this effect will depend on the mediator concentration but also on the pore diameter that seems to vary between the preparations.

9. SECM chronoamperometric measurements of the dye regeneration

This Chapter describes SECM transient measurements at DSSC in I^-/I_3^- electrolytes by monitoring current transients at the SECM probe positioned at a known distance above the N719/TiO_2 film while the incident light was switched on-off.

9.1. SECM transients at UME with switched light illumination

The UME positioned at a known distance (e.g. 3 µm) above the N719/TiO_2 film allows monitoring directly the I_3^- production or I^- consumption by photo-oxidized dye D^+ on DSSC. We investigated the transient (chronoamperometric) response at UME for the dye regeneration using SECM in the FB, substrate-generation/tip-collection (SG-TC) and redox competition (RC) modes. The reaction schemes for the SECM working modes in DSSCs are shown in Figure 9.1a, Figure 9.2a and Figure 9.3a along with measured SECM transients Figure 9.1b, Figure 9.2b and Figure 9.3b, respectively. For all transient measurements, the irradiation intensity from the green LED light source was kept at 25.5×10^{-9} mol cm^{-2} s^{-1}, since optimal photo-oxidation of the dye molecules was observed at this intensity. Note that Figure 9.1b, Figure 9.2b and Figure 9.3b show only representative transients, where the change in i_T was monitored by periodically blocking the light path to the sample. The time at which the light was switched on and off is indicated by arrows.

In the case of FB mode, the electrolyte contained only I_3^- as the redox active species (Figure 9.1a). In this case, the resulting transients $i_T(t)$ rise to a maximum when the light is switched on and during irradiation the i_T decays approximately exponentially for about 10 s, before it attains a steady-state value (Figure 9.1b). The UME tip was biased at -0.7 V thereby it continuously reduces I_3^- to I^-, while light switched on and off. In the dark, the UME generated I^- can diffuse and accumulate in porous nanoparticulate film. When the light is suddenly switched on a maximum i_T was observed due to the high flux of I_3^- emitting from the reduction of D^+ by the accumulated I^-. A slow decay to steady-state during irradiation show that accumulated I^- is depleted inside the film. Dye regeneration depends then on I^- coming from the UME to the region of the film directly below UME. When the irradiation is switched off, i_T returns to its initial value with approximately the same rate as for the off-on change of illumination (Figure 9.1b), again indicating the process is significantly controlled by internal diffusion. The steady-state i_T is reproducible and induced repeatedly under several on-off cycles, implying that N719-sensitizer regeneration is fairly regular.

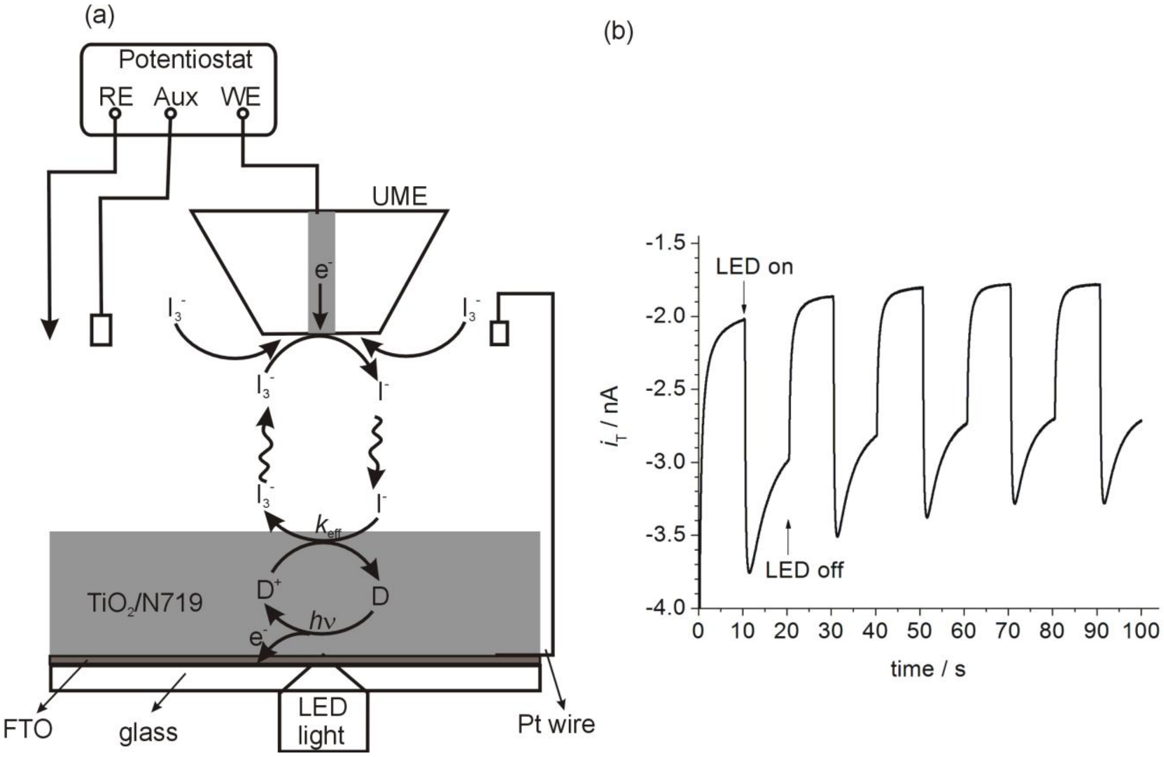

Figure 9.1 (a) A scheme of the SECM feedback mode measurement above N719/TiO_2 surface. The distance between the UME and the DSSC is exaggerated to show the reaction. The real distance d is smaller than the UME radius thereby establishing a thin layer. (b) The corresponding amperometric current-time transients for the dye regeneration rate in a solution containing 0.94 mM $[I_3^-]$ in 0.1M LiTFS-acetonitrile with r_T = 12.5 µm, d = 3 µm and switching green LED on and off.

In the SG-TC mode, the electrolyte initially contained exclusively I^- (Figure 9.2a). Other conditions were the same as for FB mode experiment in Figure 9.2a. This experiment was directed at detection of I_3^- generated by the illuminated dye-sensitized film. When the substrate was not illuminated, only background UME currents (below 10 pA) were observed. As soon as the substrate was illuminated, i_T rose to its steady-state value, confirming the oxidation of I^- by the photo-oxidized dye D^+ on the substrate surface generating I_3^- that is subsequently detected at the UME by oxidation. The small decrease of the UME current after the peak is caused by diffusional shielding of the UME. If I^- is exhausted in the small gap between the UME (including its insulating sheath), I^- has to diffuse to the DSSC because not all I_3^- coming from the sample reaches the UME where it could be regenerated. This diffusional process is hindered. It has been calculated for irreversible reactions at the sample and the probe in similar electrode geometries [270]. The irradiation lasted for about 100 s resulting in fairly constant i_T. When the light is switched off, $i_T(t)$ returned to its initial value. The rate of decrease is rather slow and clearly longer than the diffusion time between tip and sample. This is not surprising because above the entire illuminated area (that is much larger than the active UME area) a macroscopic diffusion layer is formed in which I^- is depleted. After stopping photo-oxidation it takes several seconds until I^- is resupplied by diffusion from the solution bulk.

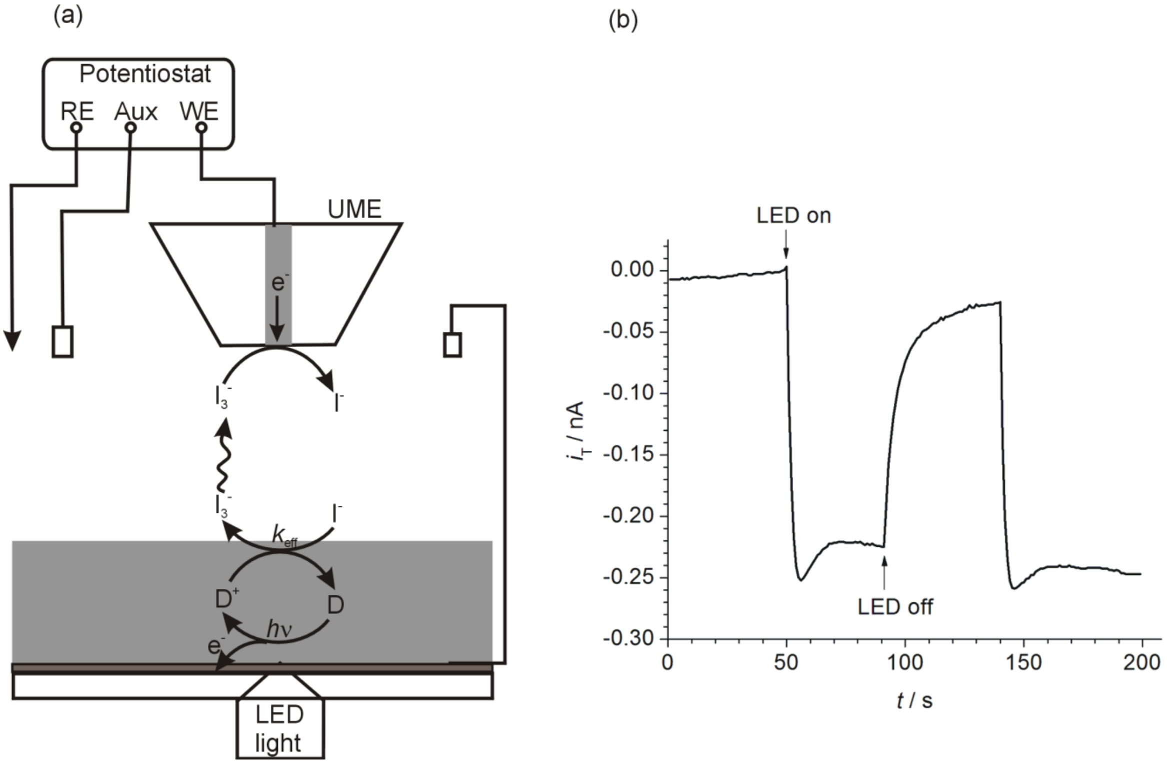

Figure 9.2 (a) A scheme of the SECM SG-TC mode measurement above N719/TiO$_2$ surface. (b) The corresponding amperometric current-time transients for the dye regeneration rate in a solution containing 1 mM [I$^-$] in 0.1M LiTFS-acetonitrile. Other conditions are the same as in Figure 9.2.

In addition, the transients were also recorded for the RC mode under conditions identical to those used for the SG-TC mode (Figure 9.3a), except for UME potential E_T = 0.25 V, which was set to oxidize I^- to I_3^-. In this mode, if the cell is under illumination, both the UME and substrate compete for I^-. In the dark only the UME oxidizes I^-. After the UME current reached a steady state value (hindered diffusion) in the dark, the light was switched on. A significant decrease of the UME current was recorded due to depletion of I^- by the illuminated DSSC. The i_T transient needed rather long times to attain a steady state value and no overshot is observed because the solution volume under the UME is constantly depleted from I^- and cannot accumulate in the film. Also the return to the steady-state UME response in the dark took longer because in this mode a macroscopic diffusion layer is formed above the sample similar to the GC mode.

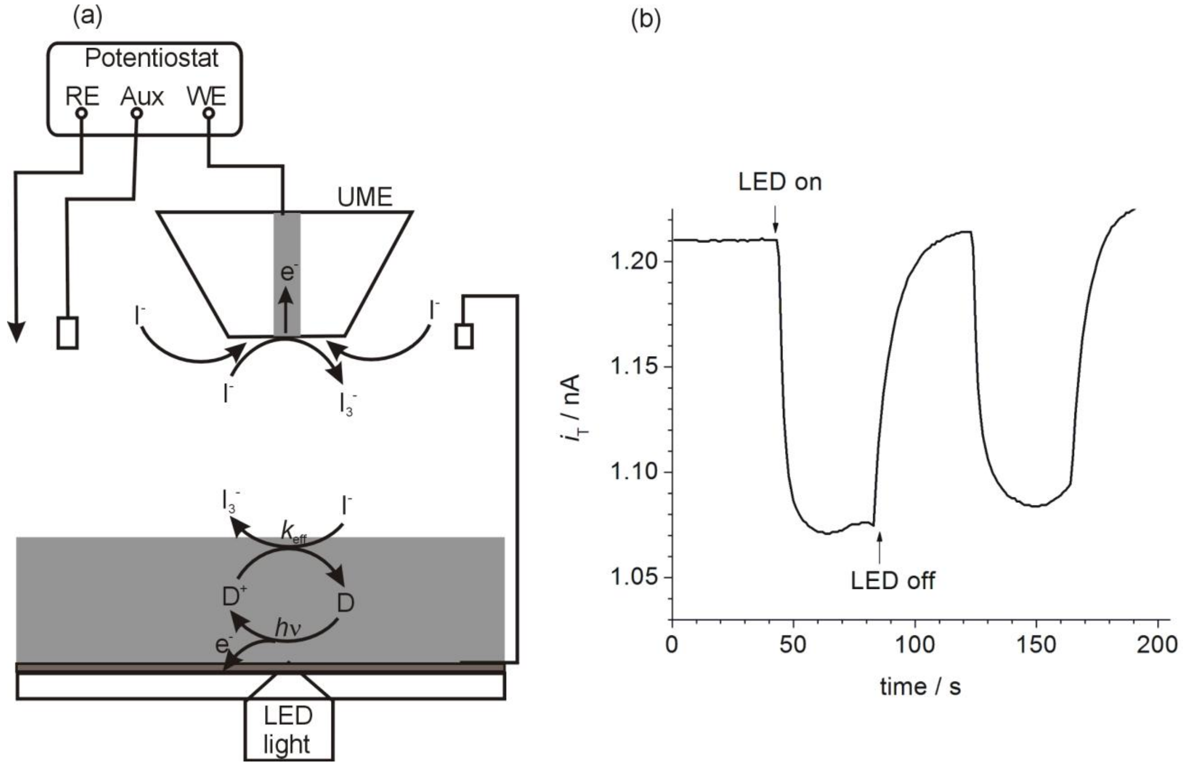

Figure 9.3 (a) A scheme of the SECM RC mode measurement above N719/TiO_2 surface. (b) The corresponding amperometric current-time transients for the dye regeneration rate in a solution containing 0.43 mM [I^-] in 0.1M LiTFS-acetonitrile. Other conditions are the same as in Figure 9.2.

The transient SECM measurements for photo-oxidized dye regeneration by I^-/I_3^- with three different working modes of SECM showed that the change in i_T with switched light illumination is very consistent. However, relatively longer reaction times compared to conventional pulse experiments on DSSC could account for the limitation of mass transport and internal diffusion through the film. As this method does not require the assembly of complete DSSC and can be carried out in shorter measurement time on materials with graded composition and structure, it can be used as a best approach for screening of dyes and electrolytes in DSSC research.

9.2. Current response at UME following switched light on N719/TiO$_2$ film

To examine the depletion rate of photo-oxidized dyes, a series of chronoamperometric measurements at the UME were carried out in the dark after switching off irradiation ($J_{h\nu}$ = 25.5 × 10^{-9} mol cm^{-2} s^{-1}) on N719/TiO$_2$ electrode for different intervals (5, 10, 15 and 20 s). A 25 µm diameter UME placed 3 µm above N719/TiO$_2$ surface in a solution contained 0.94 mM [I_3^-] dissolved in acetonitrile electrolyte. After each irradiation interval, E_T was stepped from 0V to -0.7 V and $i_T(t)$ was monitored (Figure 9.4a). Initially, $i_T(t)$ in the dark above N719/TiO$_2$ film was recorded to see the effect of pure hindered mediator diffusion towards the UME (Figure 9.4b, curve 1). Figure 9.4b, curves 2-5 represent $i_T(t)$ responses after applying light pulses on the substrate for 5, 10, 15 and 20 s, respectively. When the electrode is irradiated in an electrolyte containing I_3^- only, D is photo-oxidized to D$^+$, but there is no mediator to recycle D$^+$ to D because the UME is kept at a sufficiently positive potential so that I_3^- is not reduced. Thus, D$^+$ is accumulated on the substrate provided that there are no degrading mechanisms due to desorption or chemical decomposition of the oxidized dye. When the light is switched off, E_T is switched to a negative value so that I_3^- is reduced to I^- at the UME. Then, I^- diffuse toward the N719/TiO$_2$ electrode and slowly regenerate the dye. This creates a feedback effect which results in higher i_T than measured in the dark experiment under otherwise identical condition. For the light pulse of 5 s all the D$^+$ formed underneath the UME is regenerated during the 5 s potential pulse and the transient merges with the dark experiment after 4 s (Figure 9.4b, curves 1 and 2). For longer light pulses, the amount of D$^+$ cannot be regenerated during the potential pulse and i_T reaches a plateau of about -3.3 nA for the 10 s illumination period, the current starts to decrease to deviate from this plateau towards the end of the potential pulse. The electrical charge Q used to photo-oxidize N719 dye at the surface was obtained by integrating the current difference between the first pulse prior to any illumination and the subsequent pulses after illuminations. The total charge calculated from each potential pulse after 5 s, 10 s, 15 s and 20 s illumination are 1.6 nC, 4.6 nC, 5.2 nC and 5.7 nC, respectively. The charge is almost tripled for 10 s illumination as compared to 5 s. For longer illumination time this decrease is not observed within the time frame of the chronoamperogramm.

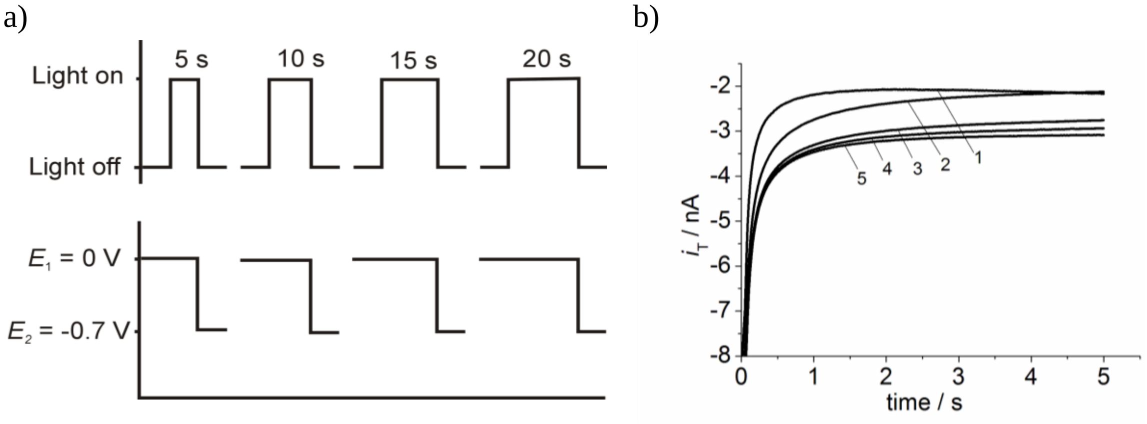

Figure 9.4 Schematic of light and potential pulses. (b) Chronoamperograms acquired in the dark (curve 1) and after light illumination of 5 s, 10 s, 15 s and 20 s (curves 2-5); *d* = 3 µm.

From transient measurements the surface concentration of the photo-oxidized dye Γ_{D^+} can be estimated assuming the sample region that is affected by the dye regeneration A = πr_s^2. The r_S can be approximated by considering the average diffusion length of the I^- generated at the UME within the pulse time $\tau = d^2/2D$ [271]. The modified radius r_S of the sample is given by[272]:

$$r_S = (2D\tau - d^2) \tag{9.1}$$

D is the diffusion coefficient of I^- and *d* is the distance of UME from the surface. In order to calculate the surface concentration of the photo-oxidized dye Γ_{D^+} from the total charge *Q*, Eq. (9.2) can be applied [272]:

$$\Gamma_{\mathrm{D}^+} = Q/(nF\pi r_S^2) \tag{9.2}$$

Given $D = 1.37 \times 10^{5}$ cm^{2} s^{-1}, $d = 3$ µm and the N719 dye surface concentration as determined from independent experiment $\Gamma_{\mathrm{D}} = 6.3 \times 10^{-8}$ mol cm^{-2}. The estimation $\Gamma_{\mathrm{D^+}}$ according to Eq. (9.1) and Eq. (9.2) leads to value of 5.15×10^{-11} mol cm^{-2} to 8.32×10^{-11} mol cm^{-2} (Table 9.1). Considering roughly 1/1000 of the dye surface concentration is expected to be in oxidized state [14], the $\Gamma_{\mathrm{D^+}}$ values are in good agreement with N719 dye surface concentration $\Gamma_{\mathrm{D}} = 6.3 \times 10^{-8}$ mol cm^{-2} as determined from UV-Vis spectroscopy. This confirms that the principle of the method is reasonable.

Table 9.1. Calculation of the surface concentration of the photo-oxidized N719 dye from four independent SECM pulse experiments. For all experiments $r_{\mathrm{T}} = 12.5$ µm, $d = 3$ µm, $D = 1.37 \times 10^{5}$ cm^{2} s^{-1}

Pulse time / s	Q /10^{-9} As	r_{S} / cm	$\Gamma_{\mathrm{D^+}}$ / 10^{-11} mol cm^{-2}
5	1.6	0.00675	5.79
10	4.6	0.00955	8.32
15	5.2	0.01170	6.27
20	5.7	0.01351	5.15

In summary, the method seems to be ideally suited to determine the dye surface concentration. Quantifying the dye content is essential for the improvement of nanocrystalline networks film and the suggested method provides straight forward prediction of its optimum concentration.

10. Quantitative characterization of shear force regulation for SECM

In this Chapter, quantitative details of shear force detection distance for SECM was explored and selected applications in the simultaneous imaging of topography and reactivity was provided. Part of this Chapter was reported in own publications [A3] and [A7].

10.1. Characterization of Pt nanoelectrodes

The shape of the microelectrodes can be determined by scanning electron microscopy (SEM). According to a procedure by Arimoto et al [273], the ultramicroelectrode was wetted by a room temperature ionic liquid (RTIL, 1-ethyl-3-methylimidazolium bis(trifluoromethyl) imide) to provide conductivity for imaging the composite of the wire inside an insulating quartz glass matrix. This avoids the use of gold or carbon sputtering that would otherwise modify the electrode. Figure 10.1a, b and c show SEM images of the prepared nanoelectrodes. A very smooth Pt nanodisk located at the center of the probe suggests the successfulness of the method used. The diameters of the glass shield r_{glass} and of the active electrode tip r_{T}, and $RG = r_{\text{glass}}/r_{\text{T}}$ of the three nanoelectrodes are given in Table 10.1.

To verify the functioning and stability of probe electrodes over sufficiently long time, steady-state cyclic voltammetry was carried out in aqueous solution of 4 mM $[\text{Ru(NH}_3)_6]^{3+}$ + 0.1 M KNO_3. The cyclic voltammograms (CVs) obtained are shown in Figure 10.1d. Sigmoidal CVs were obtained. The measured diffusion-limited steady-state UME currents showed stable and consistent values over a repeated cycling. The diffusion-limited steady-state current allows determination of probe geometry and size.

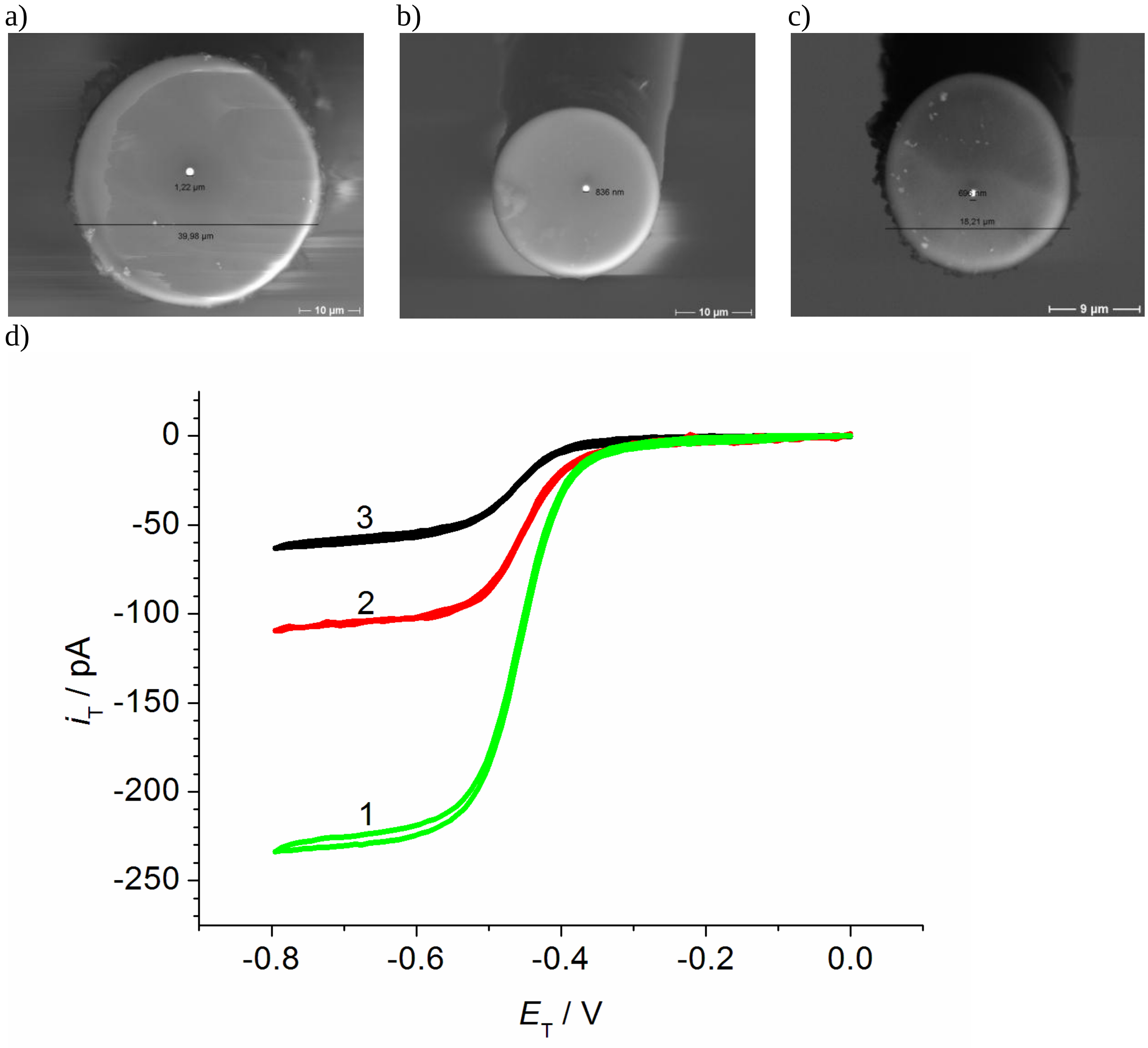

Figure 10.1 SEM image of a shear force SECM probe tip made from a laser pulled quartz glass capillary with a Pt wire inside. A typical steady state CV response of a Pt nanoelectrode probe in a solution of 4 mM $[Ru(NH_3)_6]^{3+}$ and 0.1 M KNO_3. CV 1 corresponds to UME a, CV 2 to UME b, CV 3 UME c.

Table 10.1. The r_{glass}, r_T and *RG* of nanoelectrodes as determined from SEM and calculate from the steady state cyclic voltammograms.

Electrode	r_{glass} / µm $^{(1)}$	r_T / nm $^{(1)}$	r_T / nm $^{(2)}$	$RG = r_{glass}/r_T$ $^{(1)}$
a	20	610	206	32
b	11	418	96	26
c	9	348	53	25

$^{(1)}$ from SEM image. $^{(2)}$ from $r_T = i_{T,\infty}/4nFDc^*$

The electrode radius can be computed from the diffusion-limited UME tip-currents using the equation, $r_T = i_{T,\infty}/4FDc^*$, where $D = 7.4 \times 10^{-6}$ cm^2 s^{-1} is the diffusion coefficient of $[Ru(NH_3)_6]^{3+}$ measured from chronoamperometry in the electrolyte used, F is Faraday's constant and $c^* = 4 \times 10^{-6}$ mol cm^{-3} is the bulk concentration of $[Ru(NH_3)_6]^{3+}$. For smaller probes, the calculated and optically determined dimension can deviate very significantly. This might be due to slightly recessed electrodes often obtained by pulling or polishing. This would lead to an r_T smaller than measured microscopically. On the other hand small metal structures sealed in insulating matrices appear larger in SECM due to charging effects. Although the use of an ionic liquid limits this effect, it is still present here.

10.2. Characterization of UME vibration properties

The vibration spectra of an oscillating nanoelectrode between 100 kHz and 300 kHz is shown in Figure 10.2 and was recorded at the applied potential of 2 V in solution with a piezo-stimulator and detector fastened to the UME body at 45^o. To determine the detected frequency of a probe oscillation, the mechanical resonance frequency was recorded with the shear force regulation software for the probe at different position from the surface. Figure 10.2 shows an example of the spectra where amplitude changes indicated by arrows are seen. Note that for a given probe electrode more than one detected frequencies could be realized but the selection of the suitable frequency was made based on its sensitivity in surface tracking during topography scans. The most sensitive frequencies are characterized by minimum noise signal in topographic line scan.

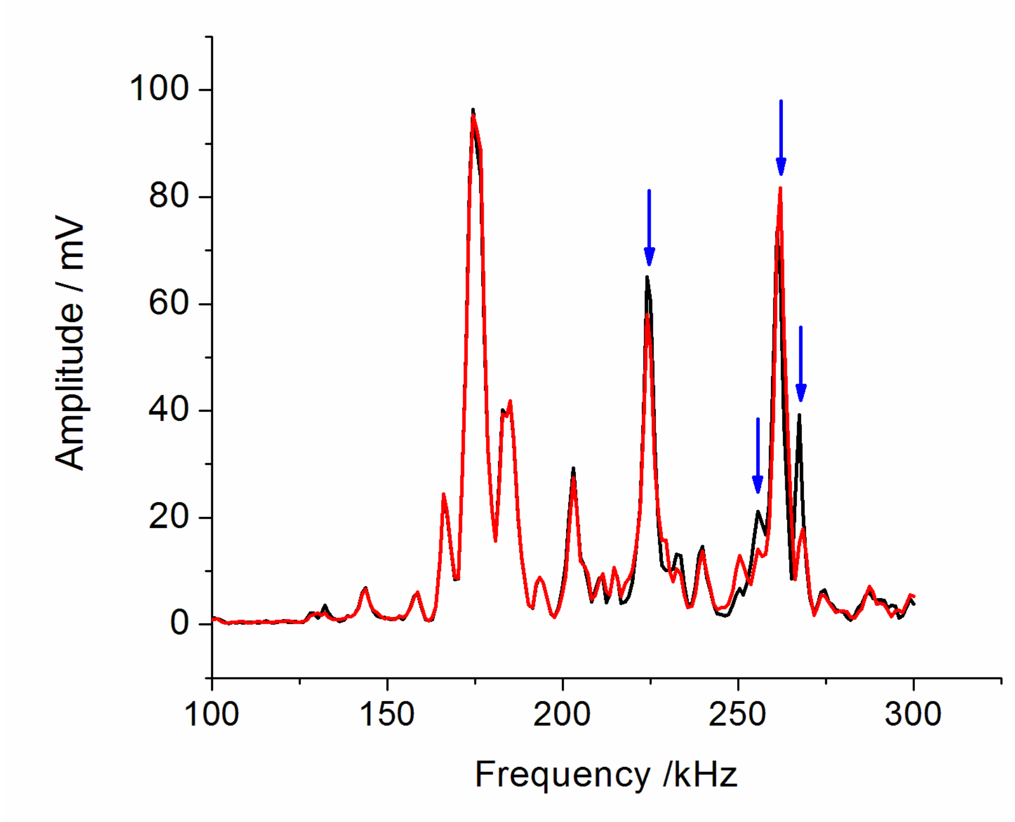

Figure 10.2. Resonance frequency spectra of the non-optical shear force detection output acquired for the nanoelectrode in solution 50 µm away from surface (black line) and closest to the surface (red curve). The arrows are suitable frequencies.

By comparing the amplitude damping at different positions, the electrode is excited at one of the detected frequencies. Figure 10.3 depicts a typical amplitude change as a function of probe-substrate separation. The approach of the probe is made with the stepper motor (having the vertical position z_1), while the distance control feedback loop at the DS4L is on.

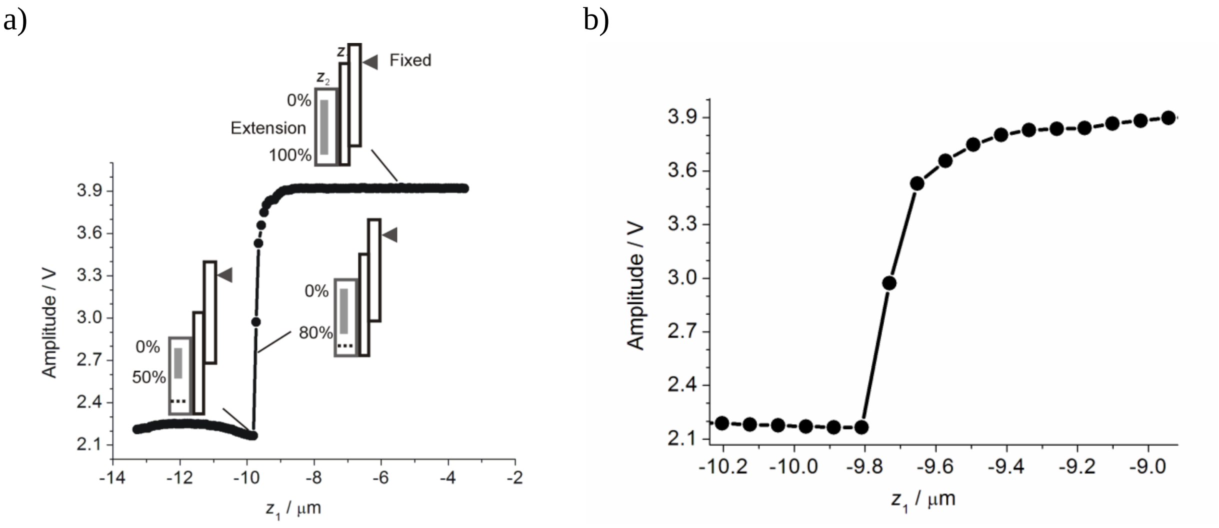

Figure 10.3. a) Amplitude change of the oscillating probe as a function of the stepper motor displacement. b) Expanded view of the region of amplitude change in (a). Parameters: detected frequency = 270 kHz, speed = 0.2 µm s^{-1}, step size = 0.1 µm.

This leads to a movement of the piezo motor (having the vertical position z_2) to the most extended position as long as the surface is not found. As the stepper motor brings the vibrating probe within about 1 µm of the sample surface, damping of the vibration is detected and the piezo motor retracts while the stepper motor is still moving towards the sample ($\Delta z_1 = -\Delta z_2$). The movement is interrupted by the user if the piezo is approximately at the midpoint of its movement range. The subsequent lateral scans are made with a fixed position z_1 of the *z*-stepper motor leaving the *z*-piezo motor to maintain a constant distance over tilted and rough samples by changing z_2.

Evaluating the amplitude and/or phase change provides the input for a distance control system. The amplitude and phase signals can be displayed on an oscilloscope which is a useful control for the correct operation of the system (Figure 10.4). If the UME is far away from the surface, the amplitude and phase signal appeared as noisy and irregular (Figure 10.4a). When the probe touches the surface, the oscilloscope signal gets deformed (Figure 10.4b). If the probe is at the shear-force detection limit, the amplitude and phase signal are constant with spikes representing the error signal to which the distance regulation feedback loop is responding (Figure 10.4c, d). The deviation from the set-point is immediately counteracted. The fast response of the signal is a pre-requisite to achieve sufficiently high lateral scan rates while maintaining distance regulation.

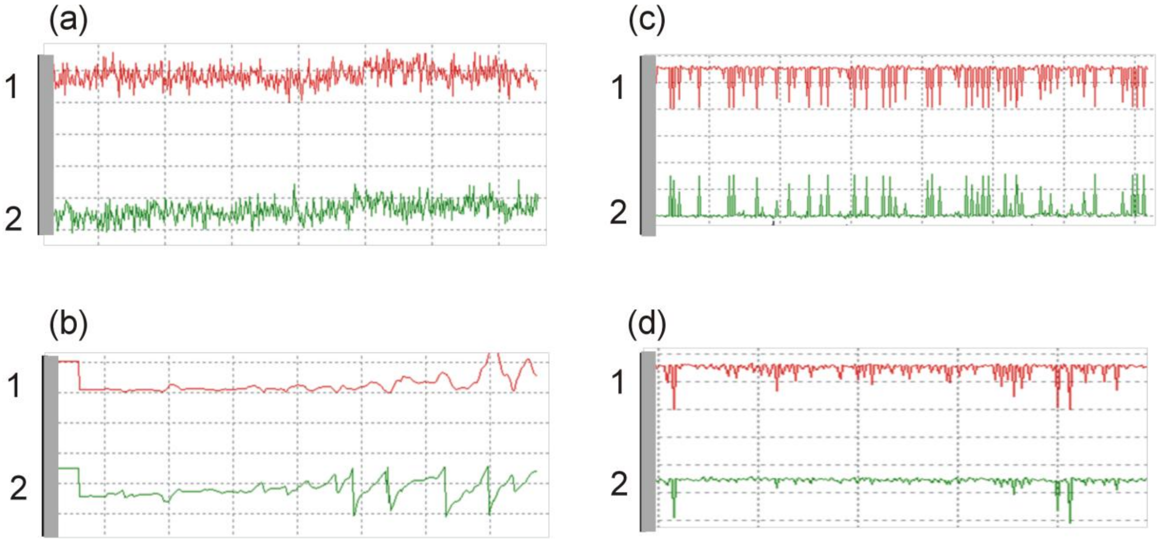

Figure 10.4. Oscilloscope output from shear force system for probe-substrate distance control. (1) Amplitude (mV) (red) and (2) phase (^{o}) (green) at the resonance frequency of the microelectrode recorded when the UME is immersed in solution and (a) far away (>700 nm) from the substrate (b) UME touching the surface, (c) and (d) when the UME is in the proximity of the substrate (500 nm-700 nm). Parameters of vibration: detected frequency = 270 kHz, amplitude = 370 mV.

Setting a pre-defined distance can be done in the following way. The electrode is approached with the shear force regulation switched-on until the surface is found. The positions $z_{1,0}$ and $z_{2,0}$ are recorded. Then the shear force regulation is switched off by setting the integral gain k_i to zero in the SXM software. Either with the stepper motor (nominal resolution 50 nm) or the piezo actuator the electrode is retracted to the desired distance. For instance in order to initiate the recording of an approach curve that starts within a reasonable distance from the surface (i.e. 15 r_T). The shear force distance regulation is switched-on again by setting k_i to values in the optimum range of 200-250. This range has been empirically determined. At too low k_i the surface is not followed accurately, while too high k_i leads to strong noise in topographical data. To separate such noise from topographical features we always record forward and backward scans as in conventional scanning force microscopy. It can then be observed at which distance from the surface (taken at the position $z_{1,0} + z_{2,0}$) the distance regulation will maintain the electrode position for a given set-point. The set-point is given as ratio of the amplitude to the amplitude in solution (optimum range 90-98 %). Several experiments showed that a stable distance regulation indicated by an oscilloscope response as in Figure 10.4c, d is obtained only in a narrow *absolute* distance range of 500-700 nm. This has important implications for the size of the active electrode area r_T that can be used with this shear force system.

The vibration of the microelectrode has a clear influence on the current response. We observe that $i_{T,\infty}$ increases under vibration and the increase of the vibration is changing from electrode to electrode as well as between different mountings of the same electrode. This is expected as the amplitude at the end of the probe varies with frequency, excitation amplitude (selected to obtain optimized response of the distance regulation, typically 350 mV). When normalizing approach curves of the same probe electrode with and without vibrations, small differences remain between the two curves indicating that qualitative imaging is well possible but quantitative studies are discouraged.

10.3. Examples of simultaneous topographic and reactivity imaging

10.3.1. Gold microstructures on a glass substrate

In order to demonstrate the imaging capability a shear force system developed in this thesis, the topography and electrochemical reactivity of gold micro bands on a glass substrate was imaged in aqueous solution of 4 mM $[Ru(NH_3)_6]Cl_3$ in 0.1 M KNO_3 (Figure 10.5). The potential of the nanoelectrode was -0.6 V (Ag-QRE). From the topography image, the height and width of gold structures was found to be 180 nm and 50 µm, respectively (Figure 10.5b), which is in a good agreement with CLSM data (Figure 10.5a). When the nanoelectrode moved above the gold band, the current signal increased due to positive feedback resulting from redox cycling (Figure 10.5b). The currents in normalized quantities changes from I_T = 0.8 over glass to I_T = 2.3 over gold bands (Figure 10.5b). With $i_{T,\infty}$ = -130 nA, this corresponds to i_T = -100 pA over glass and i_T = -300 pA over gold. A two dimensional scan shows that the tilt seen in the topographic image (Figure 10.5c) is compensated (Figure 10.5d) and that fine structures in the topography as well as the current response are visible.

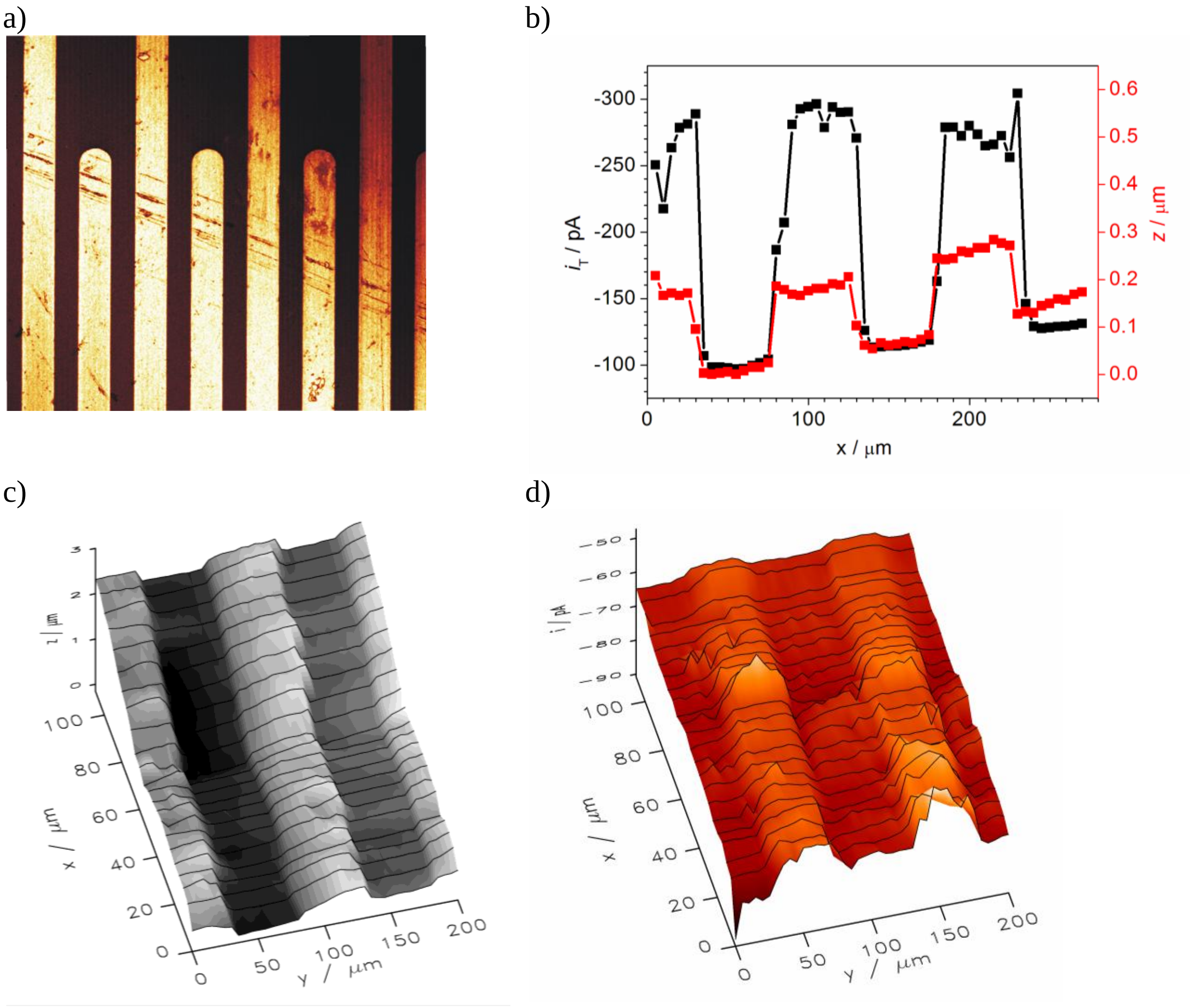

Figure 10.5 a) CLSM image. (b) line scan of topography and reactivity simultaneously, (c) topography image and (d) SECM feedback image with the shear-force mode. Working solution: 4 mM $[Ru(NH_3)_6]Cl_3$ + 0.1 M KNO_3; E_T = -0.6 V (vs. Ag QRE), scan rate 20 µm s^{-1}, step size 5 µm. r_T = 350 nm, amplitude = 370 mV, used frequency =270 kHz.

10.3.2. Platinum interdigitated array printed on ceramic materials

Figure 10.6a CLSM topographic image of Pt interdigitated array printed on ceramic materials. Figure 10.6b is a SECM-shear force line scan for both topography and reactivity simultaneously. Figure 10.6c and d shows the topographic and reactivity image obtained simultaneously. The analysis of the SECM-shear force topographic responses shows the height 1 µm and width 46 µm for the Pt structures on the surface, which is in agreement with the data obtained from the supplier. The sample was maintained intentionally tilted to proof the concept outlined in Section 4.5. The tilt effect is clearly visualized in topography scan, while the current response remained reproducible over different region on the surface of scanned area. Higher i_T was observed over Pt structure due to positive feedback back effect whereas i_T becomes reduced over ceramic layer due to hindered diffusion effect. Small spike like features were noticed in the current response which were absent in topographic image. These are characteristic for defects in Pt coating or the presence of impurities in material surface, at least in the resolution scale of the probe used in this experiment. However, appropriate description of this observation requires the knowledge of the exact material composition of the surface. As this sample was received from Industry to test the working principle of instrument, details about the sample should remain confidential.

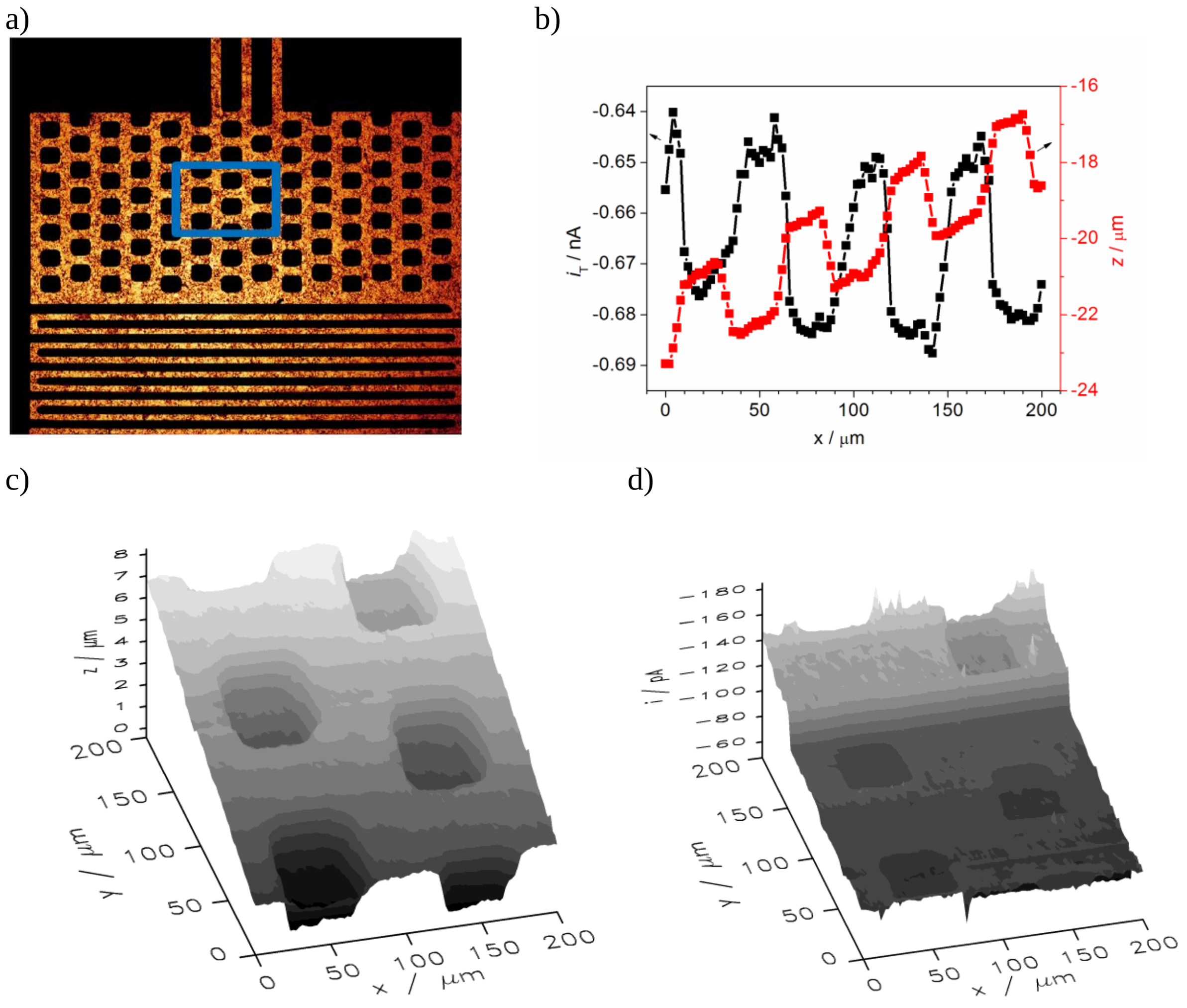

Figure 10.6 (a) CLSM image of a Pt-microstructure on ceramic material. (b) Topography and reactivity line scan obtained simultaneously. (c) topographic and (d) reactivity images recorded simultaneously with shear force distance regulated SECM. Working solution: 4 mM $Ru(NH_3)_6Cl_3$ + 0.1 M KNO_3; E_T = -0.6 V, translation rate 25 µm s^{-1}, step size 5 µm, r_T = 300 nm

10.3.3. Sintered gold tracks on polyimide films

The electrochemical reactivity of the sintered gold tracks was investigated using shear force SECM in the feedback mode [A3]. A nanoelectrode was scanned in a constant distance over the sample comprising two recessed gold tracks. The topography and the electrochemical reactivity were recorded simultaneously by storing the position signal of the piezo actuator used for maintaining a constant working distance (i.e. the topography signal) and the nanoelectrode current (electrochemical reactivity). Figure 10.7shows the topographic signal and the SECM feedback current from a 700 µm line scan (Figure 10.7a) and a stacked 3D plot of the topography and SECM feedback current of a 700 µm × 500 µm image (Figure 10.7b). The measured currents over gold are significantly larger than over polyimide. A homogeneous contribution of the electrochemical reactivity of the sintered nanoparticles can be seen. The spikes in the topographic image that are observed completely the same in a reverse scan image are due to the shear force response over polymeric materials.

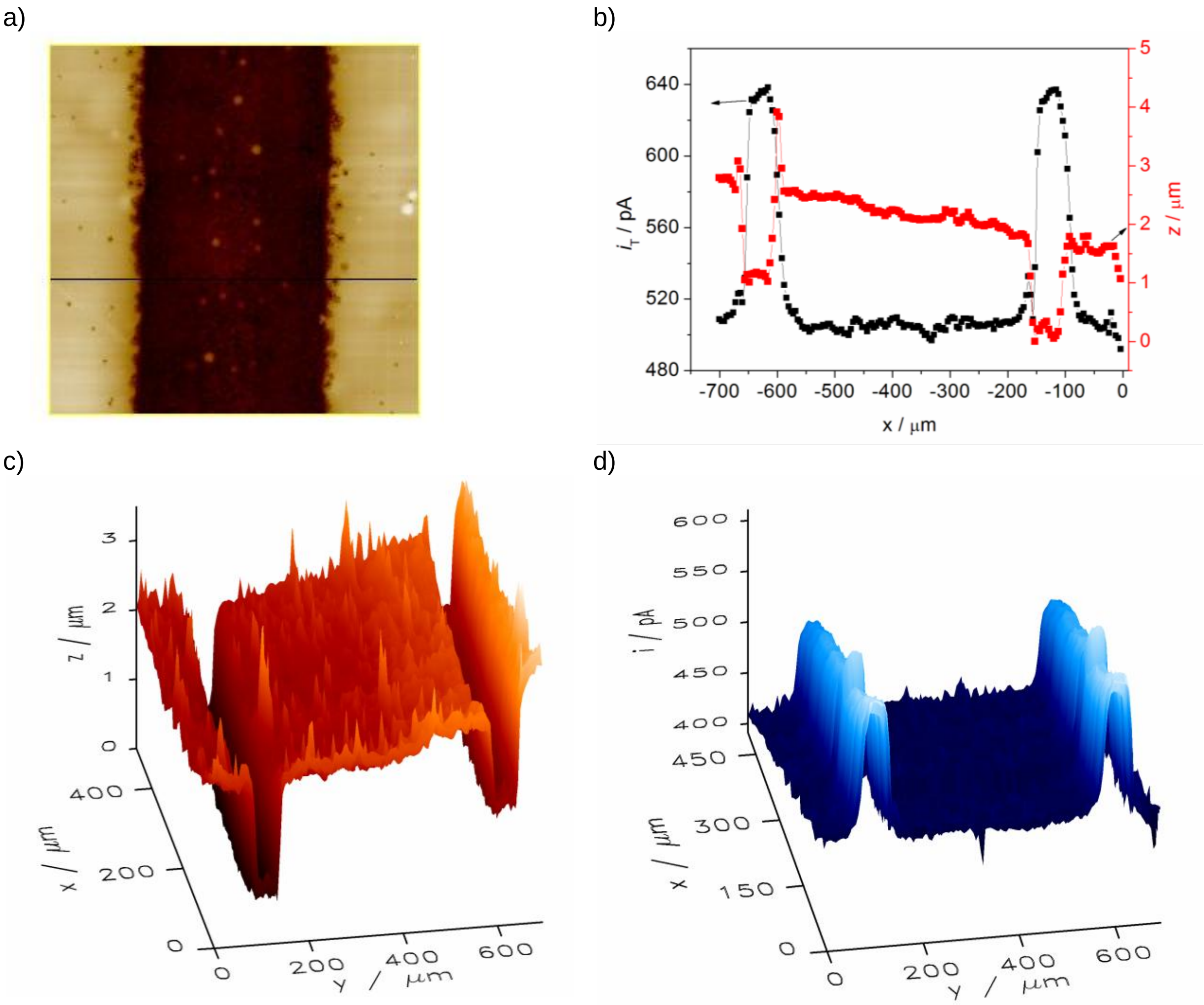

Figure 10.7 Shear-force based SECM in 2 mM FcMeOH and 0.1 M KNO_3; E_T = 0.3 V, translation rate 25 µm s^{-1}, step size 5 µm. Line scan (a) and SECM image over two sintered gold tracks with simultaneously recorded topographic (c) and surface reactivity (d) information.

10.3.4. D149-sensitized ZnO films

Figure 10.8a shows an AFM topography image of D149/ZnO film. Rough topographic features in microscale were realized within a 5 µm x 5 µm area. The SECM in the shear-force mode could be used to acquire high resolution imaging of porous dye-sensitized solar cell electrodes. At the dye-sensitized electrode under illumination electrochemical reactions associated with the electrolyte species and photo-oxidized dye were considered to map the inhomogeneity in localized photoelectrochemical activity. Locations that possessed non-uniform SECM probe currents under illumination were compared at the edge of illuminated D149/ZnO film-FTO substrate (Figure 10.8b). An increase in a probe current over sensitized electrode surface compared bare FTO region under the same condition indicates the presence of photoreactivity. Furthermore non-uniform current responses at the probe were detected implying heterogeneity in surface reaction. This study was directed to investigate the relationship between structure and function of dye sensitized nanoporous metal oxide grains with sub-micrometer resolution.

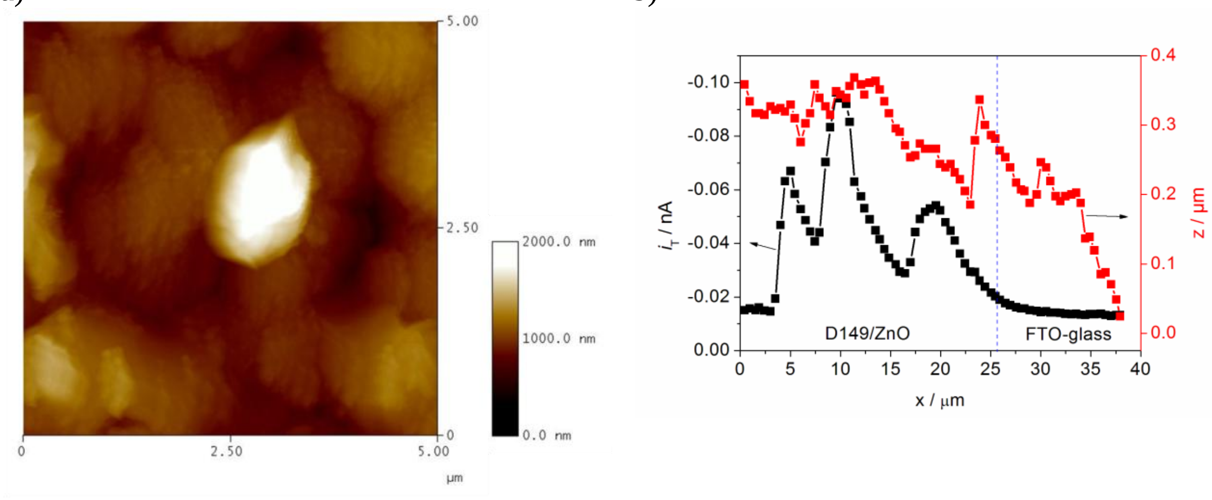
a)

b)

Figure 10.8 (a) AFM topography image of D149/ZnO film. Shear-force based SECM in 5 mM I_3^- and 0.1 M TBAS; E_T = 0.7 V, translation rate 0.5 µm s^{-1}, step size 0.2 µm. Line scan (a) topography (b) photoelectrochemical reactivity under illumination at the edge of D149/ZnO film-FTO glass.

In general, new contributions for high resolution SECM were addressed in this Chapter. SEM characterization of nanoelectrodes by charging in RTIL is an extraordinary finding and could be directly adapted to visualize any insulating materials by SEM without gold or carbon sputtering. The absolute working distance for which stable responses are obtained is in the range of 500-700 nm. As demonstrated with model examples the method developed could be successfully implemented to investigate the relationship between functional and structural characteristics of dye-sensitized solar cells.

11. Summary and outlook

This thesis has focused on the use of scanning electrochemical microscopy to characterize dye sensitized solar cells (DSSCs). DSSCs are promising solar electricity generation devices which are inexpensive, light weight, portable, flexible, transparent and fabricated from materials which do not add direct contamination to the environment. At the heart of DSSC function is the photo-oxidation and regeneration of a dye molecule. The regeneration of dye molecules by oxidizing iodide ions in solution is one of the essential steps in the charge separation process. This reaction is commonly studied by transient absorbance techniques that are very difficult and expensive. Due to this reason there is a serious lack of detailed data on the rate of dye regeneration to optimize cell efficiency and to scale up device manufacturing.

In this thesis it is found that SECM feedback measurement allowed complete quantification of the dye regeneration rate at a microscopic sample. This was illustrated with approach curve measurements on model dye sensitized samples under illumination. The method is a relatively simple procedure compared to transient absorbance techniques. Two kinetic models based on the dye regeneration rate law of order 1.5 and 1 with respect to I^- were developed and tested. With both kinetic models consistent values of effective dye regeneration rate constants and $\phi_{h\nu}$ were found suggesting that either model could empirically describe the feedback approach curve data for dye regeneration.

The kinetic model of the reaction order 1.5 with respect to iodide has been reported previously by this group and Chapter 7 in this thesis expanded significantly on that work, describing detailed experimental verification of this model by variation of the excitation wavelength, light intensities and mediator concentrations and exploring the possibility to use the model for alternative more efficient dye sensitized electrodes. It was found that for the regeneration process of Eosin Y and D149 dyes, the effective heterogeneous rate constant k_{ox}

of similar magnitude is obtained. This shows that bimolecular reaction rate constant between I^- and the two organic dyes is similar despite very different overall efficiencies of light-induced charge transfer found for the two dyes that are obvious from the $\phi_{h\nu}$ values for Eosin Y and D149. A direct correlation between optical absorbance of dye-sensitized ZnO films and the photoexcitation cross-section of dye molecules was observed from SECM kinetic data analysis.

The kinetic model of first order with respect to iodide was intended to incorporate detailed molecular mechanism of dye regeneration process and to address structural variations within the pore system on functional characteristics of dye-sensitized films from different characterization methods into predictive models. Using this model in Section 8.1, we described the use of a state-of-the-art dye sensitized electrode N719/TiO_2 and explored the effects of changing the solvent identity, electrolyte cation and its concentration on the kinetics. It was found that acetonitrile electrolytes resulted in faster N719 regeneration rates than EMimTFS, chosen as an example of RTIL. The rate is still faster after correction for the faster external diffusion of the redox electrolyte. The effect of the studied cations is qualitatively the same in acetonitrile and RTIL-based electrolyte solutions. The effect of cations such as Li^+ is a down shift of the conduction band edge that is expected to accelerate the injection rate of the photoexcited dye but also the recombination rate between electrons and dye molecules. Several further reasons could additionally contribute to the observation made here such as differences in surface concentration of I^- induced by cation adsorption, the changes in local viscosity of the electrolytes and variation in the internal structure of the dye sensitized electrode due to intermolecular interaction of dye and specific cations. Even though the SECM feedback method measures a rate constant k'_{ox} of the combined effect of dye regeneration kinetics and recombination processes, it complements information from DSSC characterization because it works on a single dye-sensitized electrode rather than on a complete cell. This allows rather straight forward testing of different electrolyte compositions on one and the same substrate without the need to construct series of complete solar cells.

In Section 8.2 the kinetic model of first order with respect to iodide was further used to explore the influence of internal film structure on the kinetics by systematically varying film thickness and dye content in the film. Considerably different effective heterogeneous first order rate constants k'_{ox} for the D149 regeneration was observed among six photoelectrodes. Correlation studies performed among structural parameters, photovoltaic performance, electron recombination and dye regeneration kinetics resulted in the following conclusion: (a) The J_{sc} increased with the total dye content Γ_{D} and, even more clearly, with the dye concentration on the inner surface $\Gamma_{\mathrm{D}}/(p \cdot l_{\mathrm{porous}})$. Close proximity of the sensitizer molecules seems to assist the photoelectrochemical efficiency rather than decreasing it by radiationless decay in dye aggregates, (b) the V_{oc} and τ showed no clear correlation to neither Γ_{D} nor $\Gamma_{\mathrm{D}}/(p \cdot l_{\mathrm{porous}})$ suggesting that they are mainly determined by the electronic structure of the semiconductor, and (c) the k'_{ox} does not depend on Γ_{D} but correlates with $\Gamma_{\mathrm{D}}/(p \cdot l_{\mathrm{porous}})$, suggesting that dye regeneration is heavily supported by close proximity of the sensitizer molecules. By systematic variation of film thickness and dye loading, non-uniform accessibility of dye molecules for I^- as well as unequal light intensity reaching dye molecules in different vertical distances from the back contact become more pronounced. Furthermore, the method reported in this thesis could be used as a model to design electrolyte redox couples and to screen dyes as well as identify suitable cations.

In Chapter 9 the measurement of transient curves by switched illumination provided reproducible UME current for several on-off cycles of N719/TiO_2 films. The method could be used for screening of dyes and electrolytes as it is less time consuming and does not require complete solar cell assembly compared to conventional techniques. Furthermore, measurement of UME current following different intervals of illumination at N719/TiO_2 film were used to examine qualitatively the local depletion of photo-oxidized adsorbed dye and to determine the dye surface concentration.

In Chapter 10, the non-optical shear force distance regulation for high resolution SECM was developed and implemented to simultaneously characterize the topography and electrochemical reactivity of substrates. The absolute working distance for a stable shear force response of 500-700 nm was estimated. Furthermore, the influence of SECM probe size on the kinetics of reaction at the substrate was explored. It was found that higher sample kinetics requires the use of a smaller electrodes and a distance regulation mechanism that can maintain smaller absolute working distances. This opens a way to characterize the inhomogeneity in localized photoelectrochemical activity on the dye-sensitized photoelectrodes that could allow understanding the relationship between structure and function of dye sensitized nanoporous metal oxide grains within nanoscale resolution. That could be used as a guideline to optimize and improve the dye-sensitized electrode preparation procedures.

A number of extensions to the work presented in this thesis are possible, which could improve the predictive qualities of the analytical model developed and enable further investigations of redox kinetics within the DSSC. An obvious extension to the model used is to explicitly consider the non-uniform accessibility of light and iodide to the dye molecule. This requires continuum simulation. The model could still be revised by considering the light scattering by the nanoparticulate film. Further extension of the model could include investigating the transient response of the cell. Efforts to replace the I^-/I_3^- redox couple in DSSC with one-electron Co complex redox couple were successful. Therefore, its redox kinetics in DSSC could be investigated in a similar fashion to the I^-/I_3^- couple using SECM. SECM can also be used to address the effect of substrate materials, its surface modification, the dye aggregate formation and the presence of coadsorbents on the dye regeneration kinetics.

In this thesis the kinetic data of SECM feedback approach curves were treated by analytical expression from Cornut and Lefrou for irreversible first order reaction at the substrate. As the reactions at the dye-sensitized electrodes are more complicated, carrying out simulations for each experimental approach curves by developing numerical models which is specific to process in the dye-sensitized solar cell electrodes is required.

Symbols and abbreviations

Symbols

Symbol	**Quantity**	**Dimension**
γ	Activity coefficient	dimensionless
$\phi_{h\nu}$	Absorption cross-section of dye molecules	cm^2 mol^{-1}
$[D^o]$	Amount of dye per volume of the porous metal oxide electrode	mol cm^{-3}
$[I_3^-]^*$	Tri-iodide bulk concentration	mM, $molcm^{-3}$
D	Diffusion coefficient	cm^2 s^{-1}
d	UME-sample separation	µm
E_T	Potential of the SECM probe	V
I_S	Normalized steady-state substrate current	dimensionless
I_T	Normalized UME current	dimensionless
i_T, $i_{T,\infty}$	UME current, Steady-state UME current	A
$I_{T,cond}$, $I_{T,ins}$	Normalized UME current for conductor and insulator	dimensionless
$J_{h\nu}$	Photon flux	mol cm^{-2} s^{-1}
J_{sc}	Short-circuit current density	A cm^{-2}
k_1, k_2	Kinetic rate constant	mol^{-1} cm^3 s^{-1}
k_{eff}	Effective heterogeneous first order rate constant	cm s^{-1}
$k_{h\nu,eff}$	Effective rate constant of light absorption and electron injection	s^{-1}
k_{inj}	Rate constant for electron injection	s^{-1}
k_{ox}, k'_{ox}	Effective rate constant for the dye regeneration	$cm^{9/2}$ $mol^{-3/2}s^{-1}$, mol^{-1} cm^3 s^{-1}
L	Normalized distance	dimensionless

l	Film thickness	µm, cm
RG	Insulation sheath to electrode ratio	dimensionless
r_{glass}	Radius of the glass sheath surrounding the UME	µm, cm
r_{T}	The radius of the active electrode	µm, cm
V_{oc}	Open-circuit potential	V
z_{offset}	Point of closest approach	µm
A	Area	cm^2
Γ_{D}	Dye loading (dye per geometric surface area)	$\mathrm{mol\ cm}^{-2}$
κ	Normalized heterogeneous first order rate constant	dimensionless
λ	Wavelength	nm

Abbrevations

AFM	Atomic Force Microscopy
a_{O}, a_{R}	Activity of the oxidized and reduced form of the redox mediator
CB, VB	Conduction band and valence band
CE	Counter electrode
CLSM	Confocal Laser Scanning Microscopy
c_{O}, c_{R}	Concentration of the oxidized and reduced form of the redox mediator
DA, AD	Digital-to-analog and analog-to-digital converter
DSSC	Dye-sensitized solar cells
E_{CB}, E_{VB}	Highest energy of the conduction band and valence band
E_{F}	Fermi level energy
E_{g}	Band gap energy
EIS	Electrochemical impedance spectroscopy

E^{o}_{redox}	Standard electrochemical potential of the redox couple
E_{ref}	Energy of the reference electrode
FB	Feedback mode
FTO, ITO	Fluorine doped tin oxide and indium tin oxide
GC	Generation-collection mode
IMPS	Intensity modulated photocurrent spectroscopy
IMVS	Intensity modulated photovoltage spectroscopy
IPCE	Incident photon to current conversion efficiency
LED	Light emitting diode
PECs	Photoelectrochemical cells
QRE	Quasi reference electrode
RC	Redox completion mode
RTIL	Room temperature ionic liquid
SECM	Scanning Electrochemical Microscopy
SEM	Scanning electron microscopy
SG/TC	Substrate generation tip- collection
TG/SC	Tip-generation substrate collection
UME	Microelectrode, ultramicroelectrode
WE	Working electrode

Chemical compounds

D149	5-[[4-[4-(2,2-diphenylethenyl)phenyl]-1,2,3,3a,4,8b-hexahydrocyclopent[b] indol-7-yl]methylene]-2-(3-ethyl-4-oxo-2-thioxo-5-thiazolidinylidene)-4-oxo-3-thiazolidineacetic acid
DMPimI	1,2-dimethyl-3-propylimidazolium iodide
DMPimTFS	1,2-dimethyl-3-propylimidazolium bis(trifluoromethylsulfonyl)imide
EMimTFS	1-ethyl-3-methylimidazolium bis(trifluoromethylsulfonyl)imide
Eosin Y	Disodium 2-(2,4,5,7-tetrabromo-6-oxido-3-oxoxanthen-9-yl)benzoate
LiTFS	Lithium bis(trifluoromethylsulfonyl)imide
N3	Ru(4,4‘-dicarboxy-2,2‘-bipyridine)$_2$(NCS)$_2$
N719	Di-tetrabutylammonium cis-bis(isothiocyanato)bis(2,2′- bipyridyl-4,4′-dicarboxylato)ruthenium(II)
TBAI	Tetrabutylammonium iodide (TBAI)
TBAS	Anhydrous tetrabutylammonium trifluoromethanesulfonate

Bibliography

[1] R. A. Kerr, *Science* **1998**, *281*, 1128.

[2] D. Anderson, S. T. Coelho, G. Doucet, I. Freudenschuss-Reichl, M. Jefferson, E. Jochem, S. Karekezi, H. Khatib, S. McDade, A. McDonald, J. R. Moreira, N. Nakicenovic, A. Reddy, H.-H. Rogner, K. R. Smith, W. C. Turkenburg, G. Wilkins, R. H. Williams, (Eds.: J. Goldemberg, T. B. Johannsson), New York, **2004**.

[3] http://en.wikipedia.org/wiki/World_energy_resources_and_consumption, **accessed 26 January, 2012**.

[4] E. Becquerel, *Comptes Rendus* **1839**, *9*, 561.

[5] D. M. Chapin, C. S. Fuller, G. L. Pearson, *J. Appl. Phys.* **1954**, *25*, 676.

[6] W. Shockley, H. J. Queisser, *J. Appl. Phys.* **1961**, *32*, 510.

[7] D. A. Cusano, *Solid-State Electron.* **1963**, *6*, 217.

[8] L. L. Kazmerski, F. R. White, G. K. Morgan, *Appl. Phys. Lett.* **1976**, *29*, 268.

[9] B. O'Regan, M. Grätzel, *Nature* **1991**, *353*, 737.

[10] M. Grätzel, *Inorg. Chem.* **2005**, *44*, 6841.

[11] M. Grätzel, *Nature* **2001**, *414*, 338.

[12] B. A. Gregg, *Coord. Chem. Rev.* **2004**, *248*, 1215.

[13] A. Hagfeldt, G. Boschloo, L. Sun, L. Kloo, H. Pettersson, *Chem. Rev.* **2010**, *110*, 6595.

[14] A. Y. Anderson, P. R. F. Barnes, J. R. Durrant, B. C. O'Regan, *J. Phys. Chem. C* **2011**, *115*, 2439.

[15] P. Bertoncello, *Energy Environ. Sci.* **2010**, *3*, 1620.

[16] B. Bozic, E. Figgemeier, *Chem. Commun.* **2006**, 2268.

[17] F. Zhang, V. Roznyatovskiy, F.-R. F. Fan, V. Lynch, J. L. Sessler, A. J. Bard, *J. Phys. Chem. C* **2011**, *115*, 2592.

[18] A. J. Nozik, *Annu. Rev. Phys. Chem.* **1978**, *29*, 189.

[19] J. Manassen, D. Cahen, G. Hodes, A. Sofer, *Nature* **1976**, *263*, 97.

[20] H. Gerischer, *Advances in Electrochem. Electrochem. Eng.* **1961**, *1*, 139.

[21] H. Gerischer, *J. Electrochem. Soc.* **1966**, *113*, 1174.

[22] A. Fujishima, K. Honda, *Nature* **1972**, *238*, 37.

[23] A. Iwase, A. Kudo, *J. Mater. Chem.* **2010**, *20*, 7536.

[24] S. D. Tilley, M. Cornuz, K. Sivula, M. Graetzel, *Angew. Chem. Int. Ed.* **2010**, *49*, 6405.

[25] C.-W. Huang, C.-H. Liao, J. C. S. Wu, Y.-C. Liu, C.-L. Chang, C.-H. Wu, M. Anpo, M. Matsuoka, M. Takeuchi, *Int. J. Hydrogen Energy* **2010**, *35*, 12005.

[26] T. Lopes, L. Andrade, H. A. Ribeiro, A. Mendes, *Int. J. Hydrogen Energy* **2010**, *35*, 11601.

[27] M. G. Walter, E. L. Warren, J. R. McKone, S. W. Boettcher, Q. Mi, E. A. Santori, N. S. Lewis, *Chem. Rev.* **2010**, *110*, 6446.

[28] R. Abe, *J. Photochem. Photobiol. C* **2010**, *11*, 179.

[29] H. Wu, Z. Zhang, *Int. J. Hydrogen Energy* **2011**, *36*, 13481.

[30] W. J. Youngblood, S.-H. A. Lee, K. Maeda, T. E. Mallouk, *Acc. Chem. Res.* **2009**, *42*, 1966.

[31] A. J. Bard, L. R. Faulkner, *Electrochemical Methods: Fundamentals and Applications*, John Wiley & Sons, New York, **2001**.

[32] R. Gomer, G. Tryson, *J. Chem. Phys.* **1977**, *66*, 4413.

[33] S. Trasatti, *J. Electroanal. Chem. Interfacial Electrochem.* **1974**, *52*, 313.

[34] R. M. Noyes, *J. Am. Chem. Soc.* **1962**, *84*, 513.

[35] A. Hagfeldt, M. Grätzel, *Chem. Rev.* **1995**, *95*, 49.

[36] W. West, *Photographic Science and Engineering* **1974**, *18*, 35.

[37] H. Gerischer, H. Tributsch, *Ber. Bunsen Ges.* **1968**, *72*, 437.

[38] R. Memming, *Faraday Discussions of the Chemical Society* **1975**, *58*, 261.

[39] R. Memming, F. Schroeppel, *Chem. Phys. Lett.* **1979**, *62*, 207.

[40] A. Yella, H.-W. Lee, H. N. Tsao, C. Yi, A. K. Chandiran, M. K. Nazeeruddin, E. W.-G. Diau, C.-Y. Yeh, S. M. Zakeeruddin, M. Graetzel, *Science* **2011**, *334*, 1203.

[41] Y. Chiba, A. Islam, Y. Watanabe, R. Komiya, N. Koide, L. Han, *Jpn. J. Appl. Phys., Part 2* **2006**, *45*, L638.

[42] M. K. Nazeeruddin, A. Kay, I. Rodicio, R. Humphry-Baker, E. Mueller, P. Liska, N. Vlachopoulos, M. Grätzel, *J. Am. Chem. Soc.* **1993**, *115*, 6382.

[43] D. Shi, N. Pootrakulchote, R. Li, J. Guo, Y. Wang, S. M. Zakeeruddin, M. Gratzel, P. Wang, *J. Phys. Chem. C* **2008**, *112*, 17046.

[44] Q. Yu, S. Liu, M. Zhang, N. Cai, Y. Wang, P. Wang, *J. Phys. Chem. C* **2009**, *113*, 14559.

[45] M. K. Nazeeruddin, P. Pechy, M. Graetzel, *Chem. Commun.* **1997**, 1705.

[46] M. K. Nazeeruddin, S. M. Zakeeruddin, R. Humphry-Baker, M. Jirousek, P. Liska, N. Vlachopoulos, V. Shklover, C.-H. Fischer, M. Grätzel, *Inorg. Chem.* **1999**, *38*, 6298.

[47] K. Hara, T. Horiguchi, T. Kinoshita, K. Sayama, H. Sugihara, H. Arakawa, *Sol. Energy Mater. Sol. Cells* **2000**, *64*, 115.

[48] A. Ehret, L. Stuhl, M. T. Spitler, *J. Phys. Chem. B* **2001**, *105*, 9960.

[49] G. Sauve, M. E. Cass, G. Coia, S. J. Doig, I. Lauermann, K. E. Pomykal, N. S. Lewis, *J. Phys. Chem. B* **2000**, *104*, 6821.

[50] N. Robertson, *Angew. Chem. Int. Ed.* **2008**, *47*, 1012.

[51] J.-H. Yum, S.-R. Jang, P. Walter, T. Geiger, F. Nueesch, S. Kim, J. Ko, M. Grätzel, M. K. Nazeeruddin, *Chem. Commun.* **2007**, 4680.

[52] F. Silvestri, I. Lopez-Duarte, W. Seitz, L. Beverina, M. V. Martinez-Diaz, T. J. Marks, D. M. Guldi, G. A. Pagani, T. Torres, *Chem. Commun.* **2009**, 4500.

[53] J.-J. Cid, J.-H. Yum, S.-R. Jang, M. K. Nazeeruddin, E. Martinez-Ferrero, E. Palomares, J. Ko, M. Grätzel, T. Torres, *Angew. Chem. Int. Ed.* **2007**, *46*, 8358.

[54] S. D. Burnside, V. Shklover, C. Barbe, P. Comte, F. Arendse, K. Brooks, M. Grätzel, *Chem. Mater.* **1998**, *10*, 2419.

[55] N. G. Park, J. van de Lagemaat, A. J. Frank, *J. Phys. Chem. B* **2000**, *104*, 8989.

[56] F. Lenzmann, J. Krueger, S. Burnside, K. Brooks, M. Grätzel, D. Gal, S. Ruehle, D. Cahen, *J. Phys. Chem. B* **2001**, *105*, 6347.

[57] K. Srikanth, M. M. Rahman, H. Tanaka, K. M. Krishna, T. Soga, M. K. Mishra, T. Jimbo, M. Umeno, *Sol. Energy Mater. Sol. Cells* **2001**, *65*, 171.

[58] T. Yoshida, J. Zhang, D. Komatsu, S. Sawatani, H. Minoura, T. Pauporte, D. Lincot, T. Oekermann, D. Schlettwein, H. Tada, D. Wöhrle, K. Funabiki, M. Matsui, H. Miura, H. Yanagi, *Adv. Funct. Mater.* **2009**, *19*, 17.

[59] N. Papageorgiou, Y. Athanassov, M. Armand, P. Bonhote, H. Pettersson, A. Azam, M. Grätzel, *J. Electrochem. Soc.* **1996**, *143*, 3099.

[60] E. Stathatos, P. Lianos, C. Krontiras, *J. Phys. Chem. B* **2001**, *105*, 3486.

[61] A. F. Nogueira, M. M. A. De Paoli, *Sol. Energy Mater. Sol. Cells* **2000**, *61*, 135.

[62] G. Oskam, B. V. Bergeron, G. J. Meyer, P. C. Searson, *J. Phys. Chem. B* **2001**, *105*, 6867.

[63] H. Nusbaumer, J.-E. Moser, S. M. Zakeeruddin, M. K. Nazeeruddin, M. Grätzel, *J. Phys. Chem. B* **2001**, *105*, 10461.

[64] P. Wang, S. M. Zakeeruddin, P. Comte, I. Exnar, M. Grätzel, *J. Am. Chem. Soc.* **2003**, *125*, 1166.

[65] E. Bellingeri, D. Marre, L. Pellegrino, I. Pallecchi, G. Canu, M. Vignolo, C. Bernini, A. S. Siri, *Superlattices Microstructures* **2005**, *38*, 446.

[66] D. C. Look, *Materials Science & Engineering, B: Solid-State Materials for Advanced Technology* **2001**, *B80*, 383.

[67] D. Wei, H. E. Unalan, D. Han, Q. Zhang, L. Niu, G. Amaratunga, T. Ryhanen, *Nanotechnology* **2008**, *19*, 424006/1.

[68] T. Loewenstein, A. Hastall, M. Mingebach, Y. Zimmermann, A. Neudeck, D. Schlettwein, *Phys. Chem. Chem. Phys.* **2008**, *10*, 1844.

[69] T. Yoshida, K. Terada, D. Schlettwein, T. Oekermann, T. Sugiura, H. Minoura, *Adv. Mater.* **2000**, *12*, 1214.

[70] T. Yoshida, T. Oekermann, K. Okabe, D. Schlettwein, K. Funabiki, H. Minoura, *Electrochemistry (Tokyo, Jpn.)* **2002**, *70*, 470.

[71] T. Yoshida, T. Pauporte, D. Lincot, T. Oekermann, H. Minoura, *J. Electrochem. Soc.* **2003**, *150*, C608.

[72] A. Hagfeldt, M. Grätzel, *Acc. Chem. Res.* **2000**, *33*, 269.

[73] M. Grätzel, *Journal of Photochemistry and Photobiology, C: Photochemistry Reviews* **2003**, *4*, 145.

[74] F. Gao, Y. Wang, D. Shi, J. Zhang, M. Wang, X. Jing, R. Humphry-Baker, P. Wang, M. Zakeeruddin Shaik, M. Gratzel, *J. Am. Chem. Soc.* **2008**, *130*, 10720.

[75] S. Ito, S. M. Zakeeruddin, R. Humphry-Baker, P. Liska, R. Charvet, P. Comte, M. K. Nazeeruddin, P. Pechy, M. Takata, H. Miura, S. Uchida, M. Grätzel, *Adv. Mater.* **2006**, *18*, 1202.

[76] S. Kambe, S. Nakade, T. Kitamura, Y. Wada, S. Yanagida, *J. Phys. Chem. B* **2002**, *106*, 2967.

[77] S. Pelet, J.-E. Moser, M. Graetzel, *J. Phys. Chem. B* **2000**, *104*, 1791.

[78] C. A. Kelly, F. Farzad, D. W. Thompson, J. M. Stipkala, G. J. Meyer, *Langmuir* **1999**, *15*, 7047.

[79] B. V. Bergeron, A. Marton, G. Oskam, G. J. Meyer, *J. Phys. Chem. B* **2005**, *109*, 937.

[80] Z.-S. Wang, K. Sayama, H. Sugihara, *J. Phys. Chem. B* **2005**, *109*, 22449.

[81] F.-T. Kong, S.-Y. Dai, K.-J. Wang, *Advances in OptoElectronics* **2007**, *2007*, 75384/1.

[82] L. Schmidt-Mende, S. M. Zakeeruddin, M. Grätzel, *Appl. Phys. Lett.* **2005**, *86*, 013504.

[83] U. Bach, D. Lupo, P. Comte, J. E. Moser, F. Weissortel, J. Salbeck, H. Spreitzer, M. Gratzel, *Nature* **1998**, *395*, 583.

[84] M. C. Buzzeo, R. G. Evans, R. G. Compton, *ChemPhysChem* **2004**, *5*, 1106.

[85] Y. Bai, Y. Cao, J. Zhang, M. Wang, R. Li, P. Wang, S. M. Zakeeruddin, M. Grätzel, *Nat. Mater.* **2008**, *7*, 626.

[86] N. Yamanaka, R. Kawano, W. Kubo, N. Masaki, T. Kitamura, Y. Wada, M. Watanabe, S. Yanagida, *J. Phys. Chem. B* **2007**, *111*, 4763.

[87] S. N. Lewis, *J. Phys. Chem. B* **1998**, *102*, 4843.

[88] A. Zaban, A. Meier, B. A. Gregg, *J. Phys. Chem. B* **1997**, *101*, 7985.

[89] P. Hoyer, H. Weller, *J. Phys. Chem.* **1995**, *99*, 14096.

[90] K. Schwarzburg, F. Willig, *J. Phys. Chem. B* **1997**, *101*, 2451.

[91] R. Koenenkamp, R. Henninger, P. Hoyer, *J. Phys. Chem.* **1993**, *97*, 7328.

[92] A. Solbrand, H. Lindstroem, H. Rensmo, A. Hagfeldt, S.-E. Lindquist, S. Soedergren, *J. Phys. Chem. B* **1997**, *101*, 2514.

[93] A. Zaban, S. Ferrere, B. A. Gregg, *J. Phys. Chem. B* **1998**, *102*, 452.

[94] N. Beermann, G. Boschloo, A. Hagfeldt, *J. Photochem. Photobiol., A* **2002**, *152*, 213.

[95] J. Bisquert, V. S. Vikhrenko, *J. Phys. Chem. B* **2004**, *108*, 2313.

[96] N. Kopidakis, E. A. Schiff, N. G. Park, J. Van de Lagemaat, A. J. Frank, *J. Phys. Chem. B* **2000**, *104*, 3930.

[97] H. Wang, P. G. Nicholson, L. Peter, S. M. Zakeeruddin, M. Gratzel, *J. Phys. Chem. C* **2010**, *114*, 14300.

[98] B. Enright, D. Fitzmaurice, *J. Phys. Chem.* **1996**, *100*, 1027.

[99] B. O'Regan, J. Moser, M. Anderson, M. Grätzel, *J. Phys. Chem.* **1990**, *94*, 8720.

[100] F. Cao, G. Oskam, P. C. Searson, *J. Phys. Chem.* **1996**, *100*, 17021.

[101] S. Y. Huang, G. Schlichthörl, A. J. Nozik, M. Grätzel, A. J. Frank, *J. Phys. Chem. B* **1997**, *101*, 2576.

[102] R. Kawano, M. Watanabe, *Chem. Commun.* **2005**, 2107.

[103] M. Zistler, P. Wachter, P. Wasserscheid, D. Gerhard, A. Hinsch, R. Sastrawan, H. J. Gores, *Electrochim. Acta* **2006**, *52*, 161.

[104] P. Wachter, M. Zistler, C. Schreiner, M. Berginc, U. O. Krasovec, D. Gerhard, P. Wasserscheid, A. Hinsch, H. J. Gores, *J. Photochem. Photobiol., A* **2008**, *197*, 25.

[105] L. M. Peter, *J. Phys. Chem. C* **2007**, *111*, 6601.

[106] L. M. Peter, *Phys. Chem. Chem. Phys.* **2007**, *9*, 2630.

[107] S. A. Haque, E. Palomares, B. M. Cho, A. N. M. Green, N. Hirata, D. R. Klug, J. R. Durrant, *J. Am. Chem. Soc.* **2005**, *127*, 3456.

[108] Q. Wang, S. Ito, M. Grätzel, F. Fabregat-Santiago, I. Mora-Sero, J. Bisquert, T. Bessho, H. Imai, *J. Phys. Chem. B* **2006**, *110*, 25210.

[109] B. J. Walter, C. M. Elliott, *Inorg. Chem.* **2001**, *40*, 5924.

[110] Y. Tachibana, J. E. Moser, M. Grätzel, D. R. Klug, J. R. Durrant, *J. Phys. Chem.* **1996**, *100*, 20056.

[111] S. Pelet, M. Grätzel, J.-E. Moser, *J. Phys. Chem. B* **2003**, *107*, 3215.

[112] I. Montanari, J. Nelson, J. R. Durrant, *J. Phys. Chem. B* **2002**, *106*, 12203.

[113] T. A. Heimer, E. J. Heilweil, C. A. Bignozzi, G. J. Meyer, *J. Phys. Chem. A* **2000**, *104*, 4256.

[114] C. Nasr, S. Hotchandani, P. V. Kamat, *J. Phys. Chem. B* **1998**, *102*, 4944.

[115] J. N. Clifford, E. Palomares, M. K. Nazeeruddin, M. Grätzel, J. R. Durrant, *J. Phys. Chem. C* **2007**, *111*, 6561.

[116] B. A. Gregg, F. Pichot, S. Ferrere, C. L. Fields, *J. Phys. Chem. B* **2001**, *105*, 1422.

[117] A. Solbrand, A. Henningsson, S. Soedergren, H. Lindstroem, A. Hagfeldt, S.-E. Lindquist, *J. Phys. Chem. B* **1999**, *103*, 1078.

[118] G. Schlichthörl, S. Y. Huang, J. Sprague, A. J. Frank, *J. Phys. Chem. B* **1997**, *101*, 8141.

[119] L. Dloczik, O. Ileperuma, I. Lauermann, L. M. Peter, E. A. Ponomarev, G. Redmond, N. J. Shaw, I. Uhlendorf, *J. Phys. Chem. B* **1997**, *101*, 10281.

[120] A. C. Fisher, L. M. Peter, E. A. Ponomarev, A. B. Walker, K. G. U. Wijayantha, *J. Phys. Chem. B* **2000**, *104*, 949.

[121] J. Bisquert, *J. Phys. Chem. B* **2002**, *106*, 325.

[122] B. C. O'Regan, K. Bakker, J. Kroeze, H. Smit, P. Sommeling, J. R. Durrant, *J. Phys. Chem. B* **2006**, *110*, 17155.

[123] R. J. Ellingson, J. B. Asbury, S. Ferrere, H. N. Ghosh, J. R. Sprague, T. Lian, A. J. Nozik, *J. Phys. Chem. B* **1998**, *102*, 6455.

[124] M. D. Archer, A. J. Nozik, Editors, *Nanostructured and photoelectrochemical systems for solar photon conversion*, **2008**.

[125] A. Zaban, M. Greenshtein, J. Bisquert, *ChemPhysChem* **2003**, *4*, 859.

[126] G. Wittstock, M. Burchardt, S. E. Pust, Y. Shen, C. Zhao, *Angew. Chem. Int. Ed.* **2007**, *46*, 1584.

[127] B. Liu, M. V. Mirkin, *J. Phys. Chem. B* **2002**, *106*, 3933.

[128] A. J. Bard, F.-R. F. Fan, D. T. Pierce, P. R. Unwin, D. O. Wipf, F. Zhou, *Science* **1991**, *254*, 68.
[129] H.-Y. Liu, F.-R. F. Fan, C. W. Lin, A. J. Bard, *J. Am. Chem. Soc.* **1986**, *108*, 3838.
[130] R. C. Engstrom, C. M. Pharr, *Anal. Chem.* **1989**, *61*, 1099.
[131] M. V. Mirkin, *Anal. Chem.* **1996**, *68*, 177.
[132] P. Sun, F. O. Laforge, M. V. Mirkin, *Phys. Chem. Chem. Phys.* **2007**, *9*, 802.
[133] F. Cortes-Salazar, M. Zhang, A. Becue, J.-M. Busnel, M. Prudent, C. Champod, H. H. Girault, *Chimia* **2009**, *63*, 580.
[134] F. Cortes-Salazar, D. Momotenko, H. H. Girault, A. Lesch, G. Wittstock, *Anal. Chem.* **2011**, *83*, 1493.
[135] S. Schmachtel, S. E. Pust, K. Kontturi, O. Forsen, G. Wittstock, *J. Appl. Electrochem.* **2010**, *40*, 581.
[136] A. R. Zeradjanin, T. Schilling, S. Seisel, M. Bron, W. Schuhmann, *Anal. Chem.* **2011**, *83*, 7645.
[137] A. J. Bard, M. V. Mirkin, Marcel Dekker, Inc., New York, Basel, **2001**, p. 650.
[138] M. Fleischmann, S. Pons, D. R. Rolison, P. P. Schmidt, *Ultramicroelectrodes,* Datatech Systems, Inc., Morganton, NC, **1987**.
[139] A. Schulte, W. Schuhmann, *Angew. Chem. Int. Ed.* **2007**, *46*, 8760.
[140] C. G. Zoski, A. M. Bond, T. E. Allinson, K. B. Oldham, *Anal. Chem.* **1990**, *62*, 37.
[141] K. B. Oldham, C. G. Zoski, *J. Electroanal. Chem.* **1988**, *256*, 11.
[142] Y. Saito, *Rev. Polarogr.* **1968**, *15*, 177.
[143] P. Liljeroth, D. Vanmaekelbergh, V. Ruiz, K. Kontturi, H. Jiang, E. Kauppinen, B. M. Quinn, *J. Am. Chem. Soc.* **2004**, *126*, 7126.
[144] B. Liu, A. J. Bard, M. V. Mirkin, S. E. Creager, *J. Am. Chem. Soc.* **2004**, *126*, 1485.
[145] H. Xiong, J. Guo, S. Amemiya, *Anal. Chem.* **2007**, *79*, 2735.
[146] J. L. Amphlett, G. Denuault, *J. Phys. Chem. B* **1998**, *102*, 9946.
[147] Y. Shao, M. V. Mirkin, *J. Phys. Chem. B* **1998**, *102*, 9915.
[148] M. V. Mirkin, F. R. F. Fan, A. J. Bard, *J. Electroanal. Chem.* **1992**, *328*, 47.
[149] A. J. Bard, M. V. Mirkin, P. R. Unwin, D. O. Wipf, *J. Phys. Chem.* **1992**, *96*, 1861.
[150] F. Forouzan, A. J. Bard, M. V. Mirkin, *Isr. J. Chem.* **1997**, *37*, 155.
[151] J. Kwak, A. J. Bard, *Anal. Chem.* **1989**, *61*, 1221.
[152] C. Lefrou, *J. Electroanal. Chem.* **2006**, *592*, 103.
[153] R. Cornut, C. Lefrou, *J. Electroanal. Chem.* **2007**, *608*, 59.
[154] L. Rajendran, S. P. Ananthi, *J. Electroanal. Chem.* **2004**, *561*, 113.
[155] J. Galceran, J. Cecilia, E. Companys, J. Salvador, J. Puy, *J. Phys. Chem. B* **2000**, *104*, 7993.
[156] C. Wei, A. J. Bard, M. V. Mirkin, *J. Phys. Chem.* **1995**, *99*, 16033.
[157] R. Cornut, C. Lefrou, *J. Electroanal. Chem.* **2008**, *621*, 178.
[158] D. T. Pierce, P. R. Unwin, A. J. Bard, *Anal. Chem.* **1992**, *64*, 1795.
[159] D. T. Pierce, A. J. Bard, *Anal. Chem.* **1993**, *65*, 3598.
[160] G. Wittstock, K.-j. Yu, H. B. Halsall, T. H. Ridgway, W. R. Heineman, *Anal. Chem.* **1995**, *67*, 3578.
[161] G. Wittstock, W. Schuhmann, *Anal. Chem.* **1997**, *69*, 5059.
[162] T. Yasukawa, T. Kaya, T. Matsue, *Electroanalysis* **2000**, *12*, 653.
[163] M. Sanchez-Sanchez Carlos, J. Solla-Gullon, J. Vidal-Iglesias Francisco, A. Aldaz, V. Montiel, E. Herrero, *J. Am. Chem. Soc.* **2010**, *132*, 5622.
[164] J. L. Fernandez, A. J. Bard, *Anal. Chem.* **2003**, *75*, 2967.
[165] M. V. Mirkin, W. Nogala, J. Velmurugan, Y. Wang, *Phys. Chem. Chem. Phys.* **2011**, *13*, 21196.

[166] K. Eckhard, X. Chen, F. Turcu, W. Schuhmann, *Phys. Chem. Chem. Phys.* **2006**, *8*, 5359.

[167] X. Chen, K. Eckhard, M. Zhou, M. Bron, W. Schuhmann, *Anal. Chem.* **2009**, *81*, 7597.

[168] A. Hengstenberg, C. Kranz, W. Schuhmann, *Chem. Eur. J.* **2000**, *6*, 1547.

[169] C. Combellas, J. Ghilane, F. Kanoufi, D. Mazouzi, *J. Phys. Chem. B* **2004**, *108*, 6391.

[170] Y. Selzer, D. Mandler, *J. Electroanal. Chem.* **1996**, *409*, 15.

[171] C. J. Slevin, J. V. Macpherson, P. R. Unwin, *J. Phys. Chem. B* **1997**, *101*, 10851.

[172] C. Zhao, G. Wittstock, *Anal. Chem.* **2004**, *76*, 3145.

[173] S. B. Basame, H. S. White, *J. Phys. Chem.* **1995**, *99*, 16430.

[174] P. James, N. Casillas, W. H. Smyrl, *J. Electrochem. Soc.* **1996**, *143*, 3853.

[175] S. B. Basame, H. S. White, *Langmuir* **1999**, *15*, 819.

[176] S. B. Basame, H. S. White, *Anal. Chem.* **1999**, *71*, 3166.

[177] I. Serebrennikova, S. Lee, H. S. White, *Faraday Discuss.* **2002**, *121*, 199.

[178] D. Mandler, A. J. Bard, *Langmuir* **1990**, *6*, 1489.

[179] B. R. Horrocks, M. V. Mirkin, A. J. Bard, *J. Phys. Chem.* **1994**, *98*, 9106.

[180] H. Maeda, K. Ikeda, K. Hashimoto, K. Ajito, M. Morita, A. Fujishima, *J. Phys. Chem. B* **1999**, *103*, 3213.

[181] S. M. Fonseca, A. L. Barker, S. Ahmed, T. J. Kemp, P. R. Unwin, *J. Chem. Soc., Chem. Commun.* **2003**, 1002.

[182] T. J. Kemp, P. R. Unwin, L. Vincze, *J. Chem. Soc., Faraday Trans.* **1995**, *91*, 3893.

[183] S. M. Fonseca, A. L. Barker, S. Ahmed, T. J. Kemp, P. R. Unwin, *Phys. Chem. Chem. Phys.* **2004**, *6*, 5218.

[184] S. K. Haram, A. J. Bard, *J. Phys. Chem. B* **2001**, *105*, 8192.

[185] J. Lee, H. Ye, S. Pan, A. J. Bard, *Anal. Chem.* **2008**, *80*, 7445.

[186] Y. Takahashi, A. I. Shevchuk, P. Novak, Y. Murakami, H. Shiku, Y. E. Korchev, T. Matsue, *J. Am. Chem. Soc.* **2010**, *132*, 10118.

[187] Y. Takahashi, A. I. Shevchuk, P. Novak, Y. Zhang, N. Ebejer, J. V. MacPherson, P. R. Unwin, A. J. Pollard, D. Roy, C. A. Clifford, H. Shiku, T. Matsue, D. Klenerman, Y. E. Korchev, *Angew. Chem. Int. Ed.* **2011**, *50*, 9638.

[188] J. Velmurugan, P. Sun, M. V. Mirkin, *J. Phys. Chem. C* **2009**, *113*, 459.

[189] Y. Lee, A. J. Bard, *Anal. Chem.* **2002**, *74*, 3626.

[190] J. Velmurugan, M. V. Mirkin, *ChemPhysChem* **2010**, *11*, 3011.

[191] P. Elsamadisi, Y. Wang, J. Velmurugan, M. V. Mirkin, *Anal. Chem.* **2011**, *83*, 671.

[192] Y. Shao, M. V. Mirkin, *J. Electroanal. Chem.* **1997**, *439*, 137.

[193] A. Anne, A. Chovin, C. Demaille, M. Lafouresse, *Anal. Chem.* **2011**, *83*, 7924.

[194] F. O. Laforge, J. Velmurugan, Y. Wang, M. V. Mirkin, *Anal. Chem.* **2009**, *81*, 3143.

[195] C. Kranz, H. E. Gaub, W. Schuhmann, *Adv. Mater.* **1996**, *8*, 634.

[196] D. O. Wipf, A. J. Bard, D. E. Tallman, *Anal. Chem.* **1993**, *65*, 1373.

[197] B. R. Horrocks, D. Schmidtke, A. Heller, A. J. Bard, *Anal. Chem.* **1993**, *65*, 3605.

[198] B. Ballesteros Katemann, A. Schulte, W. Schuhmann, *Chem. Eur. J.* **2003**, *9*, 2025.

[199] J. V. Macpherson, P. R. Unwin, A. C. Hillier, A. J. Bard, *J. Am. Chem. Soc.* **1996**, *118*, 6445.

[200] A. G. Ruiter, K. O. van der Werf, J. A. Veerman, M. F. Garcia-Parajo, W. H. Rensen, N. F. van Hulst, *Ultramicroscopy* **1998**, *71*, 149.

[201] A. Kueng, C. Kranz, A. Lugstein, E. Bertagnolli, B. Mizaikoff, *Angew. Chem. Int. Ed.* **2003**, *42*, 3238.

[202] C. E. Gardner, P. R. Unwin, J. V. Macpherson, *Electrochem. Commun.* **2005**, *7*, 612.

[203] A. Ueda, O. Niwa, K. Maruyama, Y. Shindo, K. Oka, K. Suzuki, *Angew. Chem. Int. Ed.* **2007**, *46*, 8238.

[204] K. McKelvey, M. A. Edwards, P. R. Unwin, *Anal. Chem.* **2010**, *82*, 6334.

[205] D. J. Comstock, J. W. Elam, M. J. Pellin, M. C. Hersam, *Anal. Chem.* **2010**, *82*, 1270.

[206] S. E. Pust, M. Salomo, E. Oesterschulze, G. Wittstock, *Nanotechnology* **2010**, *21*, 105709.

[207] M. Salomo, S. E. Pust, G. Wittstock, E. Oesterschulze, *Microelectron. Eng.* **2010**, *87*, 1537.

[208] J. Wiedemair, B. Balu, J.-S. Moon, D. W. Hess, B. Mizaikoff, C. Kranz, *Anal. Chem.* **2008**, *80*, 5260.

[209] A. Davoodi, A. Farzadi, J. Pan, C. Leygraf, Y. Zhu, *J. Electrochem. Soc.* **2008**, *155*, C474.

[210] H. Shin, P. J. Hesketh, B. Mizaikoff, C. Kranz, *Anal. Chem.* **2007**, *79*, 4769.

[211] M. Ludwig, C. Kranz, W. Schuhmann, H. E. Gaub, *Rev. Sci. Instrum.* **1995**, *66*, 2857.

[212] N. Baltes, L. Thouin, C. Amatore, J. Heinze, *Angew. Chem. Int. Ed.* **2004**, *43*, 1431.

[213] C. Cougnon, K. Bauer-Espindola, D. S. Fabre, J. Mauzeroll, *Anal. Chem.* **2009**, *81*, 3654.

[214] M. Etienne, A. Schulte, S. Mann, G. Jordan, I. D. Dietzel, W. Schuhmann, *Anal. Chem.* **2004**, *76*, 3682.

[215] B. Ballesteros Katemann, A. Schulte, W. Schuhmann, *Electroanalysis* **2004**, *16*, 60.

[216] R. Brunner, A. Bietsch, O. Hollricher, O. Marti, *Rev. Sci. Instrum.* **1997**, *68*, 1769.

[217] T. Yoshida, M. Iwaya, H. Ando, T. Oekermann, K. Nonomura, D. Schlettwein, D. Woehrle, H. Minoura, *Chem. Commun.* **2004**, 400.

[218] C. Nunes Kirchner, K. H. Hallmeier, R. Szargan, T. Raschke, C. Radehaus, G. Wittstock, *Electroanalysis* **2007**, *19*, 1023.

[219] T. Asmus, G. K. Wolf, *Nuclear Instruments & Methods in Physics Research, Section B Beam Interactions with Materials and Atoms* **2000**, *166-167*, 732.

[220] F.-R. F. Fan, C. Demaille, in *Scanning Electrochemical Microscopy* Eds.: A. J. Bard, M. V. Mirkin), Marcel Dekker, New York, Basel, **2001**, p. 75.

[221] Y. Shao, M. V. Mirkin, G. Fish, S. Kokotov, D. Palanker, A. Lewis, *Anal. Chem.* **1997**, *69*, 1627.

[222] B. Ballesteros Katemann, W. Schuhmann, *Electroanalysis* **2002**, *14*, 22.

[223] V. A. Macagno, M. C. Giordano, *Electrochim. Acta* **1969**, *14*, 335.

[224] M. T. Zanni, B. J. Greenblatt, A. V. Davis, D. M. Neumark, *J. Chem. Phys.* **1999**, *111*, 2991.

[225] M. Grätzel, *Pure Appl. Chem.* **2001**, *73*, 459.

[226] V. Ruiz, P. Liljeroth, B. M. Quinn, K. Kontturi, *Nano Lett.* **2003**, *3*, 1459.

[227] J. Zhang, A. L. Barker, D. Mandler, P. R. Unwin, *J. Am. Chem. Soc.* **2003**, *125*, 9312.

[228] Y. Shen, K. Nonomura, D. Schlettwein, C. Zhao, G. Wittstock, *Chem. Eur. J.* **2006**, *12*, 5832.

[229] J. Schnadt, P. A. Bruehwiler, L. Patthey, J. N. O'Shea, S. Soedergren, M. Odelius, R. Ahuja, O. Karis, M. Baessler, P. Persson, H. Siegbahn, S. Lunell, N. Martensson, *Nature* **2002**, *418*, 620.

[230] C. P. Andrieux, J. M. Saveant, *J. Electroanal. Chem.* **1982**, *142*, 1

[231] K. Nonomura, D. Komatsu, T. Yoshida, H. Minoura, D. Schlettwein, *Phys. Chem. Chem. Phys.* **2007**, *9*, 1843.

[232] T. Oekermann, T. Yoshida, H. Minoura, K. G. U. Wijayantha, L. M. Peter, *J. Phys. Chem. B* **2004**, *108*, 8364.

[233] E. A. Meulenkamp, *J. Phys. Chem. B* **1999**, *103*, 7831.

[234] G. Boschloo, A. Hagfeldt, *Acc. Chem. Res.* **2009**, *42*, 1819.

[235] B. H. Farnum, J. M. Gardner, G. J. Meyer, *Inorg. Chem.* **2010**, *49*, 10223.

[236] G. Boschloo, A. Hagfeldt, *Inorg. Chim. Acta* **2008**, *361*, 729.

[237] F. O. Laforge, T. Kakiuchi, F. Shigematsu, M. V. Mirkin, *J. Am. Chem. Soc.* **2004**, *126*, 15380.

[238] F. O. Laforge, T. Kakiuchi, F. Shigematsu, M. V. Mirkin, *Langmuir* **2006**, *22*, 10705.

[239] K. R. J. Lovelock, F. N. Cowling, A. W. Taylor, P. Licence, D. A. Walsh, *J. Phys. Chem. B* **2010**, *114*, 4442.

[240] M. Carano, A. M. Bond, *Aust. J. Chem.* **2007**, *60*, 29.

[241] A. W. Taylor, F. Qiu, J. Hu, P. Licence, D. A. Walsh, *J. Phys. Chem. B* **2008**, *112*, 13292.

[242] J. Ghilane, C. Lagrost, P. Hapiot, *Anal. Chem.* **2007**, *79*, 7383.

[243] D. A. Walsh, K. R. J. Lovelock, P. Licence, *Chem. Soc. Rev.* **2010**, *39*, 4185.

[244] P. Wang, S. M. Zakeeruddin, J. E. Moser, M. K. Nazeeruddin, T. Sekiguchi, M. Grätzel, *Nat. Mater.* **2003**, *2*, 402.

[245] A. Fukui, R. Komiya, R. Yamanaka, A. Islam, L. Han, *Sol. Energy Mater. Sol. Cells* **2006**, *90*, 649.

[246] Z. Kebede, S.-E. Lindquist, *Sol. Energy Mater. Sol. Cells* **1999**, *57*, 259.

[247] P. Wachter, C. Schreiner, M. Zistler, D. Gerhard, P. Wasserscheid, H. J. Gores, *Microchim. Acta* **2008**, *160*, 125.

[248] Z. Yu, M. Gorlov, G. Boschloo, L. Kloo, *J. Phys. Chem. C* **2010**, *114*, 22330.

[249] S.-H. A. Lee, A.-M. S. Jackson, A. Hess, S.-T. Fei, S. M. Pursel, J. Basham, C. A. Grimes, M. W. Horn, H. R. Allcock, T. E. Mallouk, *J. Phys. Chem. C* **2010**, *114*, 15234.

[250] S. Nakade, T. Kanzaki, W. Kubo, T. Kitamura, Y. Wada, S. Yanagida, *J. Phys. Chem. B* **2005**, *109*, 3480.

[251] P. Wang, S. M. Zakeeruddin, J.-E. Moser, M. Grätzel, *J. Phys. Chem. B* **2003**, *107*, 13280.

[252] F. Fabregat-Santiago, J. Bisquert, E. Palomares, L. Otero, D. Kuang, S. M. Zakeeruddin, M. Grätzel, *J. Phys. Chem. C* **2007**, *111*, 6550.

[253] P. Wang, C. Klein, R. Humphry-Baker, M. Zakeeruddin Shaik, M. Gratzel, *J. Am. Chem. Soc.* **2005**, *127*, 808.

[254] M. Yanagida, K. Miyamoto, K. Sayama, K. Kasuga, M. Kurashige, Y. Abe, H. Sugihara, *J. Phys. Chem. C* **2007**, *111*, 201.

[255] A. N. M. Green, E. Palomares, S. A. Haque, J. M. Kroon, J. R. Durrant, *J. Phys. Chem. B* **2005**, *109*, 12525.

[256] H. Usui, H. Matsui, N. Tanabe, S. Yanagida, *J. Photochem. Photobiol., A* **2004**, *164*, 97.

[257] K. Keis, E. Magnusson, H. Lindstrom, S.-E. Lindquist, A. Hagfeldt, *Sol. Energy Mater. Sol. Cells* **2002**, *73*, 51.

[258] Y. Tachibana, K. Hara, K. Sayama, H. Arakawa, *Chem. Mater.* **2002**, *14*, 2527.

[259] M. Pastore, F. De Angelis, *ACS Nano* **2010**, *4*, 556.

[260] D. F. Watson, G. J. Meyer, *Annu. Rev. Phys. Chem.* **2005**, *56*, 119.

[261] S. Uchida, *Vol. 2009*, **2009**, p. Dye collection for DSSC.

[262] S. Peulon, D. Lincot, *J. Electrochem. Soc.* **1998**, *145*, 864.

[263] L. Peter, *Acc. Chem. Res.* **2009**, *42*, 1839.

[264] J. Bisquert, F. Fabregat-Santiago, I. Mora-Sero, G. Garcia-Belmonte, S. Gimenez, *J. Phys. Chem. C* **2009**, *113*, 17278.

[265] A. Fattori, L. M. Peter, H. Wang, H. Miura, F. Marken, *J. Phys. Chem. C* **2010**, *114*, 11822.

[266] C. Zhao, G. Wittstock, *Angew. Chem.* **2004**, *116*, 4264.

[267] M. Bearns, H. Hofmann, A. Renken, in *Chemische Reaktionstechnik: Lehrbuch der Technischen Chemie Band 1, Vol. 3* Georg Thieme Verlag, Stuttgart, New York, **1999**, p. 134.

[268] C. Nunes Kirchner, M. Träuble, G. Wittstock, *Anal. Chem.* **2010**, *82*, 2626.

[269] M. Burchardt, M. Träuble, G. Wittstock, *Anal. Chem.* **2009**, *81*, 4857.

[270] Y. Shen, M. Träuble, G. Wittstock, *Anal. Chem.* **2008**, *80*, 750.

[271] A. J. Bard, G. Denuault, R. A. Friesner, B. C. Dornblaser, L. S. Tuckerman, *Anal. Chem.* **1991**, *63*, 1282.

[272] M. J. W. Ludden, J. K. Sinha, G. Wittstock, D. N. Reinhoudt, J. Huskens, *Organic & Biomolecular Chemistry* **2008**, *6*, 1553.

[273] S. Arimoto, H. Kageyama, T. Torimoto, S. Kuwabata, *Electrochem. Commun.* **2008**, *10*, 1901.

List of own publications

[A1 Yan Shen, Ushula Mengesha Tefashe, Kazuteru Nonomura, Thomas Loewenstein, Derck Schlettwein, Gunther Wittstock, “Photoelectrochemical Kinetics of Eosin Y-sensitized Zinc Oxide Films Investigated by Scanning Electrochemical Microscopy under Illumination with Different LED”, *Electrochim. Acta*, 55 (**2009**) 458-464. doi:10.1016/j.electacta.2009.08.062

[A2] Ushula Mengesha Tefashe, Thomas Loewenstein, Hidetoshi Miura, Derck Schlettwein, Gunther Wittstock, “Scanning Electrochemical Microscope Studies of Dye Regeneration in Indoline (D149)-sensitized ZnO Photoelectrochemical Cells”, *J. Electroanal. Chem.*, 650 (**2010**) 24-30. doi:10.1016/j.jelechem.2010.09.014

[A3] Andreas Lesch, Dmitry Momotenko, Fernando Cortés-Salazar, Ingo Wirth, Ushula Mengesha Tefashe, Frank Meiners, Britta Vaske Hubert H. Girault and Gunther Wittstock “Fabrication of Soft Gold Microelectrode Arrays as Probes for Scanning Electrochemical Microscopy”, *J. Electroanal. Chem.*, 666 **(2012)** 52-61**,** doi:10.1016/j.jelechem.2011.12.005

[A4] Ushula Mengesha Tefashe**,** Kazuteru Nonomura, Nick Vlachopoulos, Anders Hagfeldt, Gunther Wittstock “Effect of Cation on Dye Regeneration Kinetics of N719-sensitized TiO_2 Films in Acetonitrile-based and Ionic-liquid-based Electrolytes Investigated by Scanning Electrochemical Microscopy”, *J. Phys. Chem. C*, 116 **(2012)** 4316-4323 doi:10.1021/jp207671w

[A5] Ushula Mengesha Tefashe, Melanie Rudolph, Thomas Lowenstein, Derck Schlettwein, Gunther Wittstock, “Photovoltaic Charactteristics and Dye Regeneration Kinetics in D149-Sensitized ZnO with Varied Dye Loading and Film Thickness” ***Submitted for publication***

[A6] Afriyanti Sumboja, Ushula Mengesha Tefashe, Gunther Wittstock, Pooi See Lee “Probing the Kinetics Properties of MnO_2 with Scanning Electrochemical Microscope for Supercapacitor Application” ***J. Power Sources,*** 207 **(2012)** 205-211. http://dx.doi.org/10.1016/j.jpowsour.2012.01.153

[A7] Ushula Mengesha Tefashe, Gunther Wittstock, “Quantitative Characterization of Shear Force Regulation for Scanning Electrochemical Microscopy” ***Submitted for publication***

Publication before starting this PhD work

[A8] Ushula Mengesha and Teketel Yohannes, “Photoelectrochemical Solar Energy Conversion Based on Blend of Poly(3-hexylthiophene) and Fullerene”, *Sol. Energy Mater. Sol. Cells*, 90 (**2006**) 3508 – 3519. doi:10.1016/j.solmat.2006.05.010

Conferences and workshops

March 2009 Oral presentation at the 7th Spring meeting of ISE, Szczyrk, Poland.

Topic: Incident Light Intensity Dependence of the Kinetics of Redox Reactions at Dye Sensitized ZnO Electrodes Investigated by Scanning Electrochemical Microscopy.

September 2010 Oral presentation at the Electrochemistry conference in Bochum, Germany.

Topic: Scanning Electrochemical Microscope Studies of Dye Regeneration in Indoline (D149)-sensitized ZnO Photoelectrochemical Cells.

May 2011 Oral presentation at the ElecNano4-7th ECHEMS, Paris, France.

Topic: High Resolution Studies of Dye-Sensitized Solar Cell Electrodes with Scanning Electrochemical Microscopy.

May 2009 Poster presentation at the Bunsentagung, Cologne, Germany.

Topic: Scanning Electrochemical Microscopy Study of Dye Regeneration Processes in Dye Sensitized Solar Cells.

September 2011 Poster presentation at the GDCh Wissenschaftsforum, Bremen, Germany.

Topic: Kinetics at the Illuminated Dye/TiO_2-electrolyte Interface Investigated by Scanning Electrochemical Microscopy.

Curriculum vitae

PERSONAL DATA

Name	Ushula Mengesha Tefashe
Date of birth	13.10.1978
Place of birth	Wolayita, Ethiopia
Marital Status	Married to Mrs. Tigist Yohannes Menta, one son
Language	Amharic (Mother tongue), Wolayita (Mother tongue), English (good), German (Conversational)

EDUCATION

04/2008-01/2012	PhD student, specialization in Electrochemistry, Department of Physical Chemistry, Carl von Ossietzky University of Oldenburg, Germany.
08/2003-07/2005	M.Sc. in Chemistry, specialization in Physical Chemistry, Addis Ababa University, Ethiopia. *Graduation*: with Distinction
07/1998-07/2002	Bachelor Degree in Chemistry, Bahir Dar University, Ethiopia. *Graduation*: First-Class Standing with Distinction
07/1995-07/1998	High School at Bodditi Senior Secondary School, Wolayita, Ethiopia. *Graduation*: with Great Distinction
08/1993-06/1995	Junior Secondary School, Bodditi, Wolayita, Ethiopia
07/1987-06/1993	Primary School at Mayo Kote Elementary School, Wolayita, Ethiopia

PROFESSIONAL EXPERIENCE

Since 04/2008	Scientific co-worker in the group of Prof. Dr. Gunther Wittstock at the Department of Physical Chemistry, University of Oldenburg, Germany.
07/2005 – 09/2007	Lecturer at the Department of Chemistry, Bahir Dar University, Ethiopia
07/2002 – 08/2003	Graduate Assistant at the Department of Chemistry, Bahir Dar University, Ethiopia

FELLOWSHIPS AND AWARDS

- German Academic Exchange Service (DAAD) Scholarship
- Outstanding Studentship Award of Faculty of Science, Bahir Dar University, 2002

Erklärung

Ich versichere hiermit, dass ich diese Arbeit selbstständig verfasst und nur die angegebenen Quellen und Hilfsmittel benutzt habe. Aus der Dissertation sind die auf der folgenden Seite genannten Veröffentlichungen hervorgegangen. Die Dissertation hat weder zu Teilen noch in Gänze einer anderen wissenschaftlichen Hochschule zur Begutachtung in einem Promotionsverfahren vorgelegen.

Oldenburg, den 30. 01. 2012

Ushula Mengesha Tefashe